UCSF
UC San Francisco Electronic Theses and Dissertations

Title
The role of cortical astrocytes in sleep regulation

Permalink
https://escholarship.org/uc/item/7x0800gj

Author
Vaidyanathan, Trisha Varma

Publication Date
2021

Peer reviewed|Thesis/dissertation

eScholarship.org Powered by the California Digital Library
University of California

The role of cortical astrocytes in sleep regulation

by
Trisha Varma Vaidyanathan

DISSERTATION
Submitted in partial satisfaction of the requirements for degree of
DOCTOR OF PHILOSOPHY

in

Neuroscience

in the

GRADUATE DIVISION
of the
UNIVERSITY OF CALIFORNIA, SAN FRANCISCO

Approved:

DocuSigned by:
Karunesh Ganguly
537133AC2605407...

Karunesh Ganguly
Chair

DocuSigned by:
Kira Poskanzer

Kira Poskanzer

DocuSigned by:
Vikaas Sohal
[illegible]...

Vikaas Sohal

DocuSigned by:
Massimo Scanziani
4AF406E430B7472...

Massimo Scanziani

Committee Members

Copyright 2021

by

Trisha Varma Vaidyanathan

Acknowledgements

There are many people who have provided me with both scientific and personal guidance, support, and love throughout my graduate studies. Without all of these incredible people, and many others, the graduate research presented here would not have been possible.

First, I would like to thank my PhD advisor and mentor, Kira Poskanzer. Kira has taught me, by example, how to be an effective, kind, and thoughtful mentor. Kira has demonstrated how to be a strong leader and she has taught me to be a careful and critical scientist. She has accomplished this while remaining an incredibly considerate, supportive, and uplifting mentor. Her optimism, her kindness, and her intuitive mentoring have pushed me through the most difficult of obstacles during this process and have given me the confidence to move forward from my PhD despite any upcoming obstacles.

Next, I would like to thank the members of my qualifying and thesis committee: Karunesh Ganguly, Massimo Scanziani, Vikaas Sohal, Anna Molofsky, and Mazen Kheirbek, for their feedback and guidance as my PhD has changed and taken shape through these years.

I would also like to thank members of the Poskanzer Lab, both past and present. I would like to thank Gregory Chin for his help setting up much of our lab, Nicole DelRosso for her contribution to AQuA and technical support, Sae Yokoyama for her unbelievable work on the sleep projects, Cameron Holman for his help with the histamine studies, and Vincent Tse for his ongoing help and support. I would like to thank Michael Reitman for the help he has provided throughout. I would also like to thank Silvia Pittolo for her guidance throughout and willingness to help on pharmacology experiments. I would like to thank Max Collard for his contributions to this work and our always exciting analysis conversations. I would also like to thank Drew

Willoughby and Caitlin Durkee for all their help establishing fiber photometry in the lab and for making the process so much fun. I would also like to thank Charlotte Taylor for her fruitful discussions and contribution to the histamine project. I would like to thank Alba Peinado for her constant mentorship and guidance, and for patiently teaching me about optics. Lastly, I would like to thank Michelle Cahill for being my primary source of support and friendship in the lab, I am so grateful to have had her by my side throughout this process.

I would also like to thank the lab of Guoqiang Yu, including Yizhi Wang and Xuelong Mi at the Virgina Polytechnic Institute and State University for all of their contributions to the development of AQuA, a truly tremendous step in my PhD.

Next, I would like to thank the class of 2015 and my many other friends at UCSF. Specifically, I would like to thank Leah Dorman, Ben Mansky, Match McGregor, Michael Reitman, Frances Cho, Selin Schamiloglu, Perry Spratt, Stephanie Holden, Lindsay Osso, and Stefan Lemke. All of these incredible scientists have not only provided scientific support as co-workers, but also a life-long friendship that I will always be grateful for.

I would like to specifically thank Selin Schamiloglu for her deep, unwavering friendship throughout these years. It is difficult to imagine this process without her and I am so grateful to have had the support of such a strong, kind, and generous woman. I would also like to thank Flora Champenois and Afsaneh Mortazavi, two incredible women I have had as my primary support system since I first began this journey ten years ago. They have lifted me up and empowered me to achieve this milestone.

Next, I would like to thank my family. I am fortunate to have had my grandparents as an incredible source of support throughout my life. I would especially like to thank my grandmother Nirmala Vaidyanathan for being my role model throughout my life. I would also like to thank

my brother Kyle Vaidyanathan for providing laughter throughout my life. Lastly, I would like to thank my parents Sheena and Vijay Vaidyanathan. Their unyielding love and support throughout my life has allowed me to move through graduate school, and their hard work and passion have set an example that I use as a guidepost for my own life.

Lastly, I would like to thank Stefan Lemke. Stefan has exemplified the mix of scientific and personal support I have received throughout this process. I would like to thank him for always making me celebrate my accomplishments – big or small, his unwavering optimism, his ability to make every aspect of this process fun, and for his unyielding love throughout my time with him.

Contributions

Chapter 1 is written by Trisha Vaidyanathan.

Chapter 2 is reproduced in entirety, with the exception of a few sections that were excluded, from:

> *Wang Y, DelRosso NV, Vaidyanathan TV, Cahill MK, Reitman ME, Pittolo S, Mi X, Yu G, Poskanzer KE. Accurate quantification of astrocyte and neurotransmitter fluorescence dynamics for single-cell and population-level physiology. Nat Neurosci. 2019 Nov;22(11):1936-1944. doi: 10.1038/s41593-019-0492-2.*

K.E.P. and G.Y. conceived and designed the study. Y.W. and G.Y. designed and implemented the AQuA algorithm, software, and simulations. N.V.D. analyzed all imaging data and provided critical conceptual input to software design. T.V.V. carried out GluSnFR experiments; M.K.C. performed *ex vivo* Ca^{2+}, GABASnFR, and GluSnFR experiments; M.E.R. performed *in vivo* Ca^{2+} imaging experiments; and S.P. performed GRAB-NE experiments. X.M. implemented the Java version of the software, and built and tested the 3D prototype. K.E.P supervised the experimental team. G.Y. supervised the computational team. Y.W., N.V.D., K.E.P, and G.Y. wrote the manuscript with input from all authors.

Chapter 3 is reproduced in entirety from:

> *Vaidyanathan TV, Collard M, Yokoyama S, Reitman ME, Poskanzer KE. Cortical astrocytes independently regulate sleep depth and duration via separate GPCR pathways. Elife. 2021 Mar 17;10:e63329. doi: 10.7554/eLife.63329.*

K.E.P and T.V.V. conceived and designed the study, and wrote the manuscript with input from all authors. T.V.V. carried out all imaging/electrophysiology experiments and analyzed the data. M.C. performed clustering and coherence analyses. S.Y. performed immunostaining experiments and analyzed the resulting images. M.E.R. contributed insight and analysis code related to low-frequency dynamics around astrocyte events.

Chapter 4 is written by Trisha Vaidyanathan and contains unpublished findings with contributions from Trisha Vaidyanathan, Charlotte R. Taylor, Omer Bayraktar, and Kira Poskanzer.

Chapter 5 is written by Trisha Vaidyanathan and contains unpublished findings with contributions from Trisha Vaidyanathan, Vincent Tse, and Kira Poskanzer.

The role of cortical astrocytes in sleep regulation

Trisha Varma Vaidyanathan

Abstract

Sleep is critical for the survival of all animals and serves many vital functions throughout the body, including brain development, cognition, immune function, and metabolic control. Indeed, sleep disorders such as insomnia can have devastating consequences on human health. Additionally, emerging evidence suggests a complex, bi-causal relationship between sleep disturbances and neuropsychiatric disorders. Despite the importance of proper sleep-wake regulation, it remains unclear how exactly the brain controls sleep-wake transitions. Historically, the focus on sleep regulation has focused exclusively on neurons, but astrocytes, the largest class of non-neuronal cells in the brain, are also positioned to play a critical role. The primary focus of this dissertation is to explore the complex role of cortical astrocytes in sleep regulation. First, we present a novel tool that allows for the accurate quantification of astrocyte calcium dynamics (Chapter 2), an essential step in studying astrocyte physiology in the context of sleep. Next, we demonstrate, for the first time, that astrocytes play a causal role in regulating distinct features of sleep through different GPCR pathways (Chapter 3). Lastly, we begin to explore the mechanistic pathways by which astrocytes regulate sleep. We explore the neuromodulator histamine as a candidate endogenous ligand for astrocytic control of sleep (Chapter 4) and we investigate astrocytic regulation of extracellular glutamate and GABA, putative functional astrocyte outputs of Gi-GPCR signaling (Chapter 5). Together, we present evidence that cortical astrocytes are a vital part of the sleep regulatory system, bringing us closer to understanding this critical behavior.

Table of Contents

Chapter 1: Introduction *1*

The anatomy of sleep 2

Neuromodulatory control of sleep 3

Cortical control of sleep 5

Glutamatergic and GABAergic contributions to slow wave activity 6

The emergence of astrocytes and astrocyte physiology 7

Astrocytes are well positioned to regulate cortical networks 9

Astrocytic functions associated with sleep 10

References 12

Chapter 2: Flexible and accurate quantification of astrocyte activity reveals novel single-cell and population-level physiology *21*

Abstract 21

Introduction 21

Results 24

Discussion 34

Methods 38

Figures 44

References 66

Chapter 3: Cortical astrocytes independently regulate sleep depth and duration via separate GPCR pathways ***70***

Abstract 70

Introduction 70

Results 74

Discussion 90

Methods 97

Figures 107

References 130

Chapter 4: Astrocytic regulation of sleep via cortical histaminergic signaling ***143***

Abstract 143

Introduction 143

Results 146

Discussion 149

Methods 154

Figures 159

References 163

Chapter 5: Astrocytic Gi-GPCR activation changes extracellular glutamate, but not GABA, during visual stimuli ***170***

Abstract 170

Introduction 171

Results 172

Discussion 176

Methods 179

Figures 185

References 191

List of Figures

Chapter 1:

Figure 1.1 Dissertation schematic 2

Chapter 2:

Figure 2.1. AquA-based event detection 44

Figure 2.2. AquA features capture heterogeneities among single astrocytes 46

Figure 2.3. AquA resolves astrocytic Ca^{2+} propagation directionality across scales 48

Figure 2.4. AquA-based detection of extracellular dynamics via astrocytic and neuronal expression of genetically encoded neurotransmitter sensors 50

Figure 2.5: Eight steps in the AquA algorithm 51

Figure 2.6: Schematic illustration of three major modules in AquA algorithm 52

Figure 2.7: Limitations of thresholding-based analysis 54

Figure 2.8: AquA features enable detailed Ca^{2+} activity plots 56

Figure 2.9: Distribution of Ca^{2+} event features 58

Figure 2.10: Cluster analysis on features generated from three spatial footprint methods 60

Figure 2.11: Defining *in vivo* burst and inter-burst events 62

Figure 2.12: Comparison of AQuA and Caltracer for event detection of astrocytic GluSnFR signals 63

Figure 2.13: AQuA performance on simulated 3D datasets 64

Chapter 3:

Figure 3.1: Cortical astrocyte Ca^{2+} event rate and SWA are negatively correlated across behavioral states 107

Figure 3.2. PCA reveals that behavioral states can be characterized by unique properties of astrocyte Ca^{2+} events 109

Figure 3.3. Astrocyte Ca^{2+} events characterize transitions from low to high SWA 110

Figure 3.4. Astrocytic Gi-DREADD-driven Ca^{2+} increases are sufficient to increase SWA during sleep 111

Figure 3.5. Astrocyte-specific expression of Gi-DREADDs across ipsilateral and contralateral cortex 113

Figure 3.6. Systemic administration of CNO does not affect astrocyte Ca^{2+} dynamics, SWA, or sleep and wake behavior 115

Figure 3.7. PCA shows that Gi-DREADD activation causes increased changes in Ca^{2+} event properties during sleep compared to wake 117

Figure 3.8. Astrocytic Gi-DREADD activation regulates local delta waves more than slow oscillations 119

Figure 3.9. Gi-DREADD activation does not affect SWA in stationary wake, but changes peak and trough delta wave amplitude during sleep 121

Figure 3.10. Cortical astrocyte Ca^{2+} dynamics exhibit bidirectional changes preceding sleep and wake transitions 122

Figure 3.11 Gq-induced Ca^{2+} is necessary for sleep-wake transitions 123

Figure 3.12. Astrocyte-specific expression of Gq-DREADDs across ipsilateral

and contralateral cortex 125

Figure 3.13. Gq-DREADD activation suppresses sleep-wake transitions by increasing bout length and decreasing bout number 127

Figure 3.14 V1 manipulation of astrocyte Ca^{2+} alters SWA in contralateral frontal cortex via changes in slow oscillations..... 128

Chapter 4:

Figure 4.1. Histaminergic axon terminals in the cortex exhibit sleep-wake dynamics..... 159

Figure 4.2: Histamine increases astrocyte Ca^{2+} via H_1Rs 160

Figure 4.3: Histaminergic signaling precedes cortical astrocyte activity *in vivo*..... 161

Chapter 5:

Figure 5.1: *In vivo* recording of spontaneous and stimulus-evoked extracellular glutamate and GABA in freely moving mice..... 185

Figure 5.2: No change in spontaneous iGluSnFR or iGABASnFR dynamics were observed after CNO administration..... 187

Figure 5.3: Gi-DREADD activation does not change the decay time of stimulus-evoked iGluSnFR or iGABASnFR 188

Figure 5.4: Gi-DREADD activation increases the magnitude of stimulus-evoked iGluSnFR but not iGABASnFR 190

Chapter 1:
Introduction

Conserved across the animal kingdom, all species regularly transition between sleep and wake with relative speed and ease. Humans spend about a third of their life in sleep. Indeed, sleep is necessary for a multitude of vital functions including brain development, energy conservation, immune response, cognition, learning, and memory[1]. As a result, proper regulation of sleep is critical for health and survival. This is exemplified in sleep disorders such as insomnia and narcolepsy, with symptoms ranging from cognitive decline to immune dysfunction[2–5]. Sleep disorders are also commonly co-morbid with other neurological diseases and may underlie many disease symptoms[6]. A precise understanding of how the brain transitions between sleep and wake is a crucial, yet missing, step towards successful treatment for these disorders.

Historically, the study of sleep-wake regulation has focused exclusively on neurons. Astrocytes – the largest class of non-neuronal cells in the brain – are also situated to play critical roles in sleep regulation. Yet, the role of astrocytes in sleep regulation is not fully understood. **This dissertation explores the role of cortical astrocytes in sleep regulation and demonstrates that cortical astrocytes serve as a central hub, processing sleep-wake cues and regulating distinct sleep features.**

In chapter 2, we develop a novel tool to accurately quantify astrocyte Ca^{2+} dynamics (**Fig. 1.1a**). This tool was a critical step to study astrocyte physiology *in vivo* in natural sleep and was used for the subsequent chapters. In chapter 3, we demonstrate that astrocytes actively regulate sleep and show that astrocytes independently regulate sleep depth and duration via separate GPCR pathways (**Fig. 1.1b**). In chapter 4, we explore histamine, a candidate endogenous ligand for the astrocytic regulation of sleep (**Fig. 1.1a**). Lastly, in chapter 5 we investigate two putative

functional astrocytic outputs of Gi-GPCR activation, the regulation of extracellular glutamate and GABA (**Fig. 1.1a**).

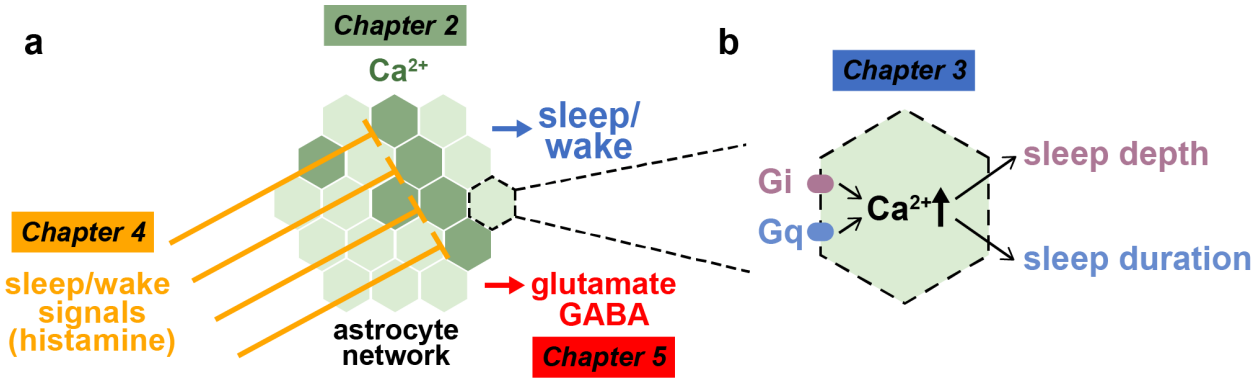

Figure 1.1: Dissertation schematic.
(a) We examined the cortical astrocyte network and its role in sleep and wake. In chapter 2 we developed a novel tool to analyze astrocyte Ca^{2+} dynamics, in chapter 4 we examined putative inputs to the astrocyte network, and in chapter 5 we examined putative outputs of the astrocyte network. **(b)** In chapter 3, we critically demonstrate that cortical astrocytes can actively regulate distinct features of sleep through different GPCR pathways.

The anatomy of sleep

While it is thought that all animals sleep, sleep can look very different across different species[7,8]. Broadly, sleep is defined as a behavioral state characterized by low arousal. In an effort to create a robust definition of sleep, a set of criteria have been put forth: (1) behavioral quiescence, (2) decreased responsiveness to stimuli, (3) rapid reversibility, which differentiates sleep from anesthetized states or coma, and (4) homeostatic regulation, in which lost sleep is compensated for upon recovery[7–9]. Although not always feasible or required, the gold standard of identifying sleep is through the use of electrophysiology recordings in the brain, such as an electroencephalogram (EEG).

Sleep is subdivided into distinct stages. As humans progress through the night, we cycle through each stage multiple times. The exact definition of each stage varies across fields and becomes further inconsistent with different model organisms. However, sleep can broadly be divided into two main stages: Rapid-eye-movement (REM) and non-rapid-eye-movement (NREM) sleep. These two stages are defined using EEG and electromyogram (EMG) recordings. REM sleep is characterized by relative desynchrony in the EEG and low, or none, muscle tone in the EMG. In contrast, NREM is defined by a characteristic synchronized rhythm in the low-frequency band (0-4Hz), termed slow-wave activity (SWA). In human sleep, NREM is further subdivided into light sleep (stage 1-2) and deep sleep, also referred to as slow-wave sleep (SWS) (stage 3-4). In rodent sleep, however, it is customary to not subdivide NREM sleep into these further stages and NREM and SWS are often used interchangeably. Different sleep stages have been linked with different sleep functions. However, some have recommended moving away from a stage-based analysis in order to avoid inconsistent conclusions across model organisms[10].

Neuromodulatory control of sleep

In the 1920's, Constantin Von Economo first identified regions in the brain responsible for the control of sleep and wake. Von Economo studied patients with encephalitis and noted that the encephalitis cases associated with lesions to anterior hypothalamus resulted in insomnia, while lesions to the posterior hypothalamus resulted in hypersomnia. He proposed that the brainstem promoted wakefulness while the anterior hypothalamus opposed these wake forces during sleep[11]. This seminal work has since been refined to result in our current understanding of the sleep-wake control centers, a model that is often referred to as a "flip-flop" switch for sleep control[12].

The wake-promoting centers of the brain are located in the brainstem and consist of neurons that release neuromodulators, including norepinephrine in the locus coeruleus, serotonin in the raphe nucleus, histamine in the tuberomammillary nucleus, dopamine in the ventral tegmental area, and acetylcholine in the pedunculopontine and laterodorsal tegmental nuclei. Sleep-promoting centers of the brain consist of the ventrolateral preoptic nucleus (VLPO) and the median preoptic nucleus (MPO). These sleep-promoting centers send inhibitory GABAergic projections to the wake-promoting centers in order to initiate sleep and inhibit arousal during sleep[12–15]. However, it has also been suggested that this model is oversimplified. Indeed, lesioning various parts of the arousal system has limited effects on sleep[13,16–20] and recent cell type specific dissection within these nuclei has revealed more complex circuitry.

Beyond the "slow" neuromodulators, the wake-promoting centers in the brainstem also contain intermingled "fast" neurotransmitters of glutamate and GABA. Genetic tools have allowed cell type specific dissection of these regions and it has been proposed that these fast neurotransmitters play more important roles in the control of these different neuromodulatory nuclei[13]. For example, it has been demonstrated that the sleep-promoting effects of the preoptic area may work specifically through GABAergic neurons that project to the histaminergic neurons in the tuberomammillary nucleus[21].

In addition to the wake- and sleep-promoting centers that have been discussed within the "flip-flop" switch, other brainstem regions are known to be critical for sleep-wake regulation. Orexinergic neurons in the dorsolateral hypothalamus play a central role in sleep regulation[22]. Activation of orexin neurons promotes wakefulness[23] and their loss is associated with the sleep disorder narcolepsy[24,25]. Orexinergic neurons activate the wake-promoting nuclei and, interestingly, they receive indirect circadian inputs from the suprachiasmatic nucleus. The basal

forebrain, a primary source of acetylcholine in the brain, also contains intermingled GABAergic neurons that are both sleep-promoting and wake-promoting[26] and it's been suggested that sleep-wake control relies also on reciprocal inhibition with the basal forebrain[14].

While the exact circuitry within these brainstem and hypothalamic nuclei remain unclear, they play a critical role in sleep-wake control. Ultimately, however, sleep and wake are defined by patterns of activity that we record in the cortex. Many of these neuromodulators send direct projections to the cortex and to the thalamus[15], but how they influence cortical circuitry to change these patterns of neural activity is relatively understudied. In Chapter 4, we address this gap by specifically studying the role of histaminergic cortical projections (**Fig. 1.1a**).

Cortical control of sleep

All stages within sleep are defined by distinct oscillatory patterns of neurons within the cortex and, further, these oscillations are capable of being generated by the cortex[10,27]. As such, the cortex is likely a critical region within the distributed circuitry that underlies sleep-wake control. However, the role of the cortex in physiological sleep is relatively understudied when compared to subcortical regions like the neuromodulatory nuclei within the brainstem and the hypothalamus.

During NREM sleep, the slow, synchronous pattern of SWA is thought to arise from thalamocortical loops. However, it likely has a strong cortical origin. Slow oscillations persist within the cortex after the thalamus has been removed[28] and in isolated cortical slabs[29,30]. Activating neurons within the cortex is also sufficient to generate slow waves[31–33]. Additionally, it has recently become appreciated that sleep features can vary heterogeneously across the cortex in a local, use-dependent manner[34–37], further suggesting sleep regulation lies within the cortex.

While the cortex has the capacity to produce sleep oscillations, it has not been demonstrated to be the mechanism used during physiological sleep nor is it understood how the cortex is integrated into other known sleep-wake regulatory areas.

Beyond having the capacity to produce sleep oscillations, recent evidence has suggested the cortex plays a role in functional regulation of sleep through sleep homeostasis. Silencing layer V pyramidal neurons within the cortex reduced the normal homeostatic response to sleep deprivation[38]. Additionally, GABAergic neurons within the cortex that express neuronal nitric oxide synthase (nNOS neurons) appear to contribute to the homeostatic regulation of sleep as well[39]. Lastly, interneurons within the prefrontal cortex can initiate sleep behavior and NREM sleep through long-range projections to the hypothalamus[40]. Together, this recent work is beginning to reveal the complex and distributed circuitry that likely underlies cortical control of sleep.

Glutamatergic and GABAergic contributions to slow wave activity

SWA is characterized by alternating active UP states and silent DOWN states in the cortex. UP states contain sustained depolarization and enhanced firing across neural populations. DOWN states are characterized by membrane hyperpolarization and reduced firing. Much of the work on how UP and DOWN states are initiated and terminated have focused on glutamate and GABA, are the main excitatory and inhibitory neurotransmitters, respectively.

The regulation of UP states has been tightly linked to glutamate and thought to depend on recurrent excitation within the cortex amongst corticocortical connections. With respect to UP state initiation, focal glutamate application in *ex vivo* cortical slabs was sufficient to initiate propagating UP states[31]. Similarly, targeted glutamate release using 2-photon uncaging increased

the rate of UP states[41]. On the other hand, the mechanism underlying the termination of UP states, and subsequent initiation of DOWN states, has been more elusive. Previously, it was thought that GABAergic inhibition was not involved and that UP states were terminated through disfacilitation and K^+ conductances[42]. Evidence against inhibition also came from early recordings showing an absence of an increase in inhibition towards the end of UP states[43]. However, it was noted that the onset of the DOWN state was much more synchronized across the cortex[44], while the UP state often propagated across cortical neurons in a wake-like fashion. This synchrony in the onset of silence suggested an active role of inhibition.

Recently, many studies have found evidence for an active role of GABAergic inhibition in generating SWA. Contrary to early studies, bursts of inhibitory activity have been found to precede the DOWN state using newer technologies, including 2-photon calcium imaging in natural sleep[45,46]. Optogenetic manipulation of interneuron sub-types have also demonstrated a causal role for inhibition in the initiation of both DOWN and UP states[47], suggesting a new model in which UP states are generated due to the absence of inhibition as opposed to the other way around. These recent advances speak to the importance of re-examining mechanistic models with new technological advances and the importance of studying these electrophysiological phenomena in physiological states as well (i.e. *in vivo* and natural sleep). In Chapter 5, we focus on the regulation of glutamate and GABA with respect to astrocytes (**Fig. 1.1a**) in the hopes of reconciling these findings on UP and DOWN state initiation with that of astrocytes.

The emergence of astrocytes and astrocyte physiology

Astrocytes are the largest non-neuronal cell type in the brain. Historically, it has been assumed that astrocytes, despite their number and extensive reach within the brain, play a

minimal role in brain function. It was observed early-on that astrocytes were electrically silent and did not seem to exhibit fluctuations in membrane potential upon any stimulation[48], in stark contrast with neurons. As such, it was easy to conclude that astrocytes did not play an important role in brain computation or function.

In 1989 it was discovered that astrocytes express functional receptors for the primary excitatory neurotransmitter glutamate, but it wasn't known what function these receptors served. Shortly after this discovery, in the 1990s, it was first observed that astrocytes do in fact exhibit excitability. Instead of electrical signals, astrocytes exhibited changes in intracellular Ca^{2+} concentration[49]. These early findings began what is called an "astrocyte revolution"[50] and astrocyte Ca^{2+} has since been studied in many different regions, brain preparations, and model organisms[51,52] and it is increasingly clear that astrocytes play critical roles in many different brain functions and behavior.

Most of the studies on astrocyte function have focused on their role at single synapses. This led to the description of the "tripartite synapse"[53], referring to the existence and active role of astrocytic processes at neuronal synapses. Astrocytes express a wide range of neurotransmitter receptors and can respond to neurotransmitters with Ca^{2+} increases[54]. Many of these receptors are G-protein coupled receptors (GPCRs) that lead to Ca^{2+} increases from the release of Ca^{2+} from intracellular stores in an inositol triphosphate (IP_3) dependent manner[55,56]. Beyond responding to synaptic activity, it has been critically demonstrated that astrocytes have a reciprocal relationship with synapses: Astrocytes can also modulate synaptic transmission. How exactly astrocytes do this has been an active debate. Specifically, it remains controversial whether astrocytes release neurotransmitters ("gliotransmitters"), how release of these transmitters occur, and what types of gliotransmitters exist[57].

Beyond gliotransmission, however, there are many established mechanisms of astrocytic control at the synapse. Astrocytes extend processes that make contact with blood vessels (termed "end feet") and participate in a lactate shuttling system via glucose transporters. Through these mechanisms, astrocytes are thought to be critical for modulating blood flow energy supplies in accordance with synaptic activity[58]. Additionally, astrocytes are critical for maintaining extracellular ion concentrations, including K^+, which has profound influence on neuronal excitability[59–61]. Astrocytes also express transporters for the uptake of neurotransmitters including glutamate and GABA, which are critical for controlling the timing of synaptic activity[62–64].

With so many different functions ascribed to astrocytes at the synapse, it is difficult to define one role of astrocytes in the brain. It appears that, instead, astrocytes likely perform multiple different functions in parallel. Indeed, it may be better to think of astrocytes, and in particular astrocyte Ca^{2+}, not as one homogenous signal, but instead of a spatiotemporal heterogenous signal that varies across multiple cellular compartments. The advent of 2-photon microscopy, that allowed for sub-cellular imaging of astrocyte Ca^{2+}, was critical to this model of astrocyte physiology and function. Indeed, the work presented in Chapter 2 moves to take advantage of this imaging data so that the spatiotemporal complexity of astrocyte physiology can be better understood (**Fig. 1.1a**).

Astrocytes are well positioned to regulate cortical networks

While most of the previous work on astrocyte biology has focused on astrocytes at single synapses, astrocytes are also very well positioned to influence neuronal activity on a larger spatial scale, modulating networks and circuits in the brain. Of particular interest is the role of

cortical astrocytes in modulating cortical networks and circuits that are known to play critical roles in various behavior including arousal-related attention[65], sensory processing[66,67], learning and memory[68–71], and sleep[10].

Astrocytes tile the cortex closely, covering all cortical layers. A single astrocyte can contact up to 100,000 synapses an influence thousands of neurons[72,73] through reciprocal communication with synapses. Further, astrocytes are connected with each other through gap junctions, allowing for rapid intercellular communication[74–76]. Together, this optimally positions astrocytes to influence large populations of neurons to regulate cortical state. In fact, astrocytes have already been implicated in regulating cortical state under anesthesia[41,74,77,78]. The extent to which astrocytes participate in cortical networks *in vivo* and in awake, non-anesthetized behaviors, however, remains largely understudied. In Chapter 3, we directly explore the role of astrocytes in NREM sleep, a behavior in which there are dramatic fluctuations in cortical state and large populations of neurons within the cortex synchronously alter their activity (**Fig. 1.1b**).

Astrocytic functions associated with sleep

Astrocytes are well positioned to actively regulate sleep through their contact with large numbers of synapses, and in fact previous work has linked astrocytes to sleep in many different ways. First, astrocytes exhibit transcriptional changes across the sleep-wake cycle[79]. In the same study, they also demonstrated using electron microscopy that astrocytes exhibit morphological changes across sleep and wake, with astrocytic processes moving further away from neuronal synapses during sleep and closer to synapses during wake[79]. Astrocytes also respond to circadian signals in the suprachiasmatic nucleus[80] and cortical astrocytes exhibit increased Ca^{2+} activity

with sleep deprivation. In fact, it is suggested that they play an important role in sleep homeostasis[81].

Many of the functions that are traditionally ascribed to astrocytes have also been implicated in sleep-wake control. For instance, pharmacological manipulation of astrocyte glutamate transporters increases cortical UP states *ex vivo*[41] and bursts of extracellular glutamate around astrocytes precede synchronous states under anesthesia[77]. Additionally, the regulation of extracellular ions K^+ and Mg^+, both of which are regulated by astrocytes, has been shown to be sufficient to control sleep-wake states[82]. The release of neurotransmitters by astrocytes, particularly adenosine and the NMDA receptor co-agonist D-serine, have also been implicated in sleep-wake regulation[83–85]. Lastly, astrocytic control of metabolic regulation has been shown to change over sleep and wake[86–88] and likely plays an important role in the homeostatic functions of sleep.

The primary focus of this dissertation is elucidating the complex role of astrocytes in sleep regulation. Using new techniques and novel analysis approaches (**Chapter 2**), we demonstrate, for the first time, that astrocytes play a causal role in the regulation of distinct features of sleep (**Chapter 3**). Further, we begin to dissect the mechanistic pathways by which astrocytes perform this critical function, including putative inputs to the astrocyte network (**Chapter 4**) and functional astrocyte outputs that alter neural activity (**Chapter 5**).

References

1. Zielinski, M. R., McKenna, J. T. & McCarley, R. W. Functions and mechanisms of sleep. *AIMS Neurosci.* **3,** 67–104 (2016).
2. Walker, M. P. Cognitive consequences of sleep and sleep loss. *Sleep Med.* **9 Suppl 1,** S29-34 (2008).
3. Brownlow, J. A., Miller, K. E. & Gehrman, P. R. Insomnia and cognitive performance. *Sleep Med. Clin.* **15,** 71–76 (2020).
4. Blackwell, J. E., Alammar, H. A., Weighall, A. R., Kellar, I. & Nash, H. M. A systematic review of cognitive function and psychosocial well-being in school-age children with narcolepsy. *Sleep Med. Rev.* **34,** 82–93 (2017).
5. Wintler, T., Schoch, H., Frank, M. G. & Peixoto, L. Sleep, brain development, and autism spectrum disorders: Insights from animal models. *J. Neurosci. Res.* **98,** 1137–1149 (2020).
6. Dahale, A. B., Singh, H. & Chaturvedi, S. K. Need for sleep clinics in psychiatric practice. *Indian J. Sleep Med.* **7,** 1–5 (2012).
7. Campbell, S. S. & Tobler, I. Animal sleep: a review of sleep duration across phylogeny. *Neurosci. Biobehav. Rev.* **8,** 269–300 (1984).
8. Joiner, W. J. Unraveling the evolutionary determinants of sleep. *Curr. Biol.* **26,** R1073–R1087 (2016).
9. Nath, R. D. *et al.* The Jellyfish Cassiopea Exhibits a Sleep-like State. *Curr. Biol.* **27,** 2984–2990.e3 (2017).
10. Genzel, L., Kroes, M. C. W., Dresler, M. & Battaglia, F. P. Light sleep versus slow wave sleep in memory consolidation: a question of global versus local processes? *Trends Neurosci.* **37,** 10–19 (2014).

11. von ECONOMO, C. Some new methods of studing the brains of exceptional persons (encephalometry and brain casts). *J. Nerv. Ment. Dis.* **71,** 300–302 (1930).
12. Saper, C. B., Fuller, P. M., Pedersen, N. P., Lu, J. & Scammell, T. E. Sleep state switching. *Neuron* **68,** 1023–1042 (2010).
13. Saper, C. B. & Fuller, P. M. Wake-sleep circuitry: an overview. *Curr. Opin. Neurobiol.* **44,** 186–192 (2017).
14. Lee, S.-H. & Dan, Y. Neuromodulation of brain states. *Neuron* **76,** 209–222 (2012).
15. Holst, S. C. & Landolt, H.-P. Sleep-Wake Neurochemistry. *Sleep Med. Clin.* **13,** 137–146 (2018).
16. Gompf, H. S. *et al.* Locus ceruleus and anterior cingulate cortex sustain wakefulness in a novel environment. *J. Neurosci.* **30,** 14543–14551 (2010).
17. Petrovic, J., Ciric, J., Lazic, K., Kalauzi, A. & Saponjic, J. Lesion of the pedunculopontine tegmental nucleus in rat augments cortical activation and disturbs sleep/wake state transitions structure. *Exp. Neurol.* **247,** 562–571 (2013).
18. Shouse, M. N. & Siegel, J. M. Pontine regulation of REM sleep components in cats: integrity of the pedunculopontine tegmentum (PPT) is important for phasic events but unnecessary for atonia during REM sleep. *Brain Res.* **571,** 50–63 (1992).
19. Gerashchenko, D., Chou, T. C., Blanco-Centurion, C. A., Saper, C. B. & Shiromani, P. J. Effects of lesions of the histaminergic tuberomammillary nucleus on spontaneous sleep in rats. *Sleep* **27,** 1275–1281 (2004).
20. Fuller, P. M., Sherman, D., Pedersen, N. P., Saper, C. B. & Lu, J. Reassessment of the structural basis of the ascending arousal system. *J. Comp. Neurol.* **519,** 933–956 (2011).
21. Chung, S. *et al.* Identification of preoptic sleep neurons using retrograde labelling and gene

profiling. *Nature* **545,** 477–481 (2017).

22. Sutcliffe, J. G. & de Lecea, L. The hypocretins: setting the arousal threshold. *Nat. Rev. Neurosci.* **3,** 339–349 (2002).
23. Adamantidis, A. R., Zhang, F., Aravanis, A. M., Deisseroth, K. & de Lecea, L. Neural substrates of awakening probed with optogenetic control of hypocretin neurons. *Nature* **450,** 420–424 (2007).
24. Hara, J. *et al.* Genetic ablation of orexin neurons in mice results in narcolepsy, hypophagia, and obesity. *Neuron* **30,** 345–354 (2001).
25. Peyron, C. *et al.* A mutation in a case of early onset narcolepsy and a generalized absence of hypocretin peptides in human narcoleptic brains. *Nat. Med.* **6,** 991–997 (2000).
26. Manns, I. D., Alonso, A. & Jones, B. E. Discharge profiles of juxtacellularly labeled and immunohistochemically identified GABAergic basal forebrain neurons recorded in association with the electroencephalogram in anesthetized rats. *J. Neurosci.* **20,** 9252–9263 (2000).
27. Adamantidis, A. R., Gutierrez Herrera, C. & Gent, T. C. Oscillating circuitries in the sleeping brain. *Nat. Rev. Neurosci.* **20,** 746–762 (2019).
28. Steriade, M., Nuñez, A. & Amzica, F. Intracellular analysis of relations between the slow (< 1 Hz) neocortical oscillation and other sleep rhythms of the electroencephalogram. *J. Neurosci.* **13,** 3266–3283 (1993).
29. Timofeev, I., Grenier, F., Bazhenov, M., Sejnowski, T. J. & Steriade, M. Origin of slow cortical oscillations in deafferented cortical slabs. *Cereb. Cortex* **10,** 1185–1199 (2000).
30. Lemieux, M., Chen, J.-Y., Lonjers, P., Bazhenov, M. & Timofeev, I. The impact of cortical deafferentation on the neocortical slow oscillation. *J. Neurosci.* **34,** 5689–5703 (2014).

31. Sanchez-Vives, M. V. & McCormick, D. A. Cellular and network mechanisms of rhythmic recurrent activity in neocortex. *Nat. Neurosci.* **3,** 1027–1034 (2000).
32. Kwan, A. C. & Dan, Y. Dissection of cortical microcircuits by single-neuron stimulation in vivo. *Curr. Biol.* **22,** 1459–1467 (2012).
33. Li, C.-Y. T., Poo, M.-M. & Dan, Y. Burst spiking of a single cortical neuron modifies global brain state. *Science* **324,** 643–646 (2009).
34. Funk, C. M., Honjoh, S., Rodriguez, A. V., Cirelli, C. & Tononi, G. Local Slow Waves in Superficial Layers of Primary Cortical Areas during REM Sleep. *Curr. Biol.* **26,** 396–403 (2016).
35. Siclari, F. & Tononi, G. Local aspects of sleep and wakefulness. *Curr. Opin. Neurobiol.* **44,** 222–227 (2017).
36. Bernardi, G., Siclari, F., Handjaras, G., Riedner, B. A. & Tononi, G. Local and widespread slow waves in stable NREM sleep: evidence for distinct regulation mechanisms. *Front. Hum. Neurosci.* **12,** 248 (2018).
37. Huber, R., Ghilardi, M. F., Massimini, M. & Tononi, G. Local sleep and learning. *Nature* **430,** 78–81 (2004).
38. Krone, L. B. *et al.* Selective silencing of layer 5 pyramidal neurons increases wake time and affects local and global sleep homeostasis. *Sleep Med.* **64,** S204 (2019).
39. Kilduff, T. S., Cauli, B. & Gerashchenko, D. Activation of cortical interneurons during sleep: an anatomical link to homeostatic sleep regulation? *Trends Neurosci.* **34,** 10–19 (2011).
40. Tossell, K. *et al.* Sleep deprivation triggers somatostatin neurons in prefrontal cortex to initiate nesting and sleep via the preoptic and lateral hypothalamus. *BioRxiv* (2020).

doi:10.1101/2020.07.01.179671

41. Poskanzer, K. E. & Yuste, R. Astrocytic regulation of cortical UP states. *Proc. Natl. Acad. Sci. USA* **108,** 18453–18458 (2011).
42. Compte, A., Sanchez-Vives, M. V., McCormick, D. A. & Wang, X.-J. Cellular and network mechanisms of slow oscillatory activity (<1 Hz) and wave propagations in a cortical network model. *J. Neurophysiol.* **89,** 2707–2725 (2003).
43. Haider, B., Duque, A., Hasenstaub, A. R. & McCormick, D. A. Neocortical network activity in vivo is generated through a dynamic balance of excitation and inhibition. *J. Neurosci.* **26,** 4535–4545 (2006).
44. Volgushev, M., Chauvette, S., Mukovski, M. & Timofeev, I. Precise long-range synchronization of activity and silence in neocortical neurons during slow-wave oscillations [corrected]. *J. Neurosci.* **26,** 5665–5672 (2006).
45. Niethard, N., Ngo, H.-V. V., Ehrlich, I. & Born, J. Cortical circuit activity underlying sleep slow oscillations and spindles. *Proc. Natl. Acad. Sci. USA* **115,** E9220–E9229 (2018).
46. Lemieux, M., Chauvette, S. & Timofeev, I. Neocortical inhibitory activities and long-range afferents contribute to the synchronous onset of silent states of the neocortical slow oscillation. *J. Neurophysiol.* **113,** 768–779 (2015).
47. Zucca, S. *et al.* An inhibitory gate for state transition in cortex. *Elife* **6,** (2017).
48. Orkand, R. K., Nicholls, J. G. & Kuffler, S. W. Effect of nerve impulses on the membrane potential of glial cells in the central nervous system of amphibia. *J. Neurophysiol.* **29,** 788–806 (1966).
49. Cornell-Bell, A. H., Finkbeiner, S. M., Cooper, M. S. & Smith, S. J. Glutamate induces calcium waves in cultured astrocytes: long-range glial signaling. *Science* **247,** 470–473

(1990).

50. Perea, G., Navarrete, M. & Araque, A. Tripartite synapses: astrocytes process and control synaptic information. *Trends Neurosci.* **32,** 421–431 (2009).
51. Bazargani, N. & Attwell, D. Astrocyte calcium signaling: the third wave. *Nat. Neurosci.* **19,** 182–189 (2016).
52. Agulhon, C. *et al.* What is the role of astrocyte calcium in neurophysiology? *Neuron* **59,** 932–946 (2008).
53. Araque, A., Parpura, V., Sanzgiri, R. P. & Haydon, P. G. Tripartite synapses: glia, the unacknowledged partner. *Trends Neurosci.* **22,** 208–215 (1999).
54. Porter, J. T. & McCarthy, K. D. Astrocytic neurotransmitter receptors in situ and in vivo. *Prog. Neurobiol.* **51,** 439–455 (1997).
55. Beck, A., Nieden, R. Z., Schneider, H.-P. & Deitmer, J. W. Calcium release from intracellular stores in rodent astrocytes and neurons in situ. *Cell Calcium* **35,** 47–58 (2004).
56. Scemes, E. & Giaume, C. Astrocyte calcium waves: what they are and what they do. *Glia* **54,** 716–725 (2006).
57. Savtchouk, I. & Volterra, A. Gliotransmission: Beyond Black-and-White. *J. Neurosci.* **38,** 14–25 (2018).
58. Attwell, D. *et al.* Glial and neuronal control of brain blood flow. *Nature* **468,** 232–243 (2010).
59. Rasmussen, R., O'Donnell, J., Ding, F. & Nedergaard, M. Interstitial ions: A key regulator of state-dependent neural activity? *Prog. Neurobiol.* **193,** 101802 (2020).
60. Rasmussen, R. *et al.* Cortex-wide Changes in Extracellular Potassium Ions Parallel Brain State Transitions in Awake Behaving Mice. *Cell Rep.* **28,** 1182–1194.e4 (2019).

61. Simard, M. & Nedergaard, M. The neurobiology of glia in the context of water and ion homeostasis. *Neuroscience* **129,** 877–896 (2004).

62. Danbolt, N. C. Glutamate uptake. *Prog. Neurobiol.* **65,** 1–105 (2001).

63. Schousboe, A., Sarup, A., Bak, L. K., Waagepetersen, H. S. & Larsson, O. M. Role of astrocytic transport processes in glutamatergic and GABAergic neurotransmission. *Neurochem. Int.* **45,** 521–527 (2004).

64. Diamond, J. S. & Jahr, C. E. Transporters buffer synaptically released glutamate on a submillisecond time scale. *J. Neurosci.* **17,** 4672–4687 (1997).

65. Harris, K. D. & Thiele, A. Cortical state and attention. *Nat. Rev. Neurosci.* **12,** 509–523 (2011).

66. Marguet, S. L. & Harris, K. D. State-dependent representation of amplitude-modulated noise stimuli in rat auditory cortex. *J. Neurosci.* **31,** 6414–6420 (2011).

67. Castro-Alamancos, M. A. Absence of rapid sensory adaptation in neocortex during information processing states. *Neuron* **41,** 455–464 (2004).

68. Tukker, J. J., Beed, P., Schmitz, D., Larkum, M. E. & Sachdev, R. N. S. Up and down states and memory consolidation across somatosensory, entorhinal, and hippocampal cortices. *Front. Syst. Neurosci.* **14,** 22 (2020).

69. Klinzing, J. G., Niethard, N. & Born, J. Mechanisms of systems memory consolidation during sleep. *Nat. Neurosci.* **22,** 1598–1610 (2019).

70. Ji, D. & Wilson, M. A. Coordinated memory replay in the visual cortex and hippocampus during sleep. *Nat. Neurosci.* **10,** 100–107 (2007).

71. Kim, J., Gulati, T. & Ganguly, K. Competing Roles of Slow Oscillations and Delta Waves in Memory Consolidation versus Forgetting. *Cell* **179,** 514–526.e13 (2019).

72. Halassa, M. M., Fellin, T., Takano, H., Dong, J.-H. & Haydon, P. G. Synaptic islands defined by the territory of a single astrocyte. *J. Neurosci.* **27,** 6473–6477 (2007).

73. Bushong, E. A., Martone, M. E., Jones, Y. Z. & Ellisman, M. H. Protoplasmic astrocytes in CA1 stratum radiatum occupy separate anatomical domains. *J. Neurosci.* **22,** 183–192 (2002).

74. Szabó, Z. *et al.* Extensive astrocyte synchronization advances neuronal coupling in slow wave activity in vivo. *Sci. Rep.* **7,** 6018 (2017).

75. Murphy-Royal, C. *et al.* Stress gates an astrocytic energy reservoir to impair synaptic plasticity. *Nat. Commun.* **11,** 2014 (2020).

76. Clasadonte, J., Scemes, E., Wang, Z., Boison, D. & Haydon, P. G. Connexin 43-Mediated Astroglial Metabolic Networks Contribute to the Regulation of the Sleep-Wake Cycle. *Neuron* **95,** 1365–1380.e5 (2017).

77. Poskanzer, K. E. & Yuste, R. Astrocytes regulate cortical state switching in vivo. *Proc. Natl. Acad. Sci. USA* **113,** E2675-84 (2016).

78. Durkee, C. A. *et al.* Gi/o protein-coupled receptors inhibit neurons but activate astrocytes and stimulate gliotransmission. *Glia* **67,** 1076–1093 (2019).

79. Bellesi, M., de Vivo, L., Tononi, G. & Cirelli, C. Effects of sleep and wake on astrocytes: clues from molecular and ultrastructural studies. *BMC Biol.* **13,** 66 (2015).

80. Brancaccio, M., Patton, A. P., Chesham, J. E., Maywood, E. S. & Hastings, M. H. Astrocytes control circadian timekeeping in the suprachiasmatic nucleus via glutamatergic signaling. *Neuron* **93,** 1420–1435.e5 (2017).

81. Ingiosi, A. M. *et al.* A role for astroglial calcium in mammalian sleep and sleep regulation. *Curr. Biol.* **30,** 4373–4383.e7 (2020).

82. Ding, F. *et al.* Changes in the composition of brain interstitial ions control the sleep-wake cycle. *Science* **352,** 550–555 (2016).

83. Papouin, T., Dunphy, J. M., Tolman, M., Dineley, K. T. & Haydon, P. G. Septal Cholinergic Neuromodulation Tunes the Astrocyte-Dependent Gating of Hippocampal NMDA Receptors to Wakefulness. *Neuron* **94,** 840–854.e7 (2017).

84. Halassa, M. M. *et al.* Astrocytic modulation of sleep homeostasis and cognitive consequences of sleep loss. *Neuron* **61,** 213–219 (2009).

85. Fellin, T. *et al.* Endogenous nonneuronal modulators of synaptic transmission control cortical slow oscillations in vivo. *Proc. Natl. Acad. Sci. USA* **106,** 15037–15042 (2009).

86. Bellesi, M., de Vivo, L., Koebe, S., Tononi, G. & Cirelli, C. Sleep and wake affect glycogen content and turnover at perisynaptic astrocytic processes. *Front. Cell Neurosci.* **12,** 308 (2018).

87. Petit, J. M. & Magistretti, P. J. Regulation of neuron-astrocyte metabolic coupling across the sleep-wake cycle. *Neuroscience* **323,** 135–156 (2016).

88. DiNuzzo, M. & Nedergaard, M. Brain energetics during the sleep-wake cycle. *Curr. Opin. Neurobiol.* **47,** 65–72 (2017).

Chapter 2:

Flexible and accurate quantification of astrocyte activity reveals novel single-cell and population-level physiology

---

Abstract

Recent work examining astrocytic physiology centers on fluorescence imaging approaches, due to development of sensitive fluorescent indicators and observation of spatiotemporally complex calcium and glutamate activity. However, the field remains hindered in fully characterizing these dynamics, both within single cells and at the population-level, because of the insufficiency of current region-of-interest-based approaches to describe activity that is often spatially unfixed, size-varying, and propagative. Here, we present an analytical framework that releases astrocyte biologists from ROI-based tools. The Astrocyte Quantitative Analysis (AQuA) software takes an event-based perspective to model and accurately quantify the complex activity in astrocyte imaging datasets. We apply AQuA to a range of *ex vivo* and *in vivo* imaging data, and uncover novel physiological phenomena in each. Since AQuA is data-driven and based on machine learning principles, it can be applied across model organisms, fluorescent indicators, experimental modes, and imaging resolutions and speeds, enabling researchers to elucidate fundamental astrocyte physiology.

Introduction

With increased prevalence of multiphoton imaging and optical probes to study the physiology of astrocytes[1-3], many groups now have the tools to study fundamental functions that previously remained unclear. Recent work has focused on new ways to decipher how astrocytes respond to

neurotransmitter and neuromodulator circuit signals[4-7] and how the spatiotemporal patterns of their activity shape local neuronal activity[8-10]. Recording astrocytic dynamics with the goal of decoding their disparate roles in neural circuitry has largely centered on cell type-specific expression of genetically encoded probes to carry out intracellular calcium (Ca^{2+}) imaging using variants of GCaMP[3]. In addition, many groups have studied astrocytic function by performing extracellular glutamate imaging using GluSnFR[2], and several more recently developed genetically encoded fluorescent probes for neurotransmitters such as GABA[11], norepinephrine (NE)[12], ATP[13], and dopamine[14] are poised to expand our understanding of astrocytic circuit biology.

Compared to neuronal Ca^{2+} imaging, astrocytic Ca^{2+} imaging using GCaMP presents particular challenges for analysis due to their complex spatiotemporal dynamics. Thus, astrocyte-specific analysis software has been developed to capture these dynamics, including techniques that divide the cell into distinct subcellular regions corresponding to their anatomy[4] or apply a watershed algorithm to identify regions-of-interest (ROIs)[15]. Likewise, GluSnFR imaging analysis techniques are based on manually or semi-manually selected ROIs, or by analyzing the entire imaging field together as one ROI[2,6,8,16]. It is worth noting that these and most, although not all[17,18], other current techniques rely on the conceptual framework of ROIs for image analysis. However, astrocytic Ca^{2+} and GluSnFR fluorescence dynamics are particularly ill-suited for ROI-based approaches, because the concept of the ROI has several inherent assumptions that cannot be satisfied for astrocytic activity data. Astrocytic Ca^{2+} signals, for example, can occupy regions that change size or location across time, can propagate within or across cells, and can spatially overlap with other Ca^{2+} signals that are temporally distinct. ROI-based approaches assume that for a given ROI, all signals have a fixed size and shape as

specified by the ROI, and all locations within the ROI undergo the same dynamics, without propagation. Accordingly, ROI-based techniques may over- or under-sample these data, thus obscuring true dynamics and hindering physiological discovery in these cells. An ideal imaging analysis framework for astrocytes would take into account, and quantify, all of these dynamic features and be free of these ROI-based analytical restrictions. In addition, an ideal tool should be applicable to astrocyte imaging data across spatial scales, encompassing subcellular, cellular, and population-wide fluorescence dynamics.

In this work, we set out to design an image analysis toolbox that would capture the complex, wide-ranging fluorescent signals observed in most dynamic astrocyte imaging datasets. We reasoned that a non-ROI-based approach would better describe the observed fluorescent dynamics, and applied probability theory, machine learning, and computational optimization techniques to generate an algorithm to do so. We name this resulting software package Astrocyte Quantitative Analysis (AQuA). In Wang & DelRosso et al., 2019, the utility of AQuA is validated by applying it to simulated datasets that reflect the specific features that make analyzing astrocyte data challenging. Here, we apply AQuA to three experimental two-photon (2P) imaging datasets—*ex vivo* Ca^{2+} imaging of GCaMP6 from acute cortical slices, *in vivo* Ca^{2+} imaging of GCaMP6 in primary visual cortex (V1) of awake, head-fixed mice, and *ex vivo* extracellular glutamate, GABA, and NE imaging. In these test cases, we find that AQuA accurately detects fluorescence dynamics by capturing fluorescence events as they change in space and time, rather than the activity from a single location in space, as in ROI-based approaches. AQuA outputs a comprehensive set of biologically relevant parameters from these datasets, including propagation speed, propagation direction, area, shape, and spatial frequency.

Using these detected events and associated output features, we uncover neurobiological phenomena that have not been previously described in astrocytes.

A wide variety of cellular and circuit functions have been ascribed to astrocytes, and a key question currently under examination in the field is whether certain types of Ca^{2+} activities observed in these cells correspond to particular neurobiological functions. However, current techniques with which to classify these observed dynamics remain inadequate since they do not capture many of the dynamics recorded in fluorescent imaging of astrocytic activity. The framework we describe here allows for a rigorous, in-depth dissection of astrocyte physiology across spatial and temporal imaging scales, and sets the stage for a comprehensive categorization of heterogeneous astrocyte activities both at baseline and after experimental manipulations.

Results

Design principles of the AQuA algorithm

To move away from ROI-based analysis approaches and accurately capture heterogeneous astrocyte fluorescence dynamics, we set out to design an algorithm to decompose raw dynamic astrocyte imaging data into a set of quantifiable events (**Fig. 2.1a, Fig. 2.5–2.7**). Here, we define an event as a cycle of a signal increase and decrease that coherently occurs in a spatially connected region, but this region is defined by the fluorescence dynamics, not *a priori* by the user or the cell morphology. Algorithmically, this definition is converted to the following two rules: 1) the temporal trajectory for an event contains only one peak (single-cycle rule, **Fig. 2.1b**) and 2) adjacent locations in the same event have similar trajectories (smoothness rule, **Fig. 2.1b**). The task of the AQuA algorithm is to detect all events, and, for each event, to identify the temporal trajectory, the spatial footprint, and how the signal propagates within the footprint.

Briefly, our strategy of event-detection is to a) explore the single-cycle rule to find peaks, which are used to specify the time window and temporal trajectory, b) explore the smoothness rule to group spatially adjacent peaks, whose locations specify the footprint, c) apply machine learning and optimization techniques to iteratively refine the spatial and temporal properties of the event to best fit the data, and d) apply statistical theory to determine whether a detected event is true or due to noise (**Fig. 2.1**).

Full statistical and computational details are provided in the Methods, but we want to highlight one technical innovation (Graphical Time Warping [GTW])[19] and one new concept (the single-source rule) that jointly enable a nuanced analysis of astrocyte fluorescence dynamics as shown below in application to experimental datasets. With GTW, we are able to consider fluorescent signal propagation as integrated into each modeled event. To the best of our knowledge, signal propagation has never been rigorously accounted for and has been considered an obstacle to analysis. With GTW, we can estimate and quantify propagation patterns in the data. With the introduction of the single-source rule (**Fig. 2.1b**), each event only contains a single initiation source and we can separate events that are initiated at different locations but meet in the middle. The single-source rule also allows us to divide large-scale activity that can occur across an entire field-of-view into individual events, each with a single initiation location.

The output of the event-based AQuA algorithm is a list of detected events, each associated with three categories of parameters: 1) the spatial map indicating where the event occurs, 2) the dynamic curve corresponding to fluorescence change over time (dF/F), and 3) the propagation map indicating signal propagation. For each event, we use the spatial map to compute the event area, diameter and shape of the domain it occupies (**Fig. 2.1c**). Using the dynamic curve, we can calculate maximum dF/F, duration, onset-time, rise-time and decay-time. Using the propagation

map, we extract event initiation location, as well as propagation path, direction, and speed. In addition, AQuA computes features involving more than one event, such as the frequency of events at a position, and the overall number of events in a specified region or cell. A complete list of features is available in Wang & DelRosso et al., 2019 and online at https://github.com/yu-lab-vt/aqua.

Validation of AQuA using simulated data

In Wang & DelRosso et al., 2019, AQuA is validated using three different simulated datasets, so that ground truth for the dynamics of each event were known. The datasets independently vary the three key phenomena observed in astrocyte imaging datasets that cause ROI-based approaches to misanalyze the data: size-variability, location-variability, and propagation. Using these datasets, AQuA's performance was quantified relative to other fluorescence image analysis tools, including CaImAn[20], Suite2P[21], CaSCaDe[15], and GECI-quant[4]. For a full description of these studies and their methods, see Wang & DelRosso et al., 2019.

AQuA enables identification of single-cell physiological heterogeneities

To test AQuA's performance on real astrocyte fluorescence imaging data and ask whether AQuA could be used for classifying Ca^{2+} activities observed in single cells, we first ran AQuA's event-detection on Ca^{2+} activity recorded from astrocytes in acute cortical slices from mouse V1 using 2P microscopy. We used a viral approach to express the genetically encoded Ca^{2+} indicator GCaMP6f[3] in layer 2/3 (L2/3) astrocytes. Unlike ROI-based approaches, AQuA detects both propagative and non-propagative activity, revealing Ca^{2+} events with a variety of shapes and

sizes (**Fig. 2.2a, left**). Further, since AQuA not only detects Ca^{2+} events' spatial footprint but also their time-course, we can apply AQuA to measure the propagation direction each event travels over its lifetime. Imaging single cells, we used the soma as a landmark, and classified events as traveling toward the soma (pink), away from the soma (purple), or static (blue) for the majority of its lifetime (**Fig. 2.2a, right**). We used AQuA's automatic feature-extraction and combined multiple measurements (size, propagation direction, duration, and minimum proximity to soma) into one spatiotemporal summary plot (**Fig. 2.2b**). Since astrocytes exhibit a wide diversity of Ca^{2+} activities across subcellular compartments[6,22,23], plotting the signals this way rather than standard dF/F transients highlights these heterogeneities, allows us to map the spatial location of the Ca^{2+} signals, and enables a quick, visual impression of a large amount of complex data (**Fig. 2.8**). We note that while the expression of GCaMP6 in these experiments enabled us to analyze events within single cells, some probes do not allow clear delineation of single cells. However, a secondary fluorophore (such as TdTomato) often serves the purpose of defining the morphology of single cells, and the AQuA software has been designed to overlay morphological masks on the dynamic fluorescence channel.

We next asked whether some subcellular regions of astrocytes have more dynamic activity than others across all analyzed cells (n=11 cells). Although we detected more static events than dynamic overall (**Fig. 2.9a**), we observed a higher proportion of dynamic events than static events in the soma (59%, **Fig. 2.2c**, **Fig. 2.9b**). We then characterized events by propagation direction and event initiation location (**Fig. 2.2d**). Events that begin close to the soma ($\leq 50^{th}$ percentile) and propagate away (purple) were on average larger than the events propagating toward the soma (pink, two-tailed t-test). Similarly, those events that began close to the soma

($\leq 50^{th}$ percentile) and propagated away had on average a longer duration than events propagating toward the soma (two-tailed t-test, **Fig. 2.2e**, **Fig. 2.9**).

One of AQuA's strengths is its ability to automatically extract a large number of features. These features can be used to form a comprehensive Ca^{2+} measurement matrix, where each row represents an event and each column an extracted feature, and which includes all events for each cell (**Fig. 2.10**). Dimensionality ` applied to this matrix can, in turn, be used to visualize each cell's Ca^{2+} signature (**Fig. 2.10**, white rows separate each individual cell). To do this, we applied t-distributed Stochastic Neighbor Embedding (t-SNE)[24], followed by k-means clustering to assign the cells to groups (**Fig. 2.10**), revealing clusters marked by cells with large differences in median frequency (**Fig. 2.2f**). Astrocytic Ca^{2+} frequency is commonly measured as the number of transients that occur over time within an ROI. Here, we instead define frequency from an event-based perspective in two ways: 1) for each event, the number of other events that overlap in time, and 2) for each event, the number of other events that overlap in space. We used these two measures (temporal and spatial overlap) and several other extracted measures (**Fig. 2.10**) to construct the matrix used for t-SNE visualization and clustering. We next tested how well our AQuA-specific features perform at clustering the heterogeneity among cells compared to two ROI-based methods (**Fig. 2.2g**), and found that the AQuA-based method outperformed the others. In fact, even when we only use AQuA-specific features for this analysis—area, temporal overlap, spatial overlap, and propagation speed—and remove all features that can be extracted from ROI-based methods, AQuA still significantly outperforms in clustering cells (**Fig. 2.10g–i**). AQuA-extracted features that correspond only to those that can be obtained by ROI-based methods—standard frequency, amplitude, duration—do not allow clustering significantly better than the ROI-based approaches themselves (**Fig. 2.10g–i**), suggesting that the AQuA-specific

features are those that best capture dynamic fluorescence features that vary among single cells. This indicates that AQuA may be used to extract data from existing *ex vivo* Ca^{2+} imaging datasets to reveal previously uncovered dynamics and sort cells into functionally relevant clusters.

In vivo astrocytic Ca^{2+} bursts display anatomical directionality

Recent interest in astrocytic activity at the mesoscale has been driven by population-level, multi-cellular astrocytic Ca^{2+} imaging[1,5,7,8,25-27]. To test the power of AQuA-based event detection, we next applied it to populations of *in vivo* astrocyte Ca^{2+} activity. Previous studies have described temporal details of astrocyte activation[4,5,7,8,25], yet have left largely unaddressed the combined spatiotemporal properties of Ca^{2+} activity at the circuit-level, across multiple cells. Here, we explored whether AQuA can uncover spatial patterns within populations of cortical astrocytes in an awake animal, and carried out head-fixed, 2P imaging of GCaMP6f activity in V1, L2/3 astrocytes. Populations of *in vivo* cortical astrocytes exhibit both small, focal, desynchronized Ca^{2+} activity[25], and large, coordinated activities[4,5] that we refer to as bursts in this context. Importantly, AQuA detected both of these classes of Ca^{2+} activity in the same *in vivo* imaging datasets, suggesting that it could be a powerful tool to investigate both kinds of activity—and the interactions between them—even within a single dataset (**Fig. 2.3a**). Similar to previous studies, we observed many (but not all) of the bursts co-occurring with locomotion periods (**Fig. 2.3b**, pink), and many events within these burst periods displayed propagation (**Fig. 2.3c**, top). These propagative events were larger in area and had greater propagation distances compared to the events that occurred during the inter-burst periods (**Fig. 2.3c**, bottom). Here, to test whether AQuA could help us understand these large bursts and discover discrete features of

this phenomenon, we next focused our investigation on all the events occurring during the burst periods (**Fig. 2.11**).

To analyze the structure of these burst-period Ca^{2+} events, we investigated fluorescence propagation across multiple spatial scales: at the level of individual events, of subregions of the imaging field encompassing multiple events, and of the entire imaging field. At the level of individual events within a single burst, plotting the individual event direction within the entire field of view did not reveal a consistent propagation direction (**Fig. 2.3d**). However, when we divided our field-of-view into equivalently sized, subregional tiles (**Fig. 2.3e**), we observed more consistent propagation direction within single subregions (**Fig. 2.3f**). When we plot the cumulative count of the percentage of bursts with regions that propagate in the same direction, we indeed observe that this curve is right-shifted compared to a simulated random assignment of majority regional propagation direction (**Fig. 2.3g**), suggesting that there does exist regularity in the propagation pattern within bursts, but that this only becomes apparent at a spatial scale larger than individual events.

Since the consistency of propagation directionality increased with increasing spatial scales, we next explored whole imaging field dynamics during Ca^{2+} burst events. We noted that the percentage of the active field of view varied across burst periods (**Fig. 2.3b**), with a wide variability from few to hundreds of events (**Fig. 2.3h**). To control for number and size of events, we used the difference between each event's onset time to calculate a single burst-wide propagation direction (**Fig. 2.3h**, black arrow). Doing so revealed a consistent posterior-medial directionality of population Ca^{2+} activity in L2/3 V1 astrocytes (**Fig. 2.3i**). Although Ca^{2+} bursts have been previously observed using GCaMP6 imaging in awake mice[4,5], consistent spatial directionality with respect to the underlying anatomy has never been described. This observed

posterior-medial directionality may be revealing anatomical and physiological underpinnings of these bursts, and since they have been shown to be at least partly mediated by norepinephrine[5,7], they could be reflective of the response of groups of cortical astrocytes to incoming adrenergic axons originating in locus coeruleus. Regardless of burst mechanism(s), these results suggest that *in vivo*, astrocytic Ca^{2+} propagation dynamics differ depending on the spatial scale examined, which may explain previously described discrepancies in dynamics.

AQuA-based detection of extracellular molecular dynamics

We next asked whether AQuA could be used to detect astrocytic fluorescent activities with distinct spatiotemporal dynamics than we observe when measuring intracellular Ca^{2+}. We decided to perform imaging of extracellular-facing probes, including GluSnFR[2], to measure extracellular glutamate dynamics, since it has been widely used for glutamate imaging[2,6,8] and astrocytes regulate extracellular glutamate concentration. In addition, GluSnFR dynamics are much faster than GCaMP dynamics, which causes detection to be very susceptible to low SNR. This can be an additional challenge and thus much previous GluSnFR analyses has relied on averaging across multiple trials. While GluSnFR has been expressed both in astrocytes and in neurons previously[2,8,16,28], how cell type-specific expression and morphology—particularly relative to synaptic and extra-synaptic glutamate release—determines its fluorescent dynamics has not been fully explored[16,28]. No previously applied analytical tools have been reported to automatically detect GluSnFR-based glutamate events to accommodate differential event sizes and shapes. Here, we explored whether application of AQuA could be used to detect cell type-specific differences in glutamate dynamics that may be based on heterogeneous underlying morphologies and cell biological mechanisms.

We expressed GluSnFR in either astrocytes or neurons using cell type-specific viruses[2] and carried out 2P imaging of spontaneous GluSnFR activity in acute cortical V1 slices from L2/3. Distinct morphological differences between astrocytic and neuronal expression of GluSnFR were evident, as has been observed previously[8,29,30] (**Fig. 2.4a**). We applied AQuA to these datasets to detect significant increases in GluSnFR fluorescence, and were able to detect events that were too small and dim to detect by eye; AQuA-detected events were confirmed by *post hoc* ROI-based analysis. Indeed, 62% of astrocytic events had an area less than the size of a single astrocyte (100 μm^2), and 8% of astrocytic and 35% of neuronal glutamate events had a small maximum dF/F (less than 0.5). Because GluSnFR events have previously been detected by spatially averaging within a single cell or across broader areas of tissue, *or* by manual detection, the events that AQuA detects are most likely missed by ROI-based methods[6,8,16] (**Fig. 2.12**). Because AQuA is designed to detect events independently from shape or size, events of heterogeneous size and shape were revealed during this analysis (**Fig. 2.4a–b**). A large proportion of these spontaneous GluSnFR events changed size over the course of the event, with 42% of total astrocytic and 32% of total neuronal glutamate events exhibiting changes in area. On average, astrocytic GluSnFR events were significantly larger ($274 \pm 39.56\ \mu m^2$) than neuronal events ($172 \pm 57.06\ \mu m^2$), sometimes encompassing an entire astrocyte (**Fig. 2.12**). Neuronal GluSnFR events were significantly more circular (**Fig. 2.4b–d**), perhaps reflecting morphological differences between cell type somata. We also found that between cell types, GluSnFR events exhibited different size dynamics (**Fig. 2.4b–c**). While there was no difference in the rate of increase in event size between astrocytes and neurons, we did observe that the rate of size decrease of astrocytic events between frames was larger than that of neuronal events (**Fig.**

2.4c), which may reflect differential synaptic and extrasynaptic glutamate dynamics in proximity to subcellular compartments of each cell type.

Once we found that AQuA-based detection was effective for quantification of spontaneous GluSnFR events, we wanted to test its performance on more spatially and temporally precise glutamate events, since GluSnFR can be used to measure synaptic release of glutamate when imaged at fast frame rates[2,31]. To do this, we performed fast (~100Hz) GluSnFR imaging while photoactivating a caged glutamate compound (RuBi-glutamate[10,32]) with a second laser beam. In these experiments, we tested uncaging pulses at various durations (25–150ms), and applied AQuA to detect these small-scale, fast events (**Fig. 2.4d**, right). Although we did observe an increase in detection accuracy (identification of event at the time and location of the laser uncaging pulse) of uncaging-defined GluSnFR events at longer uncaging durations, AQuA detection still showed high accuracy levels at shorter durations, with a minimum of 96% average accuracy across durations (**Fig. 2.4d**, right; n = 5 cells, 3 replicates/cell). These results indicate that AQuA works well for fluorescent event detection at fast frame rates.

We lastly wanted to demonstrate that AQuA can be used for other extracellular-facing probes that are relevant for astrocyte-neuron physiology. To do this, we imaged and analyzed two recently developed genetically encoded probes that sense extracellular neurotransmitters: GABASnFR[11] and GRAB-NE[12], which report GABA and NE dynamics, respectively. We expressed GABASnFR (**Fig. 2.4e**, left) in cortical astrocytes and GRAB-NE in cortical neurons (**Fig. 2.4f**, left), and performed *ex vivo* 2P imaging before and after bath application of either NE or GABA. In both cases, we used AQuA to detect events as the neurotransmitter contacted the fluorescent sensors. For GABASnFR expression in individual astrocytes, we observed that each event increased in both fluorescence amplitude and area with cell-specific dynamics (**Fig. 2.4e**,

right). While the widespread neuronal expression of GRAB-NE did not allow for cell-specific analysis, it did allow us to observe waves of NE as it was bathed over the slice. Here, AQuA enabled detection of the dynamic spatial location, amplitude, and area of these waves as they progressed across the slice (**Fig. 2.4f**, right), indicating that AQuA may be useful to quantify propagating wavefronts in other contexts. Together, results in this section suggest that AQuA-based detection can be used to quantify the dynamics of extracellular molecules at a range of speeds and spatial spreads, across multiple cell types and expression patterns.

Discussion

With the development and application of a flexible event-based analysis tool for astrocyte imaging datasets, we hope to enable many research groups to accurately quantify observed fluorescence dynamics, including those that are un-fixed, propagative, and size varying. Here, we demonstrate that AQuA performs better than many other image analysis methods—including those designed for astrocytic and neuronal applications—on simulated datasets, and describe fluorescent event detection in several types of datasets, using the genetically encoded GCaMP, GluSnFR, GABASnFR, and GRAB-NE indicators. Because AQuA is data-driven, it can be applied to datasets that have not been directly tested here, including those captured under different imaging magnifications and spatial resolutions, as well as confocal or wide-field imaging systems. In addition, since the AQuA algorithm functions independently from frame rate, datasets captured with faster or slower frame rates[17,25] are also just as amenable to an event-based analysis with AQuA as those shown here. Further, AQuA is applicable to fluorescent indicators other than the ones tested here, particularly those that exhibit complex dynamics.

We envision the AQuA software and its underlying algorithm as enabling problem-solving for a wide range of astrocyte physiological questions, both because AQuA accurately captures dynamics exhibited by commonly used fluorescent indicators and because there are more features extracted by AQuA that can be analyzed than those extracted by existing methods. Since AQuA-specific features were able to capture heterogeneities we observed among single cells when imaging Ca^{2+}, we posit that these features may be more physiologically relevant than the standard measurements (amplitude, frequency, duration) used to describe astrocytic physiological differences, although these standard measures are also features extracted by AQuA. In the current work, we use these multiple features to describe the spontaneous astrocyte activity in cortex, but with varying spatial scale, fluorescent probe, and experimental preparation. In future work, we and others can apply AQuA-based analyses to other brain regions and layers to describe potential functional heterogeneities among astrocytes[33]. Beyond baseline differences, we expect that AQuA will be a powerful tool to quantify physiological effects of pharmacological, genetic, and optogenetic manipulations, among others. These manipulations and subsequent analyses would allow researchers to examine both astrocyte-intrinsic and -extrinsic physiology, depending on whether astrocytes, neurons, or another brain cell type is being changed.

Significant disagreement in the field remains about basic physiological functions of astrocytes. Perhaps the most outstanding issue is whether astrocytes undergo vesicular release of transmitters such as glutamate. While we don't address this controversial topic in the current work, we expect that the heterogeneous activities that we uncover using an AQuA-based analysis of GluSnFR may be key in determining different sources of glutamate in neural circuits under different conditions, and could help untangle some of the conflicting data in this arena. Our tool

enabled us to identify extracellular glutamate changes not only by cell type, but also by event size and shape dynamics, demonstrating an in-depth analysis of GluSnFR data. The event-based analytical tools presented here may be particularly useful as next-generation GluSnFR variants become available and make multiplexed imaging experiments increasingly accessible[31].

When surveying astrocyte Ca^{2+} imaging data, experimental regimes can largely be grouped into two categories: single-cell, usually *ex vivo* imaging and population-wide, *in vivo* imaging focusing on large-scale activity of many cells. Experimental data and neurobiological conclusions from these two groups can differ quite widely, or even conflict. This may be due, in part, to the large, population-wide bursts observed with the onset of locomotion *in vivo*. Many techniques used to analyze these bursting events—all ROI-based—can under-sample events that occur between bursts by swamping out smaller or shorter signals. Here, we present a technique that can be used to sample small- and large-scale activity in the same dataset or across datasets, in order to bridge spatiotemporal scales these datasets. As such, this event-based analysis tool has the potential to aid researchers in resolving outstanding physiological problems, while also tackling new ones.

As demonstrated by its utility with Ca^{2+}, glutamate, GABA, and NE datasets, AQuA also has the potential to be applied to many other fluorescence imaging datasets that exhibit non-static or propagative activity. Although we designed AQuA specifically to study dynamic astrocyte fluorescence, it is open-source and user-tunable, and we anticipate that experimentalists will find it advantageous in other contexts in which neuronal or non-neuronal cells exhibit non-static or propagative fluorescence activity. For example, recently described Ca^{2+} activity in oligodendrocytes displays some similar properties to that in astrocytes[34,35] and AQuA-based analysis may be useful. Likewise, subcellular compartments in neurons, such as dendrites or

dendritic spines, have also been shown to exhibit propagative, wave-like Ca^{2+} signals[36] and large-scale, whole-brain neuronal imaging can capture burst-like, population-wide events[37].

While we predict that the potential applications are wide, it is also important to note the limitations of AQuA, and be clear about when it will not be the most effective approach. Since AQuA detects local fluorescence changes as events, it is not well suited to strictly morphological dynamics, such as those observed in microglia, and it does not improve on the many excellent tools built for analyzing somatic neuronal Ca^{2+} activity[20,21], where ROI assumptions are well satisfied. In addition, AQuA was optimized for and tested on 2D datasets, as these comprise the majority of current imaging experiments in the field. As techniques for volumetric imaging rapidly advance, an extension to accommodate 3D imaging experiments will be necessary. We expect that AQuA is expandable to 3D datasets, based on the fact that the algorithmic design is not restricted to 2D assumptions. Although developing a full version of a 3D extension is beyond the scope of this paper, we have built a 3D prototype to test the feasibility of extending events from 2D to 3D (**Fig. 2.13**). Using a simulated 3D dataset based on published[17] astrocytes, the prototype performed well on 3D data, including detection of various event sizes and signal propagation rates (**Fig. 2.13**). These results suggest that a full 3D AQuA extension—including the optimization of computational efficiency and visualization—will work on real 3D datasets in the future. In addition, the results demonstrate that AQuA is a flexible and robust platform that can accommodate new types of data without large changes to the underlying algorithm.

Methods

Viral injections and surgical procedures

For slice experiments, neonatal mice (Swiss Webster, P0–P4) were anesthetized by crushed ice anesthesia for 3 minutes and injected with 90nL total virus of *AAV5-GFaABC1D.Lck-GCaMP6f*, *AAV5-GFaABC1D.cyto-GCaMP6f, AAV1-GFAP-iGluSnFR, AAV1-hsyn-iGluSnFR, AAV2-GFAP-iGABASnFR.F102G, and AAV9-hsyn-NE2.1* at a rate of 2–3nL/sec. Six injections 0.5μm apart in a 2x3 grid pattern with 15nL/injection into assumed V1 were performed 0.2μm below pial surface using a UMP-3 microsyringe pump (World Precision Instruments). Mice were used for slice imaging experiments at P10–P23.

For *in vivo* experiments, adult mice (C57Bl/6, P50–P100) were given dexamethasone (5mg/kg) subcutaneously prior to surgery and then anesthetized under isoflurane. A titanium headplate was attached to the skull using C&B Metabond (Parkell) and a 3mm diameter craniotomy was cut over the right hemisphere ensuring access to visual cortex. Two 300nL injections (600nL total virus) of *AAV5-GFaABC1D.cyto-GCaMP6f* were made into visual cortex (0.5–1.0mm anterior and 1.75–2.5mm lateral of bregma) at a depth of 0.2–0.3mm and 0.5mm from the pial surface, respectively. Virus was injected at a rate of 2nL/s, with a 10min wait following each injection to allow for diffusion. Following viral injection, a glass cranial window was implanted to allow for chronic imaging and secured using C&B metabond[38]. Mice were given at least ten days to recover, followed by habituation for three days to head fixation on a circular treadmill, prior to imaging.

Two-photon imaging

All 2P imaging experiments were carried out on a microscope (Bruker Ultima IV) equipped with a Ti:Sa laser (MaiTai, SpectraPhysics). The laser beam was intensity-modulated using a Pockels cell (Conoptics) and scanned with linear or resonant galvonometers. Images were acquired with a 16x, 0.8 N.A. (Nikon, *in vivo* GCaMP and *ex vivo* GRAB-NE) or 40x, 0.8. N.A. objective (Nikon, *ex vivo* GCaMP, GluSnFR, and GABASnFR) via a photomultiplier tube (Hamamatsu) using PrairieView (Bruker) software. For imaging, 950nm (GCaMP), 910nm (GluSnFR and GABASnFR), or 920nm (GRAB-NE) excitation and a 515/30 emission filter was used.

Ex vivo imaging

Coronal, acute neocortical slices (400µm thick) from P10–P23 mice were cut with a vibratome (VT 1200, Leica) in ice-cold cutting solution (in mM): 27 $NaHCO_3$, 1.5 NaH_2PO_4, 222 sucrose, 2.6 KCl, 2 $MgSO_4$, 2 $CaCl_2$. Slices were incubated in standard continuously aerated (95% O_2/5% CO_2) artificial cerebrospinal fluid (ACSF) containing (in mM): 123 NaCl, 26 $NaHCO_3$, 1 NaH_2PO_4, 10 dextrose, 3 KCl, 2 $CaCl_2$, 2 $MgSO_4$, heated to 37°C and removed from water bath immediately before introducing slices. Slices were held in ACSF at room temperature until imaging. Experiments were performed in continuously aerated, standard ACSF. 2P scanning for all probes was carried out at 512x512 pixel resolution. Acquisition frame rates were 1.1Hz (GCaMP), 4–100Hz (GluSnFR), 6Hz (GABASnFR), and 1.4Hz (GRAB-NE). For GluSnFR imaging and RuBi-glutamate uncaging experiments, GluSnFR imaging was performed at 950nm excitation to ensure that no RuBi-glutamate was released during scanning. Acquisition rates were between 95–100Hz, using resonant galvonometers. 300µM RuBi-glutamate was

added to the circulating ACSF and using a second MaiTai laser tuned to 800nm, five uncaging points were successively uncaged at each cell at durations indicated in the figure and at power <3mW that were shown in control experiments to cause no direct cell activation.

In vivo GCaMP imaging

At least two weeks following surgery mice were head-fixed to a circular treadmill and astrocyte calcium activity was visualized at ~2Hz effective frame rate from layers 2/3 of visual cortex with a 512x512 pixel resolution at 0.8 microns/pixel. Locomotion speed was monitored using an optoswitch (Newark Element 14) connected to an Arduino.

AQuA algorithm and event detection

Astrocytic events are heterogeneous and varying with respect to many aspects of their properties. In AQuA, we extensively applied machine learning techniques to flexibly model these events, so that our approach is data-driven and physiologically relevant parameters are extracted from the data instead of imposing *a priori* assumptions. Probability theory and numerical optimization techniques were applied to optimally extract fluorescent signals from background fluctuations. Here, we delineate the eight major steps in AQuA (**Fig. 2.5**), discuss motivations behind the algorithm design, and describe key technical considerations in further detail.

Step 1: data normalization and preprocessing. This step removes experimental artifacts such as motion effects, and processes the data so that noise can be well approximated by a standard Gaussian distribution. Particular attention is paid to the variance stabilization, estimate of baseline fluorescence, and variance. Step 2: detect active voxels. Step 3: identify seeds for peak

detection. Step 4: detect peaks and their spatiotemporal extension. These three steps work together to achieve peak detection. To detect peaks we start from a seed, which is modeled as a spatiotemporal local maximum. However, since random fluctuations due to background noise can also result in local maxima, we need to detect active voxels such that only the local maxima on the active voxels are considered as seeds. Here, active voxels are those likely to have signals. Step 5: cluster peaks to identify candidates for super-events. Temporarily ignoring the single-source requirement, the set of spatially-adjacent and temporally-close peaks is defined as a super-event. However, clustering results of spatially adjacent peaks are not super-events themselves, because a peak group may consist of noise voxels and temporally distant events. Step 6: estimate the signal propagation patterns. Step 7: Detect super-events. To get super-events from peak clusters, we compute the temporal closeness between spatially adjacent peaks by estimating signal propagation patterns. The propagation pattern for each event is also important for its own sake, by providing a new way to quantify activity patterns. Step 8: split super-event into individual events with different sources. A super-event is split into individual events by further exploiting propagation patterns. Based on propagation patterns within a super-event, the locations of event initiation are identified as local minima of the onset time map. Each initiation location serves as the event seed. Individual events are obtained by assigning each pixel to an event based on spatial connectivity and temporal similarity

Detailed descriptions of each step and pseudocode are available in the Methods section of Wang & DelRosso et al., 2019.

Open-source software for analyzing and visualizing dynamic fluorescent signals in astrocytes.

Applying software engineering principles, we developed an open-source toolbox for astrocyte fluorescent imaging data with detailed user guidelines. The software not only implements the AQuA algorithm for detecting events, but also provides an integrated environment for users to see the results, interact with the analysis, and combine other types of data such as cell/region masks and landmarks. There are two versions of the software with the same functionality, based on MATLAB or Fiji. The software is freely available at https://github.com/yu-lab-vt/aqua where detailed documents and example applications can be found. A list of extracted features is available in Wang & DelRosso et al., 2019. Here, we highlight several important functions of the software.

First, the software implements AQuA and provides several options to export the event-detection results, including TIFF files with color-coded events, event features in Excel, and MATLAB or Java data structures to be used by other programs. Second, the software can display analysis results by adding color to the raw video, where color encodes the value of a user-defined extracted feature such as propagation speed. Users can specify which feature to be displayed, either an existing feature in AQuA or a user-designed feature based on features provided by AQuA. We provide several pre-defined colormaps, but allow users to manually define colormaps as well. AQuA also provides a side-by-side view, to simultaneously display two features or a raw video plus one feature. Third, the software provides a convenient way to interactively view detected events and their associated features. By clicking on an event, the dF/F curve for the event is shown in a separate panel below the video, and the time-frames during which the event occurs are highlighted in red. The values of several other features for that event are also shown in another panel. The software allows multiple events to be selected simultaneously, so that their

curves and features can be plotted together and compared. Fourth, the software provides both automatic and manual ways to proofread the results. For automatic proofreading, events are filtered by setting desired ranges for features-of-interest. Alternatively, users can choose the ‘delete/restore’ button and manually click an event to remove it. Fifth, the software provides flexible ways to incorporate cell morphology or landmark information. Users can manually supply cell morphology or regional information such as the cell boundary, which can assign events to individual cells. Users can also provide landmark information such as the location of a pipette for pharmacological application. Users can also load cell, region, or landmark information from other data sources, such as another fluorescence channel that captures cell morphology. The software can extract landmark-related features for each event, including the direction of propagation relative to a landmark.

Figures

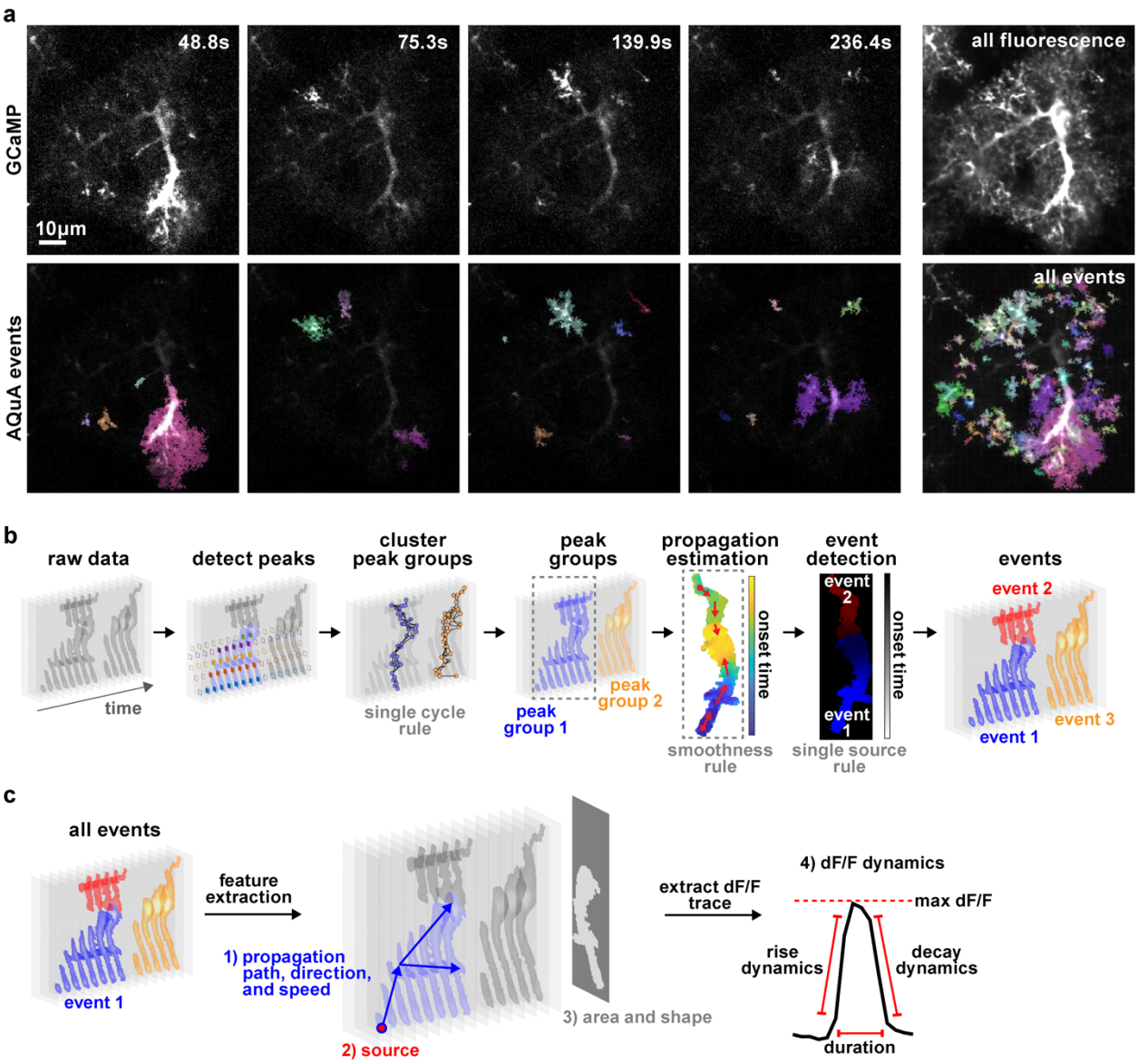

Figure 2.1: AQuA-based event detection.
(a) Individual representative frames from 5-min *ex vivo* astrocytic GCaMP imaging experiment (top) with AQuA-detected events shown below. Each color represents individual event and is chosen at random. Right column shows the average GCaMP fluorescence (top) and all AQuA-detected events (bottom) from the entire movie. Note that contrast is different between rows to highlight events. **(b)** Flowchart of AQuA algorithm. Raw data is visualized as a stack of images across time with grey level indicating signal intensity. In the *detect peaks* panel, five peaks are detected and highlighted by solid diamonds, each color denoting one peak. Based on the single-cycle rule and spatial adjacency of the apexes (solid dots) of each peak, peaks are clustered into spatially disconnected groups. Based on smoothness, propagation patterns are estimated for each

peak group. By applying the single-source rule, two events are detected for peak group 1. Three total events are detected. (**c**) Feature extraction. Based on the event-detection results, AQuA outputs four sets of features relevant to astrocytic activity: 1) propagation-related (path, direction, and speed); 2) source of events, indicating where an event is initiated; 3) features related to the event footprint, including area and shape. Event 2 is plotted here; 4) features derived from the dF/F dynamics.

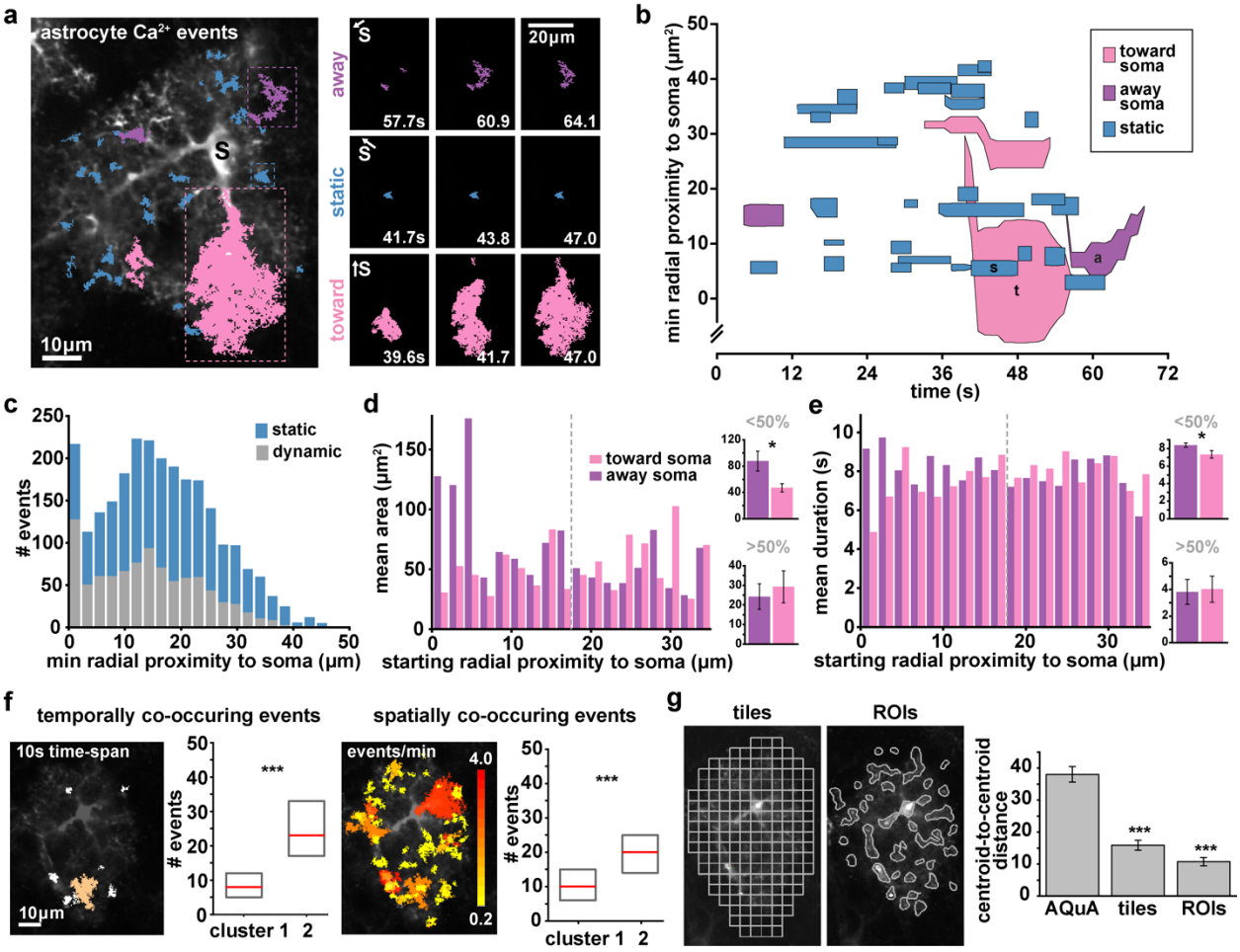

Figure 2.2: AQuA features capture heterogeneities among single astrocytes.
(**a**) Representative GCaMP6f *ex vivo* image (left) with AQuA events overlaid from 1 min of a 5 min movie. Soma marked with black s. (Right: Representative image sequence for each propagation direction class (blue = static, pink = toward soma, purple = away from soma. Soma direction marked with s and white arrow. (**b**) Spatiotemporal plot of Ca^{2+} activity from 1 min of movie. Each event is represented by a polygon that is proportional to its area as it changes over its lifetime. (**c**) Distribution of dynamic and static events as a function of minimum distance from soma (chi-square test, ***p<0.001, n=5 slices, 11 cells). All bin widths calculated by Freedman-Diaconis's rule. (**d**) Left: Propagative event size versus starting distance from soma, segregated by propagation direction. Dashed gray line denotes half the distance between the soma and the cell border. Right: Average event area for those that start <50% (top) and >50% (bottom) of the distance from the soma, (one-tailed paired t-test, *p<0.05). (**e**) Left: Event duration versus starting distance from soma. Right: Average event duration for those that start <50% (top) and >50% (bottom) of the distance from the soma (one-tailed paired t-test, *p<0.05). (**f**) Two event-based measurements of frequency: events with activity overlapping in time (left) and in space (right;). Left: one example event (orange) co-occurs with six other events (white) within 10s. Right: event colors indicate event number/min (0.2–4) at each location. Median (red) and interquartile range (gray) from cells in each cluster in **Fig. 2.10** (one-tailed Wilcoxon rank sum, ***p<0.001). (**g**) Quantification of centroid distances between cells from two clusters

determined by t-SNE plots of Ca^{2+} activity using features calculated from ROIs and 5x5μm tiles (top), (bottom, one-tailed paired t-test, ***$p<0.001$).

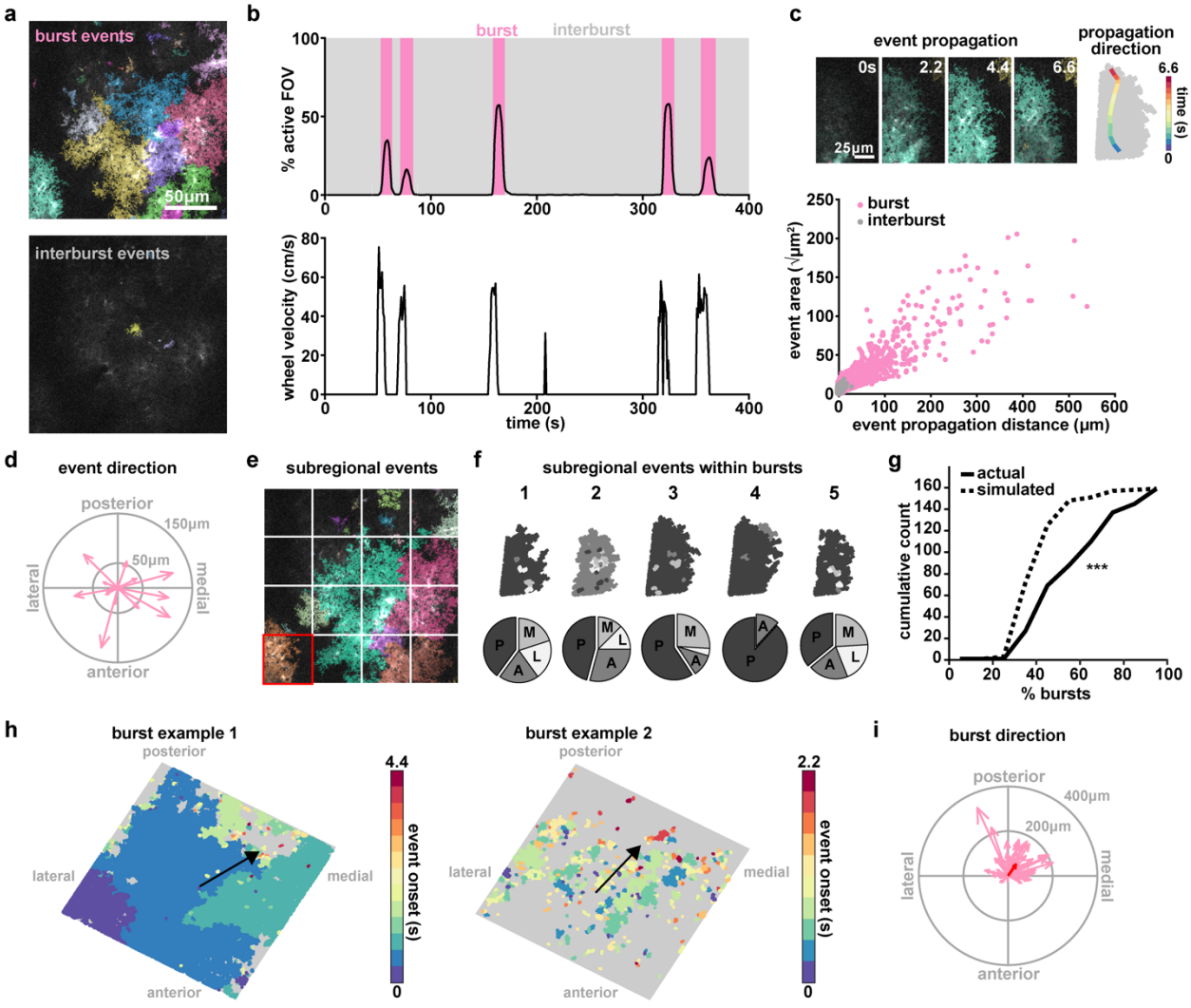

Figure 2.3: AQuA resolves astrocytic Ca^{2+} propagation directionality across scales.
(**a**) Representative *in vivo* GCaMP6f images during a burst period (top) and inter-burst period (bottom) with overlaid AQuA-detected events. (**b**) Population Ca^{2+} events represented as percentage of the imaging field active as a function of time. Burst periods (pink) are identified when Ca^{2+} activity exceeds more than 1% of the active field of view and exceeds more than 10% of the maximum number of event onsets. (**c**) *In vivo* Ca^{2+} events propagate with specific directionality. Top: representative propagative event that occurred during the burst period in panel a. The propagation direction (change of centroid relative to its original location) for each frame is overlaid on the event (right). Bottom: Total propagation distance versus event size for all events within bursts (n=6 mice, 66 bursts, 14,967 events). (**d**) Event propagation direction from all events over the entire field in the burst shown in *e*. Length of arrow indicates propagation distance. (**e**) To test consistency of subregional directionality during bursts, sixteen 96x96μm tiles are overlaid on images. (**f**) Top: All events within highlighted tile in *d* (*red square*) for five burst periods, color-coded by propagation direction (top). Bottom: Event

propagation direction distributions (P=posterior; A=anterior; M=medial; L=lateral). (**g**) Cumulative distribution of percentage of bursts with events (within individual tiles/regions) propagating in the same direction in actual (solid) and simulated (dashed) data (one-tailed Wilcoxon rank sum, ***p<0.001) (**h**) Two representative maps of population burst propagation direction with each event color-coded by their onset time relative to the beginning of the burst period, demonstrating variability of burst size. (**i**) Burst propagation direction calculated from onset maps in *h* (n=66 bursts). Event locations from the first 20% of the frames after burst onset are averaged together to determine burst origin. Event locations from 20% of the last frames after burst onset are averaged together and the difference between this and the origin determines burst propagation distance. Red arrow denotes average of all bursts.

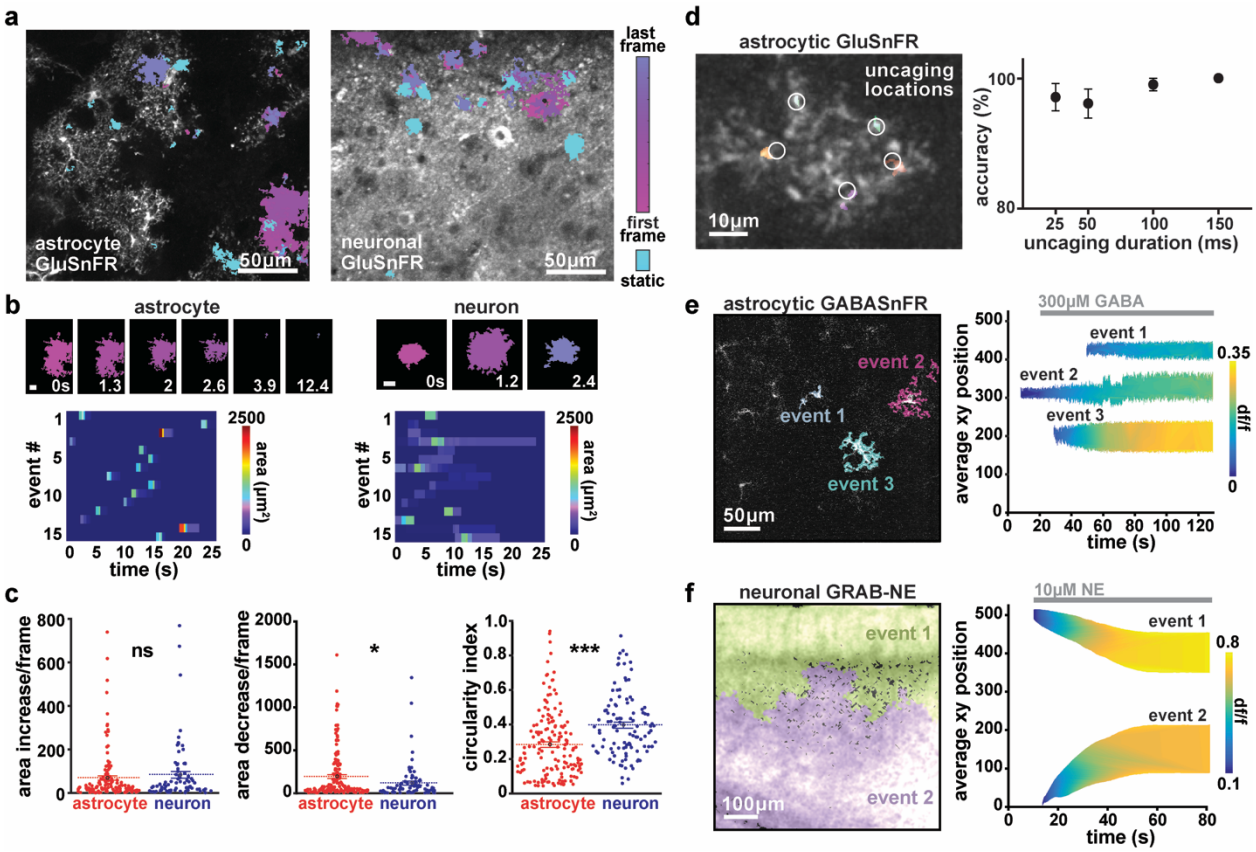

Figure 2.4: AQuA-based detection of extracellular dynamics via astrocytic and neuronal expression of genetically encoded neurotransmitter sensors.
(**a**) Representative images of *ex vivo* slices with expression of astrocytic (left) or neuronal (right) GluSnFR. Color indicates detected events. Those with dynamic shape are shown in magenta, and static events in cyan. (**b**) Examples of timecourse of astrocytic (left, top) and neuronal (right, top) glutamate events. Scale bar = 10µm. Raster plot of area of astrocytic (left, bottom) and neuronal (right, bottom) glutamate events. (**c**) Size dynamics (area increase [left] and decrease [middle] per frame) and shape (circularity index, right) of glutamate events when GluSnFR is expressed on astrocytes (red) or neurons (blue). (**d**) Left: Single astrocyte expressing GluSnFR, with AQuA-detected events (colors) with ~100Hz frame rate imaging and 25–150ms uncaging of RuBi-glutamate. Uncaging locations marked with white circles. Right: Percent correct events detected by AQuA, depending on duration of the laser uncaging pulse. (**e**) Example of three AQuA-detected events at single timepoint (97s) after addition of 300µM GABA to slice with astrocytes expressing GABASnFR (left). Right: Detected events before and after addition of 300µM GABA (gray bar) to circulating bath. Events are plotted to display spatial position in imaging field (y-axis), event area (height), and gradually increasing amplitude (color) over time. (**f**) Left: two detected events in cortical slice expressing GRAB-NE in neurons after addition of 10µM NE. Right: Events plotted to display spatial position (y-axis), event area (height), and amplitude (color) dynamics over the course of the experiment. In (e) and (f), average xy position at each timepoint is calculated using the following equation: (((xLoc-1)*frameSize) + yLoc)/frameSize.

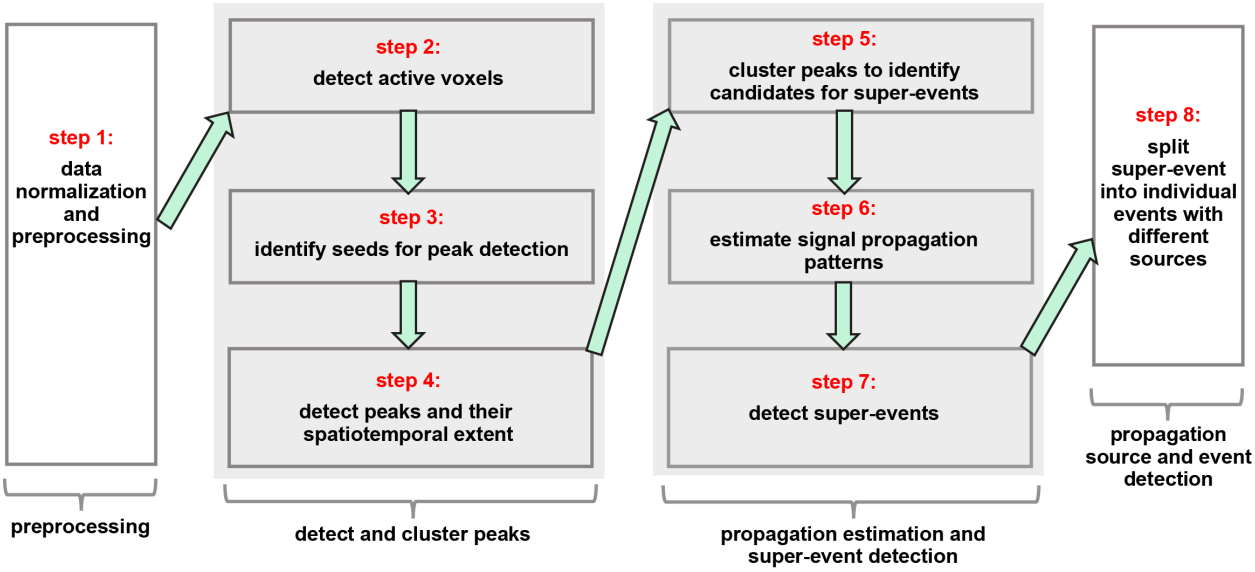

Figure 2.5: Eight steps in the AQuA algorithm. The eight steps can be grouped into four modules indicated by brackets below panels. The last three modules are further illustrated in **Fig. 2.6**.

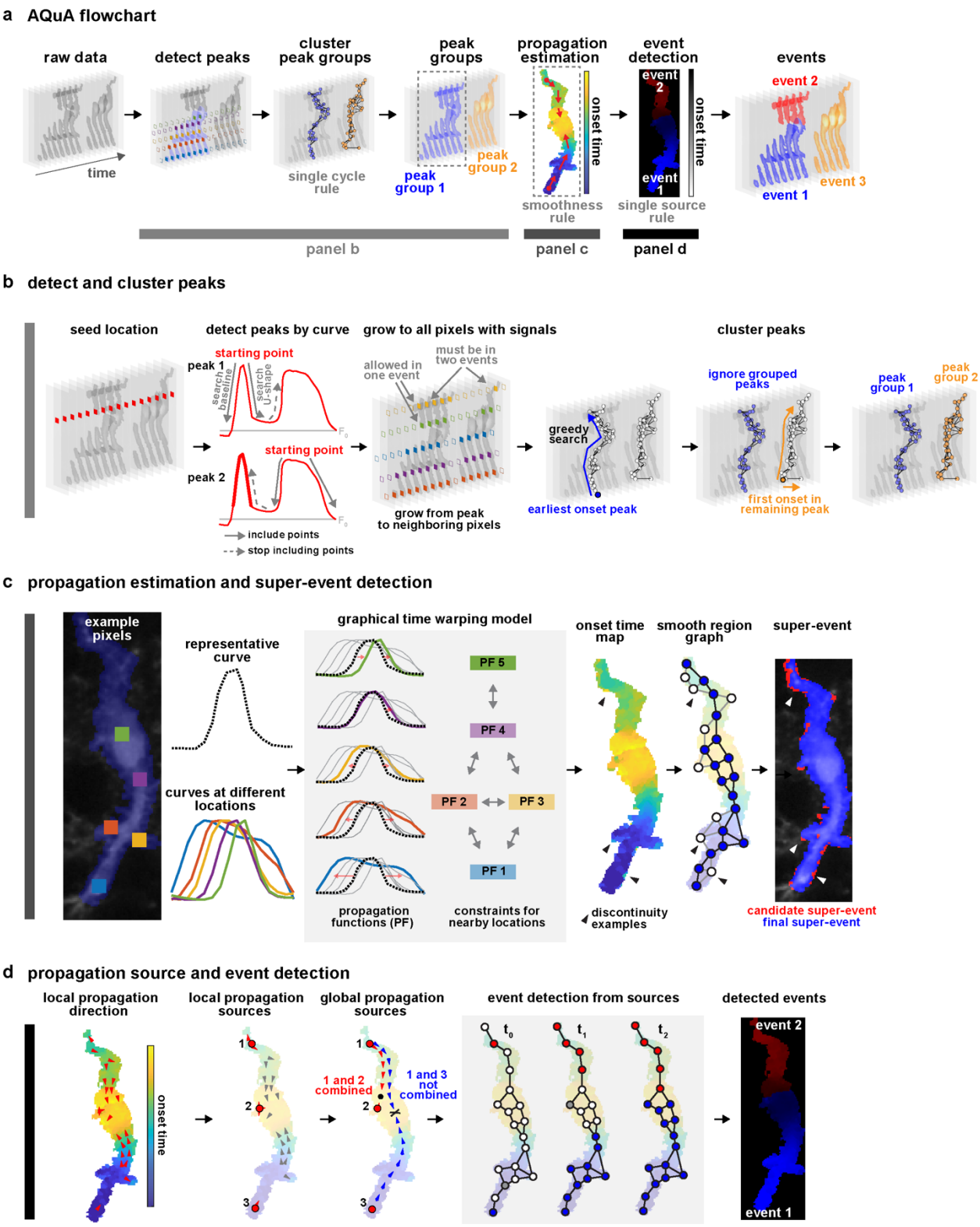

Figure 2.6: Schematic illustration of three major modules in AQuA algorithm. Curves and regions taken from a real data set. (**a**) **AQuA flowchart**, with three gray bars below indicating where the three major modules are located with respect to the AQuA flowchart. (**b**) **detect and cluster peaks:** curves in the *detect peaks by curve* panel are associated with the

location labeled by the red diamond in the *seed location* panel. One curve may have multiple peaks, which are detected one-by-one. Once a peak is detected at a seed location, the peak is spatially extended to include its neighboring pixels as in the *grow to all pixels with signals* panel. Clustering of peaks starts from the peak with the earliest onset time and includes its spatially adjacent peaks based on the two inclusion rules shown in the *grow to all pixels with signals* panel. Two peaks at one location are never clustered into one group. Once the greedy search strategy can't find more peaks to include, it stops and one peak group is formed. Then, to find another peak group, the greedy search restarts from the first onset in the remaining peaks. The process is repeated until no peaks remain. (**c**) **Propagation estimation and super-event detection:** This module is applied to each peak group. The five colored curves are the dynamics of the five exemplar pixels with corresponding colors. The dashed curve is the representative or reference curve. In the *graphical time warping model* panel, red arrows indicate how the reference curve can be warped to represent the curve at each location. The graphical time warping model incorporates the information that nearby locations should have more similar curves than distant locations. A double-headed arrow between two functions informs the model that these curves should be warped similarly to the reference curve. As a comparison, if there is no double-headed arrow between curves, dissimilar warping functions are allowed. Once the warping function is calculated by the graphical time warping model, onset time is computed for each pixel, resulting in an onset time map. Note discontinuity of onset time examples at black triangles. These pixels are removed to obtain the final super-event, which may contain multiple events and are subject to the next operation. (**d**) **Propagation source and event detection:** Local propagation sources are obtained by finding local minima on the onset time map. According to the rules described in Methods, some local sources will be combined/merged, resulting in global propagation sources. Briefly, if the path between two local sources does not have to go through a location with a late onset time, these two local sources are combined. Then, each global propagation source leads to an event. Each event is obtained by growing each global source to include its neighboring pixels. In the *event detection from sources* panel, solid dots are pixels already assigned to an event, white dots are unexplored pixels, and grey dots are explored but await a later decision to be assigned to an event.

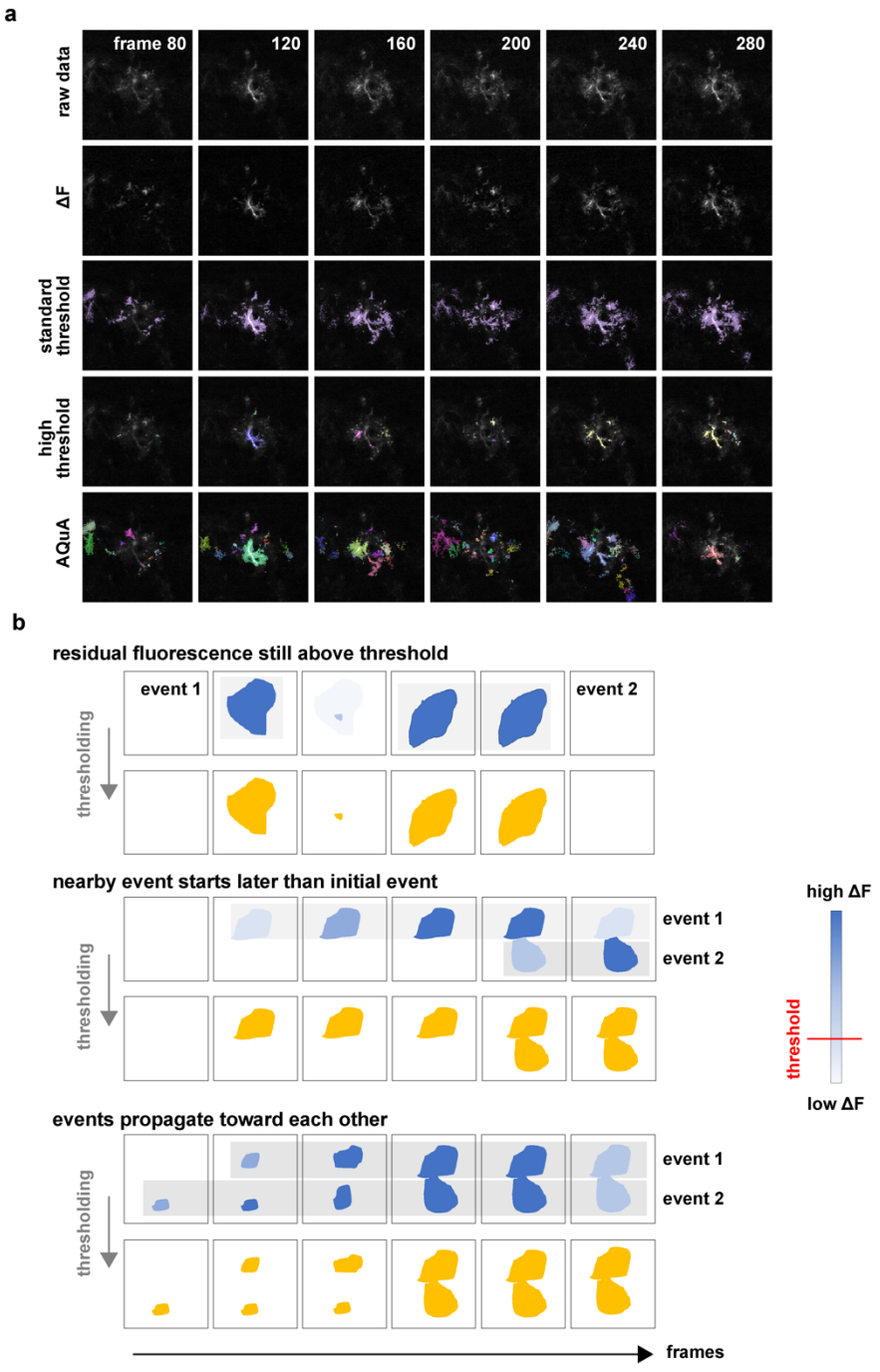

Figure 2.7: Limitations of thresholding-based analysis.
(**a**) *Top row*: Six example frames of *ex vivo* data smoothed with a Gaussian kernel of σ=0.5 after square root transformation. *Second row*: Baseline for each pixel is estimated with a 20-frame time window, noise level is estimated as σ_noise, and baseline is subtracted from raw data to obtain ΔF. *Third row*: Standard threshold is set at 3σ_noise. Many individual events are erroneously detected as one very long and large spatiotemporal component, for reasons graphically explained in (b). *Fouth row*: A high threshold (10σ_noise) leads to loss of many true events, and many detected events are incomplete. Each color indicates an event. *Fifth row*:

AQuA-detection avoids the pitfalls in threshold-setting and identifies each individual event. (**b**) Two events are incorrectly connected after thresholding (incorrect events in yellow in each sub-panel). Intensity color bar on right, with red indicating the threshold, refers to all panels. *Top*: Between multiple events in the same location, even though the intensity drops a lot, not all pixels will fall below the threshold. Each event is shown with a gray bounding box. The super-voxel step in AQuA solves this problem by finding a time window for each seed, and spatially extending the windows. *Middle*: Neighboring events are initiated at distinct times, but are spatiotemporally connected at a later time. If two regions have very different onset times, AQuA will treat them as different events in the super-event detection step. *Bottom*: Two events can be separated when they appear, but meet after propagating. In the event detection step, AQuA distinguishes these events based on the single-source rule.

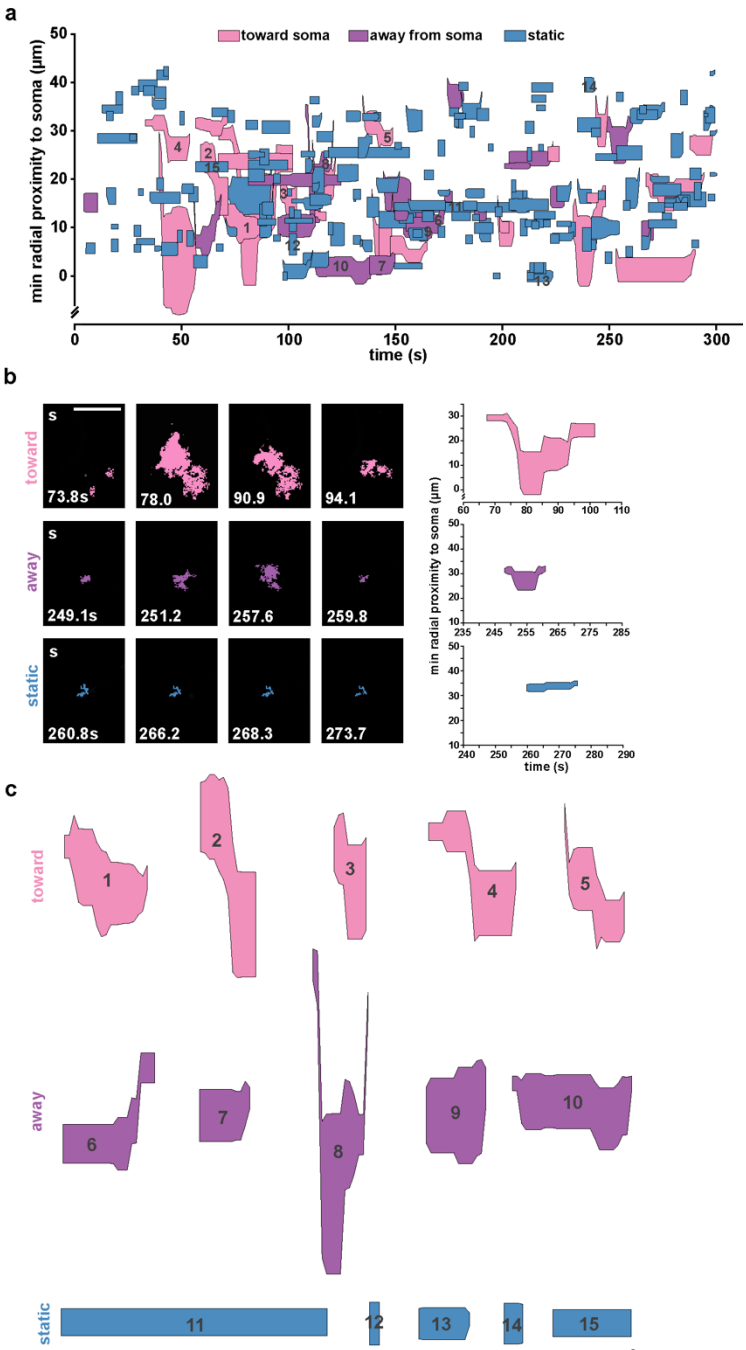

Figure 2.8: AQuA features enable detailed Ca^{2+} activity plots.
(**a**) Spatiotemporal plot of Ca^{2+} activity from a five minute movie (the first minute of which is shown in **Fig. 2.2b**). Each event is represented by a polygon that is proportional to the area of the event as it changes over its lifetime, and color-coded by propagation direction. (**b**) Example time series illustrating how propagation direction is determined (left). A propagation direction score is calculated for each event by multiplying the Euclidian distance between the event pixels' proximity to the soma at each frame by each pixel's intensity. The overall score is the summation of this weighted pixel intensity distance over the lifetime of the event. Therefore, if more pixels with higher intensity move toward the soma it will be classified as such (top). While some events appear in the plot as moving toward the soma, they are actually calculated as moving away from

the soma (middle) since we are only displaying the minimum event proximity to the soma in the spatiotemporal plot, but calculate each pixel's proximity to the soma when generating propagation score. Further, pixel intensity is first thresholded at 0.3dF/F. Therefore, events that move toward or away from the soma yet have pixel intensities below threshold (bottom) appear to have a propagation direction when plotted, yet have a zero propagation direction score when calculated. (**c**) Additional events plotted for each propagation direction category to demonstrate range of detected/plotted events. Scale is not equivalent to events shown in *b*, but is equivalent within entire group shown here.

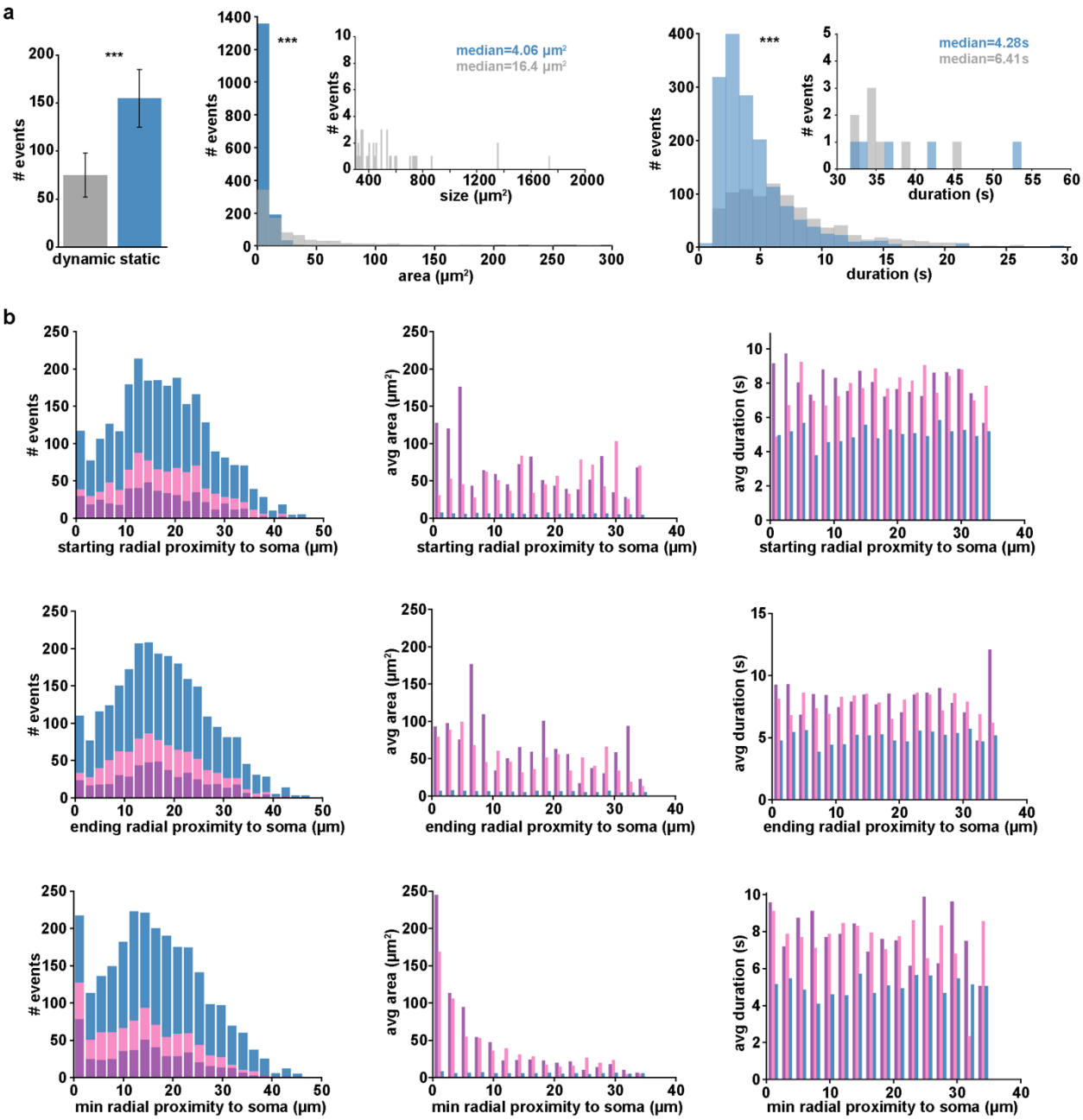

Figure 2.9: Distribution of Ca^{2+} event features.

(**a**) Left: total number of Ca^{2+} events that are dynamic (gray, propagation direction score > 0) and static (blue, propagation direction score = 0) within the 2D imaging plane, ***p < 0.001, n=11 cells, chi-square test for independence. Middle: distribution of Ca^{2+} event area for dynamic and static events, ***p < 0.001, one-tailed Wilcoxon rank sum test. Right: distribution of Ca^{2+} event duration for dynamic and static events, ***p < 0.001, one-tailed Wilcoxon rank sum test (right). (**b**) Distribution, average area, and average duration of events propagating toward soma (pink),

away from soma (purple), and static events (blue) compared to starting distance from soma (top row), ending distance from soma (middle row), and minimum distance from soma (bottom row). Bin widths calculated by Freedman-Diaconis's rule.

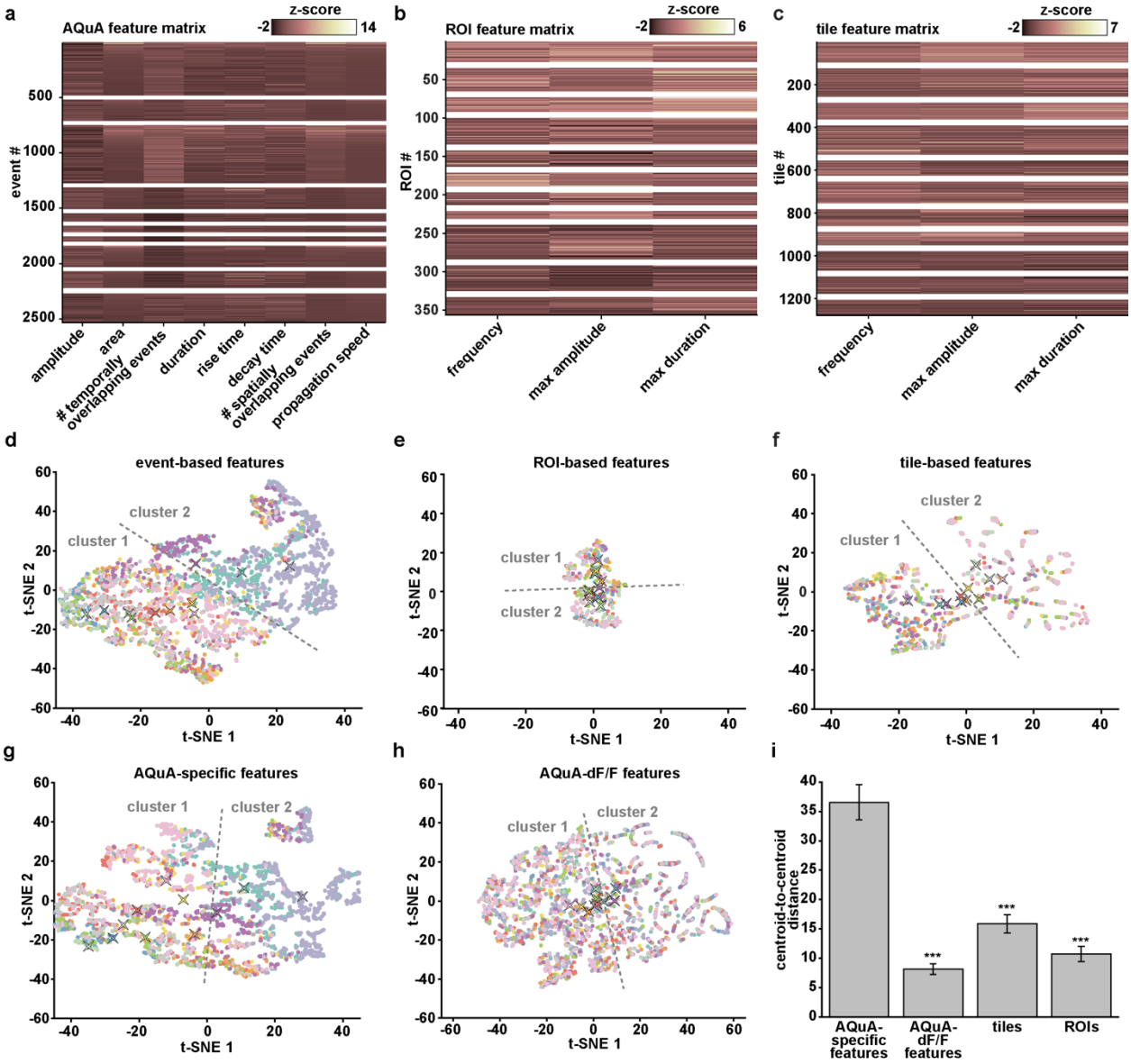

Figure 2.10: Cluster analysis on features generated from three spatial footprint methods. (**a**) Heatmap of *z*-scores for eight AQuA features (x-axis) describing each event. White boxes demarcate events and features from individual cells. (**b–c**) Top: heatmaps of *z*-scores for three features describing the Ca^{2+} activity at each ROI (*b*) or tile (*c*) location. ROIs detected using average projection image with a 5μm square filter applied (for ROIs) or 5x5μm tiles, based on fluorescence intensity and size. Ca^{2+} events with signals > 0.03dF/F and two times the noise of each individual trace were selected. Pixels within each ROI or tile were averaged and dF/F was calculated by dividing each value by the mean values from the previous 25 seconds. (**d–f**) t-SNE visualizations of each cell's Ca^{2+} activity using features calculated using AQuA (*d*), ROIs (*e*), and tiles (*f*). High dimensional data (*a–c*) are reduced are displayed in two dimensions. Points that are clustered closer together can be interpreted as having more similar Ca^{2+} activity features. K-means clustering boundary denoted as dashed line. (**g–h**) t-SNE plots using only subsets of AQuA-calculated features from (*a*) and (*d*). (**g**) t-SNE plot of only the features specific to AQuA

and not shared with ROI or tile analysis. (**h**) Plot using only AQuA-extracted features that correspond to those in ROI- or tile-based analyses. (**i**) Comparison of difference between two clusters generated from the t-SNE analysis followed by k-means clustering. Note increased separation using AQuA-specific features compared to others. (One-tailed paired t-test, ***$p<0.001$)

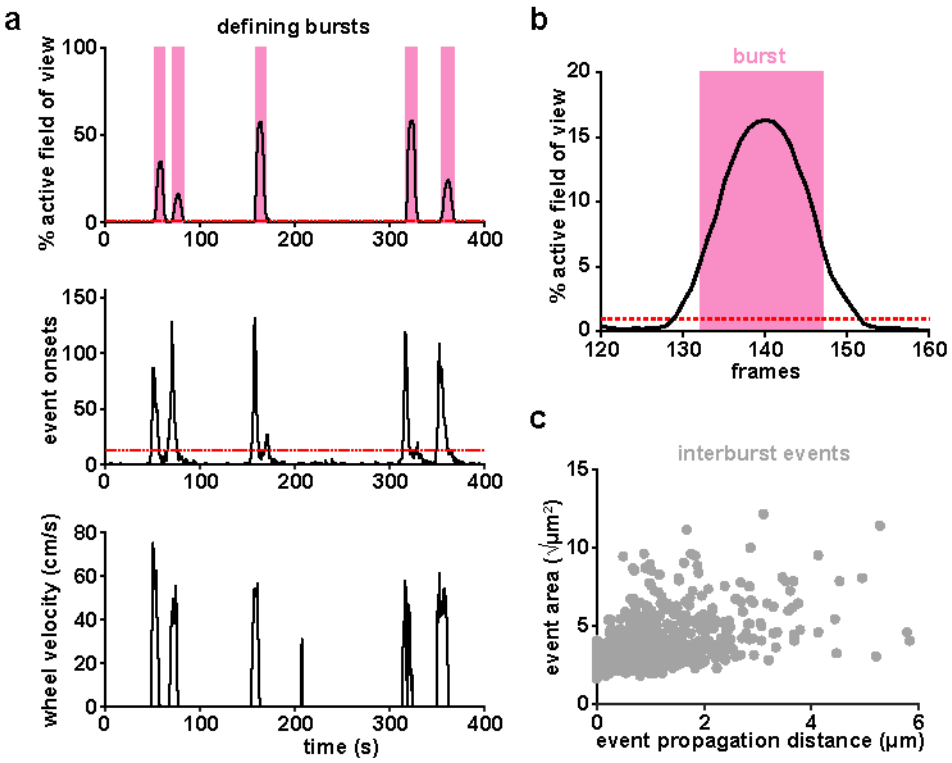

Figure 2.11: Defining *in vivo* burst and inter-burst events.
(**a**) Population Ca^{2+} events represented as two temporal traces: percentage of imaging field active (top) and number of AQuA event onsets (middle). Burst periods (pink) are defined from the top trace as periods when Ca^{2+} activity exceeds 1% of the active field of view (red dashed line, top), and exceeds 10% of the maximum number of event onsets (red dashed line, middle). Burst periods correlate with wheel velocity of the treadmill (bottom). (**b**) Burst onset is defined as the first frame in which 10% of the peak is exceeded and burst offset is defined as the last frame exceeding 10% of the peak. (**c**) The relationship between all interburst events' total propagation distance and size, similar to the burst events plotted in **Fig. 2.3c**.

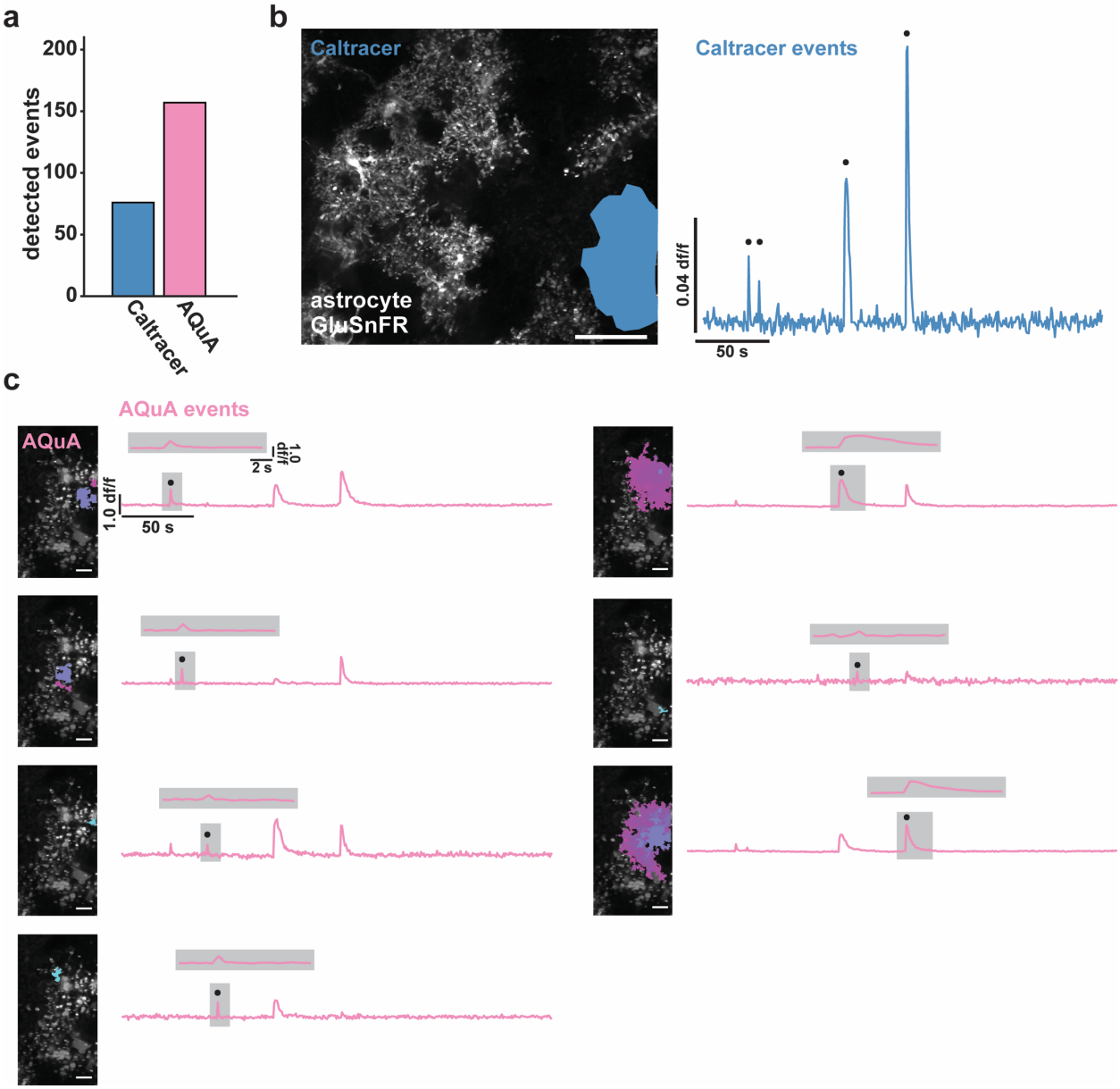

Figure 2.12: Comparison of AQuA and Caltracer for event detection of astrocytic GluSnFR signals.

(**a**) Applied to the same data sets, AQuA detects 157 events, while Caltracer[2,9], using a rising faces algorithm, detects 76 events with manually defined single-cell ROIs. (**b**) ROI example (left) and temporal trace with detected events marked by black circle using Caltracer software. Scale bar = 50µm. (**c**) AQuA-detected events from the same cell as in (b), and corresponding temporal traces (black dot, specific events shown above each trace). Scale bar = 10µm.

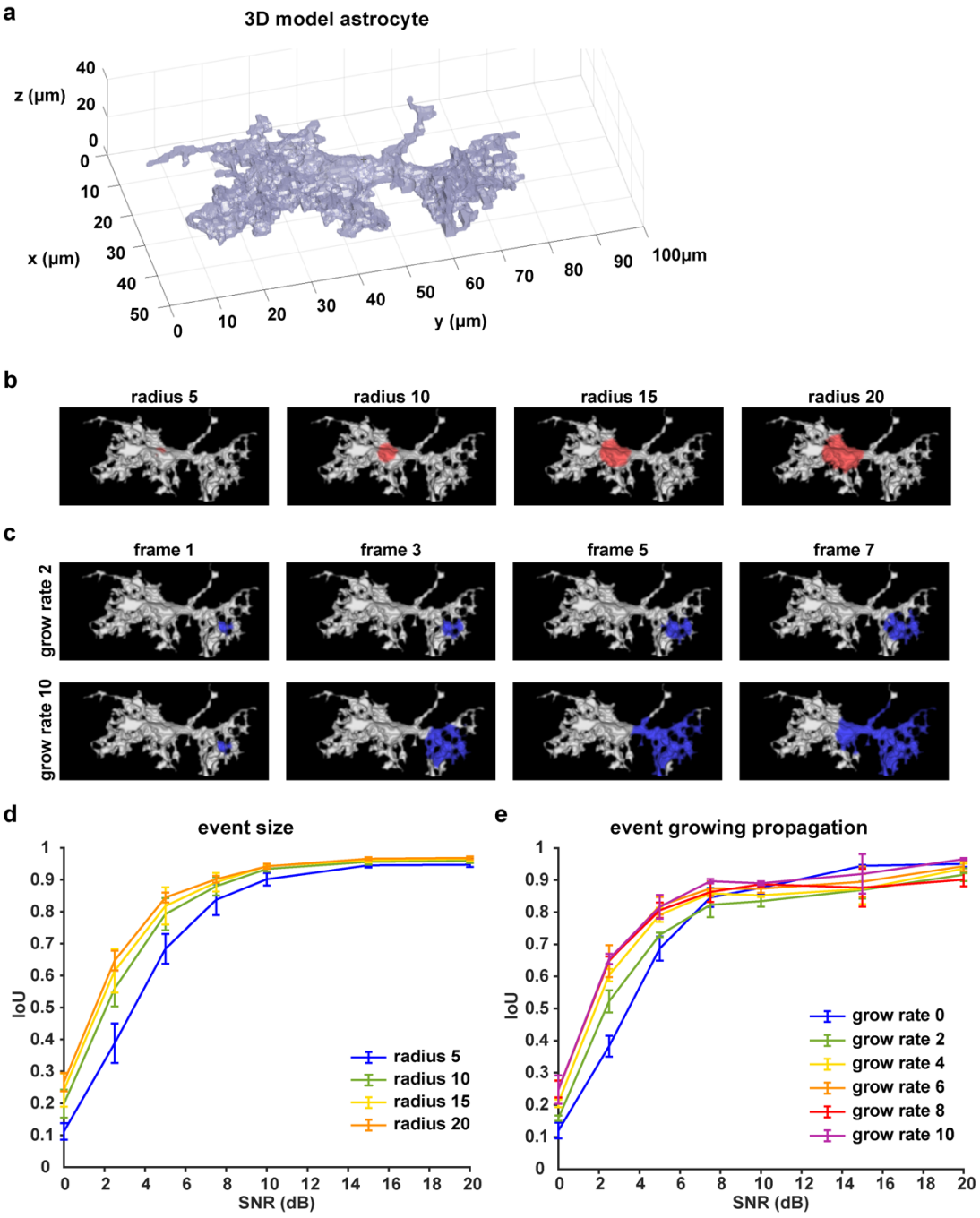

Figure 2.13: AQuA performance on simulated 3D datasets.
(**a**) The 3D model used for performance testing the 3D AQuA extension was extracted from real imaging data[17]. (**b**) Example of simulated data in which event size varies; each column represents a different event radius. (**c**) Examples of simulated events with slow (top row, growth rate 2) and fast (bottom row, growth rate 10) growing propagation rates. (**d**–**e**) Results of AQuA performance on simulated datasets with respect to varying SNR under independently varying event (**d**) size and (**e**) growing propagation rates. IoU (intersection over union) measures the overlap between detected and ground-truth events. An IoU of 1 is the best performance achievable, indicating that all detected events are ground-truth and all ground-truth events are

detected. The bars on each curve indicate the 95% confidence interval calculated from 5 independent replications of simulation, where each simulation contains 10–20 events.

References

1. Srinivasan, R. *et al.* New Transgenic Mouse Lines for Selectively Targeting Astrocytes and Studying Calcium Signals in Astrocyte Processes In Situ and In Vivo. *Neuron* **92,** 1181–1195 (2016).
2. Marvin, J. S. *et al.* An optimized fluorescent probe for visualizing glutamate neurotransmission. *Nat. Methods* **10,** 162–170 (2013).
3. Chen, T.-W. *et al.* Ultrasensitive fluorescent proteins for imaging neuronal activity. *Nature* **499,** 295–300 (2013).
4. Srinivasan, R. *et al.* Ca(2+) signaling in astrocytes from Ip3r2(-/-) mice in brain slices and during startle responses in vivo. *Nat. Neurosci.* **18,** 708–717 (2015).
5. Paukert, M. *et al.* Norepinephrine controls astroglial responsiveness to local circuit activity. *Neuron* **82,** 1263–1270 (2014).
6. Haustein, M. D. *et al.* Conditions and constraints for astrocyte calcium signaling in the hippocampal mossy fiber pathway. *Neuron* **82,** 413–429 (2014).
7. Ding, F. *et al.* α1-Adrenergic receptors mediate coordinated Ca2+ signaling of cortical astrocytes in awake, behaving mice. *Cell Calcium* **54,** 387–394 (2013).
8. Poskanzer, K. E. & Yuste, R. Astrocytes regulate cortical state switching in vivo. *Proc. Natl. Acad. Sci. U.S.A.* 201520759 (2016). doi:10.1073/pnas.1520759113
9. Ma, Z., Stork, T., Bergles, D. E. & Freeman, M. R. Neuromodulators signal through astrocytes to alter neural circuit activity and behaviour. *Nature* **539,** 428–432 (2016).
10. Poskanzer, K. E. & Yuste, R. Astrocytic regulation of cortical UP states. *Proc. Natl. Acad. Sci. U.S.A.* **108,** 18453–18458 (2011).
11. Looger, L. L. A genetically encoded fluorescent sensor for in vivo imaging of GABA.

bioRxiv 322578 (2018). doi:10.1101/322578

12. Feng, J. *et al.* A Genetically Encoded Fluorescent Sensor for Rapid and Specific In Vivo Detection of Norepinephrine. *Neuron* (2019). doi:10.1016/j.neuron.2019.02.037
13. Lobas, M. A. *et al.* A genetically encoded single-wavelength sensor for imaging cytosolic and cell surface ATP. *Nature Communications* **10,** 711 (2019).
14. Patriarchi, T. *et al.* Ultrafast neuronal imaging of dopamine dynamics with designed genetically encoded sensors. *Science* **360,** eaat4422 (2018).
15. Agarwal, A. *et al.* Transient Opening of the Mitochondrial Permeability Transition Pore Induces Microdomain Calcium Transients in Astrocyte Processes. *Neuron* **93,** 587–605.e7 (2017).
16. Armbruster, M., Hanson, E. & Dulla, C. G. Glutamate Clearance Is Locally Modulated by Presynaptic Neuronal Activity in the Cerebral Cortex. *J. Neurosci.* **36,** 10404–10415 (2016).
17. Bindocci, E. *et al.* Three-dimensional Ca(2+) imaging advances understanding of astrocyte biology. *Science* **356,** eaai8185 (2017).
18. Wu, Y.-W. *et al.* Spatiotemporal calcium dynamics in single astrocytes and its modulation by neuronal activity. *Cell Calcium* **55,** 119–129 (2014).
19. Wang, Y. *et al.* Graphical Time Warping for Joint Alignment of Multiple Curves. *Neural Information Processing Systems* 3648–3656 (2016).
20. Giovannucci, A. *et al.* CaImAn: An open source tool for scalable Calcium Imaging data Analysis. *bioRxiv* 339564 (2018). doi:10.1101/339564
21. Pachitariu, M. *et al.* Suite2p: beyond 10,000 neurons with standard two-photon microscopy. (2016). doi:10.1101/061507

22. Poskanzer, K. E. & Molofsky, A. V. Dynamism of an Astrocyte In Vivo: Perspectives on Identity and Function. *Annu. Rev. Physiol.* **80,** 143–157 (2018).

23. Shigetomi, E. *et al.* Imaging calcium microdomains within entire astrocyte territories and endfeet with GCaMPs expressed using adeno-associated viruses. *J. Gen. Physiol.* **141,** 633–647 (2013).

24. van der Maaten, L. & Hinton, G. Visualizing Data using t-SNE. *Journal of Machine Learning Research* **9,** 2579–2605 (2008).

25. Stobart, J. L. *et al.* Cortical Circuit Activity Evokes Rapid Astrocyte Calcium Signals on a Similar Timescale to Neurons. *Neuron* **98,** 726–735.e4 (2018).

26. Kanemaru, K. *et al.* In vivo visualization of subtle, transient, and local activity of astrocytes using an ultrasensitive Ca(2+) indicator. *Cell Rep* **8,** 311–318 (2014).

27. Nimmerjahn, A., Mukamel, E. A. & Schnitzer, M. J. Motor behavior activates Bergmann glial networks. *Neuron* **62,** 400–412 (2009).

28. Parsons, M. P. *et al.* Real-time imaging of glutamate clearance reveals normal striatal uptake in Huntington disease mouse models. *Nature Communications* **7,** 11251 (2016).

29. Jiang, R., Diaz-Castro, B., Looger, L. L. & Khakh, B. S. Dysfunctional Calcium and Glutamate Signaling in Striatal Astrocytes from Huntington's Disease Model Mice. *J. Neurosci.* **36,** 3453–3470 (2016).

30. Hefendehl, J. K. *et al.* Mapping synaptic glutamate transporter dysfunction in vivo to regions surrounding Aβ plaques by iGluSnFR two-photon imaging. *Nature Communications* **7,** 13441 (2016).

31. Marvin, J. S. *et al.* Stability, affinity, and chromatic variants of the glutamate sensor iGluSnFR. *Nat. Methods* **15,** 936–939 (2018).

32. Fino, E. *et al.* RuBi-Glutamate: Two-Photon and Visible-Light Photoactivation of Neurons and Dendritic spines. *Front Neural Circuits* **3,** 2 (2009).

33. Chai, H. *et al.* Neural Circuit-Specialized Astrocytes: Transcriptomic, Proteomic, Morphological, and Functional Evidence. *Neuron* **95,** 531–549.e9 (2017).

34. Baraban, M., Koudelka, S. & Lyons, D. A. Ca 2+ activity signatures of myelin sheath formation and growth in vivo. *Nat. Neurosci.* **19,** 190 (2017).

35. Krasnow, A. M., Ford, M. C., Valdivia, L. E., Wilson, S. W. & Attwell, D. Regulation of developing myelin sheath elongation by oligodendrocyte calcium transients in vivo. *Nat. Neurosci.* **93,** 9887 (2017).

36. Higley, M. J. & Sabatini, B. L. Calcium signaling in dendritic spines. *Cold Spring Harb Perspect Biol* **4,** a005686–a005686 (2012).

37. Keller, P. J. & Ahrens, M. B. Visualizing whole-brain activity and development at the single-cell level using light-sheet microscopy. *Neuron* **85,** 462–483 (2015).

38. Goldey, G. J. *et al.* Removable cranial windows for long-term imaging in awake mice. *Nat Protoc* **9,** 2515–2538 (2014).

39. Pnevmatikakis, E. A. & Giovannucci, A. NoRMCorre: An online algorithm for piecewise rigid motion correction of calcium imaging data. *J. Neurosci. Methods* **291,** 83–94 (2017).

40. Müller, M. *Information Retrieval for Music and Motion*. (Springer Science & Business Media, 2007). doi:10.1007/978-3-540-74048-3

41. Wang, Y. *et al.* Automated Functional Analysis of Astrocytes from Chronic Time-Lapse Calcium Imaging Data. *Front Neuroinform* **11,** 48 (2017).

Chapter 3:

Cortical astrocytes independently regulate sleep depth and duration via separate GPCR pathways

---

Abstract

Non-rapid eye movement (NREM) sleep, characterized by slow-wave electrophysiological activity, underlies several critical functions, including learning and memory. However, NREM sleep is heterogeneous, varying in duration, depth, and spatially across the cortex. While these NREM sleep features are thought to be largely independently regulated, there is also evidence that they are mechanistically coupled. To investigate how cortical NREM sleep features are controlled, we examined the astrocytic network, comprising a cortex-wide syncytium that influences population-level neuronal activity. We quantified endogenous astrocyte activity in mice over natural sleep and wake, then manipulated specific astrocytic G-protein-coupled receptor (GPCR) signaling pathways *in vivo*. We find that astrocytic Gi- and Gq-coupled GPCR signaling separately control NREM sleep depth and duration, respectively, and that astrocytic signaling causes differential changes in local and remote cortex. These data support a model in which the cortical astrocyte network serves as a hub for regulating distinct NREM sleep features.

Introduction

Sleep is characterized by distinct electrophysiological features that reflect the rhythmic activity of large populations of neurons. One phase of sleep—non-rapid eye movement (NREM) sleep—is critical for several important functions including memory consolidation/destabilization

and synaptic homeostasis[1–8]. These functions are thought to require slow-wave activity (SWA), the distinct oscillatory pattern of neural activity in the cortex that occurs during NREM sleep and differentiates it from the relatively desynchronized activity during wakefulness and REM sleep. However, neural activity during NREM sleep is not uniform over the course of sleep, but varies in duration and depth (as measured by SWA intensity). Past work has demonstrated that NREM sleep duration and depth can be independently controlled[9,10]. Indeed, the circuit mechanisms known to underlie sleep depth and duration are largely independent from each other and operate on very different time-scales: sleep duration is mediated by subcortical nuclei that receive direct input from circadian centers and drive sleep/wake transitions through release of neuromodulatory signals[11–13]. On the other hand, SWA intensity is largely regulated by cortical and thalamocortical circuits[14–21]. While these two physiological measures of sleep have been mostly described in non-overlapping mechanistic terms, there is also physiological evidence that sleep depth and duration can be coupled. For example, cortical Ca^{2+} signaling can act on a millisecond time-scale to modulate cortical synchrony during SWA while also engaging longer-term signaling cascades that regulate the sleep/wake cycle[22,23]. Thus, the extent to which the neural mechanisms underlying sleep depth and duration are linked remains unclear.

The cortex—where mammalian sleep is most often measured—is a brain region where neural mechanisms underlying sleep duration and sleep depth coincide: many neuromodulatory nuclei associated with sleep/wake transitions send direct projections to the cortex[24–27], and the cortex plays an instrumental role in generating and propagating SWA during sleep[17,21,28–34]. Further, cortical SWA intensity can be locally regulated, leading to heterogeneity of SWA across cortex[35–37]. However, how the cortex integrates separate regulatory signals to orchestrate activity across sleep and wake is unknown. In untangling sleep mechanisms, both in cortex and

throughout the brain, the historical focus has almost exclusively been on neurons and neuronal circuits. Yet astrocytes—the largest class of non-neuronal brain cells—are also situated to play critical roles in sleep regulation within the cortex. Astrocytes tile the cortex, can participate in bidirectional communication with thousands of neurons[38–41], exhibit morphological and transcriptional changes during sleep[42], and regulate SWA under anesthesia[43–45]. Further, multiple canonical astrocytic functions are also associated with sleep/wake regulation, including regulation of extracellular glutamate[44,46], extracellular ion dynamics[47], release of neurotransmitters[48–50], and metabolic regulation[51–53].

Astrocyte physiology is primarily measured via intracellular calcium (Ca^{2+}) dynamics, which vary widely in size, shape, and location, and can propagate within or even between cells[54–58]. Because imaging complex astrocyte Ca^{2+} activity *in vivo* is relatively new, it remains unknown whether these diverse astrocytic Ca^{2+} dynamics map onto different circuit functions. However, the potential of astrocytes to influence large populations of cortical neurons across different time-scales is significant[59,60]. The majority of astrocyte Ca^{2+} activity is thought to result from upstream activation of G-protein coupled receptors (GPCRs)[45,61–63]. Importantly, many astrocytic GPCRs are activated by neuromodulators, including those associated with sleep/wake regulation, such as norepinephrine, acetylcholine, and histamine. Since GPCRs regulate a diverse array of Ca^{2+}-dependent intracellular signals on many different time-scales[64,65], they are prime candidates for differentially regulating individual features of NREM sleep, such as duration and depth. A downstream target of GPCRs, the inositol triphosphate type 2 receptor (IP_3R2), has been recently shown to be involved in sleep regulation[66]. In astrocytes, both Gi- and Gq-coupled GPCRs activate IP_3R2s and lead to increases in intracellular Ca^{2+}[45,67,68], while also engaging separate signaling cascades. Despite this, scant attention has been paid to whether the activation of

different astrocytic GPCRs, and resulting Ca^{2+} signals, have differential effects on the surrounding neural circuit. Indeed, GPCR signaling in astrocytes may underlie mechanisms by which astrocytes perform multiple, parallel functions in the neural circuit.

Here, we leveraged a recently developed image analysis tool that captures the spatiotemporal complexity of astrocyte Ca^{2+} dynamics[54] and astrocyte-specific chemogenetics to investigate the mechanisms by which cortical astrocytes both link and independently regulate different features of NREM sleep via GPCR signaling. To do this, we carried out *in vivo* two-photon (2P) imaging of astrocyte Ca^{2+} while recording electrophysiological sleep rhythms to examine astrocyte Ca^{2+} changes across natural sleep and wake. We find that endogenous Ca^{2+} activity is inversely correlated with SWA and exhibits bidirectional changes prior to sleep-wake transitions. Using chemogenetics to selectively manipulate astrocytic Gi- and Gq-GPCR pathways, we demonstrate that astrocytes actively regulate both NREM sleep duration and depth, via separate GPCR signaling pathways: astrocytic Gi-induced Ca^{2+} is sufficient to increase SWA (sleep depth), while sleep-wake transitions (sleep duration) is dependent on Gq-GPCRs. We demonstrate a role for astrocytes in both local and cortex-wide sleep regulation; manipulating astrocytic Ca^{2+} in primary visual cortex (V1) alters not only local SWA, but also affects SWA in contralateral frontal cortex (FC). Further, we find that while local changes in SWA arise from greater changes in delta waves, remote SWA effects in FC are due to increases in slow oscillations. Since these two slow waves underlie different functions, our data support the concept that astrocytes exert different effects on neuronal populations depending on both the type of GPCR activated *and* their localization within cortical circuits. Together, our data support a role for the cortical astrocytic network as a hub for the regulation of sleep depth and duration across cortex.

Results

Accurate detection of astrocyte Ca^{2+} events in vivo *across sleep and wake*

To study the role of astrocytes in sleep regulation, we conducted 2P imaging of astrocyte Ca^{2+} dynamics as animals naturally transitioned between sleep and wake states[28,69]. To specifically express the Ca^{2+} indicator GCaMP6f in cortical astrocytes, we injected mice with *AAV-GFAP-GCaMP6f* 2–4 weeks before experiments (**Fig. 3.1b**, left). Electrodes were implanted for local field potential (LFP) and electromyogram (EMG) recordings (**Fig. 3.1b**, right) to assess sleep state. During recording sessions, mice were head-fixed on a horizontal treadmill, and locomotion was recorded (**Fig. 3.1a**). To control for the effect of circadian rhythm and sleep pressure, all recording sessions took place between ZT 2–5. Experiments were conducted after mice had been previously habituated to head-fixation to allow natural sleep. To analyze astrocyte Ca^{2+} activity, we used our recent tool, AQuA[54], an event-based approach to detect spatiotemporally distinct Ca^{2+} events without predetermined regions-of-interest (ROIs). This allowed automatic detection of individual astrocyte Ca^{2+} events, independent of size and shape, across sleep and wake (**Fig. 3.1c**).

Cortical astrocyte Ca^{2+} frequency and SWA are negatively correlated across behavioral states.

To investigate the relationship between *in vivo* cortical astrocyte activity and NREM sleep we first quantified the relationship between Ca^{2+} event rate and SWA (0.5–4Hz power), a marker of NREM sleep depth. By dividing entire 2–3 hr recordings into two-minute bins, we found that Ca^{2+} event rate and SWA were negatively correlated (**Fig. 3.1d**), i.e when SWA is low, astrocyte Ca^{2+} event rate is high, and vice versa. This finding suggests astrocytes may play

roles regulating SWA, an idea supported by previous studies demonstrating that astrocyte Ca^{2+} plays a causal role in driving low frequency-dominated cortical states under anesthesia[43,44,50].

To determine whether the negative correlation between astrocyte Ca^{2+} and SWA is specific to a particular behavioral state, we analyzed our data by dividing recording periods into sleep, locomotory wake, and stationary wake (**Fig. 3.1e**). We separated wake by locomotion to quantify Ca^{2+} dynamics independently from large Ca^{2+} bursts that occur with locomotion onset[54,70,71]. As predicted by the negative correlation between event rate and SWA (**Fig. 3.1d**), we found that Ca^{2+} event rate was highest during locomotory wake, lower during stationary wake, and lowest during sleep (**Fig. 3.1f**). To confirm, we compared SWA in the three behavioral states and found an inverse relationship of Ca^{2+} event rate, namely SWA was highest during sleep, lower during stationary wake, and lowest during locomotory wake (**Fig. 3.1g**). These findings are supported by recent work demonstrating the same pattern of Ca^{2+} activity across similar behavioral states, using an ROI-based image analysis approach[66], confirming that our event-based image analysis can generate comparable results when the same metrics are quantified. Together, these data demonstrate that changes in Ca^{2+} event frequency co-occur with major changes in behavioral state, consistent with levels of SWA.

To explore whether each behavioral state can be characterized by the types of astrocytic Ca^{2+} events that occur during these states, we first compared the events' size, duration, and amplitude. As predicted by the large, synchronous bursts observed during locomotion, we found locomotory wake Ca^{2+} events were larger in size and duration than events observed in the other two states. However, when we controlled for locomotion we did not find differences in size, duration, or amplitude of events between sleep and stationary wake when these features were compared individually (**Fig. 3.2a**). However, astrocyte events have many other features beyond

size, duration, and amplitude, such as event perimeter or propagation. Because of this spatiotemporal complexity, we next used a dimensionality reduction approach, implementing principal component analysis to explore whether astrocyte Ca^{2+} events differed among behavioral states. This approach allowed us to incorporate 20 different event features calculated by AQuA. We found that the first three principal components (PCs) represented spatial-, temporal-, and amplitude-related features respectively. We then focused on the five PCs that explained the most variance in the imaging data (**Fig. 3.2b**) and compared them among the three behavioral states. While the largest differences in each PC were between locomotory wake and the other two states, we also found significant differences between sleep and stationary wake in all five PCs examined (**Fig. 3.2c**). Together, this analysis demonstrates that while no state-specific differences are observed by comparisons of individual event features, there are unique spatial, temporal, and amplitude signatures of sleep-specific astrocyte Ca^{2+} events when multiple features are incorporated.

We next examined the relationship between astrocyte Ca^{2+} event frequency and SWA within stationary behavioral states and found, similar to Fig. 3.1d, a negative correlation between Ca^{2+} frequency and SWA (**Fig. 3.1h**). The strong association found between Ca^{2+} frequency and SWA during sleep, namely high Ca^{2+} activity during sleep periods of low SWA and vice versa, is suggestive of a possible role of astrocytic Ca^{2+} specifically in sleep depth. Lastly, we explored the role of IP_3R2 in the relationship between astrocyte Ca^{2+} activity and SWA since IP_3R2s are enriched in astrocytes[72], underlie a significant fraction of astrocytic Ca^{2+} dynamics through Ca^{2+} release from intracellular stores[73], and IP_3R2 KO mice show a total decrease in SWA during NREM sleep[66]. To test whether the inverse relationship of astrocyte Ca^{2+} and SWA is dependent on IP_3R2s, we next imaged astrocyte Ca^{2+} dynamics over natural sleep and wake in IP_3R2 KO

mice[74]. Similar to previous work[75], we noted a reduction, but not complete abolishment, of Ca^{2+} events in IP_3R2 KO mice. In IP_3R2 KO mice, Ca^{2+} event rate and SWA were negatively correlated, but the correlation was decreased compared to controls (**Fig. 3.1i**), suggesting the astrocyte-SWA relationship is at least partially dependent on the IP_3R2. The change in correlation between control and IP_3R2 KO was most dramatic in sleep, implicating IP_3R2-dependent astrocytic Ca^{2+} signaling in the regulation of SWA intensity in the sleep state. Since both Gq- and Gi-GPCR signaling can increase Ca^{2+} in astrocytes through IP_3R2s[45,68] and astrocytes express many GPCRs that have been implicated in sleep-wake regulation[45,61–63], the relationship between astrocytic Ca^{2+} and SWA may result from astrocytic sensing of sleep-wake cues through GPCR signaling.

Transitions from low to high SWA are centered around astrocyte Ca^{2+} events

To understand how astrocyte Ca^{2+} activity is related to SWA on a shorter time-scale, we asked whether consistent electrophysiological changes occur in the seconds around the onset of astrocyte Ca^{2+} events. As earlier, we separated the recordings by sleep, stationary wake, and locomotory wake states (**Fig. 3.3a**). Although SWA was, by definition, highest during sleep, we also observed significant fluctuation between periods of relative high and low SWA within each behavioral state (**Fig. 3.3b**). We next calculated Ca^{2+} event-triggered averages of SWA, separated by behavioral state. Because the majority of locomotory wake Ca^{2+} events were in bursts tied to locomotion onset, we focused on sleep and stationary wake states. We found a pattern in which Ca^{2+} events were preceded by decreases in SWA and followed by increases in SWA (**Fig. 3.3c**, left). This modulation was significantly higher during sleep compared to stationary wake (**Fig.**

3.3d). Further, this SWA modulation was decreased in IP_3R2 KO mice (**Fig. 3.3c,** right, **2d**), indicating partial dependence of this relationship on IP_3R2s (as in **Fig. 3.1i**).

This specific pattern of SWA change centered on astrocyte Ca^{2+} events—low SWA before astrocyte events and higher afterward—suggests an active role of astrocytes in regulating sleep depth. Specifically, we speculate that astrocytes may be associated with a homeostatic process that increases SWA in response to a transient decrease in SWA. Although we cannot determine this from the data shown here, several lines of evidence support this hypothesis: astrocytes exhibit Ca^{2+} increases in response to many neuromodulators associated with decreased low-frequency power[76–79] and cortical astrocytes have the ability to increase low-frequency power[43,44]. If, in fact, astrocyte Ca^{2+} events are "triggered" by decreases in SWA, we would expect to observe more Ca^{2+} events when SWA is low, which we indeed found in the correlation analysis above (**Fig. 3.1d, H**). While many other cell types may also play roles in a SWA homeostatic process, we wondered whether astrocytes may be involved in the consistent increase in SWA that we observe after astrocyte Ca^{2+} event onsets (**Fig. 3.3c**). To address this question, we next used chemogenetics to specifically manipulate GPCR pathways that shape astrocyte Ca^{2+} dynamics.

Gi-driven astrocyte Ca^{2+} increases are sufficient to increase SWA during sleep

To test whether astrocyte Ca^{2+} may play a causal role in SWA control, we acutely manipulated cortical astrocyte Ca^{2+}, since genetic manipulations—such as IP_3R2 KO—can lead to compensatory developmental effects. Because IP_3R2 can mediate the astrocyte-SWA relationship (**Fig. 3.1i, 2c–d**), and both Gi- and Gq-GPCR mediated Ca^{2+} changes in astrocytes are dependent on the IP_3R2 pathway[45,67,68], we chose to use Designer Receptors Exclusively

Activated by Designer Drugs (DREADDs)[80] to selectively manipulate GPCR pathways in astrocytes. The inhibitory neurotransmitter GABA has been implicated in cortical synchrony during sleep through the mediation of synchronous DOWN states[16,19,81] and the excitatory neurotransmitter glutamate has been implicated in cortical UP states[21,46]. Astrocytes respond to both GABA and glutamate via Gi-GPCRs (via $GABA_B$ and mGluR3 receptors in adults)[45,67,68]. Thus we chose the inhibitory human M4 muscarinic receptor DREADD (hM4Di) to selectively drive this well described Gi-GPCR pathway in astrocytes (**Fig. 3**).

The same experimental setup as earlier (**Fig. 3.1a**) was used, but mice were co-injected with *AAV-GFAP-GCaMP6f* and *AAV-GFAP-hM4D(Gi)-mCherry* to express both GCaMP6f and Gi-DREADD specifically in cortical astrocytes (**Fig. 3.4a–b, Fig. 3.5**). In these experiments, we monitored the effects of I.P. administration of the hM4Di agonist clozapine-N-oxide (CNO, 1mg/kg) on Ca^{2+} dynamics, SWA, and sleep state. Because of the known sedative effects of CNO, we first verified that CNO itself (1mg/kg, I.P) did not alter Ca^{2+} dynamics or sleep features in the absence of DREADD expression. We found no change in Ca^{2+} dynamics or sleep features between administration of 1 mg/kg CNO and the saline control (**Fig. 3.6**). While Gi-DREADD has been used in astrocytes *in vivo* previously, its effects on astrocytic Ca^{2+} have not yet been established during natural wake and/or sleep. Here, we confirmed that Gi-DREADD activation indeed altered astrocyte Ca^{2+}, causing an increase in event frequency across the entire 2-hr recording period after CNO administration (**Fig. 3.4c–d**). This finding is consistent with studies of astrocytic Ca^{2+} activity in *ex vivo* slices and in anesthetized mice[45,68,82]. Next, we asked whether Gi-induced Ca^{2+} event increases were sufficient to alter SWA. We found that activation of Gi-DREADDs by CNO significantly increased SWA during sleep compared to a saline injection in the same animal (**Fig. 3.4e**). In contrast, total time spent in sleep and wake was not

affected by Gi-DREADD activation (**Fig. 3.4f, H**). Thus, although the total duration of sleep did not change, the sleep was characterized by higher SWA, or greater sleep depth. Together, these data demonstrate that regulation of SWA and sleep duration can be separated, and that astrocyte Ca^{2+}, through Gi-GPCR activation, is sufficient to increase SWA during sleep. We hypothesized that astrocytes were part of a homeostatic mechanism regulating SWA, where in response to decreases in SWA, astrocyte Ca^{2+} causes an increase in SWA. Here, we artificially increased Ca^{2+} beyond endogenous levels through Gi-GPCR signaling and found we could drive SWA increases above control levels, consistent with the hypothesis that astrocytes are part of a homeostatic mechanism that regulates SWA.

Because we found similar relationships between endogenous Ca^{2+} dynamics and SWA in sleep and stationary wake (**Fig. 3.1h**, **Fig. 3.3c–d**), we next quantified the effect of Gi-GPCR activation on SWA during wake. In contrast to the change in SWA during sleep (**Fig. 3.4e**), we found no change in SWA during the entire wake state (**Fig. 3.4g**). Likewise, when calculating SWA only in the stationary wake state, we observed no significant difference in SWA (**Fig. 3.5f**). This negative result suggests that a different mechanism underlies the astrocyte-SWA relationship in wake, and assigns the role of Gi-induced Ca^{2+} dynamics to regulating SWA specifically during sleep. To investigate this difference, we performed PCA on the Ca^{2+} data collected after saline or CNO administration. We found that CNO resulted in significantly larger differences in multiple PCs for sleep relative to wake (**Fig. 3.7**). This selective change in Ca^{2+} event properties during sleep, but not wake, may explain the sleep-specific effects in SWA.

Because the astrocyte-SWA relationship is partly dependent on IP_3R2s (**Fig. 3.1i, 2c–d**), we tested whether the effect of Gi-GPCR activation on SWA was also dependent on IP_3R2s by repeating these Gi-DREADD experiments in IP_3R2 KO mice. Unlike control mice (**Fig. 3.4c–**

d), CNO administration did not significantly increase astrocyte Ca^{2+} in IP_3R2 KO mice (**Fig. 3.4i**), demonstrating that Gi-DREADD-induced Ca^{2+} events rely, at least in part, on IP_3R2. In accordance with the lack of change in Ca^{2+} in the IP_3R2 KO animals, we also observed no significant change in SWA with CNO administration (**Fig. 3.4j**), indicating that the change in sleep depth we observe (**Fig. 3.4e**) is dependent on IP_3R2.

Gi-DREADD astrocyte activation regulates delta waves more than slow oscillations

While NREM sleep is broadly characterized by SWA, it has become increasingly clear that there are two main types of slow-waves: delta waves and slow oscillations[2,3,15,18,83–85]. These two types of slow-waves are characterized by different regulatory mechanisms and are associated with distinct functions in NREM sleep. Delta waves are thought to promote the weakening of memories, while slow oscillations support memory consolidation[2,3]. In light of our finding that astrocytic Gi-GPCR-induced Ca^{2+} is sufficient to increase sleep SWA (**Fig. 3.4e**), we explored whether this increase could be attributed to specific changes in delta waves or slow oscillations. A specific change could point to specific roles of astrocytic Gi-signaling in sleep. For this analysis, we implemented an established approach to distinguish delta waves and slow oscillations by their distinct waveforms[3]. Slow oscillations had larger positive peaks and larger positive-to-negative deflections that occurred within 500ms (**Fig. 3.8a–b**). Across recordings, slow oscillations and delta waves were differentiated by their peak and trough amplitudes using k-means clustering (**Fig. 3.8c**).

We first looked at the effect of astrocytic Gi-DREADD activation on the number of identified delta waves and slow oscillations, and found no effect on the rate of delta waves or slow oscillations during sleep (**Fig. 3.8e**). This negative result was expected by this analysis,

because delta waves and slow oscillations were identified using amplitude percentile thresholds (see Methods) that were set for each individual recording. However, when quantifying the amplitude of these waveforms, we noted increases in the mean amplitude, particularly for delta waves (**Fig. 3.8f, I**). Indeed, by plotting peak vs. trough amplitude, we observed a clear change in delta waves after CNO, resulting in higher peak and lower trough amplitudes (**Fig. 3.8g**). This change was smaller in the slow oscillation waveforms (**Fig. 3.8j**). Similarly, we quantified the change in total peak – trough amplitude after CNO administration. While we saw a significant increase in size for delta waves (**Fig. 3.8h**) and slow oscillations (**Fig. 3.8k**) compared to saline controls in the same animal, the change in delta waves was significantly higher than that for slow oscillations (**Fig. 3.8l, Fig. 3.9**). Together, these data demonstrate that astrocyte Ca^{2+}, through Gi-GPCR signaling, preferentially increases SWA by altering delta wave amplitude. Delta waves are more local than slow oscillations, and are thought to be generated within the cortex[2,37,83,85–87]. Given that our Gi-astrocytic manipulation is restricted to a small portion of cortex (**Fig. 3.5**), the result that astrocytic Gi-DREADD activation affects delta waves more than slow oscillations may indeed be expected.

Cortical astrocyte Ca^{2+} dynamics exhibit bidirectional changes before sleep/wake transitions

We next wondered whether astrocytes might play a role beyond the regulation of sleep depth, to also influence sleep duration. Data here (**Fig. 3.3**) suggest that a component of astrocyte signaling may be important for sleep/wake state transitions, which would directly affect sleep duration. To study these transitions, we first examined endogenous cortical astrocyte Ca^{2+} dynamics in the 30s leading up to transitions between sleep or wake. We found a pattern in which Ca^{2+} events consistently increased before the sleep-to-wake transition and decreased

before the wake-to-sleep transition (**Fig. 3.10a**). This is supported by a recent study that demonstrated, using an alternative image analysis technique, that Ca^{2+} increases preceding sleep-to-wake transitions[66]. We next divided all sleep and wake periods, regardless of length, into three equal bins (**Fig. 3.10c**). This allowed us to study how astrocyte Ca^{2+} dynamics generally change throughout a sleep or wake period. In so doing, we found that Ca^{2+} event rate increased in the last third of sleep and decreased in the last third of wake (**Fig. 3.10d**). Since Ca^{2+} event rate is higher during wake than sleep (**Fig. 3.1f**) and Ca^{2+} events occur after dips in SWA (**Fig. 3.3c**), the increase in event rate preceding the transition to wake could reflect a gradual shift in SWA to a wake state. In fact, various ascending brainstem neuromodulatory neurons associated with wakefulness have been shown to increase firing prior to the transition to wake and decrease firing prior to the transition to sleep[88–92]. Astrocytes express receptors and exhibit increased Ca^{2+} dynamics in response to many of these neuromodulators[76–79]. Thus, this change in event rate prior to sleep/wake transitions may be due to neuromodulator-driven GPCR signaling in astrocytes.

We reasoned that if the Ca^{2+} dynamics observed around state transitions were due to astrocytic GPCR signaling, we would expect that these Ca^{2+} dynamics would be altered in IP_3R2 KO mice. As predicted, we found that the changes in event rate preceding transitions were abolished in IP_3R2 KO mice (**Fig. 3.10b**). When quantifying the change in event rate in the last third of sleep and wake for IP_3R2 KO mice, we found that IP_3R2 KO mice did not exhibit the same increase in event rate in the last third of sleep (**Fig. 3.10d**, left). However, the change in event rate observed during wake was unchanged in IP_3R2 KO mice (**Fig. 3.10d**, right), suggesting a specific role of IP_3R2s in sleep. Since Gi-DREADD activation did not affect sleep

duration (**Fig. 3.4f**), we next tested the hypothesis that Gq-GPCR-mediated Ca^{2+} signaling in astrocytes regulates sleep/wake transitions.

Gq-DREADD activation suppresses astrocyte Ca^{2+} dynamics in vivo

To drive the astrocytic Gq-GPCR pathway and test for a role of astrocyte Ca^{2+} in mediating sleep/wake transitions, we selectively expressed the human M3 muscarinic receptor DREADD (hM3Dq) in astrocytes. We were also motivated by the knowledge that neuromodulatory signals play an important role in mediating sleep and wake transitions[11–13,93], and many of these endogenous signals can act at Gq-GPCRs in astrocytes[72,82]. We used a similar approach as above (**Fig. 3.4a**), but here selectively expressed GCaMP6f and the Gq-DREADD in astrocytes (**Fig. 3.11a–b, Fig. 3.12**). As above, we imaged astrocyte Ca^{2+} after I.P. CNO administration to confirm the effect of Gq-DREADD activation on Ca^{2+} activity *in vivo.* Although astrocytic Gq-DREADD activation *in vivo* has been performed previously[45,94–96], validation of Gq-DREADD-mediated astrocytic Ca^{2+} increases has only been performed under anesthesia or *ex vivo*, in part because several *in vivo* astrocyte DREADD experiments have been carried out in brain regions that are less accessible than cortex[94,96]. Thus, the effect of Gq-DREADD activation on Ca^{2+} in awake mice has not been previously reported. Canonically, Gq-GPCR signaling results in an increase in Ca^{2+} activity via IP_3-dependent release of intracellular Ca^{2+}[74]. However, we were surprised to find that Ca^{2+} dynamics only increased in the first 5–10 minutes after I.P. injection of CNO (150.9%±135.9). After this initial period of increased Ca^{2+} events, Ca^{2+} dynamics were almost completely abolished (-97.3% ± 0.79%, **Fig. 3.11c–d, Fig. 3.12h**). This "silent" state of Ca^{2+} dynamics lasted for the rest of the entire recording (2–3 hrs).

To test whether this unexpected result was due to CNO concentration (1mg/kg), we administered lower doses of CNO. While the initial period of increased Ca^{2+} dynamics was slightly longer (15–20 min) following administration of a ten-fold lower dose of CNO (0.1mg/kg), this very low dose still resulted in a strong reduction in Ca^{2+} events for long time periods (**Fig. 3.12f–h**). The observed inhibition of astrocyte Ca^{2+} could be due to depletion of intracellular Ca^{2+} stores and/or interference with store-operated Ca^{2+} channels[97]. To compare the inhibition of Ca^{2+} events with changes in fluorescence, we used an ROI-based approach to analyze fluorescence in somas and processes after CNO administration. We found that fluorescence in both somas and processes remained elevated above baseline after 1 mg/kg CNO (**Fig. 3.12i**), which suggests that Ca^{2+} levels may be clamped at saturating levels. Together, these results indicate that 1) we cannot assume that Gq-DREADD activation simply increases astrocytic Ca^{2+} *in vivo*, and 2) when feasible, astrocytic experiments using chemogenetics *in vivo* should be validated individually, particularly for those involving circuit function and animal behavior.

To test whether the astrocytic Ca^{2+} silencing we observed following Gq-DREADD activation could be reproduced with endogenous GPCR signaling, we measured Ca^{2+} activity in *ex vivo* cortical slices in response to a cocktail of neuromodulators associated with wakefulness, including norepinephrine, acetylcholine, dopamine, and histamine. We adapted methodology[47], using half the concentration of each neuromodulator as previously, since each experiment involved two total applications of this "wake cocktail" (20μM norepinephrine, 5μM acetylcholine, 5μM dopamine, 2.5μM histamine). We also included TTX in the circulating bath to block neuronal firing. As predicted from previous studies reporting astrocytic Ca^{2+} increases to various neuromodulators[76–79,98], we observed a dramatic increase in Ca^{2+} activity in response

to the cocktail (**Fig. 3.12j**). However, after this initial increase in Ca^{2+}, GCaMP fluorescence did not return to baseline levels, but remained high and further Ca^{2+} events were almost completely absent (**Fig. 3.12j**), similar to *in vivo* dynamics observed 5–10 minutes after CNO administration. To test whether this "silent" state altered the astrocytic response to further neuromodulatory input, we bath-applied a second round of the wake cocktail. In contrast to the initial Ca^{2+} increase, we observed no further increase in astrocyte Ca^{2+} (**Fig. 3.12j**). We speculate that the mechanism underlying the inability of astrocytes to respond to a second dose of wake cocktail may be similar to that underlying the inhibition of Ca^{2+} dynamics *in vivo* in response to circulating CNO.

Gq-induced Ca^{2+} dynamics regulate sleep-wake transitions

The finding that Gq-DREADD chemogenetics can inhibit an intracellular GPCR signaling pathway in astrocytes makes this is a particularly useful tool for understanding astrocytes' roles in cortical state regulation. To investigate whether astrocytes regulate sleep duration, we focused on the long period of Ca^{2+} suppression in these experiments. We found that mice spent significantly more time in sleep after CNO administration (**Fig. 3.11e**, left). Further, in the absence of Gq-GPCR-mediated Ca^{2+} events, mice made fewer sleep-to-wake transitions (**Fig. 3.11f**, left) and accordingly, we observed fewer sleep bouts of longer duration (**Fig. 3.13a**). This suggests that the IP_3R2-dependent increase in event rate prior to sleep-to-wake transitions (**Fig. 3.10**) is important to transition the cortex to the wake state. The transition data (**Fig. 3.10**) also showed that endogenous Ca^{2+} decreases toward the end of wake periods, just prior to wake-to-sleep transitions (**Fig. 3.10**). Thus, we wondered whether Ca^{2+} suppression via Gq-DREADDs would affect wake as well. We observed a decrease in the percent time awake (**Fig. 3.11e**, right),

as predicted by the increase in sleep observed (**Fig. 3.11e**, left). However, we also observed less frequent transitions out of wake, demonstrating that astrocyte Ca^{2+} is important for both wake-to-sleep transitions (**Fig. 3.11f**, right), and sleep-to-wake transitions (**Fig. 3.11f**, left). As predicted from the decrease in transitions, we also observed fewer wake bouts and wake bouts of longer duration (**Fig. 3.13b**). We hypothesize that decreased astrocytic Ca^{2+} prior to wake-to-sleep transitions (**Fig. 3.10**) is important for the transition to sleep, but astrocytes were unable to make this significant decrease due to clamped Ca^{2+} in these experiments.

If Gq-GPCR signaling is an important bidirectional regulator of sleep/wake transitions, we would expect that increases in Gq-GPCR signaling to have the opposite effect from decreased Gq-GPCR Ca^{2+} signaling. We thus used data from the short, initial period with elevated Ca^{2+} activity to ask whether this is the case. Because this period is so short (5–10 min), we were somewhat limited in our analysis. However, of the animals that exhibited some sleep in either the CNO or saline condition (n=4), we observed a significant decrease in the percent time sleeping (**Fig. 3.11g**). This bidirectional change in sleep time strongly supports the hypothesis that Gq-GPCR-mediated Ca^{2+} plays a critical role in regulating sleep duration. Interestingly, we did not observe a change in the amount of sleep with Gi-GPCR activation (**Fig. 3.4f**), which similarly increased Ca^{2+} dynamics. This difference between Gq- and Gi-mediated Ca^{2+} increases indicates an important functional dissociation between Gq- and Gi-GPCR-mediated Ca^{2+} activity in astrocytes and highlights the likelihood that other signaling molecules involved in GPCR signaling cascades play roles in regulating sleep-wake transitions. Because we observed a significant increase in sleep depth in response to the Ca^{2+} increase with Gi-DREADDs (**Fig. 3.4e**), we also wondered whether Ca^{2+} suppression via Gq-DREADDs would have an opposing effect. In contrast to manipulation of the Gi-GPCRs, we found that Ca^{2+} suppression via Gq-

GPCR manipulation had no significant effect on SWA during sleep (**Fig. 3.11h**). This suggests that astrocytic regulation of SWA is specifically dependent on the Gi-GPCR pathway and provides further evidence that astrocytic Gi- and Gq-GPCR signaling regulate separable sleep/wake features.

Local Gi-DREADD activation of cortical astrocytes can drive changes in remote cortical sleep features

SWA during NREM sleep is considered a widespread phenomenon, involving the synchronization of neurons across the entire cortex. While widespread oscillatory activity has been observed in several animal models[16,20], recent work has also emphasized the existence of more local and asynchronous sleep[2,35–37,85,87]. The morphology and interconnectedness of cortical astrocytes and astrocytic networks make them well positioned to mediate neural activity across broad swaths of cortex. Cortical astrocytes are non-overlapping, in all cortical layers, gap junctionally coupled, and contain highly ramified processes that can contact tens of thousands of synapses[38]. We therefore wondered how they may be involved in both local and remote changes in cortical synchronization in sleep. To address this question, we implanted a second electrode to record EEG in the contralateral frontal cortex (FC-EEG, **Fig. 3.14a**). This second electrode was far (both rostral-caudally and medial-laterally) from the imaging window/LFP electrode in V1, but still over cortex (**Fig. 3.14a, Fig. 3.5, Fig. 3.12**).

Astrocyte Ca^{2+} dynamics are associated with changes in coherence between V1 and contralateral FC

With two recording sites, we first explored endogenous relationships between astrocytic Ca^{2+} events in V1 and cortical state in contralateral FC in sleep. Using Ca^{2+} event-triggered averages, we found a similar relationship with V1 Ca^{2+} events and FC as previously described (**Fig. 3.3c**): SWA in FC decreased before and increased after V1 Ca^{2+} event onsets, although the magnitude of this modulation was smaller than that observed locally (**Fig. 3.14c**). To look at the synchronization between these cortical areas, we examined the coherence between local V1 and remote FC oscillations. We found that the V1-FC coherence (between 5–10Hz) was higher immediately following astrocyte Ca^{2+} events when compared to coherence measured from randomly chosen epochs (**Fig. 3.14d**). We also found an increase in astrocyte event-locked coherence (0–15Hz) at the end of sleep periods, in the 15s prior to sleep-to-wake transitions (**Fig. 3.14e**). These data provide evidence that astrocytes may be involved in mediating endogenous cortex-wide physiological activity.

Local cortical astrocyte activation increases SWA and slow oscillations in remote cortex

We next tested whether astrocytes play a causal role in brain-wide SWA during sleep using Gi-DREADD activation in V1 and the FC-EEG. To assess how the spread of astrocytic DREADD expression compared with the location of the two recording electrodes, we performed immunohistochemistry on brain slices across the rostral-caudal axis (**Fig. 3.5d**). As expected, the majority of expression was centered around the V1-LFP electrode where viruses had been injected, while no expression was observed in FC at the site of the EEG electrode (**Fig. 3.5e**). To assess a causal role for astrocyte Ca^{2+} in brain-wide oscillatory activity, we compared the effect

of Gi-DREADD activation of V1 astrocytes at both V1-LFP and FC-EEG electrodes. Here, we found that increasing Ca^{2+} via Gi-DREADDs in V1 was sufficient to increase SWA in the contralateral frontal cortex, although this increase was smaller than that observed in V1 (**Fig. 3.14f–h**). We also found that the SWA change was accounted for by a significant increase in slow oscillation amplitude, but not delta wave (**Fig. 3.14i–j**). This is in contrast with the greater delta wave change observed locally (**Fig. 3.8i**). Moreover, the change in slow oscillation amplitude in FC (**Fig. 3.14j**, 6.8±2.2%) was similar to the change of the slow oscillation amplitude in V1 (**Fig. 3.8l**, 8.8±3.2%), suggesting that slow oscillations generated in V1 travelled to FC. These results indicate that astrocytes can influence cortex-wide dynamics on a large scale via specific changes to the slow oscillation component of SWA.

Discussion

Using simultaneous 2P imaging of astrocyte Ca^{2+} and electrophysiology across wake and sleep, we have demonstrated that cortical astrocytes regulate distinct features of sleep via differential GPCR signaling. We showed IP_3R2-dependent Ca^{2+} activity is inversely correlated with SWA and changes bidirectionally prior to sleep-wake transitions. With chemogenetics, we demonstrated that astrocyte Ca^{2+} is sufficient to increase SWA during sleep through specific enhancement of delta waves. This is specific to Gi-, not Gq-, GPCR-induced Ca^{2+}. In contrast, Gq-, but not Gi-, GPCR Ca^{2+} signaling is important for mediating sleep/wake transitions. Lastly, we demonstrated that astrocyte Ca^{2+} has far-reaching, cortex-wide effects on SWA and slow oscillations.

Sleep depth and sleep length are separable

We found that astrocytic Gi-DREADD activation increases SWA, but not sleep duration, while Gq-DREADD activation altered sleep duration but not SWA. This suggests a separation in the mechanisms underlying sleep depth, measured by SWA, and sleep duration. Previous work has also shown separation in sleep depth and duration by demonstrating that following sleep deprivation, recovery sleep has higher sleep depth but the duration is not significantly changed[9,10]. On the other hand, Ca^{2+} has been suggested to mechanistically link the regulation of sleep duration and depth[22,23]. Interestingly, our data supports both these ideas. We found that endogenous astrocyte Ca^{2+} is modulated in relation to both sleep duration (**Fig. 3.10**) and sleep depth (**Fig. 3.1**). Nevertheless, we were able to affect one without the other by selectively manipulating different GPCR pathways, suggesting these mechanisms are also separable.

The two-process model of sleep regulation has attributed the regulation of sleep duration to the interaction of sleep pressure, measured by SWA, and circadian rhythm[99–101]. Our findings that Gi-DREADD activation increased SWA without affecting sleep duration (**Fig. 3.4e, f**) suggests that SWA does not directly influence sleep duration. However, we cannot discount the two-process model from this data alone, since we did not investigate the effect of circadian rhythm, nor did we directly study sleep homeostasis; our recordings were performed at the same time of day and were limited to 2–3 hours. In fact, astrocyte Ca^{2+} changes with circadian rhythm in the suprachiasmatic nucleus[102] and increases with sleep need after sleep deprivation[103]. Longer recordings and sleep deprivation interventions to examine astrocytic integration of circadian signals and sleep pressure will be informative. Additionally, our methodology led us to focus on the role of astrocyte GPCR signaling in NREM sleep regulation, although previous work has demonstrated astrocyte Ca^{2+} changes with REM sleep[66,103,104]. The further study of astrocytic

regulation of REM sleep may reveal interesting differences between regulation of behavioral sleep and cortical state, which is similar between REM sleep and wake. Indeed, our data suggests that Gi-GPCR signaling would be much attenuated during REM sleep, which is characterized by a lack of SWA.

Since astrocytes differentially control SWA and sleep/wake transitions, we hypothesize that Gi- and Gq- GPCR activation in astrocytes—while both drive Ca^{2+} changes—lead to different downstream effects which may elucidate new mechanisms of sleep regulation. In fact, many astrocytic functions associated with sleep may be important, such as extracellular glutamate regulation[44], extracellular ion dynamics[47], and adenosine release[48]. While we don't yet know what downstream astrocytic effects underlie the sleep changes observed here, we have established that the functional astrocytic output is a not a simple consequence of changed Ca^{2+} levels in the cell, but rather of signaling downstream of either Gi- or Gq-GPCRs. Many new optical sensors, such as those for glutamate[105], ATP[106,107], and adenosine[108], in combination with astrocyte-specific manipulations, may be useful to link specific GPCR-driven Ca^{2+} dynamics with relevant astrocyte outputs.

Functional dissociation between Gi- and Gq-GPCR Ca^{2+} signaling in astrocytes

The activation of both astrocytic Gi- and Gq-GPCRs increases intracellular Ca^{2+}[45,67,68], and yet we observed a functional dissociation between manipulation of the Gi- and Gq-GPCR pathways. These data underscore the complexity of Ca^{2+} signals in astrocytes and demonstrate that caution is necessary when attributing astrocytic Ca^{2+} increases to one specific downstream function. Many different roles have been attributed to astrocytes, suggesting astrocytes have the capacity to perform several functions in parallel. Our findings suggest that, through GPCR

signaling, astrocytes interpret Ca^{2+} dynamics within the cell differently, resulting in different functional outputs. This may be a consequence of the many other signaling molecules downstream of Gi- and Gq-GPCRs, including phospholipase C or protein kinase A. Tools such as AQuA[54] that allow the accurate capture of complex astrocyte Ca^{2+} signaling are a first step in elucidating how Ca^{2+} dynamics map to the myriad of functions associated with astrocytes. The next step we took was to extract meaning from these signals by analyzing the multi-dimensional nature of astrocyte Ca^{2+} signals. We used PCA to reduce the 20 different properties describing each Ca^{2+} event and revealed differences that weren't observed with individual comparisons of event rate, duration, size, or amplitude (**Fig. 3.2, Fig. 3.7**). This both illustrates the complexity of astrocyte Ca^{2+} signaling and emphasizes the importance of implementing more robust analysis tools.

Understanding how Gi- and Gq-GPCR activation gives rise to different effects on sleep will require further examination of these signaling pathways in astrocytes. First, we will need to identify the specific endogenous ligands during sleep that alter SWA and sleep/wake transitions. Candidates for sleep/wake transitions include neuromodulators, since many Gq-GPCRs for neuromodulators are expressed by astrocytes. In contrast, regulation of SWA has been attributed to both GABA[16,19,81] and glutamate[21,46]. GABA and glutamate are attractive candidate endogenous ligands because astrocytic GABAergic (via $GABA_B$) and glutamatergic (via mGluR3 in adults) signaling are both mediated via Gi-GPCRs. Acute, astrocyte-specific knock-out of these receptors will provide important insight into the relevant receptors. Importantly, astrocyte-specific knock-outs will also reveal whether Gi-GPCR signaling is necessary to regulate SWA. While we demonstrated that astrocytic Gi-GPCR signaling is sufficient to alter SWA, other signaling cascades and cell types may also play important roles in SWA regulation.

Second, further studies will be required to understand how intracellular signaling cascades for Gi- and Gq-GPCRs differ in astrocytes. Using PCA, we found differences in the effect of Gi-DREADD activation on Ca^{2+} in sleep versus wake, suggesting the action of the Gi-DREADD may be interacting with endogenous signaling that differs across behavioral states. Both Gi- and Gq-GPCRs increase Ca^{2+} via IP_3R2[45], and we similarly noted a partial dependence on IP_3R2 in both Gi- and Gq-GPCR-mediated sleep effects (**Fig. 3.4, 3.10**). This only partial dependence on IP_3R2s in this data could be due to compensation for global IP_3R2 absence, but it could also indicate that perhaps other signaling molecules unique to Gq- and Gi-signaling are critical for the sleep features described here. In fact, 1.4% of all astrocyte transcripts are regulated by sleep/wake state[42] and multiple biochemical assays have already identified various important molecules in sleep/wake regulation[109–111]. Similar molecular studies specifically focused on astrocytic GPCR signaling will be critical to further understand the regulation of sleep duration and depth.

Chemogenetic activation of astrocytes

While astrocytes have previously been implicated in sleep physiology[42,47–49,51–53,66,103,104,112–114], we present the first example of an acute *in vivo* astrocytic manipulation that changes natural sleep. Acute manipulation via chemogenetics was advantageous because DREADD activation mimics endogenous signaling pathways known to be important in astrocyte signaling. However, it is still critical to properly validate these tools specifically in astrocytes, especially since they were developed and have been more widely used in neurons. While astrocytic Gq-DREADD activation can increase Ca^{2+} under anesthesia[45,95], we report for the first time the effect of Gq-DREADD activation on astrocyte Ca^{2+} in awake mice, both for long time

periods (2–3 hrs) and with several CNO concentrations. Gq-DREADD activation increased Ca^{2+} only for a short time after CNO injection, after which we observe a complete suppression of Ca^{2+} activity for several hours, for all CNO concentrations (**Fig. 3.11c–d, Fig. 3.12**). This unexpected result points to the importance of validating DREADD responses for each *in vivo* experiment when feasible.

We think that it is most likely that the opposite effects of CNO on Ca^{2+} activity in Gi-DREADD- and Gq-DREADD-expressing astrocytes reveal important differences in the Gi and Gq signaling pathways. However, these results may also indicate that expression levels of Gi- and Gq-DREADD may be more different than expected based on the observed immunostaining. Another possibility is that differential Ca^{2+} responses may be caused by differences in CNO action on Gi- and Gq-DREADD receptors. For example, CNO may be less efficacious on Gi-DREADDs in astrocytes. This possibility could be tested by determining whether higher doses of CNO are sufficient to suppress Ca^{2+} with Gi-DREADD.

Differential regulation of local and cortex-wide sleep

Two unique slow-waves have been characterized in NREM sleep: delta waves and slow oscillations[2,3,15,18,83–85]. Here, we found that astrocytic Gi-DREADD activation increases SWA by preferentially increasing the amplitude of delta waves in V1 (**Fig. 3.8**). This data supports existing literature suggesting delta waves are generated locally within the cortex by the spreading of DOWN states[2,37,83,85–87]. Since our Gi-DREADD manipulation was restricted within the cortex (**Fig. 3.5**) and DOWN states are thought to be generated through GABAergic inhibition[14,16,19,81], we hypothesize that Gi-GPCR signaling in astrocytes mediates the local synchronization of delta

waves via control of inhibition. Additionally, astrocytes may also mediate synchronization of UP states through glutamate[21,46].

In addition to the increase in delta waves, we observed a smaller, but significant, increase in slow oscillation amplitude that was equal in magnitude to that observed in contralateral FC (**Fig. 3.14**). This suggests that cortical astrocytes may have influence over more global, cortex-wide neural activity. We explored this further and found that SWA in contralateral FC was modulated around endogenous Ca^{2+} events recorded in V1. Further, we found that coherence between V1 and FC was increased immediately following astrocyte Ca^{2+} events. Interestingly, coherence was increased in the range of 5–10Hz, which is higher than expected for slow oscillations, but might also indicate a role for astrocytes in the connectivity across cortex during REM or wake. The synchronization across broad areas of cortex may involve astrocytic gap junctions[43,114], which could mediate fast recruitment of neurons in synchronous waves. If this is indeed the mechanism, our findings indicate that GPCR activation regulates gap junction coupling in astrocytes, which can be explicitly tested[115].

Slow oscillations are more global than delta waves. Here, the change in slow oscillation amplitude with CNO administration was similar in V1 and FC (**Fig. 3.14j)**. One explanation for this finding is that activation of V1 astrocytes is sufficient to recruit subcortical circuitry, such as thalamocortical circuits, that can underlie brain-wide synchronous events[116,117]. This hypothesis is supported by studies showing subcortical "bottom-up" regulation of slow oscillations[15,83,85] and a role of astrocytes in mediating communication between different brain areas[118,119], and could be tested by simultaneously recording from thalamus and cortex during astrocyte activation.

Recent work indicates that slow oscillations and delta waves have distinct functions in memory during NREM sleep[2,3]. Since Gi-driven astrocyte Ca^{2+} preferentially drives changes in delta waves locally, we might expect that astrocytic activity in sleep is more involved in forgetting than memory consolidation. This could be tested by quantifying the effect of Gi-DREADD activation during sleep following a learning paradigm, such as fear conditioning. Further, a light-activated Gi-GPCR[120] in astrocytes would provide temporal control for selective Gi-DREADD activation specifically during NREM sleep following learning, to further explore how astrocytic effects on sleep impact cortical memory functions.

Methods

Animals

All procedures were carried out using adult mice (C57Bl/6, P50–100) in accordance with protocols approved by the University of California, San Francisco Institutional Animal Care and Use Committee (IACUC). All animals were housed in a 12:12 light-dark cycle with food and water provided *ad libitum*. Male and female mice were used for all experiments. IP_3R2 KO mice (Dr. Katsuhiko Mikoshiba, RIKEN) carry null alleles for *Itpr2*. Following surgery, all animals were singly housed, to protect electrodes, with additional enrichment.

Surgical procedures

Adult mice (C57Bl/6, P50–100) were administered dexamethasone (5mg/kg, s.c.) prior to surgery and anesthetized with isoflurane. A custom-made titanium headplate was attached to the skull using C&B Metabond (Parkell), and a 3mm diameter craniotomy was created over visual cortex. A titanium wire was inserted in V1 lateral to the craniotomy, and a bone screw was

inserted in contralateral V1 for reference (all measurements from bregma, -3.5mm, 1.2mm lateral). Two twisted titanium wires were inserted in the nuchal muscles for EMG recordings. In a subset of animals, an additional bone screw for EEG was inserted into FC, contralateral to the craniotomy (+2.7mm, 1.2mm lateral).

For endogenous Ca^{2+} imaging, two 300nL injections of *AAV5-GFaABC1D.cyto-GCaMP6f* were made in the brain before placing the cranial window. For Gi-DREADD experiments, two injections of *AAV5-GFaABC1D.cyto-GCaMP6f* (200nL each, 400nL total) and *AAV5-GFAP-hM4D(Gi)-mCherry* (100–200nL each, 200–400nL total) were co-injected. For Gq-DREADD experiments, two injections of *AAV5-GFaABC1D.cyto-GCaMP6f* (200–300nL each, 400–600nL total) and *AAV5-hM3D(Gq)-mCherry* (200–500nL each, 400–1000nL total) were injected before placing cranial window. All injections were 0.2–0.3mm from the pial surface, -0.5 – -3.5mm, 1.2–2.5mm lateral at 30–60nL/min, followed by a 10-min wait for diffusion. Following viral injection, a glass cranial window for chronic imaging was implanted and secured using C&B metabond[121]. Post-operative care included administration of 0.05mg/kg buprenorphine and 5mg/kg carpofen. Mice were allowed ten days to recover, then were habituated to head-fixation on a circular treadmill for five days, prior to imaging. For DREADD experiments, mice were habituated for 1–2 days.

In vivo *two-photon imaging and electrophysiology*

2P imaging experiments were carried out on a microscope (Bruker Ultima IV) equipped with a Ti:Sa laser (MaiTai, SpectraPhysics). The laser beam was intensity-modulated using a Pockels cell (Conoptics) and scanned with linear galvonometers. Images were acquired with a 16x, 0.8 N.A. Nikon objective via a photomultiplier tube (Hamamatsu) using PrairieView

(Bruker) software. For GCaMP imaging, 950nm excitation and a 515/30 emission filter was used. All recordings started at ZT 2. Mice were head-fixed to a circular treadmill and Ca^{2+} activity was recorded at ~1.7Hz effective frame rate from layer 2/3 of visual cortex with a 512×512 pixel resolution at ~1μm/pixel. Locomotion speed was monitored using an optoswitch (Newark Element 14) connected to an Arduino. For LFP and FC-EEG, differential recordings were acquired using the contralateral bone screw as a reference. For EMG, differential recordings were acquired using the two wires implanted in the nuchal muscles. All recordings were amplified (Warner) with a gain of 1K, high-pass filtered at 0.1Hz, and low-pass filtered at 10KHz. Electrophysiology and locomotion recordings were acquired simultaneously with 2P imaging at 1KHz using PrairieView (Bruker) software.

Image analysis

Astrocyte Ca^{2+} image analysis was performed using Astrocyte Quantitative Analysis (AQuA) software[54]. Videos were preprocessed by registering images using the ImageJ plugin MOCO[122]. Events were detected using AQuA (in MATLAB) using the *in-vivo-GCaMP-cyto* preset. Signal detection threshold was adjusted for each video after manually checking for accurate detection, to account for slight differences in noise. AQuA outputs were further analyzed in MATLAB. Event count was quantified using the onset of each event, as detected by AQuA. For ROI analysis, somatic traces were extracted from ROIs hand-drawn using the blow-lasso tool in Fiji. Somatic ROIs were then removed using a mask, and process ROIs were created by applying $10um^2$ tiles across the field of view.

Sleep scoring

LFP and EEG recordings were first manually inspected for movement artifacts, which were removed by excluding data exceeding 5 SD from the mean. Similarly, drifting baselines were adjusted by a high-pass filter with a cut-off frequency of 0.3Hz. All electrophysiology acquired on the same day were pooled together and z-scored. A spectrogram was then calculated using a moving window of 10s, stepping every 5s. Locomotory data were used to identify each 5s bin as *stationary* if no locomotion was detected, or *locomotory* otherwise. The absolute value of z-scored EMG recordings was used to quantify mean EMG amplitude for each 5s bin.

A bin was identified as NREM sleep if 1) the slow-wave ratio (0.5–4Hz/8–20Hz) was >0.5 SD from the mean, 2) the animal was stationary, and 3) the EMG was <5 SD from the mean. Similarly, a bin was identified as REM sleep if it had not been quantified as NREM, and 1) theta power (6–10 Hz) >0.25 SD from the mean, 2) the animal was stationary, and 3) the EMG was <0.4 SD from the mean. All remaining times were characterized as wake. Each behavioral period was identified by finding the start and end of consecutive 5s bins of the same behavioral state. For all analysis, sleep periods <10–15s were excluded, with the exception of the sleep/wake transition analysis (**Fig. 3.10**), in which sleep periods <30s were excluded. Each wake period was further divided into 1s bins, and characterized as *stationary* if no movement was detected and *locomotory* otherwise. Consecutive 1s bins of locomotion within each wake period were identified as a *locomotory wake* period and consecutive 1s bins of no locomotion within each wake period were identified as a *stationary wake* period. Stationary wake periods <15s were excluded. We included a "buffer" in which the first 10s of a stationary wake period was excluded if that stationary wake period immediately followed a locomotory wake period because Ca^{2+} bursts during locomotion often persist for ~10s after locomotion ceases.

Slow oscillation and delta wave detection

To differentiate slow oscillations and delta waves, we set thresholds for amplitude and peak-to-trough duration[3,83,84,87,123]. First, LFP and EEG was filtered for the slow wave band (0.1–4Hz) using two filters: a high-pass Butterworth filter (second order, cutoff at 0.1Hz) and a low-pass Butterworth filter (fourth order, cut-off at 4Hz). Next, we identified all positive-to-negative zero crossings, preceding peaks, and following troughs that occurred during NREM sleep. Because gamma oscillations are nested in UP states[124–127], we used high-gamma to verify that the identified peaks were DOWN states and the troughs were UP states: LFP and EEG recordings were bandpass filtered for 80–100Hz, and high-gamma amplitude was quantified during peaks and troughs. If the mean peak high-gamma was greater than the mean trough high-gamma, we inverted the signal and repeated the analysis.

Slow oscillations were identified as zero crossings with 1) preceding peaks >85th percentile, 2) following troughs <40th percentile, and 3) peak-to-trough duration of 150–500ms. Delta waves were identified as zero crossings with 1) preceding peaks <85th percentile, 2) following troughs <40th percentile, and 3) peak-to-trough duration >100ms.

In vivo *DREADD activation*

At the start of each experiment (ZT 2), mice were weighed and head-fixed on the treadmill. Leads from the amplifier were connected to the LFP, EEG, and EMG electrodes. A 10-min baseline recording was acquired first, prior to any injection. When this baseline recording was completed, CNO or saline (0.9%) was administered (I.P.). The imaging/recording began immediately after injection. CNO was diluted in saline from a stock of 60mM each day and a

volume was measured for the desired dose (0.1–1.0mg/kg). An equal volume of saline was injected on control days. The sequence of CNO and saline control days was randomized amongst mice.

Ex vivo *2P imaging*

For acute slice experiments, neonatal mice (C57Bl/6, P0–4) were anesthetized by crushed ice anesthesia for 3 min and injected with *AAV5-GFaABC1D.cyto-GCaMP6f* at a rate of 2–3nL/s. Six injection sites (0.5μm apart in a 2×3 grid pattern, at 0.8μm and 0.15–0μm below the pial surface) over assumed V1 were chosen. 30nL/site (360nL total) was injected with a microsyringe pump (UMP-3, World Precision Instruments). Coronal, acute V1 slices (400μm thick) from P25–P30 mice were cut with a vibratome (VT 1200, Leica) in ice-cold cutting solution (in mM): 27 $NaHCO_3$, 1.5 NaH_2PO_4, 222 sucrose, 2.6 KCl, 2 $MgSO_4$, 2 $CaCl_2$. Slices were incubated in standard continuously aerated (95% O_2/5% CO_2) artificial cerebrospinal fluid (ACSF) containing (in mM): 123 NaCl, 26 $NaHCO_3$, 1 NaH_2PO_4, 10 dextrose, 3 KCl, 2 $CaCl_2$, 2 $MgSO_4$, heated to 37°C and removed from water bath immediately before introducing slices. Slices were held in ACSF at room temperature until imaging. Experiments were performed in continuously aerated, standard ACSF. 2P imaging was carried out as for *in vivo* imaging described above. Experiments began with a 10-min incubation in 1μM TTX, followed by a 2-min baseline video to record spontaneous activity. To record responses to the wake cocktail (20μM norepinephrine, 5μM acetylcholine, 5μM dopamine, 2.5μM histamine), a 5-min video was acquired in which the cocktail was added to the bath at the start. The frame at which the cocktail entered the imaging chamber was recorded for each experiment. A second video was then acquired, repeating bath-application of the wake cocktail.

Principle Components Analysis

To quantify differences in endogenous astrocyte Ca^{2+} events across behavioral periods, PCA was used to reduce the 20 AQuA outputs to 5 PCs, accounting for 73% of the variance in the original event features. The 5 PC scores for each astrocyte event in each behavioral state across all mice were used to construct empirical cumulative distribution functions (CDFs) for each PC in each behavioral state. The CDFs for stationary wake and sleep were compared for each PC using a two-sample Kolmogorov-Smirnov (K-S) test. In Gi-DREADD experiments, separate PCA was performed to reduce the 20 output features, as above, to 5 PCs accounting for 69% of the variance. For each PC, and for each mouse, four empirical CDFs were constructed from the PC scores of recorded events, corresponding to each combination of saline or CNO as intervention, and NREM sleep or wake as behavioral state. Within each behavioral state, the K-S distance was computed between the corresponding saline and CNO distributions, to estimate the effect of CNO administration on the given PC's score distribution during that behavioral period. To assess differences between these effects in different behavioral states for a given PC, the K-S distances between the distributions in saline and CNO trials across all mice were compared between NREM sleep and wake using a Wilcoxon signed-rank test.

Quantifying coherence

To quantify functional connectivity between V1 and FC, we computed spectral coherence between the two signals in saline-administration sessions. Coherence spectra were calculated in a 1.5s window following the onset of astrocyte events using Welch's averaged periodogram method, utilizing a Hann window and a fast Fourier transform size of 1024 samples, as implemented in SciPy. Event-aligned coherence spectra were compared against coherence

spectra aligned to randomly chosen time-points. Random time-points were chosen uniformly between the start of each dataset and 1.5s (the duration of the coherence analysis window) from the end, in equal numbers to the original astrocyte events for each dataset. To compare between astrocyte- and random-aligned coherence, each mouse's median event-aligned and random-aligned coherence spectra were calculated; a paired two-tailed *t*-test was then performed at each frequency between the event-aligned median values and corresponding random-aligned median values for all mice. To control the familywise error rate across compared frequencies, the Bonferroni correction was applied to the resulting *p*-values.

This analysis was extended to quantify coherence changes at sleep-to-wake transitions. Coherence spectra were computed as above in a 1.5s window following astrocyte events during NREM sleep, and following uniformly randomly selected events that coincided with NREM sleep. These spectra were separated into bins based on proximity of the corresponding event onset (or random alignment point) to the next sleep-to-wake transition, with each bin encompassing 2s relative to the transition; the window most proximal to the transition was truncated to 0.5s to avoid overlap of the 1.5s window for coherence computation with the subsequent wake period. Coherence values within 0–15Hz were averaged in each time bin; averaged coherence values were then compared between the astrocyte- and random-aligned cases in each bin using an unpaired two-tailed *t*-test. To control the familywise error rate across compared time bins, the Bonferroni correction was applied to the resulting *p*-values.

Immunohistochemistry

After physiology experiments were complete, mice were intracardially perfused with 4% PFA. Brains were collected, immersed in 4% PFA overnight at 4°C and switched to 30% sucrose

for two days before being frozen on dry ice and stored at -80°C. Brains were sliced coronally (40μm thick) on a cryostat. Slices were stored in cryoprotectant at -20°C until staining. 17–24 slices/mouse were chosen to span from +2.8 to -4.24 mm from bregma; each slice was 280μm from the proximate slice. Slices were washed with PBS, 5min x 3, then with 0.1% PBS-TX for 30min. Slices were next washed with 10% NGS (Invitrogen) for 1 hr, followed by an overnight incubation of 2% NGS, rat α-mCherry (1:1000, ThermoFischer), rabbit α-NeuN (1:1000, EMD Millipore), and chicken α-GFP (1:3000, Aves Lab) in 4°C. Slice were next rinsed with 1x PBS x 3 before incubating for 2 hr at room temperature with goat α-rat Alexa Fluor 555 (1:1000), goat α-rabbit 405 (1:1000), and goat α-chicken Alexa Fluor 488 (1:1000). Slices were washed again with PBS 3x for 5 min before slide-mounting and coverslipping using Fluoromount.

Whole coronal slice images were taken using an AxioImager Z2 upright epiflorescent microscope (Zeiss). 5x images were acquired, and z-stacks were stitched together with Zen Software. Images were segmented using WEKA[128]: A classifier was trained to segment 5x images into three classes: 1) pixels containing fluorescence, 2) pixels containing non-fluorescent brain tissue, and 3) pixels containing background. The classifier was then applied to the full dataset, and images were checked manually for accurate segmentation. Each segmented image was manually divided in Fiji to isolate each hemisphere. Quantification of viral spread was calculated in MATLAB by normalizing the number of fluorescent pixels to the number non-fluorescent pixels within the tissue for each hemisphere.

To analyze colocalization of mCherry and NeuN at single-cell resolution, 63x images were taken on a spinning disk confocal (Zeiss). Slides were oil-immersed and two slices/animal (-3.8 and -2.3 from bregma) were imaged. In these slices, eight images were taken at random,

spanning the total area in which virus was expressed. Colocalization of mCherry and NeuN was performed using Fiji.

Quantification and statistical analysis

All statistical tests used, definition of center and dispersion measurements, and exact n values can be found for each figure in the corresponding figure legend. Additional information regarding statistical tests described in the relevant sections. For all figures, significance levels defined as the following: *: $p<0.05$, **: $p<0.005$, ***: $p<0.0005$.

Figures

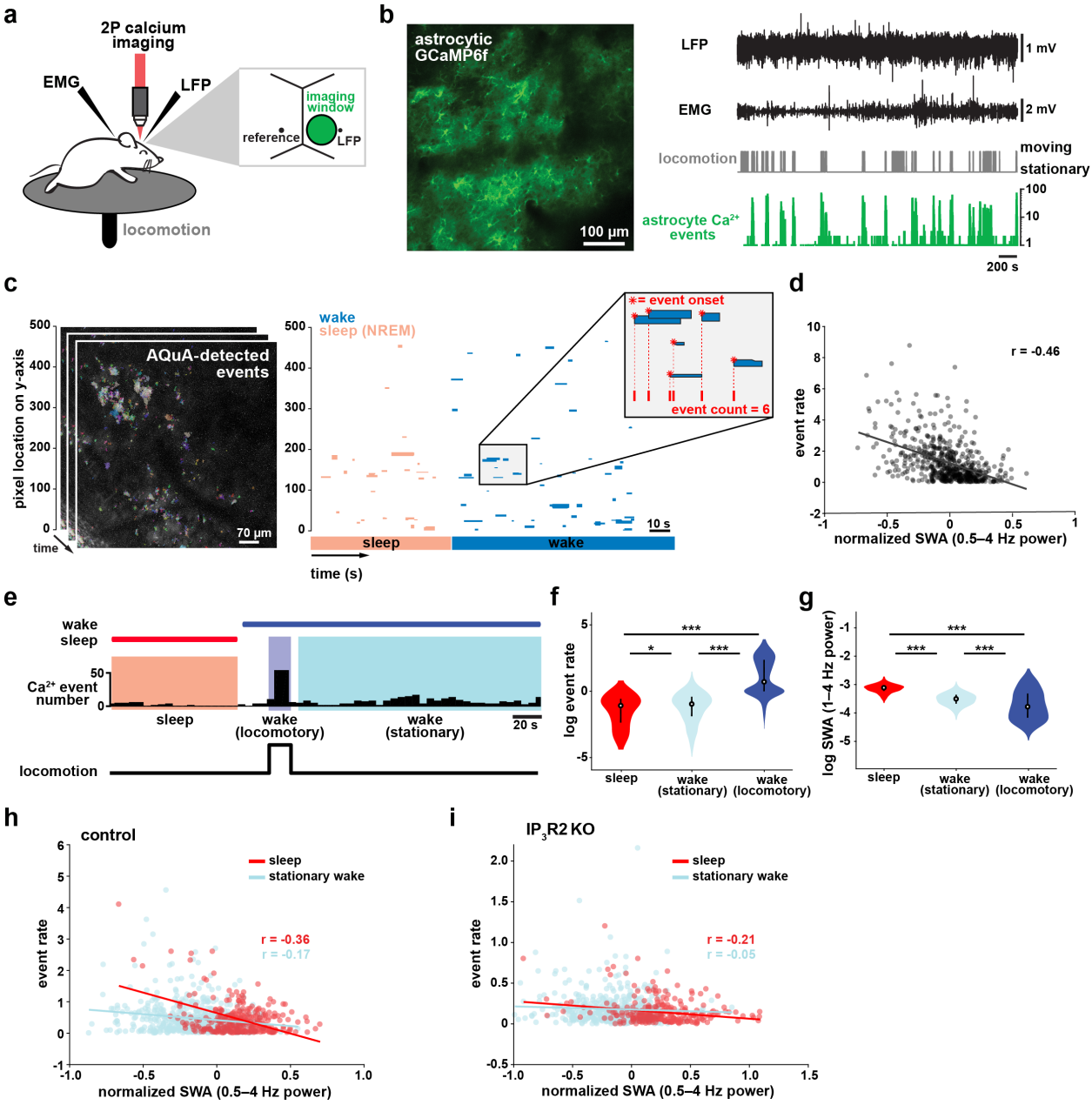

Figure 3.1: Cortical astrocyte Ca^{2+} event rate and SWA are negatively correlated across behavioral states.

(a) Experimental *in vivo* imaging and electrophysiology setup. Mice expressing astrocytic GCaMP6f were head-fixed on a horizontal treadmill to record astrocyte Ca^{2+}, LFP, EMG, and locomotion. **(b)** Left: example image of GCaMP6F expression in L2/3 V1 astrocytes in an awake, head-fixed mouse. Right: example of LFP, EMG, locomotion, and astrocyte Ca^{2+} event data using this experimental setup. **(c)** Left: AQuA[112] detects astrocyte Ca^{2+} events in 3-min GCaMP time series. Right: representative spatiotemporal plot of AQuA-identified Ca^{2+} events

displaying event time and duration on the x-axis, and the unidimensional (y) spatial extent on the y-axis. Events are color-coded by behavioral state (wake=blue, NREM sleep=pink). Inset demonstrates that event count throughout paper is quantified using event onset. **(d)** Ca^{2+} event rate and SWA are negatively correlated (Pearson's correlation, $p<0.0005$). Each point represents a single 2-min bin. (for all data in this figure except panel i, n=4 mice, 19 hrs) **(e)** Example of Ca^{2+} event rate (bottom row) across three behavioral states: NREM sleep, locomotory wake, and stationary wake. **(f)** Across animals, Ca^{2+} event rate is lowest during sleep, higher during stationary wake, and highest during locomotory wake, while **(g)** the inverse is true for SWA (for f and g, rank sum test, data are represented as median, 25^{th}, and 75^{th} percentile). **(h)** Ca^{2+} event rate and SWA are negatively correlated within each behavioral period: sleep (red, Pearson's correlation, $p<0.0005$) and stationary wake (cyan, Pearson's correlation, $p<0.0005$) **(i)**, but Ca^{2+} events in IP_3R2 KO mice are less correlated with SWA in sleep (Pearson's correlation, $p<0.0005$) and stationary wake (Pearson's correlation, $p>0.05$, n=5 mice, 22 hrs)

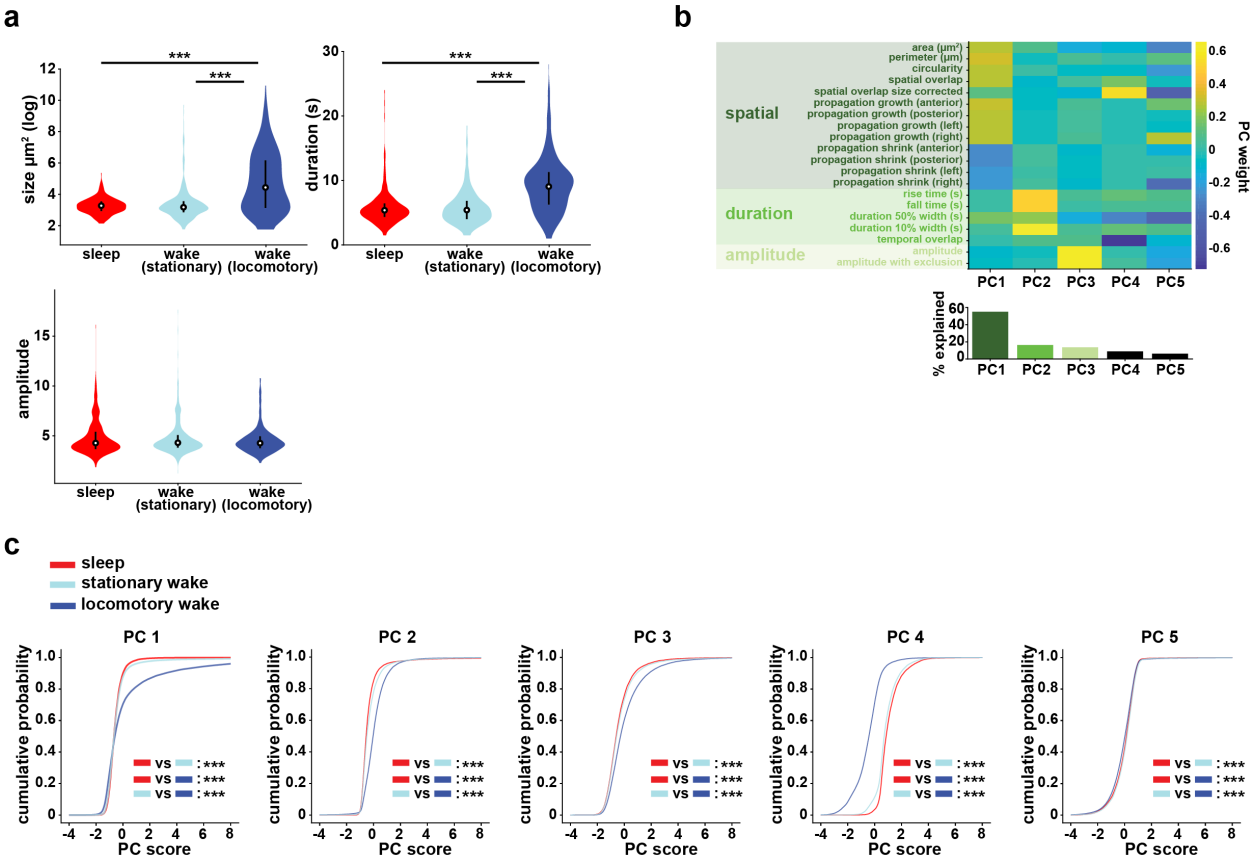

Figure 3.2: PCA reveals that behavioral states can be characterized by unique properties of astrocyte Ca^{2+} events.

(a) Individual quantification of Ca^{2+} event size (top left), duration (top right), and amplitude (bottom) across sleep, stationary wake, and locomotory wake reveal significant differences in size and duration between locomotory wake and the other two states, but no difference between sleep and stationary wake (rank sum test). Data are represented as median, 25th, and 75th percentile (n=4 mice, 19 hrs, 1,089 locomotory wake periods, 443 stationary wake periods, 285 sleep periods). **(b)** Top: Weight matrix extracted from PCA, incorporating 20 Ca^{2+} event properties obtained with AQuA (n=4 mice, 19 hrs, 87,189 events). PC 1 largely represents spatial features, PC 2 represents temporal features, and PC 3 represents features associated with amplitude. Bottom: Percent of variance explained by each PC. **(c)** Cumulative distribution of the score for each PC for sleep, stationary wake, and locomotory wake events demonstrates significant differences among all three states (two-sample Kolmogorov-Smirnov test).

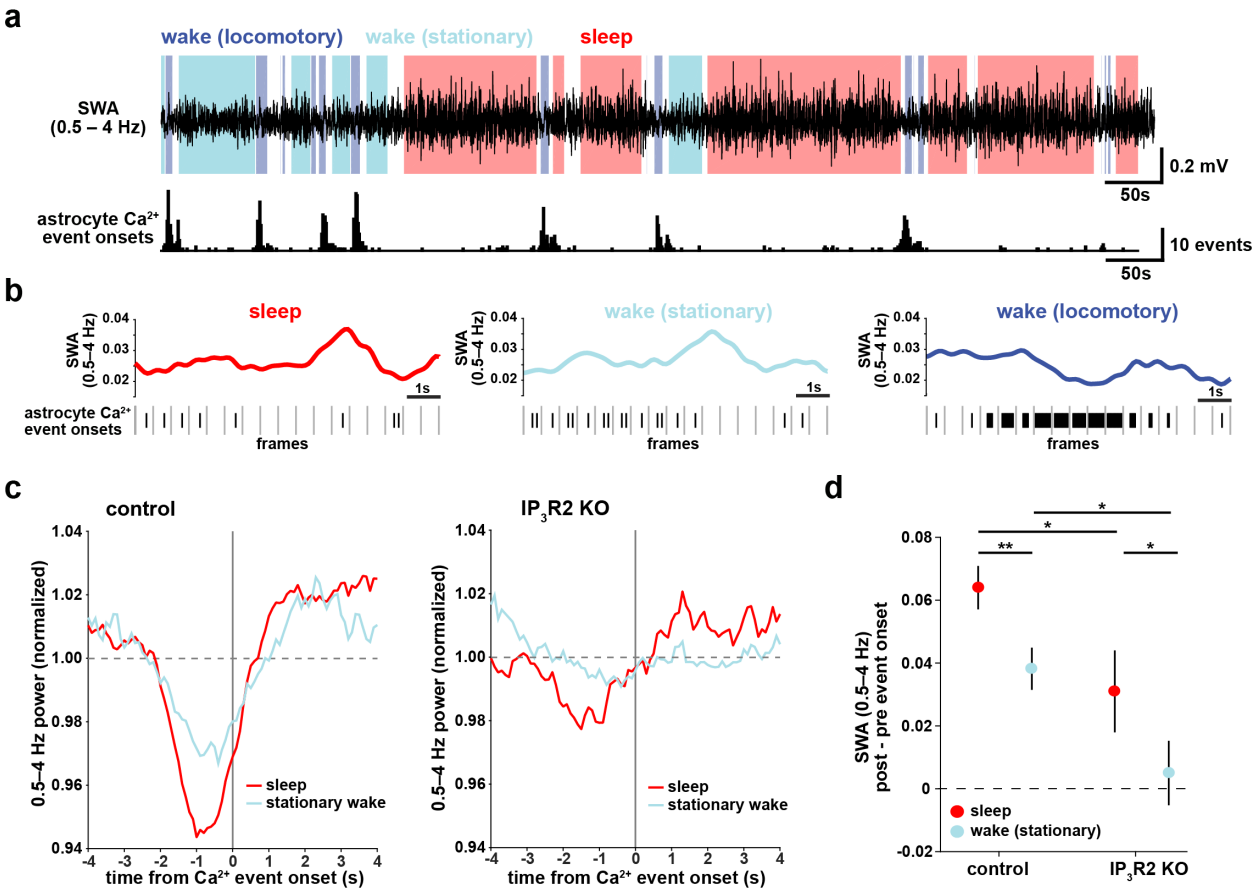

Figure 3.3: Astrocyte Ca^{2+} events characterize transitions from low to high SWA.
(a) Example of SWA obtained by filtering LFP (0.5–4 Hz) recordings (top), with corresponding astrocyte Ca^{2+} events (bottom). Behavioral state denoted by color: sleep (red) and wake (locomotory in blue, stationary in cyan). **(b)** Example traces of SWA fluctuations for each behavioral state (top) and raster plot of Ca^{2+} events (below) to demonstrate that across behavioral states, SWA fluctuates at similar levels. **(c)** Left: Average Ca^{2+} event-triggered traces reveal astrocyte Ca^{2+} event onsets occur after a relative decrease in SWA and are followed by an increase in SWA during sleep (red) and stationary wake (cyan). Right: This relationship is diminished in IP_3R2 KO mice, where less modulation around Ca^{2+} events is observed. Line width=SEM. (control: n=4 mice, 19 hrs; IP_3R2 KO: n=5 mice, 22 hrs) **(d)** SWA modulation across the 2s before and after Ca^{2+} onset demonstrates modulation is highest during sleep (red) and dependent on expression of IP_3R2 (rank sum test, data represented as mean±SEM).

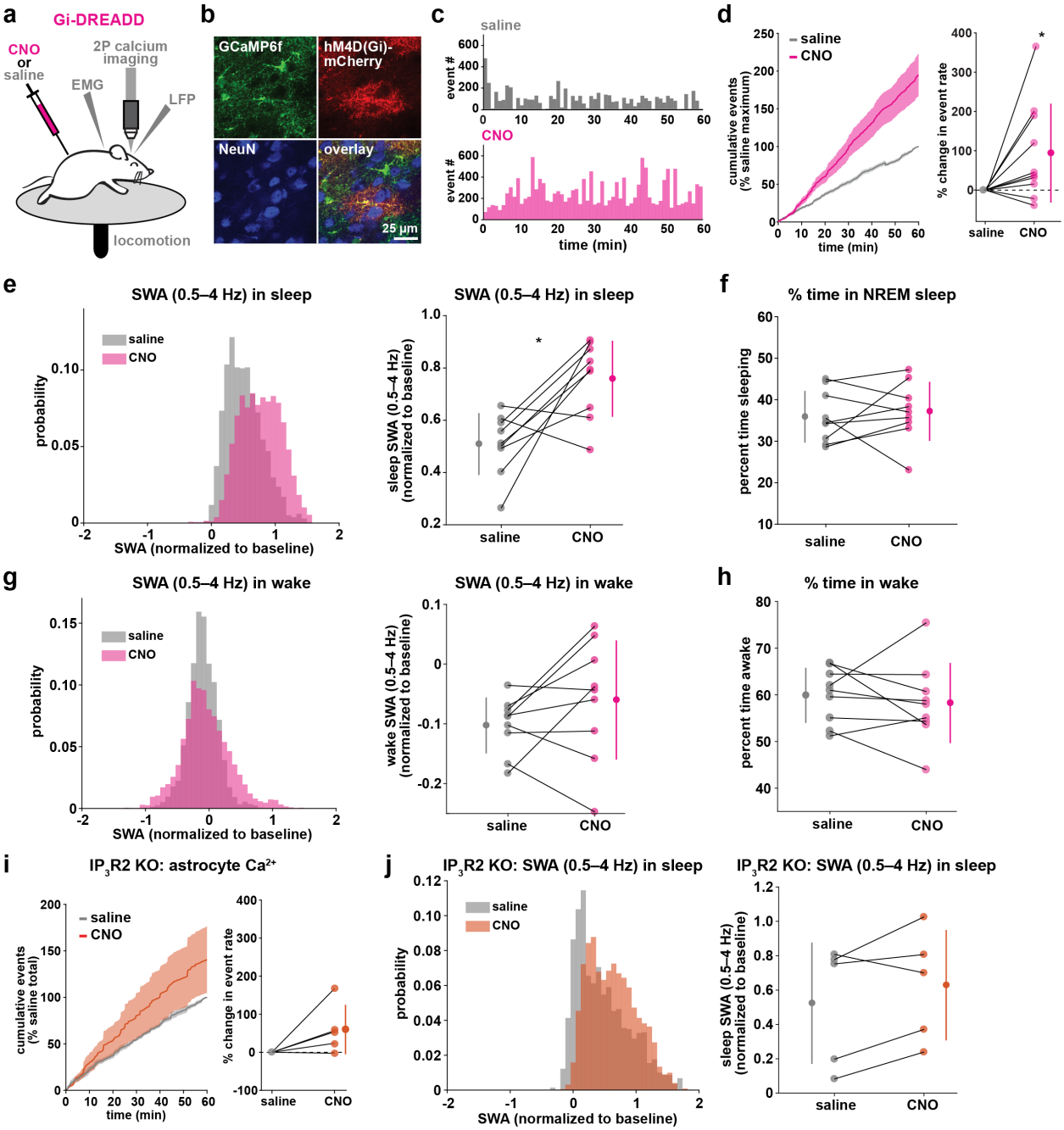

Figure 3.4: Astrocytic Gi-DREADD-driven Ca^{2+} increases are sufficient to increase SWA during sleep.

(a) Experimental setup. Mice were co-injected with *GFAP-cyto-GCaMP6f* and *GFAP-hM4D(Gi)-mCherry* AAVs. After I.P. injection of either 1mg/kg CNO or saline, astrocyte Ca^{2+}, LFP, EMG, and locomotion were recorded. **(b)** Post-experiment immunohistochemistry demonstrates astrocyte-specific expression of Gi-DREADD and GCaMP6f. $mCherry^{+}$ cells (red) exhibit typical astrocyte morphology and do not co-localize with neurons (NeuN, blue). **(c)** Representative astrocyte Ca^{2+} response in one animal in which CNO (pink, bottom) causes increased Ca^{2+} events compared with saline (gray, top). **(d)** Left: Cumulative Ca^{2+} event count for all mice after CNO (pink) shows higher event rate compared to saline (gray). Error

bars=SEM. (n=10 mice, 1-hr recordings). Right: Change in event rate for each mouse with CNO compared to saline (paired *t*-test). For panels d–j, data are represented by the mean for each individual animal, and the population as mean±SD. **(e)** Left: Administration of CNO (pink) results in rightward shift of the SWA distribution during sleep compared to saline (gray), using 5s bins. Right: Summary statistics, by animal, show increased SWA during sleep after CNO. (for panels e–h, n=9 mice, 2-hr recordings, paired *t*-test) **(f)** Percent time in NREM sleep does not differ between saline and CNO conditions. **(g)** Distribution of SWA (left) and summary statistics across mice (right) show that SWA during wake, in contrast with sleep (e), is unchanged between conditions. **(h)** Percent time awake, similar to time in NREM sleep (f), is similar between conditions. **(i)** CNO administration (orange) in IP_3R2 KO mice expressing astrocytic Gi-DREADDs causes no significant change in Ca^{2+} event number compared to saline (gray) as shown by the cumulative event count (left, error bars =SEM) and summary statistics per mouse (right, paired *t*-test) (for experiments in i–j, n=5 mice, 2-hr recordings). **(j)** Distribution of SWA during sleep (left) and summary statistics (right) show that, in contrast to controls (e), sleep SWA is unchanged between saline (gray) and CNO (orange) conditions in IP_3R2 KO mice (paired *t*-test).

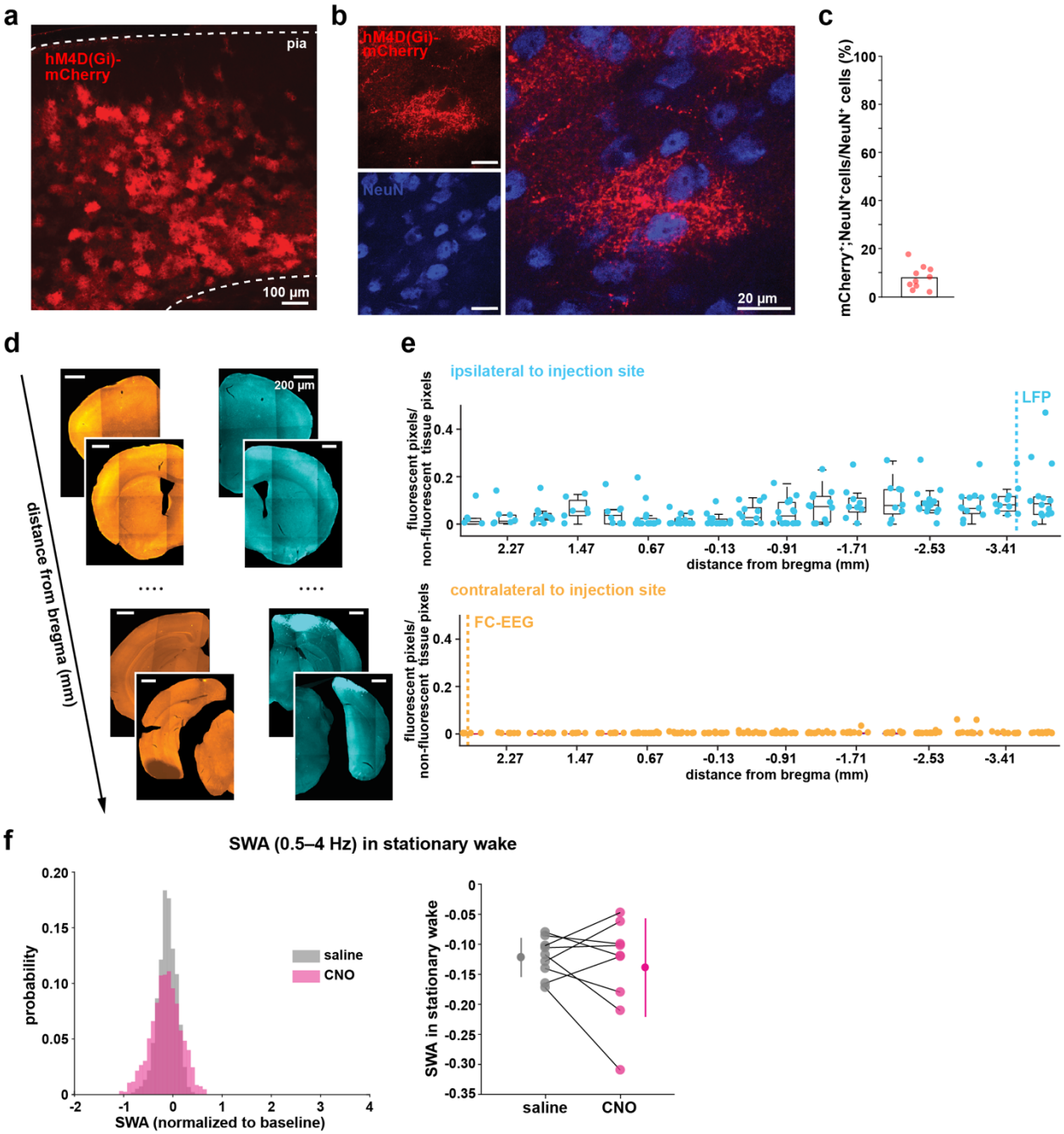

Figure 3.5: Astrocyte-specific expression of Gi-DREADDs across ipsilateral and contralateral cortex.

(a) Representative post-experiment immunohistochemistry demonstrating widespread astrocyte-specific expression of Gi-DREADDs across cortical layers. Note stereotypical bush-like astrocytic morphology of mCherry$^+$ cells. **(b)** Representative 63x magnification confocal immunohistochemistry images of mCherry (red) and NeuN (blue) staining used to identify non-specific expression of DREADDs. **(c)** Percentage of NeuN$^+$ identified cells that were also mCherry$^+$. **(d)** Schematic demonstrating analysis of cortex-wide Gi-DREADD expression spread on the hemisphere ipsilateral and contralateral to the viral injection site. **(e)** Expression spread in brain slices sampled from rostral to caudal for the ipsilateral (top, cyan) and contralateral

hemisphere (bottom, orange) demonstrates expression is highest in the ipsilateral rostral brain areas, near the LFP recording site (dashed line, cyan). There is no expression near the FC-EEG recording site (dashed line, yellow). Expression spread for each slice was calculated by normalizing the number of fluorescent pixels to the size of the brain tissue. Data represented with boxplots marking the medians, 25th, and 75th percentiles. **(f)** Distribution of SWA (left), and summary statistics across mice (right, paired *t*-test) show that SWA during stationary wake, similar to all wake (Fig. 3.4g) and in contrast with sleep (Fig. 3.4e), is unchanged between saline and CNO conditions (n=9 mice, 2-hr recordings). Data represented by mean for each animal and population mean±SD.

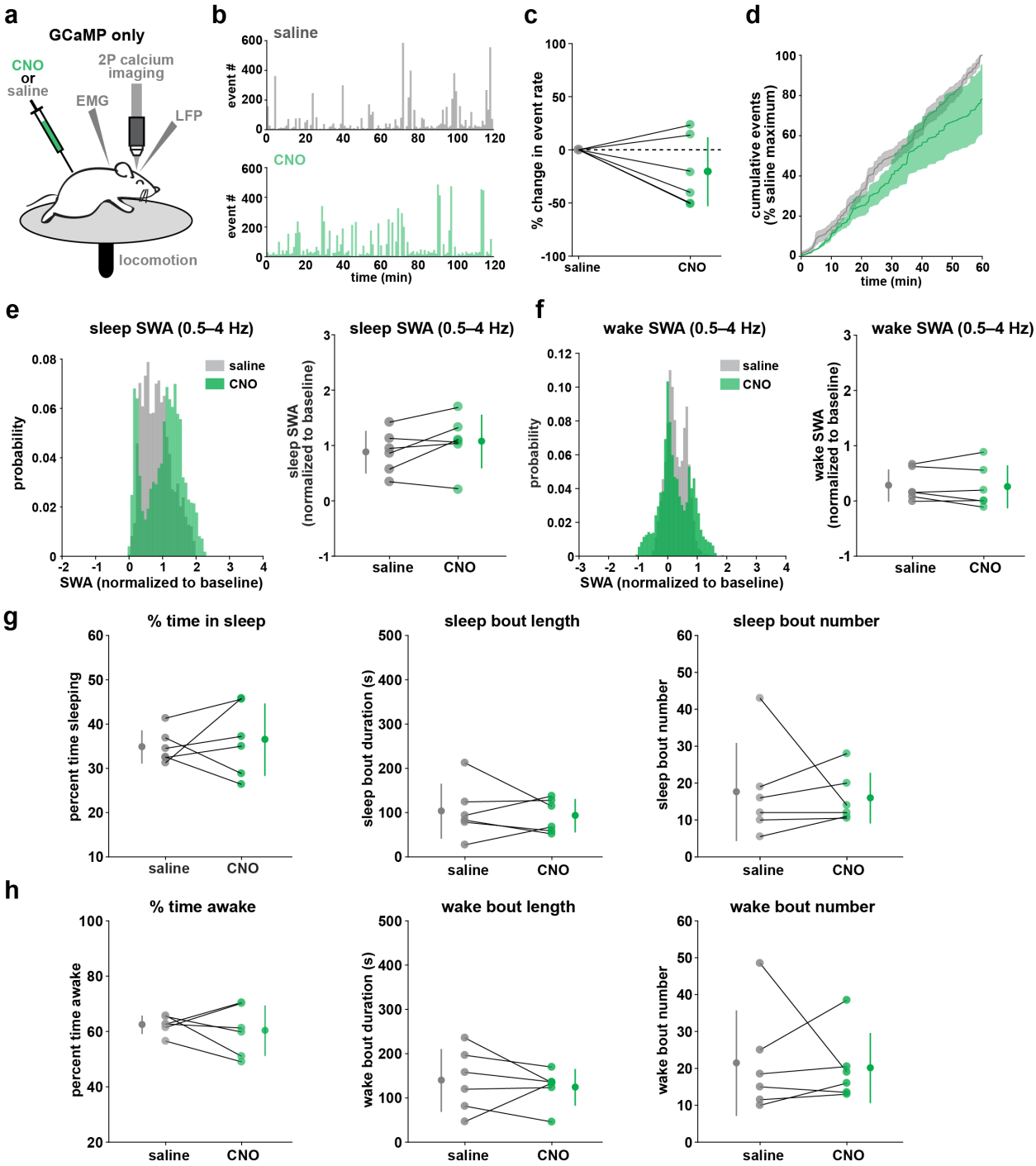

Figure 3.6: Systemic administration of CNO does not affect astrocyte Ca^{2+} dynamics, SWA, or sleep and wake behavior.

(a) Experimental setup. Mice were injected with only *GFAP-cyto-GCaMP6f* AAV. After I.P. injection of either 1mg/kg CNO or saline, astrocyte Ca^{2+}, LFP, EMG, and locomotion were recorded to assess effects of CNO. **(b)** Example astrocyte Ca^{2+} response in one animal in which CNO (green, bottom) does not change Ca^{2+} event number compared with saline (gray, top). **(c)** Ca^{2+} event rate with CNO demonstrates no significant change across mice compared to saline (paired *t*-test, data represent mean for each mouse and population mean±SD, n=6 mice, 2-hr

recordings) **(d)** Cumulative Ca^{2+} event count for all mice shows no change between CNO (green) and saline (gray) conditions (error bars=SEM, n=6 mice, 1-hr recordings). **(e)** Left: Administration of CNO (green) does not change SWA distribution during sleep compared to saline (gray), using 5s bins. Right: Summary statistics show no change in SWA during sleep after CNO (for e–h, data represented by mean for each animal and population mean±SD, n=6 mice, 2-hr recordings, paired *t*-test). **(f)** Left: CNO (green) does not change SWA distribution during wake compared to saline (gray), using 5s bins. Right: No change in SWA during wake after CNO. **(g)** Time spent in NREM sleep (left), mean sleep bout length (middle), and mean sleep bout number (right) do not differ between saline and CNO conditions. **(h)** Time spent in wake (left), mean wake bout length (middle), and mean wake bout number (right) do not differ between saline and CNO conditions.

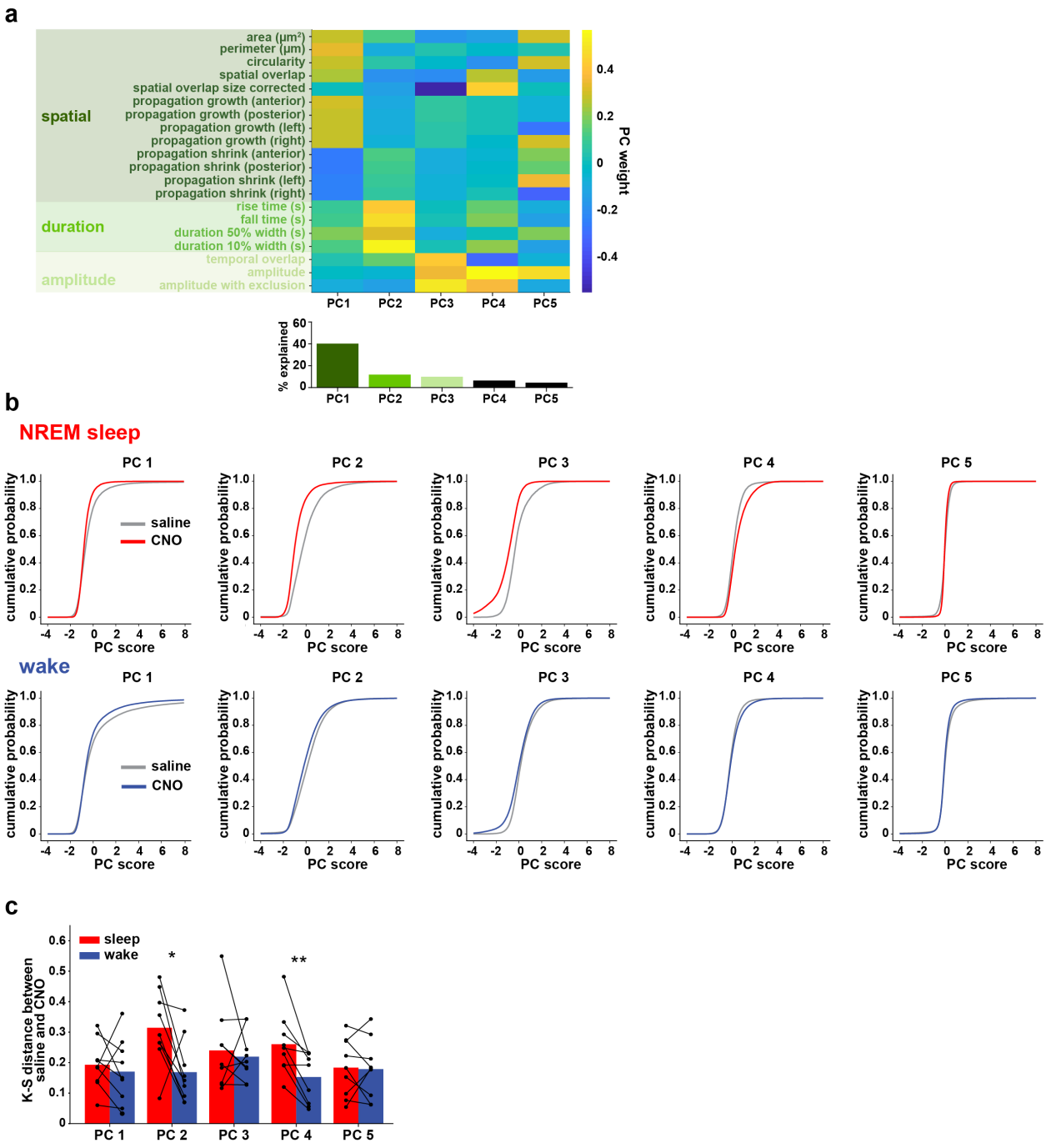

Figure 3.7: PCA shows that Gi-DREADD activation causes increased changes in Ca^{2+} event properties during sleep compared to wake.

(a) Top: Weight matrix extracted from PCA, incorporating 20 Ca^{2+} event properties obtained with AQuA (n=10 mice; 2-hr recordings; 204,172 events). PC 1 largely represents spatial features, PC 2 represents temporal features, and PC 3 represents features associated with amplitude. Bottom: Percent of variance explained by each PC. **(b)** Top: Cumulative distribution of the score for each PC for sleep events after saline or CNO administration, demonstrating clear differences in multiple PCs compared with wake (bottom). Bottom: Cumulative distribution of the score for each PC for wake events is similar between saline and CNO (n=10 mice for saline,

9 mice for CNO condition, 2-hr recordings; 33,882 sleep events; 153,646 wake events). **(c)** K-S distance between the saline and CNO distributions in panel b demonstrates significant differences between sleep and wake in the effect of CNO on PC 2, PC 4, and PC 5 (Wilcoxon signed rank test, n=9 mice, median event number/mouse=4,139).

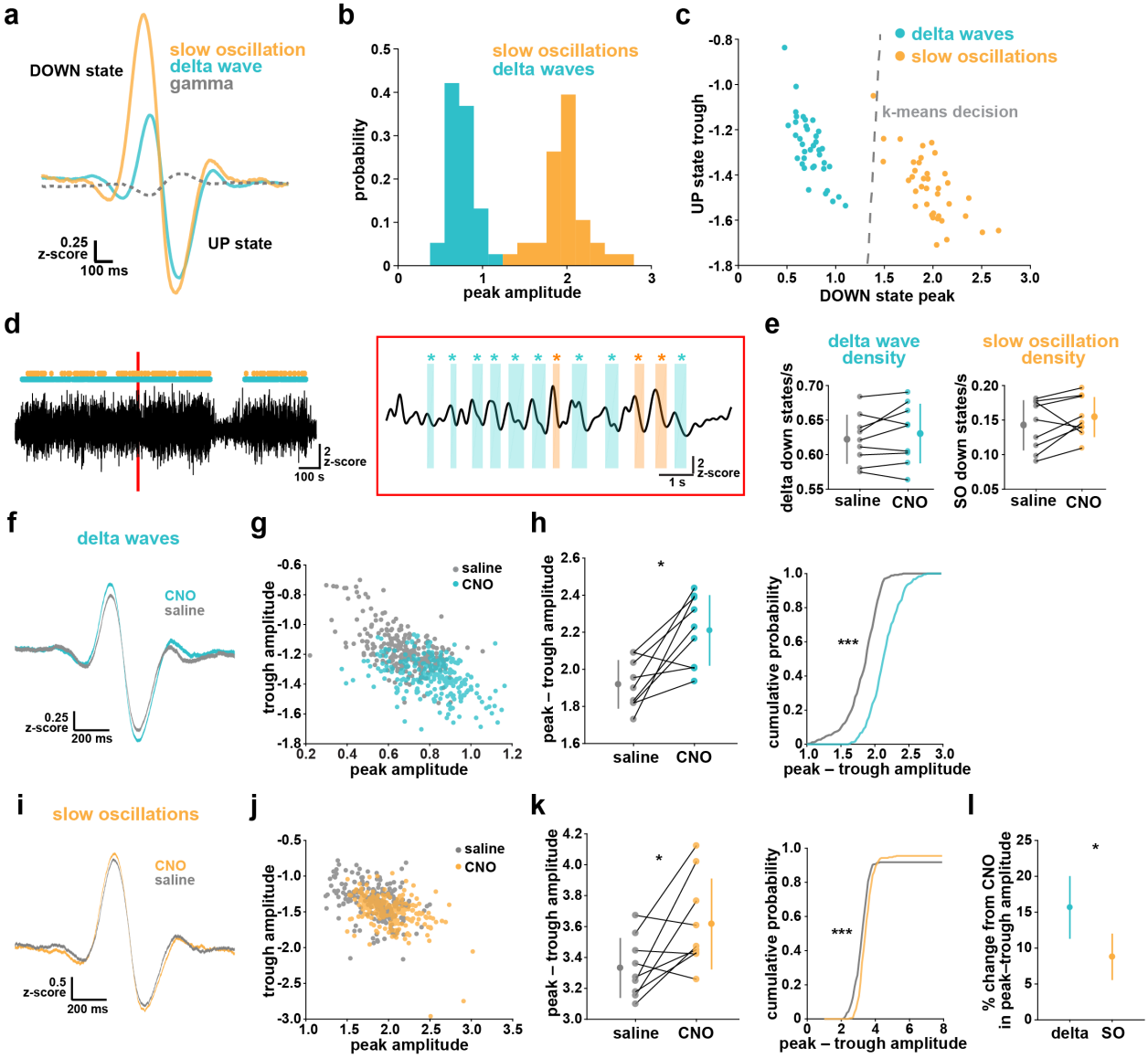

Figure 3.8: Astrocytic Gi-DREADD activation regulates local delta waves more than slow oscillations.

(a) Mean of all identified slow oscillations (orange) and delta waves (cyan) (n=31,966 delta waves, 7,855 slow oscillations) in saline condition, including mean LFP amplitude filtered for high-gamma (gray, 80–100Hz) demonstrating lower gamma during DOWN state and higher gamma during UP state (for panels a–c, n=10 mice, 38 hrs). **(b)** Peak amplitude separation between slow oscillations and delta waves. **(c)** Peak vs. trough amplitude for slow oscillations and delta waves is separable by K-means clustering (dashed line). **(d)** Left: Example of filtered LFP (0.1–4Hz) for a 20-min recording. Slow oscillations (orange) and delta waves (cyan) indicated. Right: A 10s window corresponding to the red box, with example waveforms of individual slow oscillations and delta waves. **(e)** Delta wave (left) and slow oscillation (right) rates do not change between conditions (for panels e; h, left; k, left; and l, data represented by mean for each animal, and the population as mean±SD, n=9 mice 2-hr recordings, paired *t*-test). **(f)** Delta waves with CNO (cyan) show higher peak and trough amplitude compared with saline (gray) (saline: n=10 mice, 16,467 waveforms; CNO: n=9 mice, 15,499 waveforms). **(g)** Peak vs.

trough amplitude for delta waves after CNO (cyan) is shifted compared with saline controls (gray) (for panels g; h, right; j; i, right, saline: n=10 mice, 257 sleep periods, CNO: n=9 mice, 246 sleep periods). **(h)** Left: Peak minus trough delta wave amplitude is higher with CNO. Right: Cumulative distribution reveals a leftward shift in the peak minus trough delta wave amplitude with CNO (two-sample Kolmogorov-Smirnov test). **(i)** Slow oscillations show minimal peak and trough amplitude change with CNO (orange) relative to saline (gray), compared with delta waves (f) (saline: n=10 mice, 3,995 waveforms, CNO: n=9 mice, 3,860 waveforms). **(j)** Peak versus trough amplitude for slow oscillations is similar between CNO (orange) and saline (gray) conditions, compared with delta waves (g). **(k)** Left: Peak minus trough slow oscillation amplitude shows a smaller, but significant, increase with CNO compared with delta waves (h left). Right: Cumulative distribution reveals a minimal shift in the peak minus trough slow oscillation amplitude after CNO administration, compared with delta waves (h, right) (two-sample Kolmogorov-Smirnov test). **(l)** Higher percent change for delta waves in peak minus trough amplitude with CNO, compared to slow oscillations.

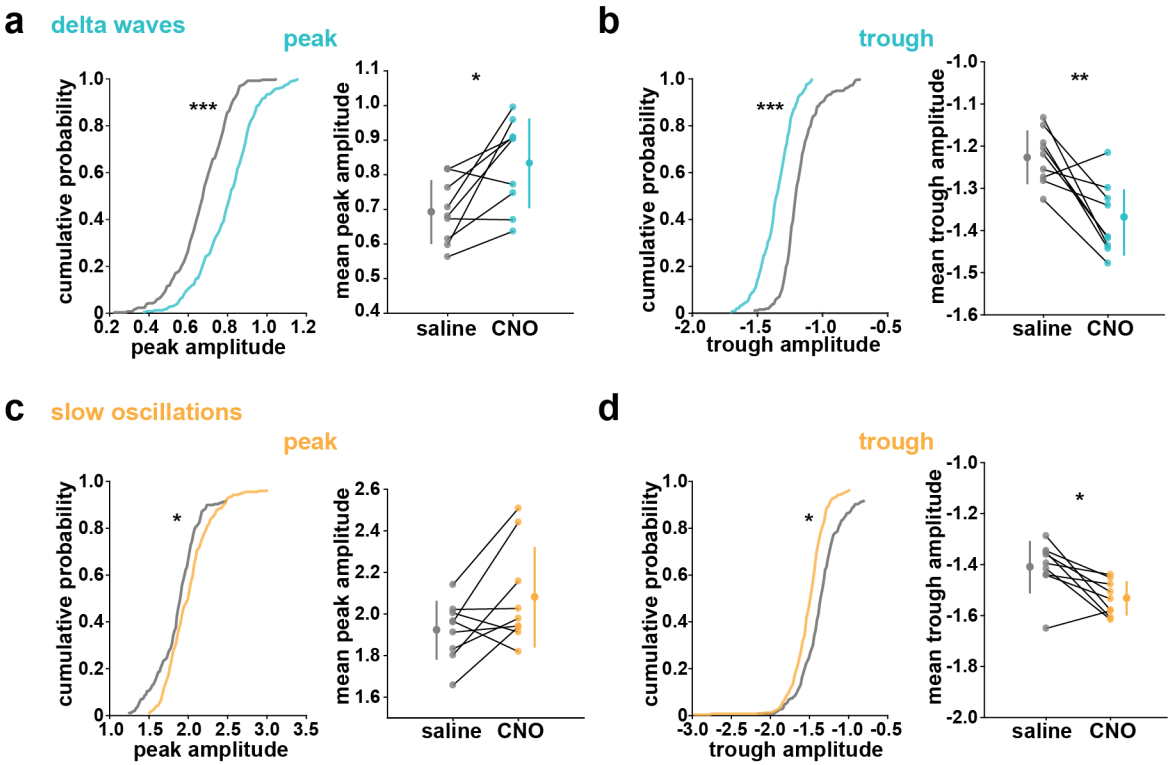

Figure 3.9: Gi-DREADD activation does not affect SWA in stationary wake, but changes peak and trough delta wave amplitude during sleep.

(a) The cumulative distribution (left) and summary statistics across mice (right) show that delta wave peak amplitude is significantly higher with CNO compared to saline (for panels a-d, n=10 mice, 38 total hrs for cumulative distribution plots, two-sample Kolmogorov-Smirnov test. n=9 mice, 2-hr recordings/mouse, paired *t*-test for the remaining figures). **(b)** Similar to (a), cumulative distribution (left) and summary statistics across mice (right) reveal significantly lower trough amplitude after CNO administration relative to saline. **(c)** The cumulative distribution (left) shows a significant but smaller shift in slow oscillation peak amplitude with CNO compared to delta waves shown in (a). Summary statistics across mice show no significant change in slow oscillation peak amplitude between conditions. **(d)** Similar to (c), the cumulative distribution (left) and summary statistics across mice (right) demonstrate a significant, but smaller, change in slow oscillation trough amplitude compared with delta wave trough amplitude (b). For all panels with summary statistics, data represented by mean for each animal and population mean±SD.

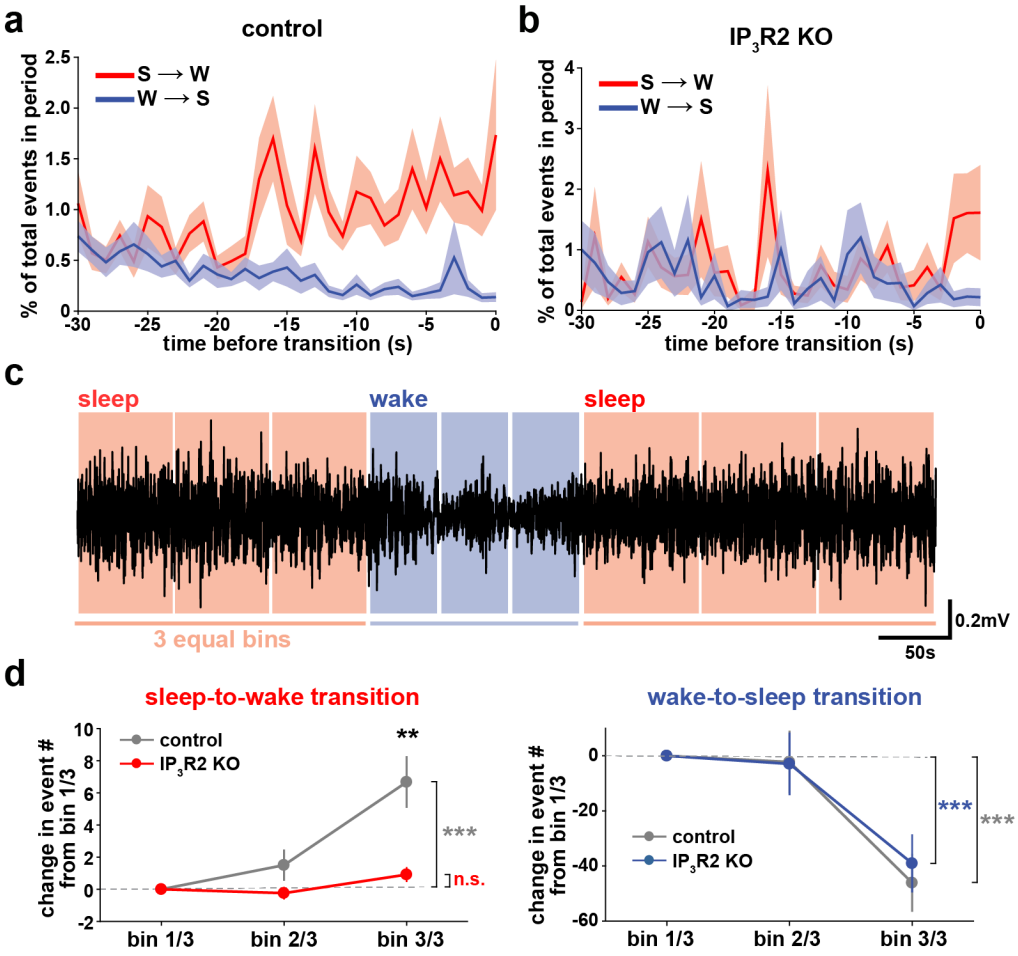

Figure 3.10: Cortical astrocyte Ca^{2+} dynamics exhibit bidirectional changes preceding sleep and wake transitions.
(a) Within each individual sleep/wake period, the proportion of all astrocyte Ca^{2+} events increases before transitions to wake (red) and decreases before transitions to sleep (blue). Error bars=SEM. **(b)** In contrast, the proportion of all Ca^{2+} events in a sleep or wake period in IP_3R2 KO mice does not consistently change preceding transitions. Error bars=SEM. **(c)** Example filtered LFP (0.5–4Hz) trace across sleep (NREM) and wake transitions. All sleep (red) and wake (blue) periods were divided in three equal bins to examine Ca^{2+} dynamics across individual behavioral states. **(d)** Change in Ca^{2+} event number across sleep and wake periods show an increase in event number in the last third of sleep (left) and a decrease in the last third of wake (right) (paired *t*-test). Change in Ca^{2+} event number across sleep periods (left) increases in the last third for control, but not for IP_3R2 KO mice (unpaired *t*-test). Data are represented as mean±SEM (controls: n=4 mice, 19 hrs; IP_3R2 KO=5 mice, 22 hrs)

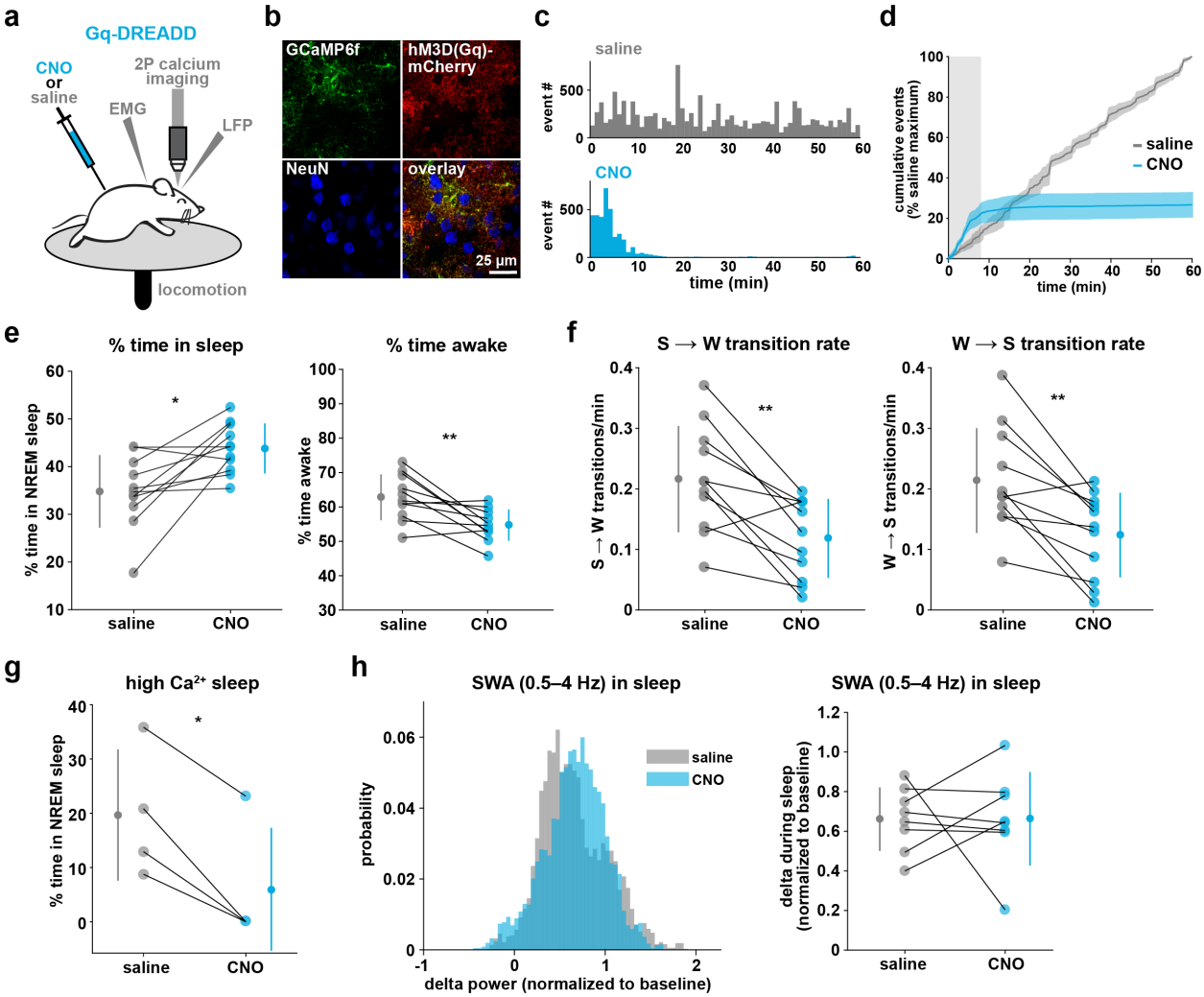

Figure 3.11: Gq-induced Ca^{2+} is necessary for sleep-wake transitions.
(a) Experimental setup. Mice were co-injected with *GFAP-cyto-GCaMP6f* and *GFAP-hM3D(Gq)-mCherry* AAVs. After I.P. injection of either 1mg/kg CNO or saline, 2P astrocyte Ca^{2+} dynamics, LFP, EMG, and locomotion were recorded. **(b)** Post-experiment immunohistochemistry demonstrates astrocyte-specific expression of the Gq-DREADD (red) and GCaMP6f (green). $mCherry^{+}$ cells exhibit typical astrocyte morphology and do not co-localize with neurons (blue, NeuN). **(c)** Representative data from a single Gq-DREADD-expressing animal. Administration of CNO (blue) causes a short initial period of elevated Ca^{2+} relative to saline administration (gray), followed by a complete suppression of all Ca^{2+} activity. **(d)** Cumulative Ca^{2+} event count after saline (gray) or CNO (blue) injection over 60 min. The initial high Ca^{2+} period (8 min, light gray box) is followed by suppression of astrocyte Ca^{2+}. (Error bars=SEM, n=3 mice, 1-hr recordings) **(e)** Left: The proportion of time mice spend sleeping after CNO administration (during Ca^{2+} suppression period) is increased relative to saline controls, and time in wake is decreased (right), suggesting Ca^{2+} suppression is sufficient to increase sleep (for e–f, and h, paired *t*-test, n=11 mice; analyses are performed in the 1 hr, 52 min period of Ca^{2+} suppression). **(f)** Sleep-to-wake transitions (left) and wake-to-sleep transitions (right) are decreased with CNO relative to saline. (**g**) During the high Ca^{2+} period after CNO administration, mice spend less time sleeping compared to saline-injected controls (paired *t*-test),

suggesting the Gq-DREADD-driven Ca^{2+} increase is sufficient to suppress sleep (n=4 mice, for e–h, data are represented as mean for each animal and population mean±SD). **(h)** Distribution of SWA (left) and summary statistics (right) show that despite Ca^{2+} changes, SWA during sleep is unaffected by Gq-DREADD activation. (n=8 mice, paired *t*-test).

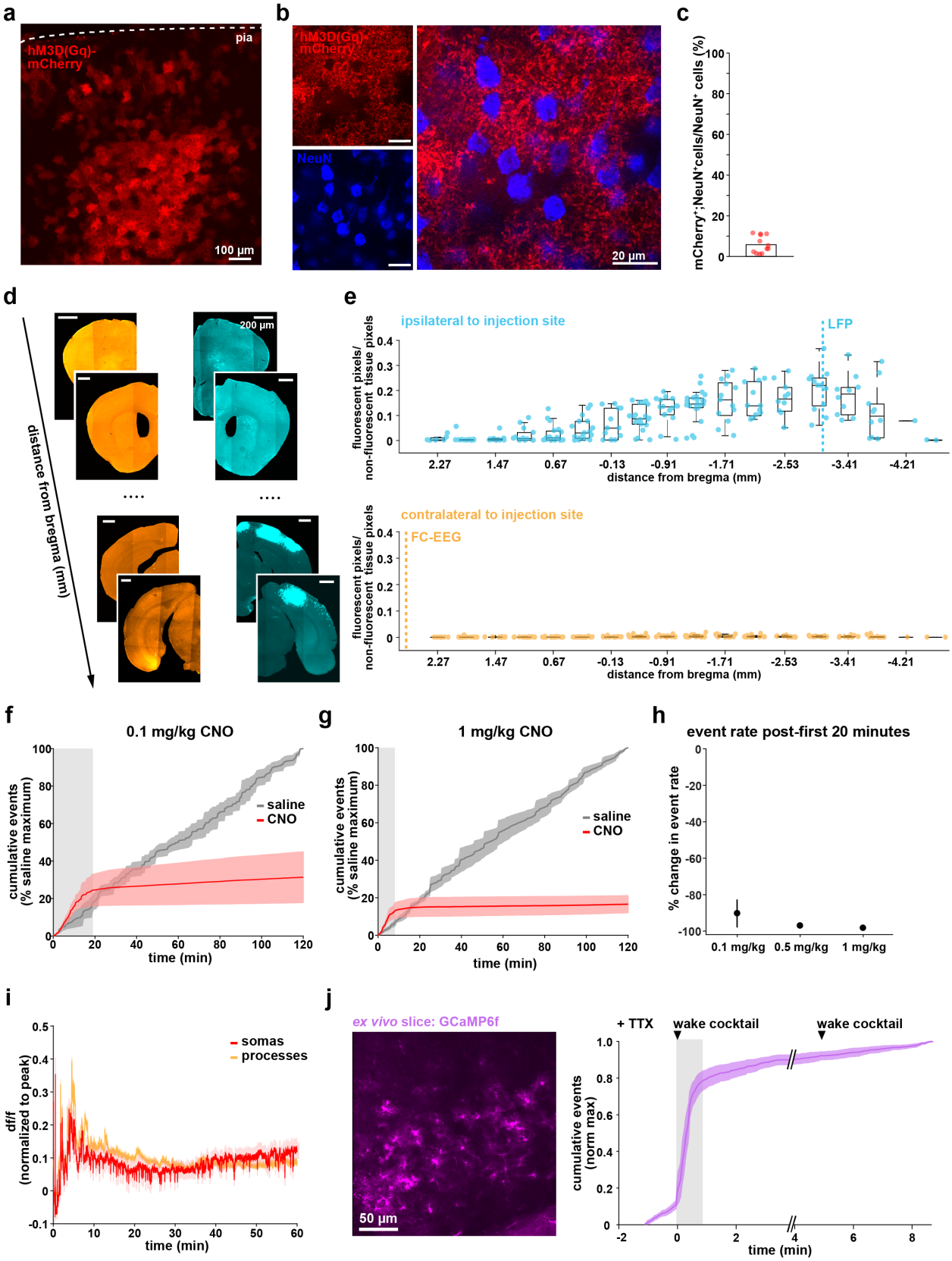
a
pia
hM3D(Gq)-mCherry
100 µm
b
hM3D(Gq)-mCherry
NeuN
20 µm
c
mCherry+:NeuN+cells/NeuN+ cells (%)
d
200 µm
distance from bregma (mm)
e
ipsilateral to injection site
LFP
fluorescent pixels/ non-fluorescent tissue pixels
distance from bregma (mm)
contralateral to injection site
FC-EEG
f
0.1 mg/kg CNO
cumulative events (% saline maximum)
saline
CNO
time (min)
g
1 mg/kg CNO
h
event rate post-first 20 minutes
% change in event rate
0.1 mg/kg
0.5 mg/kg
1 mg/kg
i
somas
processes
df/f (normalized to peak)
time (min)
j
ex vivo slice: GCaMP6f
50 µm
+ TTX
wake cocktail
wake cocktail
cumulative events (norm max)
time (min)

Figure 3.12: Astrocyte-specific expression of Gq-DREADDs across ipsilateral and contralateral cortex.
(a) Representative post-experiment immunohistochemistry demonstrating astrocyte-specific expression of Gq-DREADDs across cortical layers. **(b)** Representative 63x confocal images of mCherry and NeuN staining to quantify non-specific DREADD expression. **(c)** Percentage of $NeuN^+$ identified cells that were also $mCherry^+$. **(d)** Schematic illustrating analysis of cortex-wide Gq-DREADD expression spread in hemispheres both ipsilateral and contralateral to viral injection site. **(e)** Expression spread in brain slices sampled from rostral to caudal for the ipsilateral (top, cyan) and contralateral hemisphere (bottom, orange) shows that expression is highest in ipsilateral rostral cortex, near the LFP recording site (dashed line, cyan). No expression is detected at the FC-EEG recording site (dashed line, yellow). Viral expression spread for each slice was calculated by normalizing the number of fluorescent pixels to the size of the brain tissue. Data represented with boxplots marking the medians, 25^{th}, and 75^{th} percentiles. **(f)** Cumulative Ca^{2+} event count for mice after administration of 0.1mg/kg CNO (red) and saline (gray) showing an initial period of elevated Ca^{2+} (gray box), followed by a dramatic suppression of Ca^{2+} events similar to 1mg/kg CNO (Error bars=SEM, n=3 mice, 1-hr recordings). **(g)** Cumulative Ca^{2+} event count for mice after 1mg/kg CNO (red) and saline (gray), as shown in Fig. 3.10d (Error bars=SEM, n=3 mice, 1-hr recordings). **(h)** Total suppression of astrocyte Ca^{2+} event rate is similar for all three tested doses of CNO (mean±SEM, 0.1mg/kg: n=3 mice, 2-hr recordings; 0.5mg/kg: n=1 mouse, 2-hr recordings; 1mg/kg: n=5 mice, 2-hr recordings). (**i**) Mean GCaMP6f fluorescence in somata and processes after administration of 1mg/kg CNO, with both remaining elevated throughout 1-hr recording (Error bars=SEM, n=3 mice, 1-hr recordings). (**j**) Left: Representative 2P image of V1 cortical astrocytes in an acute, *ex vivo* slice. Right: Cumulative events across two consecutive 5-min videos demonstrating a large response to the first application of a "wake" cocktail (black triangles), but not the second (error bars=SEM, n=2 mice, 8 slices).

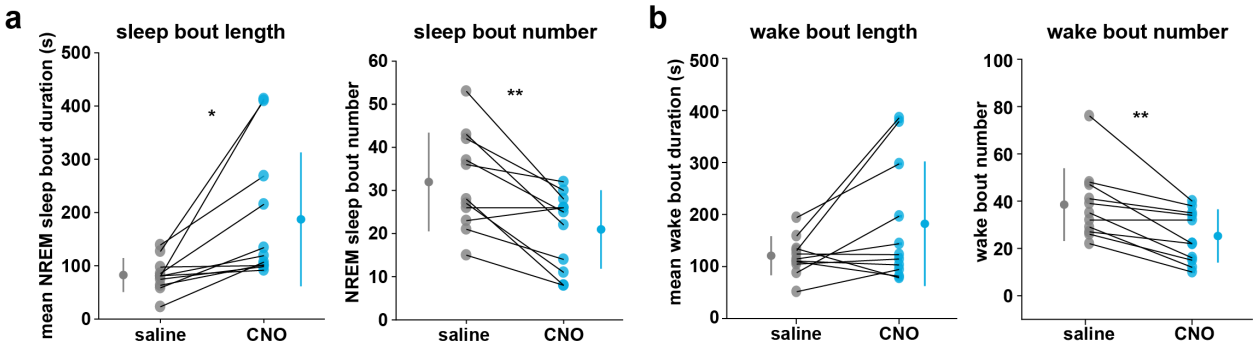

Figure 3.13: Gq-DREADD activation suppresses sleep-wake transitions by increasing bout length and decreasing bout number.

(a) Left: Mean sleep bout length after CNO administration is increased compared to saline controls, suggesting Ca^{2+} dynamics are necessary for sleep-to-wake transitions. Right: Mean sleep bout number observed after CNO administration is decreased compared to saline controls. For all panels, n=11 mice. Analyses are performed during the 1 hr, 52 min period when Ca^{2+} is suppressed, all paired *t*-tests. **(b)** Left: Mean wake bout length after CNO administration is increased relative to saline, suggesting Ca^{2+} dynamics are necessary for wake-to-sleep transitions, similar to sleep-to-wake transitions in (a). Right: Mean number of wake bouts after CNO, and during Ca^{2+} suppression, is decreased relative to saline.

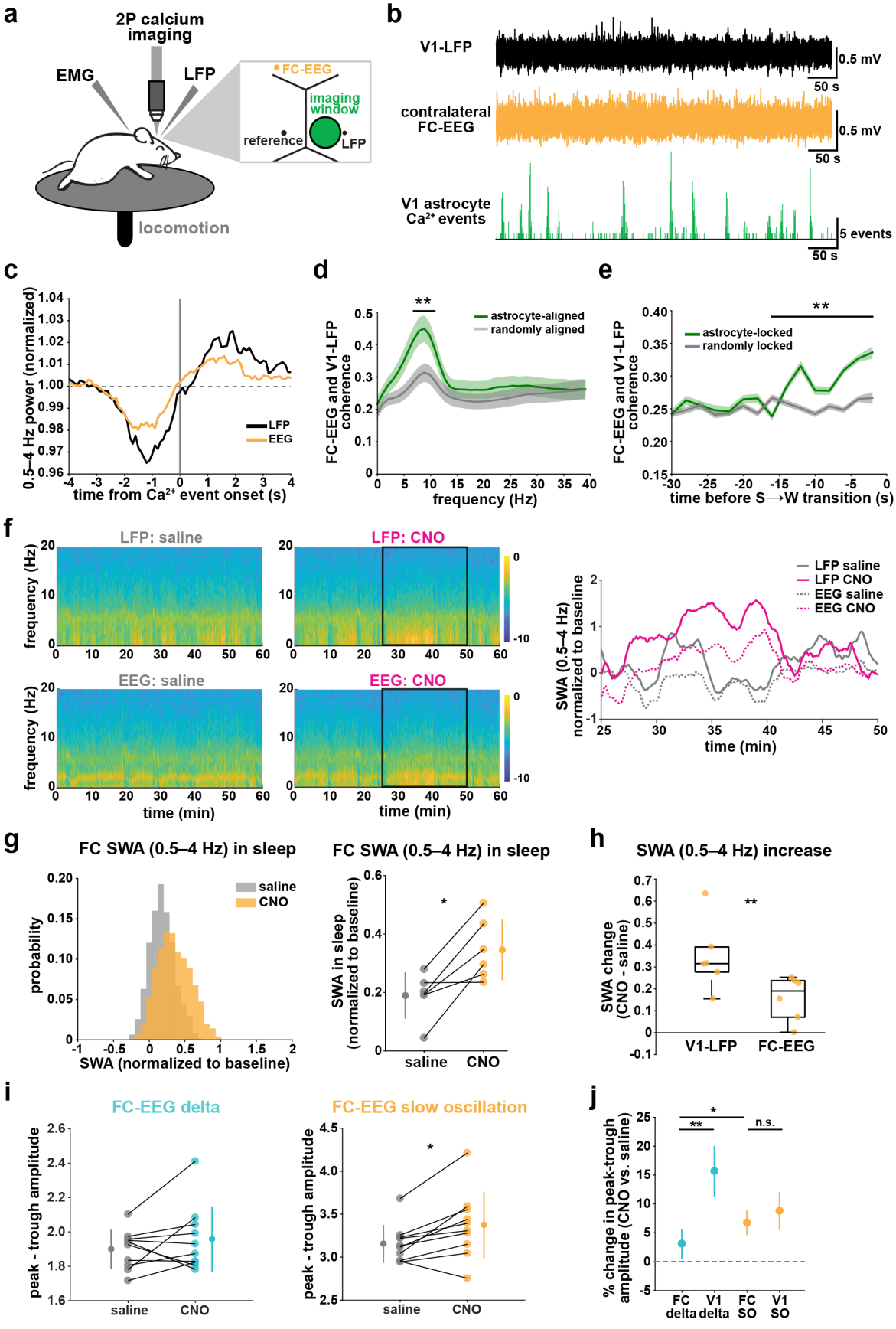
a
2P calcium imaging
EMG
LFP
FC-EEG
imaging window
reference
LFP
locomotion
b
V1-LFP
0.5 mV
50 s
contralateral FC-EEG
0.5 mV
50 s
V1 astrocyte Ca2+ events
5 events
50 s
c
0.5–4 Hz power (normalized)
LFP
EEG
time from Ca2+ event onset (s)
d
**
astrocyte-aligned
randomly aligned
FC-EEG and V1-LFP coherence
frequency (Hz)
e
**
astrocyte-locked
randomly locked
FC-EEG and V1-LFP coherence
time before S→W transition (s)
f
LFP: saline
LFP: CNO
EEG: saline
EEG: CNO
frequency (Hz)
time (min)
LFP saline
LFP CNO
EEG saline
EEG CNO
SWA (0.5–4 Hz) normalized to baseline
time (min)
g
FC SWA (0.5–4 Hz) in sleep
saline
CNO
probability
SWA (normalized to baseline)
FC SWA (0.5–4 Hz) in sleep
SWA in sleep (normalized to baseline)
saline
CNO
h
SWA (0.5–4 Hz) increase
SWA change (CNO - saline)
V1-LFP
FC-EEG
i
FC-EEG delta
peak - trough amplitude
saline
CNO
FC-EEG slow oscillation
peak - trough amplitude
saline
CNO
j
n.s.
% change in peak-trough amplitude (CNO vs. saline)
FC delta
V1 delta
FC SO
V1 SO

Figure 3.14: V1 manipulation of astrocyte Ca^{2+} alters SWA in contralateral frontal cortex via changes in slow oscillations.
(a) Experimental setup. Mice were co-injected with *GFAP-cyto-GCaMP6f* and *GFAP-hM4D(Gi)-mCherry* AAVs. 2P astrocyte Ca^{2+} dynamics in right V1, LFP local to the imaging field, EEG in the contralateral frontal cortex (orange), EMG, and locomotion were recorded. **(b)** Representative data from simultaneous recordings from V1-LFP (black), contralateral frontal cortex EEG (orange), and V1 astrocyte Ca^{2+} imaging (green). (c) Average V1-Ca^{2+} event-triggered traces of FC-EEG SWA (orange) reveal a similar, but smaller, fluctuation of SWA around Ca^{2+} event onsets compared with V1-LFP (black). (d) Coherence between V1-LFP and FC-EEG is higher after astrocyte event onset (green), compared to randomly sampled time points (gray) (paired *t*-test, n=13 mice, median event number/mouse=7,512 events). Error bars=SEM. (e) Astrocyte-locked coherence (0–15Hz) increases before sleep-to-wake transitions (unpaired *t*-test, n=13 mice, median event number/mouse=417 events). **(f)** Left: Example spectrograms from simultaneously recorded population-level electrophysiology: V1-LFP (top row) and FC-EEG (bottom row) following saline (left column) or CNO (right column) injection. Right: SWA corresponding to the black rectangle marked in the spectrograms demonstrates that CNO (pink) increased SWA in V1-LFP (solid lines) and FC-EEG (dashed lines) compared to saline (gray). **(g)** Distribution of SWA (left) and summary statistics across mice (right, paired *t*-test) demonstrate that SWA in FC-EEG is increased after activation of V1 Gi-DREADD-expressing astrocytes by CNO (data represented as mean for each animal and population mean±SD, n=7 mice, 2-hr recordings). **(h)** Change in SWA measured by V1-LFP or FC-EEG demonstrate that CNO increases SWA in both measurements, but more in V1-LFP recordings (paired *t*-test). Data represented using box plots with median, 25^{th}, and 75^{th} percentile. (**i**) Peak-to-trough amplitude for delta waves (cyan, left) and slow oscillations (yellow, right) in saline (gray) and CNO conditions in FC (paired *t*-test). (**j**) Percent change in peak-trough amplitude for delta waves (cyan) and slow oscillations (yellow) in CNO vs. saline (paired *t*-test, data represented as mean±SEM). There is a greater change in amplitude for slow oscillations than delta waves in FC after Gi-DREADD activation in V1.

References

1. Klinzing, J. G., Niethard, N. & Born, J. Mechanisms of systems memory consolidation during sleep. *Nat. Neurosci.* **22,** 1598–1610 (2019).
2. Genzel, L., Kroes, M. C. W., Dresler, M. & Battaglia, F. P. Light sleep versus slow wave sleep in memory consolidation: a question of global versus local processes? *Trends Neurosci.* **37,** 10–19 (2014).
3. Kim, J., Gulati, T. & Ganguly, K. Competing Roles of Slow Oscillations and Delta Waves in Memory Consolidation versus Forgetting. *Cell* **179,** 514–526.e13 (2019).
4. Tononi, G. & Cirelli, C. Sleep and the price of plasticity: from synaptic and cellular homeostasis to memory consolidation and integration. *Neuron* **81,** 12–34 (2014).
5. Diekelmann, S. & Born, J. The memory function of sleep. *Nat. Rev. Neurosci.* **11,** 114–126 (2010).
6. Tononi, G. & Cirelli, C. Sleep function and synaptic homeostasis. *Sleep Med. Rev.* **10,** 49–62 (2006).
7. Tononi, G. & Cirelli, C. Sleep and synaptic down-selection. *Eur. J. Neurosci.* **51,** 413–421 (2020).
8. Ji, D. & Wilson, M. A. Coordinated memory replay in the visual cortex and hippocampus during sleep. *Nat. Neurosci.* **10,** 100–107 (2007).
9. Dijk, D. J. & Beersma, D. G. Effects of SWS deprivation on subsequent EEG power density and spontaneous sleep duration. *Electroencephalogr. Clin. Neurophysiol.* **72,** 312–320 (1989).
10. Patrick, G. T. W. & Gilbert, J. A. Studies from the psychological laboratory of the University of Iowa: On the effects of loss of sleep. *Psychol. Rev.* **3,** 469–483 (1896).

11. Holst, S. C. & Landolt, H.-P. Sleep-Wake Neurochemistry. *Sleep Med. Clin.* **13,** 137–146 (2018).

12. Saper, C. B. & Fuller, P. M. Wake-sleep circuitry: an overview. *Curr. Opin. Neurobiol.* **44,** 186–192 (2017).

13. Lee, S.-H. & Dan, Y. Neuromodulation of brain states. *Neuron* **76,** 209–222 (2012).

14. Chen, J.-Y., Chauvette, S., Skorheim, S., Timofeev, I. & Bazhenov, M. Interneuron-mediated inhibition synchronizes neuronal activity during slow oscillation. *J. Physiol. (Lond.)* **590,** 3987–4010 (2012).

15. Steriade, M., McCormick, D. A. & Sejnowski, T. J. Thalamocortical oscillations in the sleeping and aroused brain. *Science* **262,** 679–685 (1993).

16. Lemieux, M., Chauvette, S. & Timofeev, I. Neocortical inhibitory activities and long-range afferents contribute to the synchronous onset of silent states of the neocortical slow oscillation. *J. Neurophysiol.* **113,** 768–779 (2015).

17. Volgushev, M., Chauvette, S., Mukovski, M. & Timofeev, I. Precise long-range synchronization of activity and silence in neocortical neurons during slow-wave oscillations [corrected]. *J. Neurosci.* **26,** 5665–5672 (2006).

18. Steriade, M. & Timofeev, I. Neuronal plasticity in thalamocortical networks during sleep and waking oscillations. *Neuron* **37,** 563–576 (2003).

19. Sheroziya, M. & Timofeev, I. Global intracellular slow-wave dynamics of the thalamocortical system. *J. Neurosci.* **34,** 8875–8893 (2014).

20. Amzica, F. & Steriade, M. Short- and long-range neuronal synchronization of the slow (< 1 Hz) cortical oscillation. *J. Neurophysiol.* **73,** 20–38 (1995).

21. Sanchez-Vives, M. V. & McCormick, D. A. Cellular and network mechanisms of rhythmic

recurrent activity in neocortex. *Nat. Neurosci.* **3,** 1027–1034 (2000).

22. Ode, K. L., Katsumata, T., Tone, D. & Ueda, H. R. Fast and slow Ca2+-dependent hyperpolarization mechanisms connect membrane potential and sleep homeostasis. *Curr. Opin. Neurobiol.* **44,** 212–221 (2017).
23. Tatsuki, F. *et al.* Involvement of Ca(2+)-Dependent Hyperpolarization in Sleep Duration in Mammals. *Neuron* **90,** 70–85 (2016).
24. Björklund, A. & Lindvall, O. in *Limbic Mechanisms* (eds. Livingston, K. E. & Hornykiewicz, O.) 307–331 (Springer US, 1978). doi:10.1007/978-1-4757-0716-8_11
25. Woolf, N. J. Cholinergic systems in mammalian brain and spinal cord. *Prog. Neurobiol.* **37,** 475–524 (1991).
26. Loughlin, S. E., Foote, S. L. & Bloom, F. E. Efferent projections of nucleus locus coeruleus: topographic organization of cells of origin demonstrated by three-dimensional reconstruction. *Neuroscience* **18,** 291–306 (1986).
27. Panula, P., Pirvola, U., Auvinen, S. & Airaksinen, M. S. Histamine-immunoreactive nerve fibers in the rat brain. *Neuroscience* **28,** 585–610 (1989).
28. Niethard, N., Ngo, H.-V. V., Ehrlich, I. & Born, J. Cortical circuit activity underlying sleep slow oscillations and spindles. *Proc. Natl. Acad. Sci. USA* **115,** E9220–E9229 (2018).
29. Stroh, A. *et al.* Making waves: initiation and propagation of corticothalamic Ca2+ waves in vivo. *Neuron* **77,** 1136–1150 (2013).
30. Luczak, A., Barthó, P., Marguet, S. L., Buzsáki, G. & Harris, K. D. Sequential structure of neocortical spontaneous activity in vivo. *Proc. Natl. Acad. Sci. USA* **104,** 347–352 (2007).
31. Massimini, M., Huber, R., Ferrarelli, F., Hill, S. & Tononi, G. The sleep slow oscillation as a traveling wave. *J. Neurosci.* **24,** 6862–6870 (2004).

32. Krone, L. B. *et al.* A role for the cortex in sleep-wake regulation. *BioRxiv* (2020). doi:10.1101/2020.03.17.996090

33. Sanchez-Vives, M. V. & Mattia, M. Slow wave activity as the default mode of the cerebral cortex. *Arch Ital Biol* **152,** 147–155 (2014).

34. Lemieux, M., Chen, J.-Y., Lonjers, P., Bazhenov, M. & Timofeev, I. The impact of cortical deafferentation on the neocortical slow oscillation. *J. Neurosci.* **34,** 5689–5703 (2014).

35. Huber, R., Ghilardi, M. F., Massimini, M. & Tononi, G. Local sleep and learning. *Nature* **430,** 78–81 (2004).

36. Funk, C. M., Honjoh, S., Rodriguez, A. V., Cirelli, C. & Tononi, G. Local Slow Waves in Superficial Layers of Primary Cortical Areas during REM Sleep. *Curr. Biol.* **26,** 396–403 (2016).

37. Siclari, F. & Tononi, G. Local aspects of sleep and wakefulness. *Curr. Opin. Neurobiol.* **44,** 222–227 (2017).

38. Halassa, M. M., Fellin, T., Takano, H., Dong, J.-H. & Haydon, P. G. Synaptic islands defined by the territory of a single astrocyte. *J. Neurosci.* **27,** 6473–6477 (2007).

39. Allen, N. J. & Barres, B. A. Signaling between glia and neurons: focus on synaptic plasticity. *Curr. Opin. Neurobiol.* **15,** 542–548 (2005).

40. Bushong, E. A., Martone, M. E., Jones, Y. Z. & Ellisman, M. H. Protoplasmic astrocytes in CA1 stratum radiatum occupy separate anatomical domains. *J. Neurosci.* **22,** 183–192 (2002).

41. Bazargani, N. & Attwell, D. Astrocyte calcium signaling: the third wave. *Nat. Neurosci.* **19,** 182–189 (2016).

42. Bellesi, M., de Vivo, L., Tononi, G. & Cirelli, C. Effects of sleep and wake on astrocytes:

clues from molecular and ultrastructural studies. *BMC Biol.* **13,** 66 (2015).

43. Szabó, Z. *et al.* Extensive astrocyte synchronization advances neuronal coupling in slow wave activity in vivo. *Sci. Rep.* **7,** 6018 (2017).

44. Poskanzer, K. E. & Yuste, R. Astrocytes regulate cortical state switching in vivo. *Proc. Natl. Acad. Sci. USA* **113,** E2675-84 (2016).

45. Durkee, C. A. *et al.* Gi/o protein-coupled receptors inhibit neurons but activate astrocytes and stimulate gliotransmission. *Glia* **67,** 1076–1093 (2019).

46. Poskanzer, K. E. & Yuste, R. Astrocytic regulation of cortical UP states. *Proc. Natl. Acad. Sci. USA* **108,** 18453–18458 (2011).

47. Ding, F. *et al.* Changes in the composition of brain interstitial ions control the sleep-wake cycle. *Science* **352,** 550–555 (2016).

48. Halassa, M. M. *et al.* Astrocytic modulation of sleep homeostasis and cognitive consequences of sleep loss. *Neuron* **61,** 213–219 (2009).

49. Papouin, T., Dunphy, J. M., Tolman, M., Dineley, K. T. & Haydon, P. G. Septal Cholinergic Neuromodulation Tunes the Astrocyte-Dependent Gating of Hippocampal NMDA Receptors to Wakefulness. *Neuron* **94,** 840–854.e7 (2017).

50. Fellin, T. *et al.* Endogenous nonneuronal modulators of synaptic transmission control cortical slow oscillations in vivo. *Proc. Natl. Acad. Sci. USA* **106,** 15037–15042 (2009).

51. Petit, J. M. & Magistretti, P. J. Regulation of neuron-astrocyte metabolic coupling across the sleep-wake cycle. *Neuroscience* **323,** 135–156 (2016).

52. Bellesi, M., de Vivo, L., Koebe, S., Tononi, G. & Cirelli, C. Sleep and wake affect glycogen content and turnover at perisynaptic astrocytic processes. *Front. Cell Neurosci.* **12,** 308 (2018).

53. DiNuzzo, M. & Nedergaard, M. Brain energetics during the sleep-wake cycle. *Curr. Opin. Neurobiol.* **47,** 65–72 (2017).

54. Wang, Y. *et al.* Accurate quantification of astrocyte and neurotransmitter fluorescence dynamics for single-cell and population-level physiology. *Nat. Neurosci.* **22,** 1936–1944 (2019).

55. Khakh, B. S. & McCarthy, K. D. Astrocyte calcium signaling: from observations to functions and the challenges therein. *Cold Spring Harb. Perspect. Biol.* **7,** a020404 (2015).

56. Shigetomi, E. *et al.* Imaging calcium microdomains within entire astrocyte territories and endfeet with GCaMPs expressed using adeno-associated viruses. *J. Gen. Physiol.* **141,** 633–647 (2013).

57. Shigetomi, E., Patel, S. & Khakh, B. S. Probing the complexities of astrocyte calcium signaling. *Trends Cell Biol.* **26,** 300–312 (2016).

58. Guerra-Gomes, S., Sousa, N., Pinto, L. & Oliveira, J. F. Functional roles of astrocyte calcium elevations: from synapses to behavior. *Front. Cell Neurosci.* **11,** 427 (2017).

59. Stobart, J. L. *et al.* Cortical circuit activity evokes rapid astrocyte calcium signals on a similar timescale to neurons. *Neuron* **98,** 726–735.e4 (2018).

60. Lind, B. L., Brazhe, A. R., Jessen, S. B., Tan, F. C. C. & Lauritzen, M. J. Rapid stimulus-evoked astrocyte Ca2+ elevations and hemodynamic responses in mouse somatosensory cortex in vivo. *Proc. Natl. Acad. Sci. USA* **110,** E4678-87 (2013).

61. Di Castro, M. A. *et al.* Local Ca2+ detection and modulation of synaptic release by astrocytes. *Nat. Neurosci.* **14,** 1276–1284 (2011).

62. Agulhon, C. *et al.* What is the role of astrocyte calcium in neurophysiology? *Neuron* **59,** 932–946 (2008).

63. Kofuji, P. & Araque, A. G-Protein-Coupled Receptors in Astrocyte-Neuron Communication. *Neuroscience* (2020). doi:10.1016/j.neuroscience.2020.03.025

64. Grundmann, M. & Kostenis, E. Temporal Bias: Time-Encoded Dynamic GPCR Signaling. *Trends Pharmacol. Sci.* **38,** 1110–1124 (2017).

65. Kholodenko, B. N., Hancock, J. F. & Kolch, W. Signalling ballet in space and time. *Nat. Rev. Mol. Cell Biol.* **11,** 414–426 (2010).

66. Bojarskaite, L. *et al.* Astrocytic Ca2+ signaling is reduced during sleep and is involved in the regulation of slow wave sleep. *Nat. Commun.* **11,** 3240 (2020).

67. Mariotti, L., Losi, G., Sessolo, M., Marcon, I. & Carmignoto, G. The inhibitory neurotransmitter GABA evokes long-lasting Ca(2+) oscillations in cortical astrocytes. *Glia* **64,** 363–373 (2016).

68. Nagai, J. *et al.* Hyperactivity with Disrupted Attention by Activation of an Astrocyte Synaptogenic Cue. *Cell* **177,** 1280–1292.e20 (2019).

69. Seibt, J. *et al.* Cortical dendritic activity correlates with spindle-rich oscillations during sleep in rodents. *Nat. Commun.* **8,** 684 (2017).

70. Paukert, M. *et al.* Norepinephrine controls astroglial responsiveness to local circuit activity. *Neuron* **82,** 1263–1270 (2014).

71. Nimmerjahn, A., Mukamel, E. A. & Schnitzer, M. J. Motor behavior activates Bergmann glial networks. *Neuron* **62,** 400–412 (2009).

72. Zhang, Y. *et al.* An RNA-sequencing transcriptome and splicing database of glia, neurons, and vascular cells of the cerebral cortex. *J. Neurosci.* **34,** 11929–11947 (2014).

73. Beck, A., Nieden, R. Z., Schneider, H.-P. & Deitmer, J. W. Calcium release from intracellular stores in rodent astrocytes and neurons in situ. *Cell Calcium* **35,** 47–58 (2004).

74. Petravicz, J., Fiacco, T. A. & McCarthy, K. D. Loss of IP3 receptor-dependent Ca2+ increases in hippocampal astrocytes does not affect baseline CA1 pyramidal neuron synaptic activity. *J. Neurosci.* **28,** 4967–4973 (2008).

75. Srinivasan, R. *et al.* Ca(2+) signaling in astrocytes from Ip3r2(-/-) mice in brain slices and during startle responses in vivo. *Nat. Neurosci.* **18,** 708–717 (2015).

76. Ding, F. *et al.* α1-Adrenergic receptors mediate coordinated Ca2+ signaling of cortical astrocytes in awake, behaving mice. *Cell Calcium* **54,** 387–394 (2013).

77. Khan, Z. U., Koulen, P., Rubinstein, M., Grandy, D. K. & Goldman-Rakic, P. S. An astroglia-linked dopamine D2-receptor action in prefrontal cortex. *Proc. Natl. Acad. Sci. USA* **98,** 1964–1969 (2001).

78. Takata, N. *et al.* Astrocyte calcium signaling transforms cholinergic modulation to cortical plasticity in vivo. *J. Neurosci.* **31,** 18155–18165 (2011).

79. Shelton, M. K. & McCarthy, K. D. Hippocampal astrocytes exhibit Ca2+-elevating muscarinic cholinergic and histaminergic receptors in situ. *J. Neurochem.* **74,** 555–563 (2000).

80. Roth, B. L. DREADDs for neuroscientists. *Neuron* **89,** 683–694 (2016).

81. Zucca, S. *et al.* An inhibitory gate for state transition in cortex. *Elife* **6,** (2017).

82. Chai, H. *et al.* Neural Circuit-Specialized Astrocytes: Transcriptomic, Proteomic, Morphological, and Functional Evidence. *Neuron* **95,** 531–549.e9 (2017).

83. Siclari, F. *et al.* Two distinct synchronization processes in the transition to sleep: a high-density electroencephalographic study. *Sleep* **37,** 1621–1637 (2014).

84. Dang-Vu, T. T. *et al.* Spontaneous neural activity during human slow wave sleep. *Proc. Natl. Acad. Sci. USA* **105,** 15160–15165 (2008).

85. Bernardi, G., Siclari, F., Handjaras, G., Riedner, B. A. & Tononi, G. Local and widespread slow waves in stable NREM sleep: evidence for distinct regulation mechanisms. *Front. Hum. Neurosci.* **12,** 248 (2018).

86. Spoormaker, V. I. *et al.* Development of a large-scale functional brain network during human non-rapid eye movement sleep. *J. Neurosci.* **30,** 11379–11387 (2010).

87. Nir, Y. *et al.* Regional slow waves and spindles in human sleep. *Neuron* **70,** 153–169 (2011).

88. Takahashi, K., Lin, J.-S. & Sakai, K. Neuronal activity of histaminergic tuberomammillary neurons during wake-sleep states in the mouse. *J. Neurosci.* **26,** 10292–10298 (2006).

89. Eban-Rothschild, A., Rothschild, G., Giardino, W. J., Jones, J. R. & de Lecea, L. VTA dopaminergic neurons regulate ethologically relevant sleep-wake behaviors. *Nat. Neurosci.* **19,** 1356–1366 (2016).

90. Aston-Jones, G. & Bloom, F. E. Activity of norepinephrine-containing locus coeruleus neurons in behaving rats anticipates fluctuations in the sleep-waking cycle. *J. Neurosci.* **1,** 876–886 (1981).

91. Lee, M. G., Hassani, O. K., Alonso, A. & Jones, B. E. Cholinergic basal forebrain neurons burst with theta during waking and paradoxical sleep. *J. Neurosci.* **25,** 4365–4369 (2005).

92. Trulson, M. E. & Jacobs, B. L. Raphe unit activity in freely moving cats: correlation with level of behavioral arousal. *Brain Res.* **163,** 135–150 (1979).

93. Scammell, T. E., Arrigoni, E. & Lipton, J. O. Neural circuitry of wakefulness and sleep. *Neuron* **93,** 747–765 (2017).

94. MacDonald, A. J., Holmes, F. E., Beall, C., Pickering, A. E. & Ellacott, K. L. J. Regulation of food intake by astrocytes in the brainstem dorsal vagal complex. *Glia* **68,** 1241–1254

(2020).

95. Bonder, D. E. & McCarthy, K. D. Astrocytic Gq-GPCR-linked IP3R-dependent Ca2+ signaling does not mediate neurovascular coupling in mouse visual cortex in vivo. *J. Neurosci.* **34,** 13139–13150 (2014).

96. Adamsky, A. *et al.* Astrocytic activation generates de novo neuronal potentiation and memory enhancement. *Cell* **174,** 59–71.e14 (2018).

97. Sakuragi, S., Niwa, F., Oda, Y., Mikoshiba, K. & Bannai, H. Astroglial Ca2+ signaling is generated by the coordination of IP3R and store-operated Ca2+ channels. *Biochem. Biophys. Res. Commun.* **486,** 879–885 (2017).

98. Pankratov, Y. & Lalo, U. Role for astroglial α1-adrenoreceptors in gliotransmission and control of synaptic plasticity in the neocortex. *Front. Cell Neurosci.* **9,** 230 (2015).

99. Borbély, A. A., Daan, S., Wirz-Justice, A. & Deboer, T. The two-process model of sleep regulation: a reappraisal. *J Sleep Res* **25,** 131–143 (2016).

100. Daan, S., Beersma, D. G. & Borbély, A. A. Timing of human sleep: recovery process gated by a circadian pacemaker. *Am. J. Physiol.* **246,** R161-83 (1984).

101. Borbely. A Two Process Model of Sleep Regulation.

102. Brancaccio, M., Patton, A. P., Chesham, J. E., Maywood, E. S. & Hastings, M. H. Astrocytes control circadian timekeeping in the suprachiasmatic nucleus via glutamatergic signaling. *Neuron* **93,** 1420–1435.e5 (2017).

103. Ingiosi, A. M. *et al.* A role for astroglial calcium in mammalian sleep and sleep regulation. *Curr. Biol.* **30,** 4373–4383.e7 (2020).

104. Foley, J. *et al.* Astrocytic ip3/ca2+ signaling modulates theta rhythm and REM sleep. *Front. Neural Circuits* **11,** 3 (2017).

105. Marvin, J. S. *et al.* An optimized fluorescent probe for visualizing glutamate neurotransmission. *Nat. Methods* **10,** 162–170 (2013).

106. Lobas, M. A. *et al.* A genetically encoded single-wavelength sensor for imaging cytosolic and cell surface ATP. *Nat. Commun.* **10,** 711 (2019).

107. Kitajima, N. *et al.* Real-time in vivo imaging of extracellular ATP in the brain with a hybrid-type fluorescent sensor. *Elife* **9,** (2020).

108. Wu, Z. *et al.* A GRAB sensor reveals activity-dependent non-vesicular somatodendritic adenosine release. *BioRxiv* (2020). doi:10.1101/2020.05.04.075564

109. Suzuki, A., Sinton, C. M., Greene, R. W. & Yanagisawa, M. Behavioral and biochemical dissociation of arousal and homeostatic sleep need influenced by prior wakeful experience in mice. *Proc. Natl. Acad. Sci. USA* **110,** 10288–10293 (2013).

110. Funato, H. *et al.* Forward-genetics analysis of sleep in randomly mutagenized mice. *Nature* **539,** 378–383 (2016).

111. Mikhail, C., Vaucher, A., Jimenez, S. & Tafti, M. ERK signaling pathway regulates sleep duration through activity-induced gene expression during wakefulness. *Sci. Signal.* **10,** (2017).

112. Ulv Larsen, S. M. *et al.* Haplotype of the astrocytic water channel AQP4 is associated with slow wave energy regulation in human NREM sleep. *PLoS Biol.* **18,** e3000623 (2020).

113. Frank, M. G. Astroglial regulation of sleep homeostasis. *Curr. Opin. Neurobiol.* **23,** 812–818 (2013).

114. Clasadonte, J., Scemes, E., Wang, Z., Boison, D. & Haydon, P. G. Connexin 43-Mediated Astroglial Metabolic Networks Contribute to the Regulation of the Sleep-Wake Cycle. *Neuron* **95,** 1365–1380.e5 (2017).

115. Murphy-Royal, C. *et al.* Stress gates an astrocytic energy reservoir to impair synaptic plasticity. *Nat. Commun.* **11,** 2014 (2020).

116. Steriade, M. Grouping of brain rhythms in corticothalamic systems. *Neuroscience* **137,** 1087–1106 (2006).

117. Crunelli, V. *et al.* Dual function of thalamic low-vigilance state oscillations: rhythm-regulation and plasticity. *Nat. Rev. Neurosci.* **19,** 107–118 (2018).

118. Kol, A. *et al.* Astrocytes Contribute to Remote Memory Formation by Modulating Hippocampal-Cortical Communication During Learning. *BioRxiv* (2019). doi:10.1101/682344

119. Sardinha, V. M. *et al.* Astrocytic signaling supports hippocampal-prefrontal theta synchronization and cognitive function. *Glia* **65,** 1944–1960 (2017).

120. Siuda, E. R. *et al.* Spatiotemporal control of opioid signaling and behavior. *Neuron* **86,** 923–935 (2015).

121. Goldey, G. J. *et al.* Removable cranial windows for long-term imaging in awake mice. *Nat. Protoc.* **9,** 2515–2538 (2014).

122. Dubbs, A., Guevara, J. & Yuste, R. moco: Fast Motion Correction for Calcium Imaging. *Front Neuroinformatics* **10,** 6 (2016).

123. Riedner, B. A. *et al.* Sleep homeostasis and cortical synchronization: III. A high-density EEG study of sleep slow waves in humans. *Sleep* **30,** 1643–1657 (2007).

124. Steriade, M., Amzica, F. & Contreras, D. Synchronization of fast (30-40 Hz) spontaneous cortical rhythms during brain activation. *J. Neurosci.* **16,** 392–417 (1996).

125. Valderrama, M. *et al.* Human gamma oscillations during slow wave sleep. *PLoS One* **7,** e33477 (2012).

126. Wolansky, T., Clement, E. A., Peters, S. R., Palczak, M. A. & Dickson, C. T. Hippocampal slow oscillation: a novel EEG state and its coordination with ongoing neocortical activity. *J. Neurosci.* **26,** 6213–6229 (2006).

127. Mena-Segovia, J., Sims, H. M., Magill, P. J. & Bolam, J. P. Cholinergic brainstem neurons modulate cortical gamma activity during slow oscillations. *J. Physiol. (Lond.)* **586,** 2947–2960 (2008).

128. Arganda-Carreras, I. *et al.* Trainable Weka Segmentation: a machine learning tool for microscopy pixel classification. *Bioinformatics* **33,** 2424–2426 (2017).

Chapter 4:

Astrocytic regulation of sleep via cortical histaminergic signaling

Abstract

The regulation of sleep and wake is critical for the health and survival of all animals. However, how sleep is regulated in the brain is not fully understood. Cortical astrocytes have been shown to actively regulate different features of sleep through GPCR signaling but the endogenous ligands that mediate this control is unknown. Neuromodulators, and specifically the neuromodulator histamine, play a critical role in the regulation of sleep-wake transitions. Whether astrocytes sense histamine signals in the cortex across sleep and wake has not been previously explored. Here, we use optical and electrophysiology techniques to demonstrate that histaminergic axons in the cortex exhibit sleep-wake dynamics and that cortical astrocytes exhibit physiological responses to histamine in the form of calcium (Ca^{2+}) increases via the histamine 1 receptor (H_1R). Together, this data support a model in which histamine serves as an endogenous ligand for astrocytic regulation of sleep.

Introduction

Across the animal kingdom, all species regularly transition between sleep and wake[1]. The importance of these transitions to our health is exemplified in sleep disorders such as insomnia and narcolepsy, with symptoms ranging from cognitive decline to immune dysfunction. Sleep disorders are also commonly co-morbid with other neurological diseases and may underlie many

disease symptoms. A precise understanding of how the brain transitions between sleep and wake is a crucial, yet missing, step towards successful treatment for these disorders.

The sleep-wake transition occurs quickly but is quite dramatic physiologically. In mammals, sleep is characterized by lack of locomotion, and is composed of two main brain-wide activity states: slow synchronous activity (non-rapid eye-movement [NREM] sleep) and rapid desynchronized activity (rapid eye-movement [REM] sleep). Wake is dominated by desynchronized activity in the brain, and locomotion. How transitions occur between such distinct brain states is not yet understood.

Recently, it has been demonstrated that astrocytes – the largest class of non-neuronal cells in the brain – play an active role in sleep regulation[2–4] (Chapter 3). Cortical astrocytes are well positioned to regulate sleep by influencing large groups of neurons at broad spatiotemporal scales. Astrocytes tile the cortex, can participate in bidirectional communication with thousands of neurons[5–8], exhibit morphological and transcriptional changes during sleep[9], and regulate SWA under anesthesia[10–12]. Specifically, it has been shown that astrocytes regulate distinct features of NREM sleep via Ca2+ (sleep depth and sleep duration), through different GPCR pathways[2] (Chapter 3). Both astrocytic Gi- and Gq-coupled GPCRs are implicated in astrocytic control of sleep, but it remains unknown what endogenous ligands mediate these effects in astrocytes.

Previous work has demonstrated the importance of neuromodulators in the regulation of sleep-wake transitions[13–15]. Specifically, it has been proposed that the mechanism of sleep-wake transitions relies on reciprocal inhibition between neuromodulator wake-promoting nuclei, such as norepinephrine, histamine, serotonin, dopamine, and acetylcholine, and sleep-promoting nuclei[16]. Critically, astrocytes express GPCRs and exhibit increased Ca^{2+} in response to many of

these neuromodulators[17–20]. These wake- and sleep-promoting nuclei are found in the brainstem and many groups have worked to dissect the circuitry between these structures[14,15,21,22]. However, sleep and wake are defined by patterns of activity measured in the cortex. How these neuromodulators ultimately drive cortical activity during sleep-wake transitions is unknown.

Histaminergic neurons in the tuberomamillary nucleus (TMN) have long been known to promote and sustain wakefulness[23–27] but have been relatively understudied compared to other neuromodulators. TMN neurons are active during wake and silent during sleep[24], regulated in a circadian fashion[28], and can bidirectionally drive arousal[23,29]. TMN neurons send projections throughout the brain, including direct projections to the cerebral cortex[30]. However, the role of these cortical projections in sleep-wake transitions is unknown. The wake-promoting effects of histamine have been shown to be specifically dependent on the histamine receptor H_1 (H_1R), a Gq-coupled G-protein coupled receptor (GPCR)[23]. Interestingly, bulk RNA sequencing data reveal cortical H_1Rs are expressed not only on neurons, but also on astrocytes[31], suggesting that astrocytes may be important in mediating the effects of histamine on sleep and wake. However, most studies on sleep and wake have focused exclusively on neurons.

Here, we focus on the role of histamine in the cortex in the regulation of sleep-wake and use optical and electrophysiological techniques to test astrocytic integration into the histaminergic signaling circuit. We present preliminary data demonstrating that TMN axon terminals in the cortex exhibit dynamics relevant to natural sleep-wake transitions. Further, we present preliminary data suggesting that astrocytes are involved in sensing histaminergic signals originating in the brainstem, and thus are potential cortical targets for orchestrating the necessary circuit-level changes that occur between sleep and wake. These preliminary data include demonstration of astrocytic expression of histamine receptors, physiological responses of

astrocytes to histamine, and *in vivo* astrocyte-histamine dynamics. Together, this data positions cortical histamine as a likely endogenous signal used by astrocytes to control on sleep-wake.

Results

In vivo *imaging of histaminergic cortical terminals across sleep and wake*

To study the role of cortical histamine signaling in sleep and wake, we conducted two-photon (2P) imaging of TMN axon terminals in the primary visual (V1) cortex as mice naturally transitioned between sleep and wake states[2,32,33]. To specifically express the Ca^{2+} indicator GCaMP6f in cortical histamine terminals, we injected *AAV-hSyn-FLEX-axon-GCaMP*[34] into the TMN of HDC-IRES-Cre mice[21] 4-6 weeks before experiments (**Fig. 4.1b**, left). Electrodes were implanted for local field potential (LFP) and electromyogram (EMG) recordings (**Fig. 4.1a**) to assess sleep state. During recording sessions, mice were head-fixed on a horizontal treadmill, and locomotion was recorded (**Fig. 4.1a**). To control for the effect of circadian rhythm and sleep pressure, all recording sessions took place between ZT 2–5. Experiments were conducted after mice had been previously habituated to head-fixation to allow natural sleep. To analyze axon dynamics, we used the MATLAB-based toolbox Suite2p[35] to automatically detect axon segments (**Fig. 4.1b**, left bottom). This allowed us to extract Ca^{2+} signals from individual axon ROIs across sleep and wake (**Fig. 4.1b**, right).

Histaminergic cortical terminals are wake-active

While the cell bodies of histamine neurons in the TMN are well known to be wake-active and change their firing rate at sleep onset and offset[24], their axon dynamics in the cortex – several millimeters away from the cell bodies – have not been characterized over sleep and wake.

We imaged the activity of histaminergic cortical axons and find that, as expected, their activity is also correlated with wake (**Fig. 4.1**). Specifically, we found an inverse relationship between axon activity and delta power (0.5-4Hz), which is the frequency range used to distinguish sleep (high delta power) and wake (low delta power) (**Fig. 4.1c**). To examine this in distinct behavioral states, we quantified the mean fluorescence of each axon ROI across sleep versus wake periods and found, as expected, that fluorescence was significantly higher during wake (**Fig. 4.1d**).

Next, we wanted to examine how histamine axon dynamics change around sleep-wake transitions. Data from single-unit cell body recordings in the TMN have demonstrated that histamine neurons cease firing during wake, before the onset of sleep[24]. We similarly find that cortical axon activity began decreasing before the onset of sleep (**Fig. 4.1e**, left). Additionally, histamine cell bodies in the TMN increase their activity following sleep offset with a latency[24]. We too observed an increase in axon activity following sleep offset (**Fig. 4.1e**, right). While the change in axon dynamics we observed around transitions was slower than reported in the previous study[24], this may be expected given the slower dynamics of GCaMP compared with electrophysiology recordings.

Astrocytes exhibit physiological responses to histamine via H_1Rs

In order to examine the role of astrocytes in histaminergic signaling, we first examined the expression of histamine receptors in cortical astrocytes. We focused on the H_1R as that is the receptor that is associated with histamine's influence on sleep and wake[23]. Using fluorescence *in situ* hybridization (FISH), we mapped cell-type specific H_1R expression across cortical layers with single-cell resolution (**Fig. 4.2**). Preliminary FISH data suggests astrocytes and neurons express similar levels of H_1Rs, which is supported by previous bulk tissue RNA sequencing

databases[31,36]. The data also suggests that many astrocytes across all cortical layers express H_1R (**Fig. 4.2a**, right), which may be expected given that histaminergic axons terminate in all layers of sensory cortex[30].

To test the hypothesis that cortical astrocytes are directly activated by histamine via H_1Rs, we performed 2P-imaging of GCaMP-expressing astrocytes in adult *ex vivo* cortical slices (**Fig. 4.2b**). Because neurons have been shown to also respond to histamine[37,38], we used TTX (1uM) to block neuron-to-astrocyte communication via action potential firing. We found astrocytes exhibited a robust Ca^{2+} response to bath application of histamine at multiple doses, and as low as 5uM (**Fig. 4.2c**). This result is supported by previous studies showing astrocytes exhibit Ca^{2+} increases in response to histamine in other brain regions[20,39]. To investigate what receptors are responsible for the Ca^{2+} increase, we added specific histamine receptor antagonists to the bath prior to bath application of histamine. We found that the H_1R-specific antagonist chlorpheniramine (20uM) blocked the astrocytic response to histamine (**Fig. 4.2d**, purple), but not the H_2R-specific antagonist cimetidine (25uM) (**Fig. 4.2d**, blue), demonstrating that astrocytes sense histamine specifically through the H_1R, further suggesting that astrocytes are part of the histaminergic regulation of sleep-wake.

Histamine signaling precedes astrocyte activity in vivo

Given that astrocytes exhibited Ca^{2+} responses to histamine *ex vivo*, we next investigated the relationship between astrocyte activity and histaminergic terminals *in vivo*. We injected *AAV-hSyn-FLEX-axon-GCaMP*[34] into the TMN and *AAV-GFAP-jRGECO* into V1 of HDC-IRES-Cre mice[21] and performed dual-color 2P imaging of histaminergic axon terminals and astrocyte Ca^{2+} activity in V1 (**Fig. 4.3a-b**). To analyze astrocyte Ca^{2+} activity, we used the astrocyte analysis

tool AQuA[40] (Chapter 1), an event-based approach to detect spatiotemporally distinct Ca^{2+} events without predetermined ROIs. This allowed automatic detection of individual astrocyte Ca^{2+} events, independent of size and shape.

We predicted that if astrocytes respond to histaminergic signals with Ca^{2+} increases, we should see histamine axon activity preceding astrocyte Ca^{2+} dynamics *in vivo.* Indeed, with preliminary data, when we examined spontaneous dynamics we observed that histamine axon activity consistently preceded astrocyte Ca^{2+} increases (**Fig. 4.3c**). To quantify the temporal relationship between astrocytes and histaminergic axons, we calculated an event-triggered average of both astrocyte and axon fluorescence around astrocyte Ca^{2+} events (**Fig. 4.3d**) and observed that histamine axon activity precedes astrocyte Ca^{2+} by ~6s (**Fig. 4.3e**). These data suggest that histamine released from the TMN can activate H_1Rs on astrocytes in the cortex.

Discussion

Using various optical techniques and electrophysiology across sleep and wake, we examined the role of cortical histamine in astrocytic regulation of sleep and wake. We present preliminary data demonstrating that histaminergic TMN axon terminals in the cortex exhibit sleep-wake dynamics and both *ex vivo* and *in vivo* evidence that cortical astrocytes are well-positioned to sense and respond to histaminergic signals via the critical sleep histamine receptor H_1R. Together, this data positions histamine as a strong candidate ligand used by astrocytes to control sleep-wake.

Histaminergic signaling in the cortex

Histamine has been identified as a key sleep-wake signal[13,15,23–27,29], but our understanding of histaminergic signaling in the brain has largely focused on histaminergic cell

bodies and circuits within the brainstem[21,24]. Histaminergic neurons send projections throughout the brain, including to the cortex – where we define sleep and wake. Here, we explored the specific cortical projections of histamine TMN neurons. We found that, as expected from the characterization of TMN cell bodies, cortical histamine terminals were wake-active (**Fig. 4.1c-d**) and exhibited bidirectional changes in activity around sleep-wake transitions (**Fig. 4.1e**), similar to what has been reported previously in the TMN[24].

The wake-promoting effects of histamine are dependent specifically on the H_1R, but not the H_2R[23,25,26]. The H_1R is a Gq-coupled GPCR, and interestingly it has been shown that manipulating Gq-GPCR signaling in cortical astrocytes can bidirectionally alter sleep duration, but has no effect on sleep depth[2] (Chapter 3). The data here suggest that astrocytic sensing of histamine would specifically result in the regulation of sleep duration, but not sleep depth. In fact, histamine has mostly been linked to the regulation of sleep-wake transitions, which would directly influence sleep duration. However, there is also evidence that histaminergic neuronal activity varies with vigilance state, with higher firing rates observed during active wake compared with quiet wake[24]. We know that the low-frequency band used to measure sleep depth (0.5-4Hz) is also higher during quiet wake than active wake. It is possible that histamine could be used to regulate the level of synchrony observed in this low-frequency range during wake as well, but unlikely that this would involve astrocytes. Astrocytes have been shown to control synchrony in this frequency range previously under anesthesia[10–12], but astrocytic control of synchrony in non-anesthetized animals was demonstrated to be specific to the sleep state, and dependent on Gi-GPCRs[2] (Chapter 3).

It is thought that histamine diffuses through the brain through volume transmission from histaminergic axons, as opposed to released specifically at synapses[29]. This raises an interesting

question regarding the spatial relationship between astrocytes and histamine signaling. Astrocytes extend processes throughout the extracellular space and are thus well-positioned to receive volumetric transmission of signals. Here, we found that histamine axon activity consistently preceded astrocyte activity (**Fig. 4.3c-e**). However, we did not demonstrate causality. The use of optogenetics to selectively activate histamine terminals in the cortex could validate the *ex vivo* evidence presented here (**Fig. 4.2**) and confirm the observed *in vivo* relationship. Further, a loss-of-function experiment conditionally knocking out H_1Rs on astrocytes while administering an anti-histamine would be integral to confirming the role of astrocytic signaling in histamine's role in sleep-wake.

Recent work has emphasized the existence of local sleep[41,42], in which regions of the cortex are in sleep-like states, while other regions are in wake-like states. However, it remains unknown how neuromodulatory axons in the cortex, which have single origins in the brainstem, are differently regulated across the cortex. Further, it's unclear to what spatial extent histamine may diffuse through the extracellular space and activate distal astrocytic receptors. Further analysis of data presented here (**Fig. 4.3**) with respect to the spatial proximity between correlated astrocyte and histamine ROIs could reveal this relationship. It has been previously shown that astrocytes can exert differential influence on NREM slow-wave activity depending on their localization within the cortex (Chapter 3). Heterogeneous histaminergic activation within the cortex may be a mechanism by which astrocytes regulate local and global sleep features.

The role of the cortex in sleep regulation

Sleep and wake are defined by patterns of neural activity recorded in the cortex, but the role of cortex in actively regulating sleep-wake has not been fully understood. There is evidence

that the cortex can generate sleep-related oscillations[41,43–48] but the exact mechanisms are unknown. Neuromodulatory nuclei in the brainstem have been shown to be sufficient to alter sleep-wake as measured in the cortex[24,49–52], but it remains unclear how these signals ultimately alter cortical activity. Here we demonstrate that histaminergic signals in the cortex exhibit dynamics relevant to sleep-wake changes in the cortex, and that astrocytes are well-positioned to sense these signals to regulate sleep. Whether histaminergic signaling in the cortex alone is sufficient to alter sleep-wake remains unknown but addressing this question with local pharmacology will be very informative. Further, exploring the function of histamine projections in other brain regions, such as the thalamus, is important in understanding the exact mechanism of cortical changes in sleep-wake.

While we have explored the role of astrocytes in histaminergic signaling in the cortex, it is important to also examine neuronal responses to histamine. Interestingly, the existing data regarding this question is somewhat contradictory, with some studies finding depressing effects of histamine via H_1R in the cortex[38], and others finding that histamine depolarizes cortical neurons via H_1R[37,53]. Further, it is still unknown how histamine might differently alter neuronal subtypes, such as different interneurons. Understanding the cell-type specific responses to histamine in the cortex will be instrumental in dissecting the mechanisms of cortical control on sleep-wake.

In this study, we focused on the neuromodulator histamine. The primary function associated with histamine is the regulation of sleep and manipulation of histamine in the brain pharmacologically has strong, robust effects on sleep. However, many other neuromodulators have also been linked with sleep and are released in the cortex, such as norepinephrine[50], dopamine[49], acetylcholine[51], and serotonin[52]. In order to better understand the mechanisms of

cortical control on sleep, it is critical to characterize the effect of these other sleep-wake signals in cortical circuits. Axon imaging as presented here (**Fig. 4.1, 4.3**) provides an opportunity to characterize the dynamics of these neuromodulators in the cortex across sleep-wake as well as the spatial extent of the signals in relation to other cell-types. While it can be difficult to isolate cortical release with optogenetic stimulation, local pharmacology using implanted cannulas in the cortex is another method by which cortex-specific effects of neuromodulators can be studied.

Lastly, while we were imaging TMN axon terminals, we focused on the action of histamine on cortical astrocytes. However, it's known that TMN histaminergic neurons also corelease the inhibitory neurotransmitter GABA[29], and that GABA plays a role in the regulation of sleep-wake as well[29,54–56]. Astrocytes also respond to GABA with Ca^{2+} increases[57,58], and further work is necessary to understand how astrocytes may be integrating these two signals during TMN neuron activity.

Astrocytic outputs following histamine activation

In this study, we suggest that cortical astrocytes are part of the histaminergic circuit that regulates sleep. Astrocytes have been shown to actively regulate sleep, but it is unknown what astrocytic functional outputs may be responsible for their influence on sleep. In fact, many astrocytic functions associated with sleep may be important, such as extracellular ion dynamics[59] or adenosine release[60].

One astrocytic function in particular, the regulation of extracellular glutamate, is an exciting candidate. Glutamate has been implicated in the generation of cortical UP states[11,53,61], a hallmark of sleep slow waves. Critically, it has been shown previously that histamine exposure up-regulates GLT-1, one of the primary glutamate transporters expressed by astrocytes, and

decreases extracellular glutamate concentrations[62]. Whether histamine alters astrocytic regulation of extracellular glutamate *in vivo*, or whether this could occur on the timescale relevant for the regulation of sleep, is unknown. Optical sensors that allow for the visualization of extracellular glutamate[63] in combination with histaminergic manipulations or histamine axon imaging could be useful in linking histaminergic signaling with this astrocytic output.

Methods

Animals

All procedures were carried out using adult mice (C57Bl/6, P50–100) in accordance with protocols approved by the University of California, San Francisco Institutional Animal Care and Use Committee (IACUC). All animals were housed in a 12:12 light-dark cycle with food and water provided *ad libitum*. Male and female mice were used. Following surgery, all animals were singly housed, to protect electrodes, with additional enrichment.

Surgical procedures

Adult mice (C57Bl/6, P50–100, HDC-IRES-Cre) underwent two surgeries. In the first surgery, mice were anesthetized with isoflurane. First, one 800nL injection of *AAV-Flex-Axon-GCaMP6f* was made in the TMN (from bregma, -2.6mm posterior, 0.95mm lateral, 5.5mm below pia). Second, using the same drilled hole as was used for the TMN injection, one 300nL injection of *AAV-GFAP-jRGECO* was made in the cortex at 0.3mm below pia surface. All injections done at 30–60nL/min and were followed by a 10- min wait for diffusion. Post-operative care included administration of 0.05mg/kg buprenorphine and 5mg/kg carpofen.

Four weeks following the first surgery, mice underwent a second surgery. Mice were administered dexamethasone (5mg/kg, s.c.) prior to surgery and anesthetized with isoflurane. A 3mm diameter craniotomy was created over visual cortex and a glass cranial window for chronic imaging was implanted and secured using C&B metabond[64]. A titanium wire was inserted in V1 lateral to the craniotomy, and a bone screw was inserted in contralateral V1 for reference (all measurements from bregma, -3.5mm, 1.2mm lateral). Post-operative care included administration of 0.05mg/kg buprenorphine and 5mg/kg carpofen. Mice were allowed ten days to recover, then were habituated to head-fixation on a circular treadmill for five days, prior to imaging.

In vivo *two-photon imaging and electrophysiology*

2P imaging experiments were carried out on a microscope (Bruker Ultima IV) equipped with a Ti:Sa laser (MaiTai, SpectraPhysics). The laser beam was intensity-modulated using a Pockels cell (Conoptics) and scanned with linear galvonometers. Images were acquired with a 16x, 0.8 N.A. Nikon objective via a photomultiplier tube (Hamamatsu) using PrairieView (Bruker) software. For GCaMP imaging, 950nm excitation and a 515/30 emission filter was used. For jRGECO imaging, 1040nm excitation and a 605/15 emission filter was used. All recordings started at ZT 2. Mice were head-fixed to a circular treadmill and Ca^{2+} activity was recorded an effective frame rate between 0.5-2Hz from layer 2/3 of visual cortex with a 512×512 pixel resolution at ~0.5-1μm/pixel. Locomotion speed was monitored using an optoswitch (Newark Element 14) connected to an Arduino. For LFP, differential recordings were acquired using the contralateral bone screw as a reference. For EMG, differential recordings were acquired using the two wires implanted in the nuchal muscles. All recordings were amplified

(Warner) with a gain of 1K, high-pass filtered at 0.1Hz, and low-pass filtered at 10KHz. Electrophysiology and locomotion recordings were acquired simultaneously with 2P imaging at 1KHz using PrairieView (Bruker) software.

Image analysis

Axon Ca^{2+} image analysis was performed using the MATLAB toolbox Suite2p[35]. A classifier was trained on each video by manually selecting ROIs that contained axon segments. All axon ROIs were then automatically selected by using the trained classifier. Selected ROIs were isolated and fluorescence traces over time were extracted. Fluorescence traces were normalized using the formula dfof = (f-x)/x where f is the raw fluorescence trace for each axon and x is the mean of the trace. Traces that contained values that exceeded 5 SD of the mean of all traces were excluded to account for artifacts in the dataset.

Astrocyte Ca^{2+} image analysis was performed using Astrocyte Quantitative Analysis (AQuA) software[54]. Videos were preprocessed by registering images using the ImageJ plugin MOCO[122]. Events were detected using AQuA (in MATLAB) using the *in-vivo-GCaMP-cyto* preset. Signal detection threshold was adjusted for each video after manually checking for accurate detection, to account for slight differences in noise. AQuA outputs were further analyzed in MATLAB. Event count was quantified using the onset of each event, as detected by AQuA. For ROI analysis, somatic traces were extracted from ROIs hand-drawn using the blow-lasso tool in Fiji. Somatic ROIs were then removed using a mask, and process ROIs were created by applying $10um^2$ tiles across the field of view.

Sleep scoring

LFP and EEG recordings were first manually inspected for movement artifacts, which were removed by excluding data exceeding 5 SD from the mean. Similarly, drifting baselines were adjusted by a high- pass filter with a cut-off frequency of 0.3Hz. All electrophysiology acquired on the same day were pooled together and z-scored. A spectrogram was then calculated using a moving window of 10s, stepping every 5s. Locomotory data were used to identify each 5s bin as *stationary* if no locomotion was detected, or *locomotory* otherwise. The absolute value of z-scored EMG recordings was used to quantify mean EMG amplitude for each 5s bin.

A bin was identified as NREM sleep if 1) the slow-wave ratio (0.5–4Hz/8–20Hz) was >0.5 SD from the mean, 2) the animal was stationary, and 3) the EMG was <5 SD from the mean. Similarly, a bin was identified as REM sleep if it had not been quantified as NREM, and 1) theta power (6–10 Hz) >0.25 SD from the mean, 2) the animal was stationary, and 3) the EMG was <0.4 SD from the mean. All remaining times were characterized as wake. Each behavioral period was identified by finding the start and end of consecutive 5s bins of the same behavioral state. For all analysis, sleep periods <10–15s were excluded.

Ex vivo *2P imaging*

For acute slice experiments, neonatal mice (C57Bl/6, P0–4) were anesthetized by crushed ice anesthesia for 3 min and injected with *AAV5-GFaABC1D.cyto-GCaMP6f* at a rate of 2–3nL/s. Six injection sites (0.5µm apart in a 2×3 grid pattern, at 0.8µm and 0.15–0µm below the pial surface) over assumed V1 were chosen. 30nL/site (360nL total) was injected with a microsyringe pump (UMP-3, World Precision Instruments). Coronal, acute V1 slices (400µm thick) from P25–P30 mice were cut with a vibratome (VT 1200, Leica) in ice-cold cutting

solution (in mM): 27 $NaHCO_3$, 1.5 NaH_2PO_4, 222 sucrose, 2.6 KCl, 2 $MgSO_4$, 2 $CaCl_2$. Slices were incubated in standard continuously aerated (95% O_2/5% CO_2) artificial cerebrospinal fluid (ACSF) containing (in mM): 123 NaCl, 26 $NaHCO_3$, 1 NaH_2PO_4, 10 dextrose, 3 KCl, 2 $CaCl_2$, 2 $MgSO_4$, heated to 37°C and removed from water bath immediately before introducing slices. Slices were held in ACSF at room temperature until imaging. Experiments were performed in continuously aerated, standard ACSF. 2P imaging was carried out as for *in vivo* imaging described above. Experiments began with a 4-min incubation in 1μM TTX. For antagonist experiments, the antagonist was added 4 minutes before histamine bath application. To record responses to histamine (50μM), a 5-min video was acquired in which histamine was added to the bath at the start.

Quantification and statistical analysis

All statistical tests used, definition of center and dispersion measurements, and exact n values can be found for each figure in the corresponding figure legend. Additional information regarding statistical tests described in the relevant sections. For all figures, significance levels defined as the following: *: $p<0.05$, **: $p<0.005$, ***: $p<0.0005$.

Figures

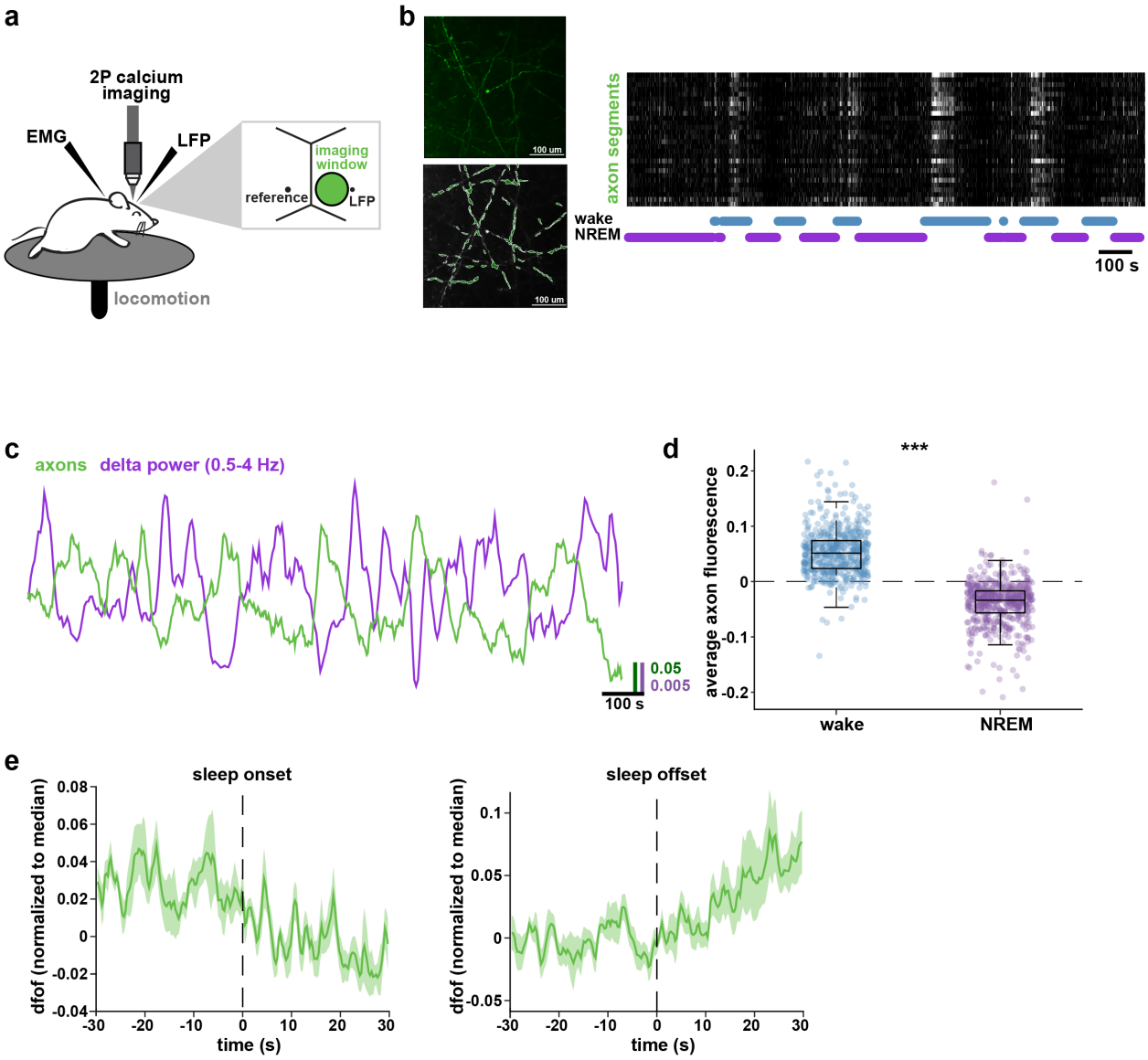

Figure 4.1: Histaminergic axon terminals in the cortex exhibit sleep-wake dynamics. **(a)** Experimental in vivo imaging and electrophysiology setup. Mice expressing axon-GCaMP6f were head-fixed on a horizontal treadmill to record axon dynamics, LFP, EMG, and locomotion over natural sleep and wake. **(b)** Left: example image of axon-GCaMP6f expression in L2/3 histaminergic axons in an awake, head-fixed mouse (top). Axon segments were automatically detected using Suite2P (bottom). Right: Example raster plot demonstrating spontaneous axon dynamics across 20 minutes of sleep-wake (bottom), each row displays dfof (grayscale) for one axon segment. **(c)** Example traces demonstrating the inverse relationship between the mean axon activity (blue) and mean delta power (orange). **(d)** Histamine axon activity was significantly higher during wake than NREM sleep (n = 3 mice, 522 axons, unpaired t-test, $p < 0.005$). **(e)** Histamine axon activity decreases prior to the onset of sleep, and increases following the offset of sleep (n = 3 mice, 522 axons, 7.5 hours, errorbars=SEM).

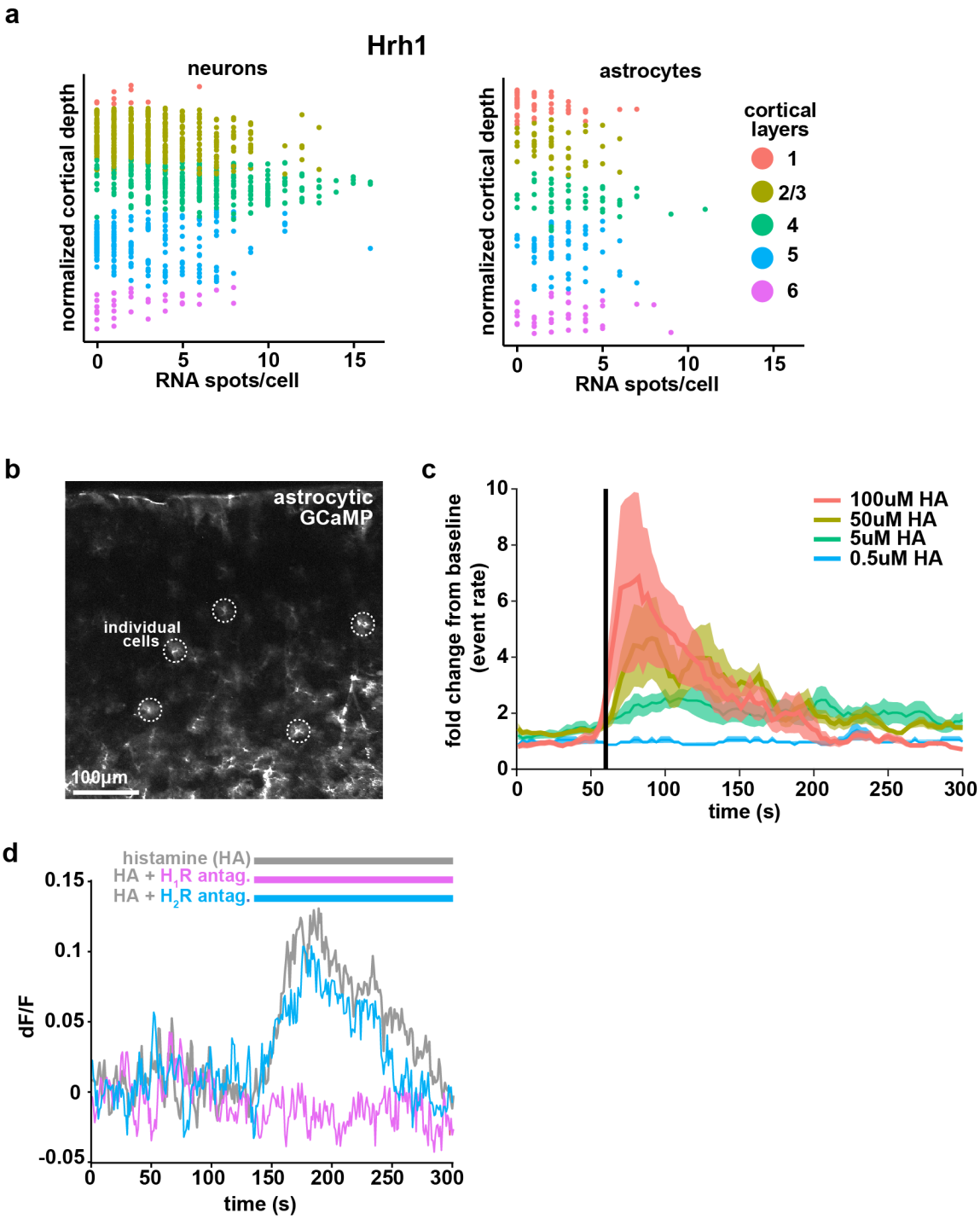

Figure 4.2: Histamine increases astrocyte Ca^{2+} via H_1Rs.
(a) H_1R FISH shows expression across cortical layers (colors) in neurons (left) and astrocytes (right) (n=1 V1 slice). **(b)** V1 cortical slice with GCaMP6-expressing astrocytes. **(c)** Histamine increase astrocyte Ca^{2+} at different doses **(d)** Histamine application directly increases astrocytic Ca^{2+} (gray trace, n=6 slices). This increase is blocked by the H_1R-specific antagonist chlorpheniramine (20uM, yellow, n=5 slices), but not the H_2R-specific antagonist cimetidine (25uM, blue, n=4 slices). 1uM TTX in all slices.

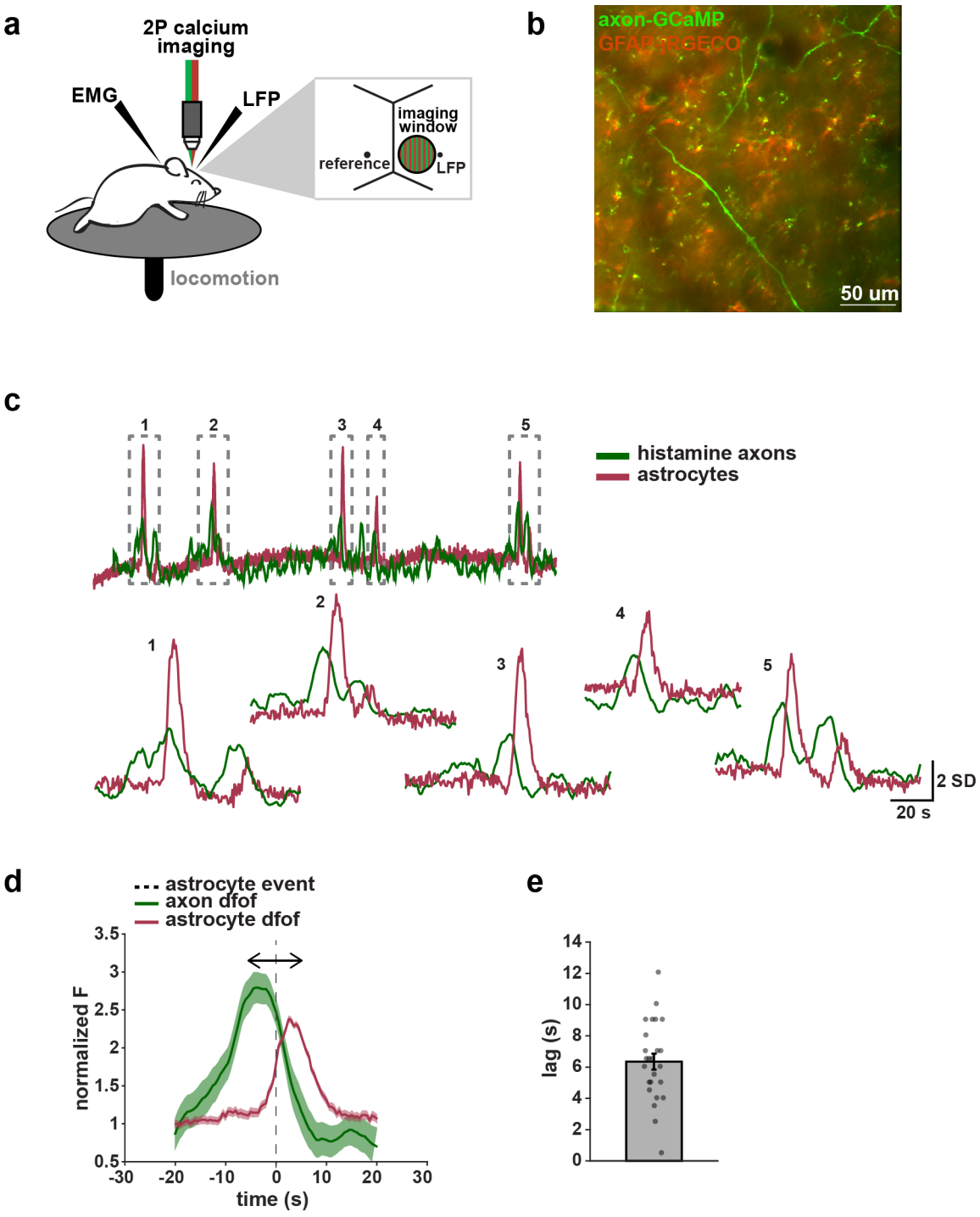

Figure 4.3: Histaminergic signaling precedes cortical astrocyte activity *in vivo*.
(a) Experimental in vivo imaging and electrophysiology setup. Mice co-expressing axon-GCaMP6f and GFAP-jRGECO were head-fixed on a horizontal treadmill to record axon dynamics, astrocyte Ca^{2+}, LFP, EMG, and locomotion over natural sleep and wake. **(b)** Expression of axon-GCaMP in TMN axons and jRGECO in astrocytes L2/3 cortex *in vivo* **(c)** Example traces showing astrocyte Ca^{2+} (red) preceded by axon-GCaMP transients (green). **(d)** All data (errorbars=SEM) demonstrate astrocyte Ca^{2+} consistently follows histaminergic axon

activity (n=3 mice, 90 axon segments, 892 astrocyte events). **(e)** The mean lag between histaminergic axon activity and astrocyte Ca^{2+} events (blue arrow in (d)) is 6.35±0.51 seconds.

References

1. Krause, A. J. *et al.* The sleep-deprived human brain. *Nat. Rev. Neurosci.* **18,** 404–418 (2017).
2. Vaidyanathan, T. V., Collard, M., Yokoyama, S., Reitman, M. E. & Poskanzer, K. E. Cortical astrocytes independently regulate sleep depth and duration via separate GPCR pathways. *Elife* **10,** (2021).
3. Bojarskaite, L. *et al.* Astrocytic Ca2+ signaling is reduced during sleep and is involved in the regulation of slow wave sleep. *Nat. Commun.* **11,** 3240 (2020).
4. Ingiosi, A. M. *et al.* A role for astroglial calcium in mammalian sleep and sleep regulation. *Curr. Biol.* **30,** 4373–4383.e7 (2020).
5. Halassa, M. M., Fellin, T., Takano, H., Dong, J.-H. & Haydon, P. G. Synaptic islands defined by the territory of a single astrocyte. *J. Neurosci.* **27,** 6473–6477 (2007).
6. Allen, N. J. & Barres, B. A. Signaling between glia and neurons: focus on synaptic plasticity. *Curr. Opin. Neurobiol.* **15,** 542–548 (2005).
7. Bushong, E. A., Martone, M. E., Jones, Y. Z. & Ellisman, M. H. Protoplasmic astrocytes in CA1 stratum radiatum occupy separate anatomical domains. *J. Neurosci.* **22,** 183–192 (2002).
8. Bazargani, N. & Attwell, D. Astrocyte calcium signaling: the third wave. *Nat. Neurosci.* **19,** 182–189 (2016).
9. Bellesi, M., de Vivo, L., Tononi, G. & Cirelli, C. Effects of sleep and wake on astrocytes: clues from molecular and ultrastructural studies. *BMC Biol.* **13,** 66 (2015).
10. Szabó, Z. *et al.* Extensive astrocyte synchronization advances neuronal coupling in slow wave activity in vivo. *Sci. Rep.* **7,** 6018 (2017).

11. Poskanzer, K. E. & Yuste, R. Astrocytes regulate cortical state switching in vivo. *Proc. Natl. Acad. Sci. USA* **113,** E2675-84 (2016).
12. Durkee, C. A. *et al.* Gi/o protein-coupled receptors inhibit neurons but activate astrocytes and stimulate gliotransmission. *Glia* **67,** 1076–1093 (2019).
13. Holst, S. C. & Landolt, H.-P. Sleep-Wake Neurochemistry. *Sleep Med. Clin.* **13,** 137–146 (2018).
14. Lee, S.-H. & Dan, Y. Neuromodulation of brain states. *Neuron* **76,** 209–222 (2012).
15. Saper, C. B. & Fuller, P. M. Wake-sleep circuitry: an overview. *Curr. Opin. Neurobiol.* **44,** 186–192 (2017).
16. Saper, C. B., Fuller, P. M., Pedersen, N. P., Lu, J. & Scammell, T. E. Sleep state switching. *Neuron* **68,** 1023–1042 (2010).
17. Ding, F. *et al.* α1-Adrenergic receptors mediate coordinated Ca2+ signaling of cortical astrocytes in awake, behaving mice. *Cell Calcium* **54,** 387–394 (2013).
18. Khan, Z. U., Koulen, P., Rubinstein, M., Grandy, D. K. & Goldman-Rakic, P. S. An astroglia-linked dopamine D2-receptor action in prefrontal cortex. *Proc. Natl. Acad. Sci. USA* **98,** 1964–1969 (2001).
19. Takata, N. *et al.* Astrocyte calcium signaling transforms cholinergic modulation to cortical plasticity in vivo. *J. Neurosci.* **31,** 18155–18165 (2011).
20. Shelton, M. K. & McCarthy, K. D. Hippocampal astrocytes exhibit Ca2+-elevating muscarinic cholinergic and histaminergic receptors in situ. *J. Neurochem.* **74,** 555–563 (2000).
21. Chung, S. *et al.* Identification of preoptic sleep neurons using retrograde labelling and gene profiling. *Nature* **545,** 477–481 (2017).

22. Shi, G. *et al.* A Rare Mutation of β1-Adrenergic Receptor Affects Sleep/Wake Behaviors. *Neuron* **103,** 1044–1055.e7 (2019).
23. Thakkar, M. M. Histamine in the regulation of wakefulness. *Sleep Med. Rev.* **15,** 65–74 (2011).
24. Takahashi, K., Lin, J.-S. & Sakai, K. Neuronal activity of histaminergic tuberomammillary neurons during wake-sleep states in the mouse. *J. Neurosci.* **26,** 10292–10298 (2006).
25. Monti, J. M., Pellejero, T. & Jantos, H. Effects of H1- and H2-histamine receptor agonists and antagonists on sleep and wakefulness in the rat. *J. Neural Transm.* **66,** 1–11 (1986).
26. Lin, J. S., Sakai, K. & Jouvet, M. Evidence for histaminergic arousal mechanisms in the hypothalamus of cat. *Neuropharmacology* **27,** 111–122 (1988).
27. Parmentier, R. *et al.* Anatomical, physiological, and pharmacological characteristics of histidine decarboxylase knock-out mice: evidence for the role of brain histamine in behavioral and sleep-wake control. *J. Neurosci.* **22,** 7695–7711 (2002).
28. Yu, X. *et al.* Circadian factor BMAL1 in histaminergic neurons regulates sleep architecture. *Curr. Biol.* **24,** 2838–2844 (2014).
29. Yu, X. *et al.* Wakefulness is governed by GABA and histamine cotransmission. *Neuron* **87,** 164–178 (2015).
30. Panula, P., Pirvola, U., Auvinen, S. & Airaksinen, M. S. Histamine-immunoreactive nerve fibers in the rat brain. *Neuroscience* **28,** 585–610 (1989).
31. Zhang, Y. *et al.* An RNA-sequencing transcriptome and splicing database of glia, neurons, and vascular cells of the cerebral cortex. *J. Neurosci.* **34,** 11929–11947 (2014).
32. Niethard, N., Ngo, H.-V. V., Ehrlich, I. & Born, J. Cortical circuit activity underlying sleep slow oscillations and spindles. *Proc. Natl. Acad. Sci. USA* **115,** E9220–E9229 (2018).

33. Seibt, J. *et al.* Cortical dendritic activity correlates with spindle-rich oscillations during sleep in rodents. *Nat. Commun.* **8,** 684 (2017).

34. Broussard, G. J. *et al.* In vivo measurement of afferent activity with axon-specific calcium imaging. *Nat. Neurosci.* **21,** 1272–1280 (2018).

35. Pachitariu, M. *et al.* Suite2p: beyond 10,000 neurons with standard two-photon microscopy. *BioRxiv* (2016). doi:10.1101/061507

36. Chai, H. *et al.* Neural Circuit-Specialized Astrocytes: Transcriptomic, Proteomic, Morphological, and Functional Evidence. *Neuron* **95,** 531–549.e9 (2017).

37. Reiner, P. B. & Kamondi, A. Mechanisms of antihistamine-induced sedation in the human brain: H1 receptor activation reduces a background leakage potassium current. *Neuroscience* **59,** 579–588 (1994).

38. Sastry, B. S. & Phillis, J. W. Depression of rat cerebral cortical neurones by H1 and H2 histamine receptor agonists. *Eur. J. Pharmacol.* **38,** 269–273 (1976).

39. Inagaki, N., Fukui, H., Ito, S., Yamatodani, A. & Wada, H. Single type-2 astrocytes show multiple independent sites of Ca2+ signaling in response to histamine. *Proc. Natl. Acad. Sci. USA* **88,** 4215–4219 (1991).

40. Wang, Y. *et al.* Accurate quantification of astrocyte and neurotransmitter fluorescence dynamics for single-cell and population-level physiology. *Nat. Neurosci.* **22,** 1936–1944 (2019).

41. Siclari, F. & Tononi, G. Local aspects of sleep and wakefulness. *Curr. Opin. Neurobiol.* **44,** 222–227 (2017).

42. Huber, R., Ghilardi, M. F., Massimini, M. & Tononi, G. Local sleep and learning. *Nature* **430,** 78–81 (2004).

43. Genzel, L., Kroes, M. C. W., Dresler, M. & Battaglia, F. P. Light sleep versus slow wave sleep in memory consolidation: a question of global versus local processes? *Trends Neurosci.* **37,** 10–19 (2014).

44. Bernardi, G., Siclari, F., Handjaras, G., Riedner, B. A. & Tononi, G. Local and widespread slow waves in stable NREM sleep: evidence for distinct regulation mechanisms. *Front. Hum. Neurosci.* **12,** 248 (2018).

45. Siclari, F. *et al.* Two distinct synchronization processes in the transition to sleep: a high-density electroencephalographic study. *Sleep* **37,** 1621–1637 (2014).

46. Nir, Y. *et al.* Regional slow waves and spindles in human sleep. *Neuron* **70,** 153–169 (2011).

47. Sanchez-Vives, M. V. & McCormick, D. A. Cellular and network mechanisms of rhythmic recurrent activity in neocortex. *Nat. Neurosci.* **3,** 1027–1034 (2000).

48. Krone, L. B. *et al.* A role for the cortex in sleep-wake regulation. *BioRxiv* (2020). doi:10.1101/2020.03.17.996090

49. Eban-Rothschild, A., Rothschild, G., Giardino, W. J., Jones, J. R. & de Lecea, L. VTA dopaminergic neurons regulate ethologically relevant sleep-wake behaviors. *Nat. Neurosci.* **19,** 1356–1366 (2016).

50. Aston-Jones, G. & Bloom, F. E. Activity of norepinephrine-containing locus coeruleus neurons in behaving rats anticipates fluctuations in the sleep-waking cycle. *J. Neurosci.* **1,** 876–886 (1981).

51. Lee, M. G., Hassani, O. K., Alonso, A. & Jones, B. E. Cholinergic basal forebrain neurons burst with theta during waking and paradoxical sleep. *J. Neurosci.* **25,** 4365–4369 (2005).

52. Trulson, M. E. & Jacobs, B. L. Raphe unit activity in freely moving cats: correlation with

level of behavioral arousal. *Brain Res.* **163,** 135–150 (1979).

53. McCormick, D. A. & Williamson, A. Modulation of neuronal firing mode in cat and guinea pig LGNd by histamine: possible cellular mechanisms of histaminergic control of arousal. *J. Neurosci.* **11,** 3188–3199 (1991).
54. Zucca, S. *et al.* An inhibitory gate for state transition in cortex. *Elife* **6,** (2017).
55. Lemieux, M., Chauvette, S. & Timofeev, I. Neocortical inhibitory activities and long-range afferents contribute to the synchronous onset of silent states of the neocortical slow oscillation. *J. Neurophysiol.* **113,** 768–779 (2015).
56. Chen, J.-Y., Chauvette, S., Skorheim, S., Timofeev, I. & Bazhenov, M. Interneuron-mediated inhibition synchronizes neuronal activity during slow oscillation. *J. Physiol. (Lond.)* **590,** 3987–4010 (2012).
57. Mariotti, L., Losi, G., Sessolo, M., Marcon, I. & Carmignoto, G. The inhibitory neurotransmitter GABA evokes long-lasting Ca(2+) oscillations in cortical astrocytes. *Glia* **64,** 363–373 (2016).
58. Mederos, S. & Perea, G. GABAergic-astrocyte signaling: A refinement of inhibitory brain networks. *Glia* **67,** 1842–1851 (2019).
59. Ding, F. *et al.* Changes in the composition of brain interstitial ions control the sleep-wake cycle. *Science* **352,** 550–555 (2016).
60. Halassa, M. M. *et al.* Astrocytic modulation of sleep homeostasis and cognitive consequences of sleep loss. *Neuron* **61,** 213–219 (2009).
61. Poskanzer, K. E. & Yuste, R. Astrocytic regulation of cortical UP states. *Proc. Natl. Acad. Sci. USA* **108,** 18453–18458 (2011).
62. Fang, Q. *et al.* Histamine up-regulates astrocytic glutamate transporter 1 and protects

neurons against ischemic injury. *Neuropharmacology* **77,** 156–166 (2014).

63. Marvin, J. S. *et al.* An optimized fluorescent probe for visualizing glutamate neurotransmission. *Nat. Methods* **10,** 162–170 (2013).

64. Goldey, G. J. *et al.* Removable cranial windows for long-term imaging in awake mice. *Nat. Protoc.* **9,** 2515–2538 (2014).

Chapter 5:

Astrocytic Gi-GPCR activation changes extracellular glutamate, but not GABA, during visual stimuli

---

Abstract

Astrocytes perform critical functions in the brain that are dependent on the sensing of neurotransmitters through G protein-coupled receptors (GPCRs). What types of astrocytic outputs occur as a consequence of different GPCR activity remain unclear, but this is a critical question in understanding how astrocytes ultimately influence brain function and behavior. Here, we investigate the functional outputs of Gi-GPCR activation, a family of GPCRs that has previously been demonstrated to be sufficient to increase slow-wave activity during sleep. By combining fiber photometry recordings of the extracellular indicators iGluSnFR and iGABASnFR with astrocyte-specific Gi-GPCR activation, we examine two putative outputs by astrocytes *in vivo*, the regulation of extracellular glutamate and the regulation of extracellular GABA. We find that Gi-GPCR activation does not change spontaneous dynamics of extracellular glutamate or GABA. However, Gi-GPCR activation did cause an increase in visual stimulus-evoked glutamate, but not GABA. Together, this data points towards a complex relationship between astrocytic inputs and outputs *in vivo* that may vary in different behavioral contexts and further suggests glutamate-specific mechanisms underlying some astrocytic Gi-GPCR dependent behaviors, including the regulation of SWA in sleep.

Introduction

Astrocytes are critical for brain function through their regulation of neuronal activity. Astrocytic function is dependent on the sensing of neurotransmitter signals that result in astrocyte activation via elevations in calcium (Ca^{2+})[1,2]. Many of the receptors expressed by astrocytes are metabotropic G protein-coupled receptors (GPCRs)[3]. Indeed, astrocytic GPCR signaling has been associated with various brain functions and behavior[4–10]. However, the astrocytic outputs that occur as a consequence of different GPCRs that ultimately mediate astrocytic functions remain unknown.

Astrocytes in the cortex are well suited to regulate neuronal network activity via their interconnectedness and ability to bidirectionally communicate with large populations of neurons[11]. In fact, cortical astrocytic GPCR signaling has been shown to be critical for the regulation of non-rapid eye movement (NREM) sleep[5,12,13], a behavior critical for learning and memory involving the rhythmic activity of large populations of cortical neurons. It has recently been demonstrated that a family of GPCRs dependent on the Gi alpha subunit (Gi-GPCRs) in cortical astrocytes is sufficient to regulate NREM slow-wave activity (SWA), a marker of sleep depth[5]. While it has been shown that Gi-GPCR activation in astrocytes increases Ca^{2+} signaling[5,7,9,14], it is unknown what the downstream astrocytic outputs are that can drive changes in SWA.

The cortex plays a critical role in the generation of SWA[15–23] and this has largely been attributed to the excitatory neurotransmitter glutamate[16,24] and the inhibitory neurotransmitter GABA[25–28]. Astrocytes respond to both glutamate and GABA through Gi-GPCRs ($GABA_B$ and mGluR3 receptors, respectively, in adults)[7,14,29] and play critical roles in the regulation of extracellular glutamate ($[glu]_e$) and extracellular GABA ($[GABA]_e$) via the uptake of glutamate

and GABA from the extracellular space via transporters[30]. Thus, the regulation of $[glu]_e$ and $[GABA]_e$ are tempting candidates for functional outputs of Gi-GPCR activation and potential mechanisms by which astrocytes may regulate SWA in sleep.

Here, we combine astrocyte-specific manipulations of the Gi-GPCR pathway with fiber photometry recordings of the indicators iGluSnFR and iGABASnFR to investigate how cortical astrocyte Gi-GPCRs change $[glu]_e$ and $[GABA]_e$ *in vivo*. We find that Gi-GPCR activation does not, as predicted, change spontaneous $[glu]_e$ or $[GABA]_e$ dynamics. However, using visual stimuli via light flash, we found that Gi-GPCR activation did increase the amplitude of evoked $[glu]_e$, but not $[GABA]_e$. Together, the data presented point toward a specific glutamatergic output of astrocytic Gi-GPCR activation and suggests the astrocytic regulation of SWA may be attributed specifically to $[glu]_e$ regulation.

Results

In vivo *recording of extracellular glutamate and GABA in freely moving mice*

To investigate the functional output of astrocytic Gi-GPCR signaling *in vivo*, we combined astrocytic Gi-GPCR activation with recordings of $[glu]_e$ and $[GABA]_e$ in freely moving mice (**Fig. 5.1a**). 2-3 weeks prior to experiments, mice were co-injected with two viruses (**Fig. 5.1b**). To activate the Gi pathway in astrocytes, we used Designer Receptors Exclusively Activated by Designer Drugs (DREADDs)[31], injecting mice with *AAV-GFAP-hM4Di-mCherry* to express the human M4 muscarinic receptor DREAD (hM4Di) in primary visual cortex astrocytes. The second virus injected was either *AAV-GFAP-SF-iGluSnFR.A184S*[32] or *AAV-GFAP-iGABASnFR*[33], to express the extracellular indicator for glutamate or GABA, respectively, in astrocytes. Following time for recovery and expression, we performed fiber

photometry recordings of iGluSnFR or iGABASnFR as mice moved around a circular chamber (**Fig. 5.1c-d**) after I.P. administration of the hM4Di agonist clozapine-N-oxide (CNO, 1mg/kg) to monitor the effect of Gi-activation on $[glu]_e$ or $[GABA]_e$. In addition to spontaneous dynamics, we also elicited $[glu]_e$ and $[GABA]_e$ events using visual stimuli in the form of a light flash with a blue LED (**Fig. 5.1a**). With both iGluSnFR and iGABASnFR, we observed consistent responses to the light flash (**Fig. 5.1e-g**).

Gi-DREADD activation does not change spontaneous extracellular glutamate or GABA dynamics

To investigate how astrocytic Gi-GPCR signaling changes $[glu]_e$ and $[GABA]_e$ we began by monitoring how CNO administration changed spontaneous $[glu]_e$ and $[GABA]_e$ compared to saline controls (**Fig. 5.2a**). We detected iGluSnFR and iGABASnFR transients by automatically locating local maxima (**Fig. 5.2b**). Interestingly, we found Gi activation did not change the frequency of iGluSnFR or iGABASnFR transients (**Fig. 5.2c**), nor did it change the amplitude of these events (**Fig. 5.2d**). This suggested that Gi-GPCR signaling in astrocytes does not significantly contribute to basal levels of glutamatergic or GABAergic signaling. We anticipate that this manipulation results in a relatively moderate activation of Gi-GPCR signaling in astrocytes given our previously published work on the resulting change in calcium (Ca^{2+}) with the same CNO dose[5]. Given that glutamate and GABA are under tight regulation in order to maintain a balance that prevents neurotoxicity, it may indeed be expected that this moderate activation of astrocytes does not result in large changes to $[glu]_e$ or $[GABA]_e$. Thus, we next wanted to investigate if there smaller changes in $[glu]_e$ or $[GABA]_e$ that could be detected.

Gi-DREADD activation does not change the decay tau of stimulus-evoked extracellular glutamate or GABA

Astrocytes express transporters for glutamate (GLT-1, GLAST)[34,35] and GABA (GAT)[36] at high levels and serve as the primary mechanism for neurotransmitter uptake in the CNS. Astrocytic uptake of glutamate and GABA is a dynamic process and critical for the fine-tuned balance of excitation and inhibition in the cortex[30,34,37–39], and thus we hypothesized that Gi-GPCR activation may regulate glutamate or GABA uptake. To test this, we examined if Gi-DREADD activation via CNO would change the decay, a measure of uptake[37,39], of iGluSnFR or iGABASnFR events.

In order to obtain a reliable measure of decay, we used a visual stimulus to elicit iGluSnFR and iGABASnFR events in the visual cortex (**Fig. 5.3a-b**, see Methods). LED light flashes resulted in consistent, stereotyped responses of both iGluSnFR and iGABASnFR –a rapid increase in fluorescence with a brief lag from LED onset (132±64ms for iGluSnFR, 112±74ms for iGABASnFR), followed by a decrease in fluorescence that dipped below baseline levels before returning to baseline (**Fig. 5.3c**). Interestingly, we observed two peaks ("early" and "late") in the response of both iGluSnFR and iGABASnFR before the fluorescence decreased to baseline (**Fig. 5.3c-d, f**). An early and late response to light flash has been reported previously in mice, cats, and humans[40–43]. Indeed the "late" component has been reported to occur after 300ms and as far as 1s following light flash[42,43] similar to the latency we observed (433±46ms for iGluSnFR and 433±16ms for iGABASnFR).

To investigate the role of Gi-GPCR signaling in glutamate and GABA uptake, we compared the response between CNO and saline conditions. We observed no discernable difference in the average LED evoked response of iGluSnFR or iGABASnFR (**Fig. 5.3c**). Next,

we specifically quantified the decay for both the "early" and "late" peak response. The "early" peak decay was linear and so we computed the time for fluorescence to decay to 33% of the max response (**Fig. 5.3d**). We observed no significant difference in this decay time between saline and CNO conditions for iGluSnFR and iGABASnFR (**Fig. 5.3e**), suggesting that glutamate and GABA uptake for this initial visual response is not affected by astrocytic Gi-GPCR signaling.

Next, we examined the decay for the "late" response. The decrease in fluorescence following the "late" response was exponential and so we quantified the decay tau by fitting an exponential curve to this portion of the trace (**Fig. 5.3f**). Similar to the "early" decay, we found no significant difference in the decay tau of the "late" response for iGluSnFR or iGABASnFR. Together, this suggested that astrocytic Gi-GPCR signaling does not affect the regulation of glutamate or GABA uptake.

Gi-DREADD activation increases the amplitude of stimulus-evoked extracellular glutamate, but not extracellular GABA

We did not observe a significant increase in the amplitude of spontaneous iGluSnFR or iGABASnFR events (**Fig. 5.2**) with Gi-DREADD activation, but we wondered whether the amplitude of evoked events would change. As described previously (**Fig. 5.3**), we examined the "early" and "late" peak response separately (**Fig. 5.4a, c**). While we observed no significant change in amplitude for the "early" iGABASnFR response (**Fig. 5.4b**, right), there was a trend towards an increase in the iGluSnFR response (**Fig. 5.4b**, left). When we quantified the "late" peak amplitude, we found there was a significant increase in the iGluSnFR response amplitude but not the iGABASnFR amplitude (**Fig. 5.4d**).

This suggests that astrocytic Gi-GPCR signaling can in fact modulate glutamatergic signaling, but not GABAergic signaling. It is possible that stimulus-evoked changes in glutamate bypass homeostatic mechanisms that prevented a similar increase to be observed with the spontaneous dynamics (**Fig. 5.2**). Alternatively, this may be a stimulus-specific mechanism. Previous work from our group has shown that astrocyte Gi-DREADD activation is sufficient to increases SWA in sleep[5], and glutamate has been shown to be sufficient to generate cortical UP states[16,24]. Together, this data support a hypothesis in which changes in $[glu]_e$ is a mechanism by which astrocytic Gi signaling modulates SWA.

This data does not inform whether the increase in $[glu]_e$ is driven by neuronal or astrocytic glutamate. However, previous work has demonstrated that astrocytic Gi-DREADD activation can increase slow-inward currents which are thought to be the result of astrocytic glutamate release[14]. Thus the increase observed here may in fact be the result of increased astrocyte-derived glutamate, but further work is necessary to confirm this.

Discussion

Using *in vivo* recordings of iGluSnFR and iGABASnFR in freely moving mice, we find that astrocyte-specific Gi-GPCR activation does not change spontaneous $[glu]_e$ or $[GABA]_e$, nor does it change the decay time of evoked $[glu]_e$ or $[GABA]_e$. We do find, however, that Gi-GPCR activation increases the amplitude of evoked $[glu]_e$ events, while $[GABA]_e$ is unchanged. This points towards a glutamate-specific mechanism of Gi-GPCR signaling and astrocytic SWA control.

Glutamatergic mechanism of astrocytic SWA regulation

In our study, we did not simultaneously measure sleep and so we cannot make any conclusions regarding the mechanism of SWA control. However, the finding that astrocytic Gi-GPCR activation changed $[glu]_e$ but not $[GABA]_e$ events (**Fig. 5.4d**) may point towards a specific mechanism underlying the previously reported astrocytic control of SWA[5] through the regulation of cortical UP states. Glutamate is sufficient to initiate cortical UP states[16] while synchronous DOWN states may be driven specifically by inhibitory GABA signaling[15,25,26,28]. Indeed, astrocytes have been linked specifically to UP states *ex vivo* previously[24].

If the observed increase in $[glu]_e$ amplitude is responsible for the Gi-GPCR control of SWA, it would suggest relatively fast regulation of $[glu]_e$ by astrocytes (within ms). Astrocytes dynamically regulate glutamate uptake on a fast timescale[44] and can shape excitatory post-synaptic events on a ms timescale[38]. However, we found no change in the decay time of iGluSnFR events with Gi-GPCR activation (**Fig. 5.3e, g**), suggesting that glutamate uptake is not dependent on the Gi-GPCR pathway. Although still debated[45], Gi-GPCR activation may instead result in astrocytic release of glutamate. This is supported by previous work showing Gi-GPCR dependent increase in slow-inward currents[14]. Glutamate release by astrocytes could occur through vesicular release[46–49] or from the reversal of glutamate transporters[50]. Future work is necessary to confirm what cell-type is the source for the increase in $[glu]_e$ upon astrocyte Gi-GPCR activation. Further, it will be necessary to confirm that Gi-GPCR activation increases $[glu]_e$ during NREM sleep via simultaneous electrophysiology recordings.

Functional outputs of astrocytic Gi-GPCR signaling

Beyond the regulation of sleep, Gi-GPCR signaling in astrocytes has been linked to other wake behaviors[6,7,51,52]. The data presented here provide important insight into astrocyte Gi-GPCR signaling. It has only been recently appreciated that, unlike neurons, astrocytic Gi-GPCR signaling increases astrocyte Ca^{2+} through an IP3R2-dependent pathway[14]. What downstream functional outputs follow this signaling pathway that ultimately affect neuronal activity and behavior has not been previously explored. Our finding that astrocytic Gi-GPCR activation can preferentially change $[glu]_e$ but not $[GABA]_e$ reveals important features of astrocyte signaling that can help elucidate the mechanism underlying other astrocyte-dependent behaviors.

The observed change in $[glu]_e$ upon Gi-GPCR activation may underlie a homeostatic role of astrocytes in maintaining excitatory/inhibitory (E/I) balance within the cortex. Indeed astrocytic sensing of glutamate and GABA via the Gi-GPCR $GABA_B$ has been previously implicated in E/I balance[53] and it has been reported that astrocytes increase glutamate transmission upon sensing of GABA via $GABA_B$ receptors *ex vivo*[14,54]. Further work is necessary to identify the type of Gi-GPCR responsible for the observed increase in $[glu]_e$ here, such as through loss-of-function experiments to remove $GABA_B$ receptors.

Spontaneous and stimulus-evoked dynamics

We observed a significant change in $[glu]_e$ amplitude with Gi-GPCR activation when we examined visual stimulus evoked $[glu]_e$ dynamics, but not when we quantified spontaneous $[glu]_e$ amplitude. This difference underscores the complexity of these signals and the varying role of astrocytes in circuit function under different behavioral contexts. One explanation for the difference is that Gi-GPCR activation always increases $[glu]_e$, but the increase is masked during

spontaneous freely-moving behaviors due to compensatory mechanisms that are not present during strong visual stimuli. Indeed, the increase in amplitude observed with visual stimuli was relatively small. Increasing the amount of Gi-GPCR activation with higher doses of CNO could reveal a similar change in spontaneous dynamics. Alternatively, Gi-GPCR induced $[glu]_e$ may be dependent on visual stimuli and may play a role in visual behavior, such as by providing increased sensitivity to future stimuli. It would be fruitful to combine astrocytic Gi-GPCR activation with visual tasks to assess the effect on visual function. Further, it would be of interest to repeat these experiments in other cortical areas. Finding similar results in other sensory areas, such as somatosensory cortex, may reveal a generalized sensory mechanism. Additionally, examining non-sensory cortical areas like frontal cortex could reveal general cortical circuit principles as well as could be relevant for higher-order functions including the generation of SWA in sleep.

Methods

Animals

All procedures were carried out using adult mice (C57Bl/6, P50–100) in accordance with protocols approved by the University of California, San Francisco Institutional Animal Care and Use Committee (IACUC). All animals were housed in a 12:12 light-dark cycle with food and water provided *ad libitum*. Male and female mice were used for all experiments. Following surgery, all animals were singly housed, to protect electrodes, with additional enrichment.

Surgical procedures

Adult mice (C57Bl/6, P50–100) were administered dexamethasone (5mg/kg, s.c.) prior to surgery and anesthetized with isoflurane. For iGluSnFR experimens, two viruses, *AAV-*

GFAP.SF-iGluSnFR.AI184S and *AAV5-GFAP-hM4D(Gi)-mCherry* were mixed in a 2:1 ratio and 600nl of the mixture was injected in V1 (from bregma, -3.5mm, 2.5mm lateral). For iGABASnFR experimens, two viruses, *AAV-GFAP-iGABASnFR2* and *AAV5-GFAP-hM4D(Gi)-mCherry* were mixed in a 2:1 ratio and 600nl of the mixture was injected in V1 (from bregma, -3.5mm, 2.5mm lateral). Injections were made 0.35mm from the pial surface followed by a 10-min wait for diffusion. Following viral injection, a fiberoptic cannula (Doric Lenses: 400um inner core, 430um outercore, 0.57 NA, 1.0mm length) was implanted 0.3mm below the pial surface and secured with a layer of superglue followed by C&B metabond. Post-operative care included administration of 0.05mg/kg buprenorphine and 5mg/kg carpofen. Mice were allowed 2-3 weeks to recover and for viral expression.

DREADD activation

Prior to fiber photometry recordings, mice were habituated to the recording setup (circular chamber lined with white alphadri bedding, and tethering via patchcords) for ~30min. At the start of each experiment day, mice were weighed and connected to the recording apparatus. Immediately before the recording was started, CNO (1mg/kg) or saline (0.9%) was administered with an I.P. injection. CNO was diluted to 300uM in saline from a stock of 60mM each day and the appropriate volume was measured for each mouse for a dose of 1mg/kg. An equal volume of saline was injected on control days. The sequence of CNO and saline control days was randomized amongst mice.

Fiber photometry recordings

Following injection of either CNO or saline, four recordings were made in the following order: spontaneous (no LED, 10-min), LED flash stimuli (10-min), spontaneous (no LED, 30-min), LED flash stimuli (10-min) for a total of 1-hour.

A rig for fiber photometry recordings was used that is similar to what has been described previously[55,56]. Brefily, we used a Tucker-Davis Technologies RZ10X Processor with a Doric Lenses fluorescence mini-cube. A 473nm LED was used for the iGluSnFR and iGABASnFR excitation and a 405nm LED was used as an isobestic control. Both LEDs (Tucker-Davis Technologies, RZ10X Processor) went through a fluorescence mini-cube (Doric Lenses) and then through patchcords that were connected to a commutator to allow for easy rotation of the animal. Following the commutator, a patchcord was connected to the fiber-optic cannula implanted in the animal. Fluorescence signals were reflected back through the mini-cube to a photoreceiver on the RZ10X Processor.

Visual stimuli

For visual stimuli recordings, a blue LED light (ThorLabs, 470nm) was fed through a LED driver (ThorLabs), and connected through a patchcord that was attached above the circular chamber. The LED driver was controlled through the Tucker-Davis Technologies RZ10X processor so that it would flash, lighting up the entire circular chamber, every 10-15s with a duration of 500ms through the fiber photometry recording. The timestamp of each LED onset was recorded alongside fiber photometry data to be used for analysis.

Pre-processing of fiber photometry data

Raw fiber photometry data were minimally preprocessed in MATLAB, similar to previously reported work[57]. First, the isobestic control channel was scaled to match the iGluSnFR or iGABASnFR channel. Next, the dfof was calculated by subtracting the SnFR signal from the scaled isobestic channel and then dividing by the scaled isobestic channel. Lastly, the signal is detrended using the MATLAB function *detrend*.

Analysis

Spontaneous dynamics

Peaks were automatically detected in the dfof traces using the MATLAB function *peakfinder*, a noise-tolerant way to detect local maxima, and manually inspected for accuracy.

Stimulus-evoked dynamics

For each animal, the dfof signal 3s before and 3s after each LED onset was taken and averaged to obtain an event-triggered average (ETA) trace. Next, the timestamp for 5 events were identified within each ETA trace: (1) onset of "early" peak, (2) onset of "late" peak, (3) "early" peak, (4) "late" peak, (5) trough.

For the onsets of peaks (events 1 and 2), the derivative of each ETA trace was calculated and the negative-to-positive zero crossings were identified. For the "early" onset, the zero crossing that corresponded to the lowest value of the ETA trace between 0 to 250ms from LED onset was chosen. For the "late" onset, the zero crossing that corresponded to the lowest value of the ETA trace between 300 to 500ms from LED onset was chosen.

For the peak times (events 3 and 4), the derivative of each ETA trace was calculated and the positive-to-negative zero crossings were identified. For the "early" peak time, the zero crossing that corresponded to the maximum value of the ETA trace between 200 to 400ms from LED onset was chosen. For the "late" peak time, the zero crossing that corresponded to the maximum value of the ETA trace between 400 to 800ms from LED onset was chosen.

For the trough (event 5), the derivative of each ETA trace was calculated and the negative-to-positive zero crossings were identified. The zero crossing that corresponded to the lowest value of the ETA trace between 500 to 2800ms from LED onset was chosen as the trough time.

The decay of the "early" peak was identified by calculating the "decay amount" by subtracting the max value from the minimum value between event 3 ("early" peak) and event 2 ("late" onset), and then finding the time within this range that the ETA trace reached 33% of the decay amount. The decay tau of the "late" peak identified by fitting an exponential function to the ETA trace between event 4 ("late" peak) and event 5 (trough) using the MATLAB function *fit*.

Immunohistochemistry

After physiology experiments were complete, mice were intracardially perfused with 4% PFA. Brains were collected, immersed in 4% PFA overnight at 4°C and switched to 30% sucrose for two days before being frozen on dry ice and stored at -80°C. Brains were sliced coronally (40μm thick) on a cryostat. Slices were stored in cryoprotectant at -20°C until staining. Slices were washed with PBS, 5min x 3, then with 0.1% PBS-TX for 30min. Slices were next washed with 10% NGS (Invitrogen) for 1 hr, followed by an overnight incubation of 2% NGS, rat α-

mCherry (1:1000, ThermoFischer), rabbit α-NeuN (1:1000, EMD Millipore), and chicken α-GFP (1:3000, Aves Lab) in 4°C. Slice were next rinsed with 1x PBS x 3 before incubating for 2 hr at room temperature with goat α- rat Alexa Fluor 555 (1:1000), goat α-rabbit 405 (1:1000), and goat α-chicken Alexa Fluor 488 (1:1000). Slices were washed again with PBS 3x for 5 min before slide-mounting and coverslipping using Fluoromount.

To analyze colocalization of mCherry and NeuN at single-cell resolution, 63x images were taken on a spinning disk confocal (Zeiss). Slides were oil-immersed and two slices/animal (-3.8 and -2.3 from bregma) were imaged. In these slices, eight images were taken at random, spanning the total area in which virus was expressed. Colocalization of mCherry and NeuN was performed using Fiji.

Quantification and statistical analysis

All statistical tests used, definition of center and dispersion measurements, and exact n values can be found for each figure in the corresponding figure legend. Additional information regarding statistical tests described in the relevant sections. For all figures, significance levels defined as the following: *: $p<0.05$, **: $p<0.005$, ***: $p<0.0005$.

Figures

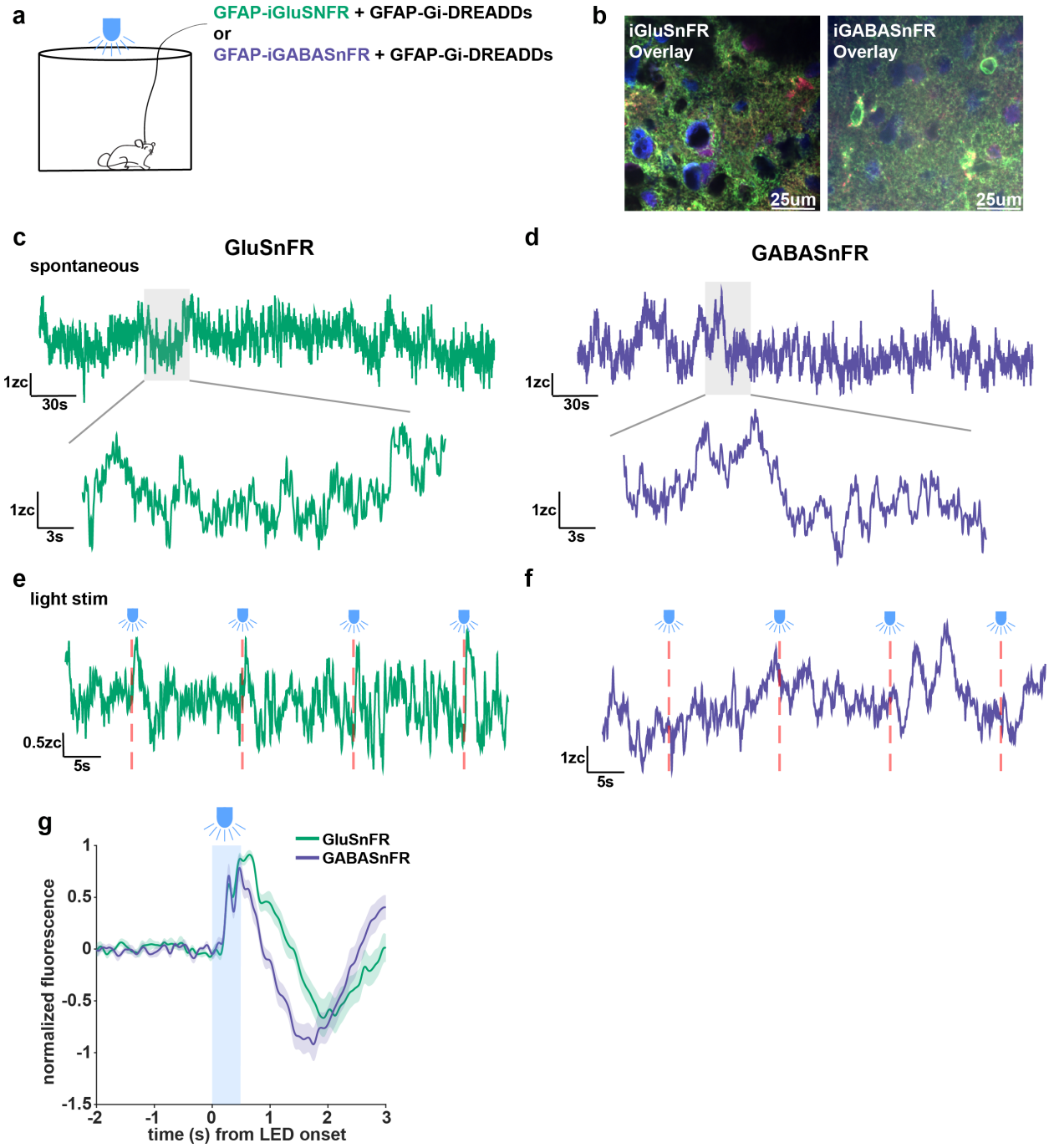

Figure 5.1: *In vivo* recording of spontaneous and stimulus-evoked extracellular glutamate and GABA in freely moving mice.
(a) Experimental *in vivo* fiber photometry setup. Mice were co-injected with either *GFAP-iGluSnFR* or *GFAP-iGABASnFR* and *GFAP- hM4D(Gi)-mCherry* AAVs. Extracellular glutamate and GABA were recorded using fiber photometry as mice moved freely in a circular chamber. **(b)** Representative immunohistochemistry images showing expression of Gi-

DREADDs (red), NeuN (blue), and iGluSnFR (left, green) or iGABASnFR (right, green). **(c)** Example of spontaneous iGluSnFR dynamics over 5min (top) and 30s (bottom). **(d)** Example of spontaneous iGABASnFR dynamics over 5min (top) and 30s (bottom). **(e)** Example showing consistent iGluSnFR responses to light flashes (red dashed lines) **(f)** Example showing consistent iGABASnFR responses to light flashes (red dashed lines) **(g)** Light-evoked average photometry response with iGluSnFR (green) and iGABASnFR (purple) (For iGluSnFR: n=10 mice. For iGABASnFR: n=9 mice. For all, 78 stimuli per mouse. Errorbars=SEM).

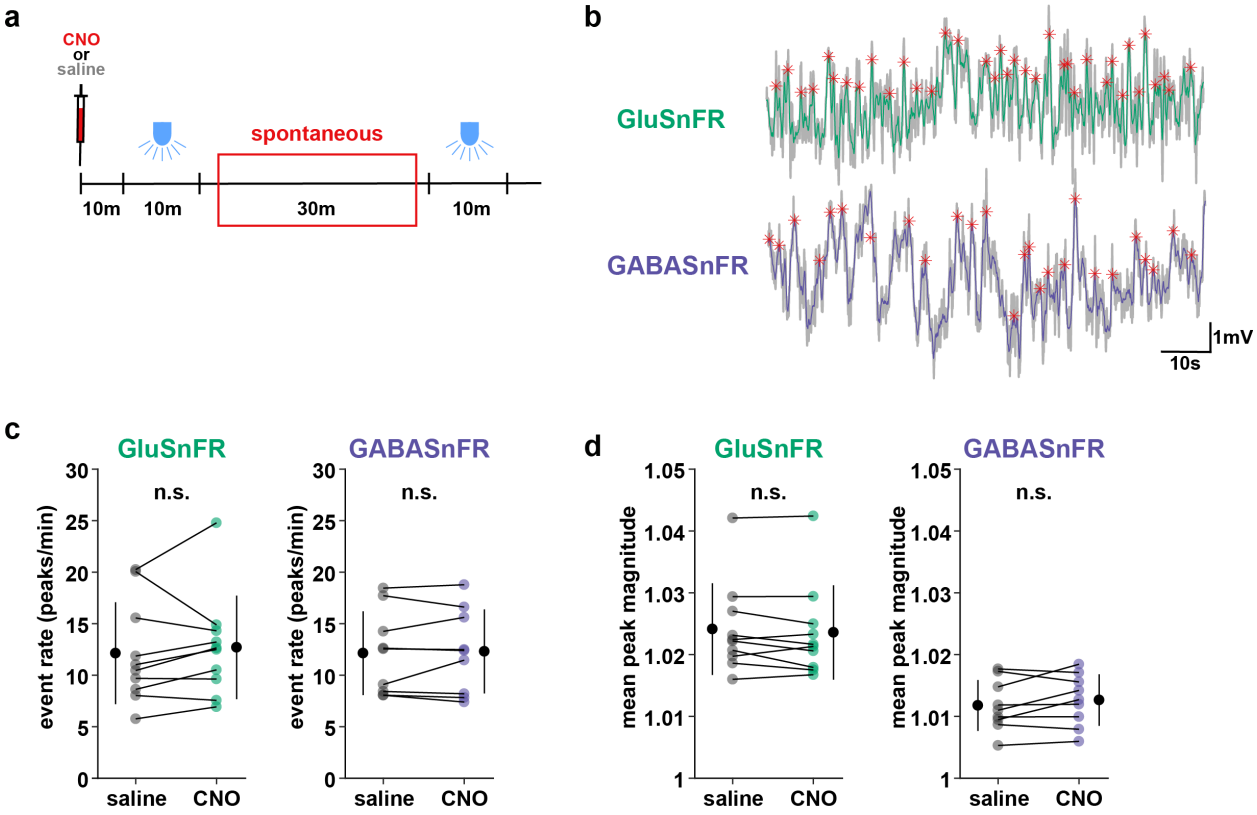

Figure 5.2: No change in spontaneous iGluSnFR or iGABASnFR dynamics were observed after CNO administration.
(a) Experimental paradigm. Photometry recordings were performed after I.P. injection of either CNO or saline, including 30min of spontaneous dynamics. **(b)** Example traces (90s) of spontaneous iGluSnFR (top, green) and iGABASnFR (bottom, purple) dynamics. Events were identified by automatically detecting peaks (red stars). **(c)** The event rate (number of peaks per min) was the same after saline and CNO administration for both iGluSnFR (left) recordings and iGABASnFR (right) recordings. **(d)** The magnitude of spontaneous events was the same after saline and CNO administration for both iGluSnFR (left) recordings and iGABASnFR (right) recordings. (For panels c-d: iGluSnFR, n=9 mice, iGABASnFR, n=9 mice. 78 stimuli per mouse, paired t-test, errorbars=SD).

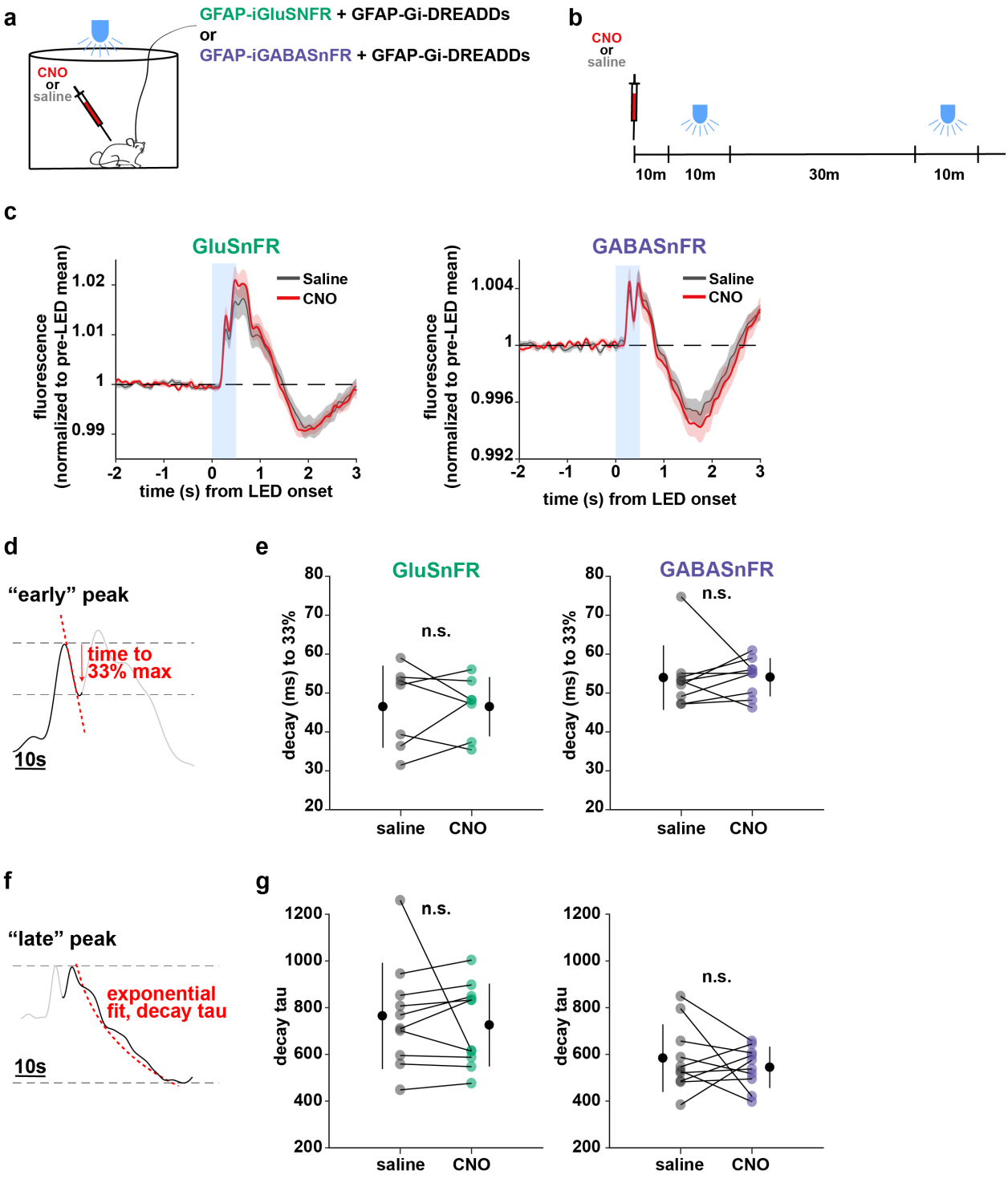

Figure 5.3: Gi-DREADD activation does not change the decay time of stimulus-evoked iGluSnFR or iGABASnFR.

(a) Experimental *in vivo* fiber photometry setup. Mice were co-injected with either *GFAP-iGluSnFR* or *GFAP-iGABASnFR* and *GFAP- hM4D(Gi)-mCherry* AAVs. After an I.P. injection of either 1mg/kg CNO or saline, extracellular glutamate and GABA were recorded using fiber photometry as mice moved freely in a circular chamber. **(b)** Experimental paradigm. 1hr photometry recordings were performed after I.P. injection of either CNO or saline, capturing

both spontaneous dynamics and visual stimulus evoked activity using light flash. **(c)** Light-evoked average iGluSnFR (left) and iGABASnFR (right) response is similar after CNO (red) or saline (gray) injection. (For iGluSnFR: n=10 mice. For iGABASnFR: n=9 mice. For all, 78 stimuli per mouse. Errorbars=SEM). **(d)** Light-evoked responses had two peaks, an "early" and a "late" response. The response decay for the early peak was quantified by calculating the time (ms) for the first peak response to decay to 33% of the max. **(e)** The "early" light-evoked response for iGluSnFR (left) and iGABASnFR (right) had similar decay times after CNO and saline administration (For iGluSnFR, n=7 mice. For iGABASnFR, n=9 mice. For all, 78 stimuli per mouse, paired t-test, errorbars=SD). **(f)** The response decay for the "late" peak was quantified by fitting an exponential function to the mean trace for each mouse. **(g)** The "late" light-evoked response for iGluSnFR (left) and iGABASnFR (right) had similar decay times after CNO and saline administration (For iGluSnFR, n=10 mice. For iGABASnFR, n=9 mice. For all, 78 stimuli per mouse, paired t-test, errorbars=SD).

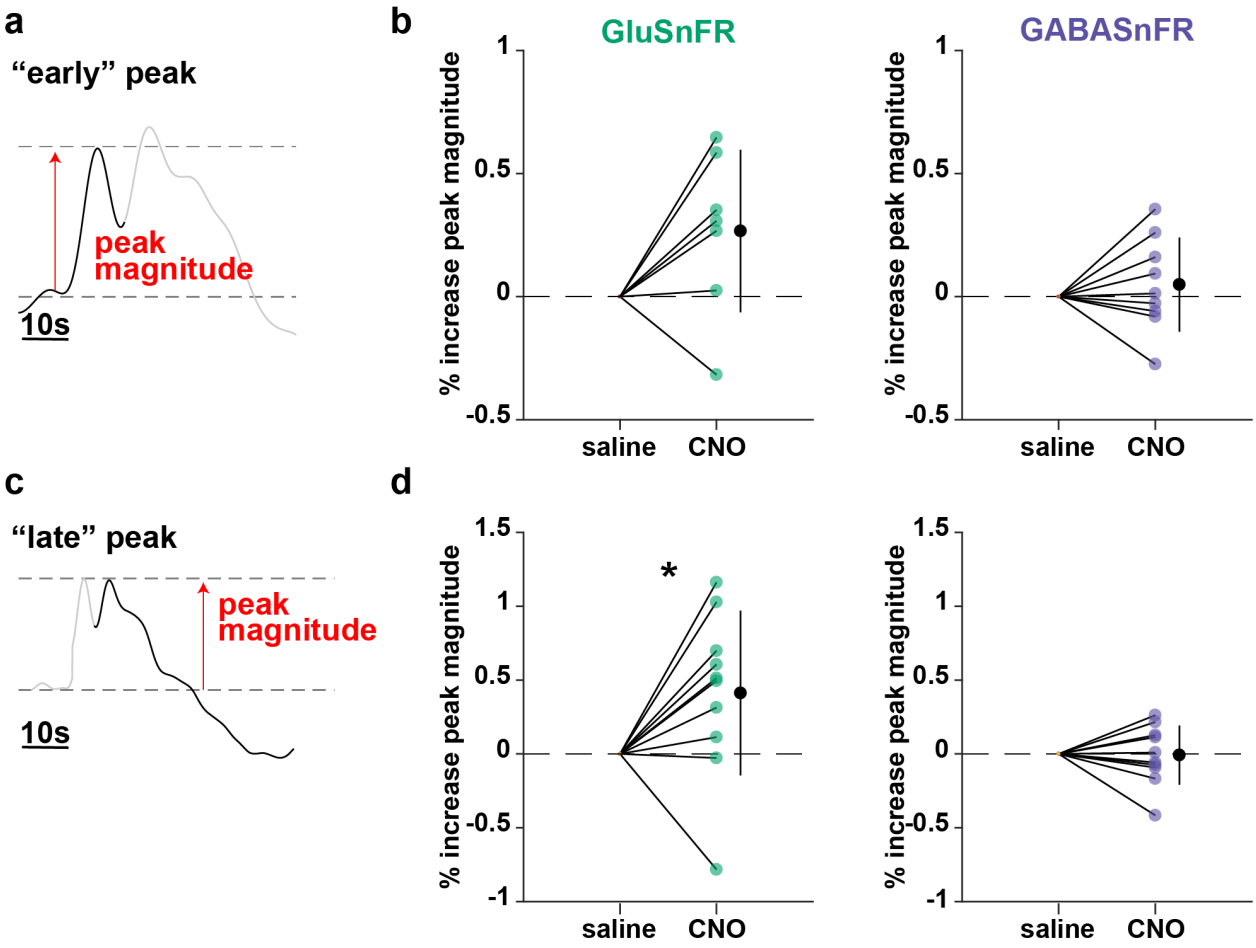

Figure 5.4: Gi-DREADD activation increases the magnitude of stimulus-evoked iGluSnFR but not iGABASnFR

(a) The magnitude of the "early" light-evoked iGluSnFR and iGABASnFR response was quantified after I.P. injection of either 1mg/kg CNO or saline. **(b)** The magnitude of the "early" iGluSnFR light-evoked response trended towards an increase after CNO administration (left), but there was no change for the iGABASnFR response. (For iGluSnFR, n=7 mice. For iGABASnFR, n=9 mice. For all, 78 stimuli per mouse, paired t-test, p = 0.07, errorbars=SD). **(c)** The magnitude of the "late" light-evoked iGluSnFR and iGABASnFR response was quantified after CNO or saline administration. **(d)** CNO administration resulted in a significant increase in the "late" light-evoked iGluSnFR response (left) but not the iGABASnFR response (right). (For iGluSnFR, n=9 mice. For iGABASnFR, n=9 mice. For all, 78 stimuli per mouse, paired t-test, errorbars=SD).

References

1. Perea, G., Navarrete, M. & Araque, A. Tripartite synapses: astrocytes process and control synaptic information. *Trends Neurosci.* **32,** 421–431 (2009).
2. Bazargani, N. & Attwell, D. Astrocyte calcium signaling: the third wave. *Nat. Neurosci.* **19,** 182–189 (2016).
3. Kofuji, P. & Araque, A. G-Protein-Coupled Receptors in Astrocyte-Neuron Communication. *Neuroscience* **456,** 71–84 (2021).
4. Bonder, D. E. & McCarthy, K. D. Astrocytic Gq-GPCR-linked IP3R-dependent Ca2+ signaling does not mediate neurovascular coupling in mouse visual cortex in vivo. *J. Neurosci.* **34,** 13139–13150 (2014).
5. Vaidyanathan, T. V., Collard, M., Yokoyama, S., Reitman, M. E. & Poskanzer, K. E. Cortical astrocytes independently regulate sleep depth and duration via separate GPCR pathways. *Elife* **10,** (2021).
6. Jones, M. E., Paniccia, J. E., Lebonville, C. L., Reissner, K. J. & Lysle, D. T. Chemogenetic Manipulation of Dorsal Hippocampal Astrocytes Protects Against the Development of Stress-enhanced Fear Learning. *Neuroscience* **388,** 45–56 (2018).
7. Nagai, J. *et al.* Hyperactivity with Disrupted Attention by Activation of an Astrocyte Synaptogenic Cue. *Cell* **177,** 1280–1292.e20 (2019).
8. Adamsky, A. *et al.* Astrocytic activation generates de novo neuronal potentiation and memory enhancement. *Cell* **174,** 59–71.e14 (2018).
9. Chai, H. *et al.* Neural Circuit-Specialized Astrocytes: Transcriptomic, Proteomic, Morphological, and Functional Evidence. *Neuron* **95,** 531–549.e9 (2017).
10. MacDonald, A. J., Holmes, F. E., Beall, C., Pickering, A. E. & Ellacott, K. L. J. Regulation

of food intake by astrocytes in the brainstem dorsal vagal complex. *Glia* **68,** 1241–1254 (2020).

11. Halassa, M. M., Fellin, T., Takano, H., Dong, J.-H. & Haydon, P. G. Synaptic islands defined by the territory of a single astrocyte. *J. Neurosci.* **27,** 6473–6477 (2007).
12. Bojarskaite, L. *et al.* Astrocytic Ca2+ signaling is reduced during sleep and is involved in the regulation of slow wave sleep. *Nat. Commun.* **11,** 3240 (2020).
13. Ingiosi, A. M. *et al.* A role for astroglial calcium in mammalian sleep and sleep regulation. *Curr. Biol.* **30,** 4373–4383.e7 (2020).
14. Durkee, C. A. *et al.* Gi/o protein-coupled receptors inhibit neurons but activate astrocytes and stimulate gliotransmission. *Glia* **67,** 1076–1093 (2019).
15. Volgushev, M., Chauvette, S., Mukovski, M. & Timofeev, I. Precise long-range synchronization of activity and silence in neocortical neurons during slow-wave oscillations [corrected]. *J. Neurosci.* **26,** 5665–5672 (2006).
16. Sanchez-Vives, M. V. & McCormick, D. A. Cellular and network mechanisms of rhythmic recurrent activity in neocortex. *Nat. Neurosci.* **3,** 1027–1034 (2000).
17. Niethard, N., Ngo, H.-V. V., Ehrlich, I. & Born, J. Cortical circuit activity underlying sleep slow oscillations and spindles. *Proc. Natl. Acad. Sci. USA* **115,** E9220–E9229 (2018).
18. Stroh, A. *et al.* Making waves: initiation and propagation of corticothalamic Ca2+ waves in vivo. *Neuron* **77,** 1136–1150 (2013).
19. Luczak, A., Barthó, P., Marguet, S. L., Buzsáki, G. & Harris, K. D. Sequential structure of neocortical spontaneous activity in vivo. *Proc. Natl. Acad. Sci. USA* **104,** 347–352 (2007).
20. Massimini, M., Huber, R., Ferrarelli, F., Hill, S. & Tononi, G. The sleep slow oscillation as a traveling wave. *J. Neurosci.* **24,** 6862–6870 (2004).

21. Krone, L. B. *et al.* A role for the cortex in sleep-wake regulation. *BioRxiv* (2020). doi:10.1101/2020.03.17.996090

22. Sanchez-Vives, M. V. & Mattia, M. Slow wave activity as the default mode of the cerebral cortex. *Arch Ital Biol* **152,** 147–155 (2014).

23. Lemieux, M., Chen, J.-Y., Lonjers, P., Bazhenov, M. & Timofeev, I. The impact of cortical deafferentation on the neocortical slow oscillation. *J. Neurosci.* **34,** 5689–5703 (2014).

24. Poskanzer, K. E. & Yuste, R. Astrocytic regulation of cortical UP states. *Proc. Natl. Acad. Sci. USA* **108,** 18453–18458 (2011).

25. Lemieux, M., Chauvette, S. & Timofeev, I. Neocortical inhibitory activities and long-range afferents contribute to the synchronous onset of silent states of the neocortical slow oscillation. *J. Neurophysiol.* **113,** 768–779 (2015).

26. Chen, J.-Y., Chauvette, S., Skorheim, S., Timofeev, I. & Bazhenov, M. Interneuron-mediated inhibition synchronizes neuronal activity during slow oscillation. *J. Physiol. (Lond.)* **590,** 3987–4010 (2012).

27. Sheroziya, M. & Timofeev, I. Global intracellular slow-wave dynamics of the thalamocortical system. *J. Neurosci.* **34,** 8875–8893 (2014).

28. Zucca, S. *et al.* An inhibitory gate for state transition in cortex. *Elife* **6,** (2017).

29. Mariotti, L., Losi, G., Sessolo, M., Marcon, I. & Carmignoto, G. The inhibitory neurotransmitter GABA evokes long-lasting Ca(2+) oscillations in cortical astrocytes. *Glia* **64,** 363–373 (2016).

30. Schousboe, A., Sarup, A., Bak, L. K., Waagepetersen, H. S. & Larsson, O. M. Role of astrocytic transport processes in glutamatergic and GABAergic neurotransmission. *Neurochem. Int.* **45,** 521–527 (2004).

31. Roth, B. L. DREADDs for neuroscientists. *Neuron* **89,** 683–694 (2016).

32. Marvin, J. S. *et al.* Stability, affinity, and chromatic variants of the glutamate sensor iGluSnFR. *Nat. Methods* **15,** 936–939 (2018).

33. Marvin, J. S. *et al.* A genetically encoded fluorescent sensor for in vivo imaging of GABA. *Nat. Methods* **16,** 763–770 (2019).

34. Danbolt, N. C. Glutamate uptake. *Prog. Neurobiol.* **65,** 1–105 (2001).

35. Anderson, C. M. & Swanson, R. A. Astrocyte glutamate transport: review of properties, regulation, and physiological functions. *Glia* **32,** 1–14 (2000).

36. Minelli, A., DeBiasi, S., Brecha, N. C., Zuccarello, L. V. & Conti, F. GAT-3, a high-affinity GABA plasma membrane transporter, is localized to astrocytic processes, and it is not confined to the vicinity of GABAergic synapses in the cerebral cortex. *J. Neurosci.* **16,** 6255–6264 (1996).

37. Armbruster, M., Hanson, E. & Dulla, C. G. Glutamate clearance is locally modulated by presynaptic neuronal activity in the cerebral cortex. *J. Neurosci.* **36,** 10404–10415 (2016).

38. Murphy-Royal, C. *et al.* Surface diffusion of astrocytic glutamate transporters shapes synaptic transmission. *Nat. Neurosci.* **18,** 219–226 (2015).

39. Parsons, M. P. *et al.* Real-time imaging of glutamate clearance reveals normal striatal uptake in Huntington disease mouse models. *Nat. Commun.* **7,** 11251 (2016).

40. Hudetz, A. G., Vizuete, J. A. & Imas, O. A. Desflurane selectively suppresses long-latency cortical neuronal response to flash in the rat. *Anesthesiology* **111,** 231–239 (2009).

41. Robson, J. G. The effects of anesthetic drugs on cortical units. *Anesthesiology* **28,** 144–154 (1967).

42. Minamisawa, G., Funayama, K., Matsumoto, N., Matsuki, N. & Ikegaya, Y. Flashing lights

induce prolonged distortions in visual cortical responses and visual perception. *Eneuro* **4,** (2017).

43. Funayama, K. *et al.* Neocortical rebound depolarization enhances visual perception. *PLoS Biol.* **13,** e1002231 (2015).
44. Diamond, J. S. & Jahr, C. E. Transporters buffer synaptically released glutamate on a submillisecond time scale. *J. Neurosci.* **17,** 4672–4687 (1997).
45. Savtchouk, I. & Volterra, A. Gliotransmission: Beyond Black-and-White. *J. Neurosci.* **38,** 14–25 (2018).
46. Jourdain, P. *et al.* Glutamate exocytosis from astrocytes controls synaptic strength. *Nat. Neurosci.* **10,** 331–339 (2007).
47. Bowser, D. N. & Khakh, B. S. Two forms of single-vesicle astrocyte exocytosis imaged with total internal reflection fluorescence microscopy. *Proc. Natl. Acad. Sci. USA* **104,** 4212–4217 (2007).
48. Zhang, Q. *et al.* Fusion-related release of glutamate from astrocytes. *J. Biol. Chem.* **279,** 12724–12733 (2004).
49. Bezzi, P. *et al.* Astrocytes contain a vesicular compartment that is competent for regulated exocytosis of glutamate. *Nat. Neurosci.* **7,** 613–620 (2004).
50. Woo, D. H. *et al.* TREK-1 and Best1 channels mediate fast and slow glutamate release in astrocytes upon GPCR activation. *Cell* **151,** 25–40 (2012).
51. Nam, M.-H. *et al.* Activation of Astrocytic μ-Opioid Receptor Causes Conditioned Place Preference. *Cell Rep.* **28,** 1154–1166.e5 (2019).
52. Kol, A. *et al.* Astrocytes contribute to remote memory formation by modulating hippocampal-cortical communication during learning. *Nat. Neurosci.* **23,** 1229–1239 (2020).

53. Mederos, S. & Perea, G. GABAergic-astrocyte signaling: A refinement of inhibitory brain networks. *Glia* **67,** 1842–1851 (2019).

54. Kang, J., Jiang, L., Goldman, S. A. & Nedergaard, M. Astrocyte-mediated potentiation of inhibitory synaptic transmission. *Nat. Neurosci.* **1,** 683–692 (1998).

55. Gunaydin, L. A. *et al.* Natural neural projection dynamics underlying social behavior. *Cell* **157,** 1535–1551 (2014).

56. Shi, G. *et al.* A Rare Mutation of β1-Adrenergic Receptor Affects Sleep/Wake Behaviors. *Neuron* **103,** 1044–1055.e7 (2019).

57. Bruno, C. A. *et al.* pMAT: An open-source software suite for the analysis of fiber photometry data. *Pharmacol. Biochem. Behav.* **201,** 173093 (2021).

Publishing Agreement

It is the policy of the University to encourage open access and broad distribution of all theses, dissertations, and manuscripts. The Graduate Division will facilitate the distribution of UCSF theses, dissertations, and manuscripts to the UCSF Library for open access and distribution. UCSF will make such theses, dissertations, and manuscripts accessible to the public and will take reasonable steps to preserve these works in perpetuity.

I hereby grant the non-exclusive, perpetual right to The Regents of the University of California to reproduce, publicly display, distribute, preserve, and publish copies of my thesis, dissertation, or manuscript in any form or media, now existing or later derived, including access online for teaching, research, and public service purposes.

DocuSigned by:
Trisha Vaidyanathan
5EF472011D8C40D...
Author Signature

8/19/2021
Date